PH.D. IN ASTRONOMY, ASTROPHYSICS
AND SPACE SCIENCE

CYCLE XXX

The origin, properties and fate of the first black holes in the Universe

Edwige Pezzulli

A.Y. 2016/2017

Supervisor: Prof. Raffaella Schneider
Co-supervisor: Dr. Rosa Valiante
Referee: Prof. Piero Madau
Referee: Prof. Priyamvada Natarajan
Coordinator: Prof. Pasquale Mazzotta
Deputy Coordinator: Prof. Roberto Capuzzo Dolcetta

"She drank from a bottle called DRINK ME
And she grew so tall,
She ate from a plate called TASTE ME
And down she shrank so small.
And so she changed, while other folks
Never tried nothin' at all."

S. Silverstein

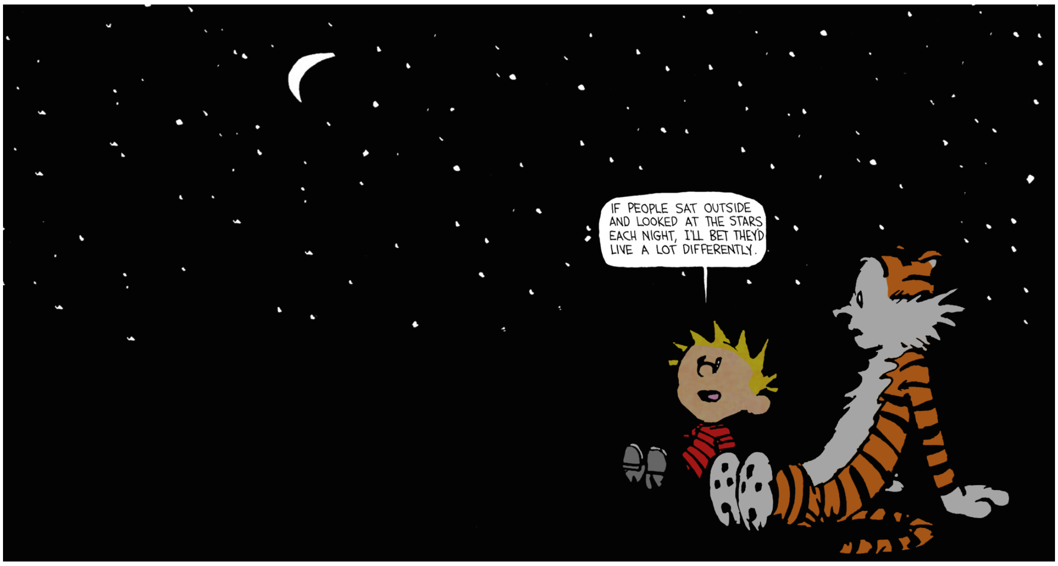

Calvin and Hobbes, Bill Watterson.

Abstract

Observations of the Universe's earliest quasars, less than 1 Gyr after the Big Bang, open the door to many questions. They are found to host supermassive black holes (SMBHs) with $M_{BH} = 10^9 - 10^{10}\, M_\odot$ (Fan et al., 2001, 2004; Mortlock et al., 2011), and BH formation models need to explain their existence and evolution in such a short time.

In the first part of this original work, we introduce the cosmological, semi-analytic code GAMETE/SuperQSOdust, which reconstructs several hierarchical merger histories of high-z bright quasars, following the time evolution of central BHs together with the mass of stars, gas, metals and dust. With this tool, we have studied the relative importance of different accretion regimes for the formation of the first quasars, with particular attention to accretion events occurring over the classical luminosity threshold - the so-called Eddington limit. We find that ~ 80 % of the final SMBH mass is grown by super-Eddington accretion, which can be sustained down to $z \sim 10$ in dense, gas-rich environments, and the average BH mass at $z \sim 20$ is $M_{\rm BH} \sim 10^4\, M_\odot$, comparable to that of direct collapse BHs.

However, stellar feedback from BH seed progenitors and winds from BH accretion disks may decrease BH accretion rates. Therefore, we studied the impact of these physical processes on the formation of $z \sim 6$ quasars, including new physical prescriptions in the model. We find that the feedback produced by the first stellar progenitors on the surrounding environment does not play a relevant role in preventing the SMBH formation. In order to grow the $z \sim 6$ SMBHs, the accreted gas must efficiently lose angular momentum. Moreover, disk winds, easily originated in the super-Eddington accretion regime, can strongly reduce duty cycles, producing a decrease in the active fraction among the progenitors of $z \sim 6$ bright quasars and thus reducing the probability to detect them.

From an observational point of view, no convincing candidates of faint progenitors of luminous high-z quasars have been selected in X-ray surveys (Treister et al., 2013; Weigel

et al., 2015; Cappelluti et al., 2016). In order to interpret this lack of detections, we have modelled the spectral energy distribution of accreting BHs. This modelling has been applied to a sample of simulated $z \sim 6$ SMBH progenitors, also taking into account the photon trapping effect which plays an important role at high accretion rates. The results show that faint progenitors are still luminous enough to be detected with current X-ray surveys. Even accounting for a maximum obscuration effect, the number of detectable BHs is reduced at most by a factor of 2. In our simulated sample, observations of faint BHs are mainly limited by their very low active fraction ($f_{act} \sim 1$ per cent), which is the result of short, supercritical growth episodes. We suggest that to detect high-z SMBH ancestors, large area surveys with shallower sensitivities, such as COSMOS Legacy and XMM-LSS+XXL, should be preferred with respect to deep surveys probing smaller fields, such as *Chandra* Deep Field South.

An alternative way of constraining the early growth of BHs is to compare theoretical models with observations of massive BHs ($M_{\rm BH} \sim 10^5\, M_\odot$) in local dwarf galaxies. To this aim, in the last part of this work, we introduced GAMESH, a simulation following the formation of a Milky Way-like halo in a well resolved cosmic volume of $(4~\rm cMpc)^3$. This model allows to follow the star formation and chemical enrichment histories of all the galaxies in the simulation box. In the near future, we plan to extend the model including a self-consistent evolution of BHs and their feedback onto the host galaxies. This will allow us to compare results obtained by different BH seeding and accretion models with observations of BH masses hosted by the Milky Way and dwarf galaxies. Here, we present a preliminary study, where we have post-processed the simulation output to analyse the mass and redshift distribution of BH seeds formed as remnants of Pop III stars, and the BH occupation fraction at $z = 0$. Our preliminary results have been obtained under the assumption that gas accretion gives a negligible contribution to BH mass growth and, hence, provide a lower limit to the mass of nuclear BHs found at $z = 0$. We compare our results with recent studies carried out by means of cosmological hydrodynamical simulations (Marinacci et al. 2014; Bonoli et al. 2016), and - given the quiescent history experienced by the Milky Way-like halo - we conclude that either (*i*) light BH remnants of Pop III stars are able to rapidly grow their masses soon after their formation, or (*ii*) that the Milky Way nuclear BH originates from more massive BH seeds, with masses comparable to the ones that characterize direct collapse BHs. In our future study, we will be able to analyse each of these two possibilities using the detailed treatment of chemical and radiative feedback effects allowed by GAMESH.

This thesis is divided into four main parts. In the first part, we introduce some basic theoretical tools for understanding the most important features of the formation of galaxies and black holes: in Chapter 1, we present the ΛCDM Cosmological Model and some fundamental properties of our Universe, including Large Scale Structures and galaxy formation, and in Chapter 2 we briefly describe the main characteristics of black holes and gas accretion disks orbiting around these compact objects. The second part of this work is dedicated to the high-z BHs: Chapter 3 is an extract from the review Valiante R., Agarwal B., Habouzit M., Pezzulli E., 2017, PASA 34, 31. In Chapter 4 we discuss the results obtained in the manuscript Pezzulli E., Valiante R., Schneider R., 2016, MNRAS, 458, 3047, and we also introduce the cosmological, semi-analytic model used for the study on the occurrence of different accretion regimes for the formation of high-z QSOs. In Chapter 5 we discuss on the sustainability of super-Eddington accretion in a cosmological context, including some prescriptions for the two negative feedback mechanisms introduced above. The results have been published in Pezzulli E., Volonteri M., Schneider R., Valiante R., 2017, MNRAS, 471, 589. Possible solutions for the current lack of faint, high-z AGNs observations are reported in Chapter 6, as investigated in Pezzulli E., Valiante R., Orofino M.C., Schneider R., Gallerani S., Sbarrato T., 2017, MNRAS, 466, 2131.

In the third part of the thesis, we turn our attention to the Local Universe and to the constraints that can be put on the evolution of nuclear BHs and their hosts from observations of the Milky Way and local dwarf galaxies. In Chapter 7 we present the results of our preliminary study on the mass and redshift distribution of BH seeds and their impact on the $z = 0$ BH occupation fraction. Finally, in Part IV, we summarize our main conclusions.

Contents

List of Acronyms

AGN Active Galactic Nuclei

BH Black Hole

BLR Broad-Line Region

CMB Cosmic Microwave Background

DCBH Direct Collapse Black Hole

DM Dark Matter

GR General Relativity

IGM Inter Galactic Medium

IMF Initial Mass Function

IR Infra-Red

ISM Inter-Stellar Medium

ISCO Innermost Stable Circular Orbit

LG Local Group

LW Lyman Werner

MBH Massibe Black Hole

NLR Narrow-Line Region

QSO Quasi-Stellar Object

SAM Semi-Analytic Model

SE Super-Eddington

SED Spectral Energy Distribution

SFR Star Formation Rate

SMBH Super Massive Black Hole

SN Super Nova

UV Ultra-Violet

Part I

Introduction

Chapter 1

The Universe

1.1 The Cosmological Model

The pillar of the Standard Hot Big Bang Cosmology is the *Cosmological Principle*, which states that the Universe is homogeneous and isotropic on large scales. This is confirmed by a growing number of observations, such as the distribution of galaxies around us, shown in Fig. 1.1 (Colless et al., 2001), and the cosmic microwave background (CMB) radiation (see Section 1.3), an image of the Universe only 380000 years after the Big Bang. These photons are coming from different parts of the sky, with a mean temperature of $< T >= 2.725$ K and a relative temperature differences of a part on 10^5.

Another fundamental property of the Standard Model is that the Universe is also expanding. It was discovered by Edwin Hubble in 1929, when he noticed that all galaxies are receding from us. Hubble measured the so-called *redshift* z from galaxy spectra, defined by the ratio

$$z = \frac{\lambda_{obs} - \lambda_{em}}{\lambda_{em}}, \tag{1.1}$$

where λ_{em} is the wavelength emitted by a galaxy and λ_{obs} is that measured by the observer. In particular Hubble found a correlation between redshifts z (and so, the velocity of recession v) and distances D of the galaxies, that for low values of redshifts takes the form of the *Hubble law*

$$v = cz = H_0 D, \tag{1.2}$$

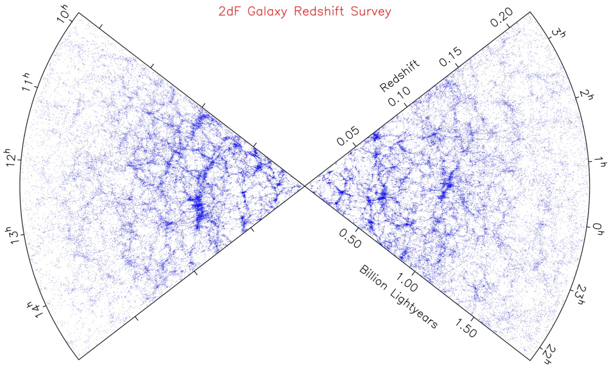

Figure 1.1. The distribution of galaxies in the complete 2dF Galaxy Redshift Survey. In the radial direction is plotted the redshift and the polar angle is the right ascension. Credit: Matthew Colless.

where c is the speed of light and H_0 is the *Hubble constant*, better described in Section 1.2.1.

Fig. 1.2 represents the original Hubble diagram that shows that the velocity of galaxies increases with distance. This is a proof that the whole Universe is expanding and that the wavelengths of photons emitted by a distant source are redshifted.

The past cosmic expansion history is recovered by solving the Einstein equations (see Section 1.2) in the background of the homogeneous and isotropic universe. However, observations of inhomogeneities in the density distribution of matter, such as clusters, galaxies and - on smaller scales - stars and planets, force us to explain how these grow out from an homogeneous background. This is done in the so-called *standard scenario*, which describes how small perturbations in the density field grow through gravitational instability, becoming non linear and then collapsing. In order to understand the nature and evolution of these density perturbations it is usual to proceed in the following way: first studying the overall dynamics by treating the universe as homogeneous and isotropic. The inhomogeneities observed are then considered as deviations from the smooth universe.

1.2 The Friedmann Model

Given the Cosmological Principle, it is necessary to construct a model of the Universe in which this principle holds. Since the predominant force on large scale is gravity, the model should be based on Einstein's General Relativity (GR). In particular, GR is a geometrical theory, therefore we must first investigate the geometrical properties of homogeneous and isotropic spaces.

The geometrical properties of space-time are described by the *metric tensor* $g_{\alpha\beta}$, a tensor such that in the equation

$$ds^2 = g_{\alpha\beta}(x) dx^\alpha dx^\beta, \tag{1.3}$$

ds represents the space-time interval between two points x^γ and $x^\gamma + dx^\gamma$.

The metric tensor determines all the geometrical properties of space-time described by the system of coordinates $\{x^\gamma\}$.

Let's suppose that we can describe the Universe as a continuous fluid and assign to each fluid element the three spatial coordinates x^i, called comoving coordinates. One can show that the most general space-time metric describing a universe in which the Cosmological Principle is satisfied is the Friedmann–Lemaître–Robertson–Walker (FLRW) metric:

$$ds^2 = dt^2 - a^2(t)\left[\frac{dr^2}{1 - Kr^2} + r^2(d\theta^2 + sin^2\theta d\phi^2)\right], \tag{1.4}$$

where we have used spherical polar coordinates (r, θ, ϕ) which are the comoving coordinates (r is by convention dimensionless); t is the proper time; $a(t)$ is a function to be determined which has the dimensions of a length and is called the *cosmic scale factor* or the *expansion parameter*, and assumes the value 1 at the present time t_0; the *curvature parameter* K is a constant which can be scaled in such a way that it takes only the values $0, \pm 1$. The cosmic scale factor is simply linked to the redshift by the relation

$$a(t) = \frac{1}{1 + z(t)}. \tag{1.5}$$

The geometrical properties of Euclidean space ($K = 0$) are well known. On the other hand, the properties of the hypersphere ($K = 1$) are complex. This space is closed, i.e. it has finite volume, but has no boundaries. The properties of a space of constant negative curvature ($K = -1$) are closer to those of Euclidean space: the hyperbolic space is open, i.e. infinite.

In cases with $K \neq 0$, the parameter a, which appears in Equation 1.4, is related to the curvature of space. In fact, the *Gaussian curvature*, C_G, is given by $C_G = K/a^2$;

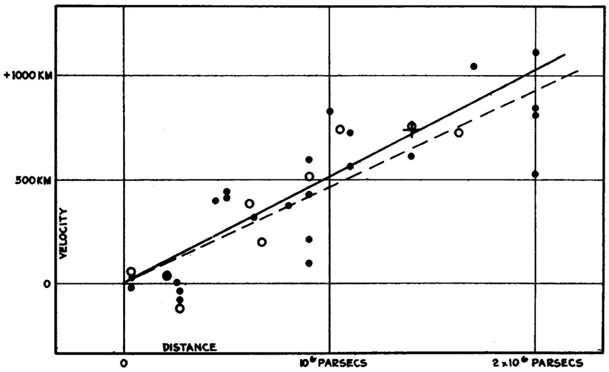

Figure 1.2. The original Hubble diagram (Hubble, 1929). Velocities of distant galaxies (units should be km s^{-1}) are plotted vs distance (units should be pc). Solid (dashed) line is the best fit to the filled (open) points which are corrected (uncorrected) for the Sun's motion (Hubble, 1929).

as expected it is positive (negative) for the closed (open) space. The *Gaussian curvature radius* $R_G = C_G^{-1/2} = a/\sqrt{K}$ is, respectively, positive or imaginary in these two cases. In cosmology one uses the term *radius of curvature* to describe the modulus of R_G; with this convention a always represents the radius of spatial curvature. Of course, in a flat universe the parameter a does not have any geometrical significance.

1.2.1 Friedmann equations

To relate the geometry of space-time, expressed by the metric tensor $g_{\alpha\beta}$, to the energy-matter content of the universe, expressed by the stress-energy tensor $T_{\alpha\beta}$, we make use of the Einstein Field Equations (EFE), a tensorial, dynamical equation which described how matter and energy change the geometry of the spacetime:

$$G_{\mu\nu} = \frac{8\pi G}{c^4} T_{\mu\nu}, \tag{1.6}$$

where $G_{\mu\nu} = R_{\mu\nu} - \frac{1}{2} g_{\mu\nu} R$ is the Einstein tensor, while $R_{\mu\nu}$ and R are the Ricci tensor and Ricci scalar, respectively.

Since we consider the Universe as a perfect fluid, the stress-energy tensor assumes the form:

$$T_{\mu\nu} = (p + \rho) u_\mu u_\nu - p g_{\mu\nu}, \tag{1.7}$$

where p is the pressure, ρ is the energy-density, and u_α is the fluid four-velocity, defined by:

$$u_\alpha = g_{\alpha\beta} u^\beta = g_{\alpha\beta} \frac{dx^\beta}{ds}, \tag{1.8}$$

$x^k(s)$ is the world line of a fluid element, i.e. the trajectory in space-time followed by the particle.

Under the assumption of the FLRW metric, the EFE yield

$$\frac{\ddot{a}}{a} = -\frac{4\pi G}{3c^2} (\rho + 3p), \tag{1.9}$$

for the time-time component, and

$$a\ddot{a} + 2\dot{a}^2 + 2Kc^2 = 4\pi G (\rho - p) a^2, \tag{1.10}$$

for the space-space components. The space-time components give 0 = 0.

Putting Equations 1.9 and 1.10 together, we obtain

$$\left(\frac{\dot{a}}{a}\right)^2 + \frac{Kc^2}{a^2} = \frac{8\pi G}{3}\rho. \tag{1.11}$$

Equations 1.9 and 1.11 represent the fundamental equations of the Standard Model. Their solution allows to determine the time evolution of the scale factor, $a(t)$, that defines the evolutionary history of the Universe.

Taking into account the cosmological constant Λ in Equation 1.6 we find the Friedmann equations

$$\left(\frac{\dot{a}}{a}\right)^2 = H^2 = \frac{8\pi}{3}\rho - \frac{K}{a^2} + \frac{\Lambda}{3}, \tag{1.12}$$

and

$$\frac{\ddot{a}}{a} = -\frac{4\pi}{3}(\rho + 3p) + \frac{\Lambda}{3}. \tag{1.13}$$

Historically the cosmological constant Λ was introduced by Einstein for the purpose of obtaining a static solution for the expansion equations, i.e. $\dot{a} \equiv 0$, but after the expansion of the Universe was discovered, he discarded it. Moreover the physical interpretation of such constant was not clear. Now the cosmological constant has been introduced again as an homogeneous energy density that causes the expansion of the Universe to accelerate and thus is part of the Standard Cosmological Model.

We rewrite the Equation 1.12 introducing the density parameter $\Omega_{0i} = \frac{\rho_{0i}}{\rho_{0c}}$, where the critical density is defined as

$$\rho_{0,c} = \frac{3H_0^2}{8\pi G} \approx 5 \times 10^{-30}\,\mathrm{g\,cm^{-3}}, \tag{1.14}$$

and obtain

$$\left(\frac{\dot{a}}{a}\right)^2 = H_0^2 \left[\Omega_{0m}\left(\frac{a_0}{a}\right)^3 + \Omega_{0r}\left(\frac{a}{a_0}\right)^4 + \Omega_{0\Lambda}\right]. \tag{1.15}$$

Equation 1.15 shows that matter scales with the expansion of the Universe as $\propto a^{-3}$, radiation as $\propto a^{-4}$ while the density of the cosmological constant Ω_Λ remains constant during cosmic evolution. It can be easily noticed that a positive cosmological constant tends to accelerate the Universe. The evidence for an accelerating expansion comes from observations of the brightness of type I a Supernovae (SNe), as reported in Riess et al. (1998). For this discovery Saul Perlmutter, Brian P. Schmidt and Adam G. Riess have been awarded the 2011 Nobel Prize in physics.

Standard Hot Big Bang Cosmology allows plenty of space for variations in its details, such as the current geometry of the Universe or its final fate, in form of free parameters called *cosmological parameters*, whose differences lead to different cosmological scenarios. The CMB, which carries a lot of information about the properties of our Universe, allows to measure most of the fundamental parameters of cosmology. The Planck Satellite, launched by European Space Agency (ESA) on 14 May 2009, provided a map of the CMB field at high angular resolution, covering at least 95 % of the sky. This allowed the high precision measurements of the cosmological parameters shown in Table 1.1, reported by Planck Collaboration et al. (2014) and adopted in this work. From Planck results we infer that at present time the Universe is dynamically dominated by the cosmological constant (70%), while the matter, mainly in the form of Dark Matter (DM), represents most of the remaining 30%.

Table 1.1. Cosmological parameters adopted in this work (Planck Collaboration et al., 2014).

Ω_{0m}	$\Omega_{0\Lambda}$	H_0
0.314	0.686	674

1.3 From the Big Bang to the first structures

The model of Universe made by matter, radiation and cosmological constant described in previous Sections, predicts a point in which a vanishes and the density diverges. This is the *Big Bang singularity*, happened $\sim$ 13.7 Gyr ago.

Despite some criticisms, the most popular theory of what happened $10^{-35} - 10^{-32}$ s after the Big Bang is called *inflation*, the exponential expansion of space the Universe experienced for a very short period ($t \sim 10^{-33}$ s) after the singularity. The occurrence of this epoch helps to explain several properties of our Universe. For instance, the present-day large-scale structure can be explained as the final product of the growth, produced by gravitational attraction, of small quantum fluctuations in the microscopic inflationary regions (see Section 1.3.1), and inflation can also explain the geometrical flatness of the Universe, its isotropy and homogeneity (see Linde 1982 for a complete discussion on Inflation).

From a dynamical point of view, the Universe has experienced different cosmic epochs, depending on the components dominating its dynamics during the cosmic expansion.

As shown in Fig. 1.3, for $t \rightarrow 0$, $a(t) \rightarrow 0$ and the component that dominated the first cosmic time was **radiation**, since:

$$\frac{\Omega_{0r}}{a(t)^4} \gg \frac{\Omega_{0m}}{a(t)^3} + \Omega_\Lambda .$$

During this cosmic epoch, the evolution of the scale parameter is $a(t) \propto \sqrt{t}$.

When

$$\frac{\Omega_{0r}}{a^4} = \frac{\Omega_{0m}}{a^3} \quad \Longrightarrow \quad a(t) = \frac{1}{1+z} = \frac{\Omega_{0r}}{\Omega_{0m}}, \tag{1.16}$$

we find the *equivalence epoch* between radiation and matter, that for the values of the cosmological parameters Ω_{0r} and Ω_{0m} found by the recent Planck satellite (Table 1.1), corresponds to a redshift $z_{eq} \simeq 3570$.

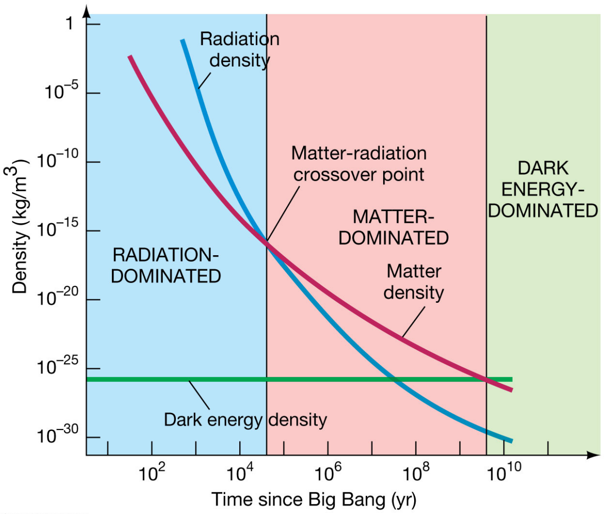

© 2011 Pearson Education, Inc.

Figure 1.3. Density behaviour of radiation (blue) matter (red) and cosmological constant (green) versus the time since Big Bang. The shaded regions represent the different cosmic epochs (reproduced from The Early Universe, Jim Brau).

The subsequent epoch was **matter dominated**, when the Universe expanded with a scale factor $a(t) \propto t^{2/3}$.

Finally, after the equivalence between matter and the cosmological constant, it began the **Λ-dominated** epoch, during which the dynamics followed an exponential expansion

$$a(t) = e^{\sqrt{\Omega_\Lambda} H_0 (t-t_0)}.$$

Another way to study the evolution of the Universe is through its thermal history, starting from the hot dense state emerging from the Big Bang and following its progressive expansion and cooling till the formation of atoms, molecules and, finally, bound structures. Given the impossibility of thermal exchanges with the outside, the cooling process of the Universe can be considered adiabatic, thus:

$$T \propto a(t)^{-1}. \tag{1.17}$$

which means that as the Universe expands, it cools.

To characterize the thermal history of the Universe, we can identify few fundamental phases, briefly described in Figure 1.4.

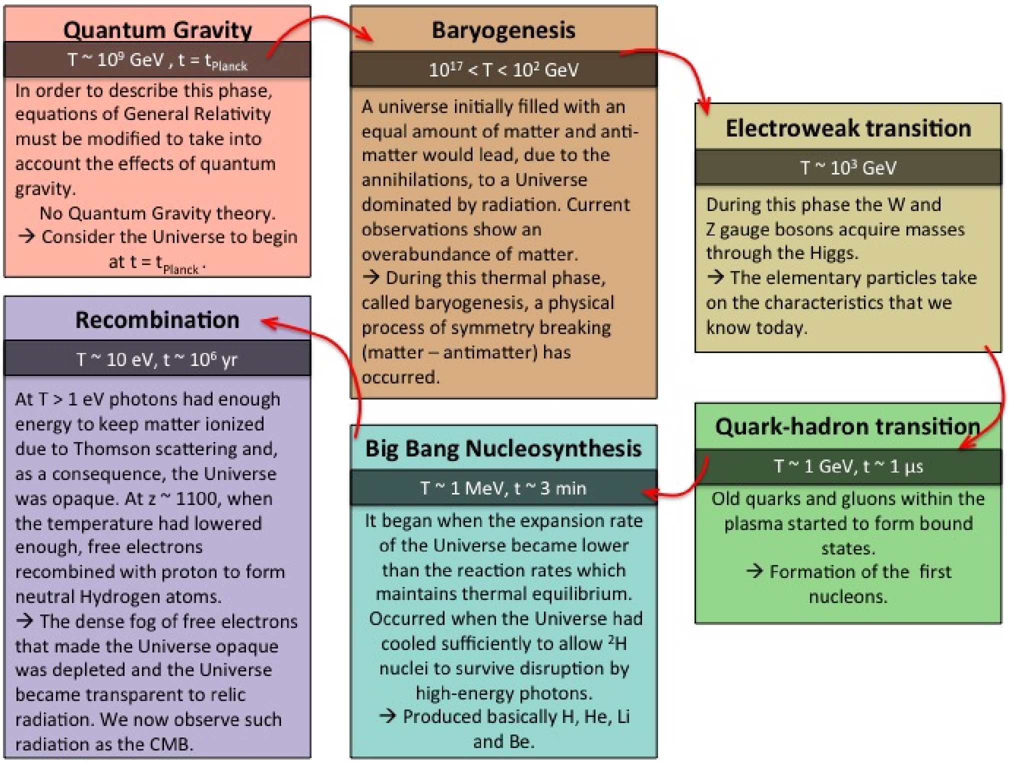

Quantum Gravity

$T \sim 10^9$ GeV , $t = t_{\mathrm{Planck}}$

In order to describe this phase, equations of General Relativity must be modified to take into account the effects of quantum gravity.

No Quantum Gravity theory.
→ Consider the Universe to begin at $t = t_{\mathrm{Planck}}$.

Baryogenesis

$10^{17} < T < 10^2$ GeV

A universe initially filled with an equal amount of matter and anti-matter would lead, due to the annihilations, to a Universe dominated by radiation. Current observations show an overabundance of matter.
→ During this thermal phase, called baryogenesis, a physical process of symmetry breaking (matter – antimatter) has occurred.

Electroweak transition

$T \sim 10^3$ GeV

During this phase the W and Z gauge bosons acquire masses through the Higgs.
→ The elementary particles take on the characteristics that we know today.

Quark-hadron transition

$T \sim 1$ GeV, $t \sim 1\ \mu s$

Old quarks and gluons within the plasma started to form bound states.
→ Formation of the first nucleons.

Big Bang Nucleosynthesis

$T \sim 1$ MeV, $t \sim 3$ min

It began when the expansion rate of the Universe became lower than the reaction rates which maintains thermal equilibrium. Occurred when the Universe had cooled sufficiently to allow ^{2}H nuclei to survive disruption by high-energy photons.
→ Produced basically H, He, Li and Be.

Recombination

$T \sim 10$ eV, $t \sim 10^6$ yr

At $T > 1$ eV photons had enough energy to keep matter ionized due to Thomson scattering and, as a consequence, the Universe was opaque. At $z \sim 1100$, when the temperature had lowered enough, free electrons recombined with proton to form neutral Hydrogen atoms.
→ The dense fog of free electrons that made the Universe opaque was depleted and the Universe became transparent to relic radiation. We now observe such radiation as the CMB.

Figure 1.4. A schematic representation of the six fundamental phases experienced by the Universe after the Big Bang. The time evolution can be followed with the direction of red arrows.

Shortly after Recombination, photons decoupled from matter in the Universe (**photon decoupling**). After that, they travelled freely through the Universe without interacting with matter, and this constitutes our current observation in the form of the Cosmic Microwave Background (CMB) radiation.

1.3.1 Linear growth

In the context of the Friedmann model we assumed the Universe to be homogeneous and isotropic, as stated by the Cosmological Principle. However, the observations show that matter in the Universe is non regularly-distributed, as there are several inhomogeneities in the form of galaxies, groups and clusters. These inhomogeneities, surrounded by empty regions (voids), are distributed in the space in mono-dimensional and two-dimensional structures called filaments and sheets. The theory of structures formation is based on the following assumption: at some time in the past there were small deviations from homogeneity. The overdense (with respect to the average) regions, collapsed due to gravitational instability. These density peaks kept growing up, forming the present day structures.

As long as the inhomogeneities are small, their growth can be studied by the *linear perturbation theory*. In this regime, the DM can be treated as a pressure-less fluid, and the set of equations describing the problem can be applied to both dark and baryonic matter. Once the deviations from the smooth universe become large, linear theory is no longer appropriate. Other techniques are developed to treat the *nonlinear evolution*, where the full Newtonian theory of gravity must be included. The equation describing this regime are referred only for DM, while for the baryons it is necessary to take into account all the baryonic physics, such as fluidodynamics and interactions between matter and radiation.

We begin our treatment of linear perturbation theory using the simplified model of a static Universe described by Newtonian theory of gravity. Our Universe can be described as a perfect fluid filled with random fluctuations in density, velocity, pressure, gravitation potential and entropy around some mean values. The equations needed to describe the density evolution of a given volume of a perfect fluid are

$$\frac{\partial \rho}{\partial t} + \nabla \cdot (\rho \mathbf{v}) = 0 \qquad \text{Continuity equation} \tag{1.18}$$

$$\frac{\partial \mathbf{v}}{\partial t} + (\mathbf{v} \cdot \nabla)\mathbf{v} + \frac{1}{\rho}\nabla p + \nabla\phi = 0 \qquad \text{Euler's equation} \tag{1.19}$$

$$\nabla^2 \phi = -4\pi G \rho \qquad \text{Poisson's equation} \tag{1.20}$$

$$\frac{\partial s}{\partial t} + \mathbf{v} \cdot \nabla s = 0 \qquad \text{Entropy conservation} \tag{1.21}$$

Let us consider a small perturbation on the above quantities, i.e. $\rho = \rho_0 + \delta\rho$, $\mathbf{v} = \delta\mathbf{v}$ ($\mathbf{v}_0 = 0$), $p = p_0 + \delta p$ and $\phi = \phi_0 + \delta\phi$ and define the dimensionless over-density $\delta(\mathbf{x})$ as

$$\delta(\mathbf{x}) \equiv \frac{\rho(\mathbf{x}) - \rho_0}{\rho_0}, \tag{1.22}$$

where ρ_0 is the average matter density over a volume V, large enough to make the Cosmological Principle to be valid. Due to the fact that it is impossible to predict primordial $\delta(\mathbf{x})$, it is generally assumed $\delta(\mathbf{x})$ to be a Gaussian field. The linear regime is valid as long as $\delta(\mathbf{x}) \ll 1$ everywhere.

Neglecting higher order terms and writing a generic fluctuation as a plain wave $\delta_i(t) = \delta_{0,i}e^{i\omega t}$ we obtain the dispersion relation:

$$\omega^2 - c_s^2 k^2 - 4\pi G\rho_0 = 0, \tag{1.23}$$

where $c_s = \partial p/\partial\rho|_s$ is the speed of sound. In Equation1.23, the value $\omega = 0$ divides two different solution regimes and defines the Jeans length-scale λ_J, i.e. the length over which the gravity amplifies overdense regions:

$$\lambda_J = \frac{2\pi}{k_J}\sqrt{\frac{\pi}{G\rho_0}}. \tag{1.24}$$

For $\lambda < \lambda_J$ we obtain oscillating solutions, while for $\lambda > \lambda_J$ the solutions are two stationary waves with an amplitude that increases (and decreases) exponentially with time.

Combining the Equations 1.18 and moving to the Fourier space, we obtain the time evolution of the perturbation for each k-mode:

$$\ddot{\delta}_k + 2\left(\frac{\dot{a}}{a}\right)\dot{\delta}_k = \left(\frac{c_s^2 k^2}{a^2} - 4\pi G\rho\right), \tag{1.25}$$

in the form of a second order differential equation that can be solved by writing explicitly the time dependence of $a(t)$ and $\rho(t)$. By solving Equation 1.25 in a matter-dominated expanding universe[1], we find the Jeans length that separated the two regimes of solution to be $\lambda_J(t) = \frac{c_s}{5}\sqrt{\frac{24\pi}{G\rho_b(t)}}$. The growing solution, which dominates for large times, takes the form

$$\delta_k(t) \propto t^{2/3} \propto a \tag{1.26}$$

while in the Λ-dominated epoque the density perturbations evolve as

$$\delta_k(t) \propto e^{-2Ht}. \tag{1.27}$$

There are two possible sequence of events that led to the formation of the structures: from the smaller scale to the larger one, i.e. large scale structures are built by the hierarchical gravitational clustering of smaller substructures (*bottom-up* scenario) or the other way around, i.e. large scale structures are the first to form and later on are disrupted to create smaller structures (*top-down* scenario). The difference between the two scenarios is a direct

---

[1] During the radiation-dominated phase, the DM perturbations are frozen by the effect of stagnation.

consequence of the nature of DM particles. In a Cold Dark Matter (CDM) scenario, within which DM particles are moving at non-relativistic speed, the structures grow hierarchically; in a Hot Dark Matter (HDM) scenario, within which DM particles are moving at relativistic speed, structures form by fragmentation of larger structures. Observations strongly favour the bottom-up scenario and as a consequence the CDM model. Indeed, if most DM were hot, all structures smaller than very massive galaxies would have been disrupted by the free streaming mechanism, while we know that such structures exist. For this reasons nowadays the bottom-up scenario is the most accepted by the cosmologists. Within it, the merging history of the halos can be traced in cosmological simulations and stored in the form of the so-called merger trees.

The Local Group (LG), which is composed by the Milky Way (MW) and our galactic neighbourhood, can be used as a laboratory for testing the predictions of the ΛCDM model. One of the most important discrepancies between ΛCDM model and observations is the so-called *missing satellite problem*, consisting in an over-abundance of predicted ΛCDM sub-halos compared to the satellite galaxies known to exist in the LG (Klypin et al., 1999). A possible explanation to this inconsistency is that there is a large number of low mass dark matter sub-halos that have not been able to attract enough baryonic matter and hence do not have detectable stars or gas in them. Therefore, a significant fraction of the accreted satellites may have been stripped apart by larger galaxies due to complex tidal interactions. Moreover, the apparent excess of substructures predicted by the theory is not just limited to the low-mass scale. In fact, simulations predict the presence of sub-halos so massive that they should not be affected by reionization, but whose internal structure seems incompatible with that of the brightest observed satellites (Boylan-Kolchin et al., 2011). This further discrepancy between simulations and observations is known as *too big to fail*. Lastly, there is also a discrepancy between the flat density profiles of dwarf galaxies and the cuspy profile predicted by N-body simulations, generally referred as the *cusp-core problem*.

Recent simulations showed that the small scale problems of ΛCDM model can be overcome by taking into account the baryon effects in the theoretical modelling (Fattahi et al., 2016).

1.3.2 Non-linear growth

So far, we considered only small perturbations ($\delta \ll 1$), but what happens to fluctuations that grow large enough to actually collapse? For instance, the DM density of the Milky Way at the Sun's position is $\sim 10^5$ times larger than the average density of the Universe. For such cases, we need to enter in the so-called *non-linear regime*, where the density evolution cannot be fully treated analytically anymore.

The simplest model for the formation of gravitationally bound structures is the *spherical collapse model*. Imagine a flat, matter dominated expanding universe with an homogeneous spherical region inside described by the density law:

$$\rho(t) = [1 + \delta(t)]\bar{\rho} \tag{1.28}$$

where $\bar{\rho}$ is the mean cosmic density $\bar{\rho} = \rho_0/a^3$. Since for small t the adimensional perturbation δ is small, the evolution of such region can be studied with the linear perturbation theory. The mass within the sphere is:

$$M = \frac{4\pi}{3} R_c^3 \rho_0 (1 + \delta) \simeq \frac{4\pi}{3} R_c^3 \rho_0, \tag{1.29}$$

where R_c is the comoving radius of the sphere of physical radius $R = aR_c$. Since the gravitational force inside a sphere depends only on the enclosed matter, over-dense sphere will evolve independently, like a closed sub-universe with density higher than the critical density. In particular, due to the enhanced gravitational force in the region, the expansion of the sphere will be slower than the rest of the universe. If the initial density is sufficiently large, at a certain time t_{ta} the expansion of the sphere will stop, reaching a maximum value for its radius $R(t_{\rm ta}) = R_{\rm ta}$ at the so-called *turn around point*. The spherical region, due to the time reversal symmetry of the equations of motion, will collapse at a time $t_{coll} = 2t_{\rm ta}$.

The spherical collapse model is based on the study of spherical perturbations which evolve depending on the values of the density contrast δ and the cosmic background model. We can identify three important values of the density contrast δ, which corresponds to three important phases of the evolution of the perturbation: the threshold beyond which the perturbation enters in the non-linear regime, $\delta_{\rm nl}$, the value at turn-around, $\delta_{\rm ta}$, and the density contrast beyond which the matter inside the perturbation can be considered as virialized

Table 1.2. Fundamental values of the density contrast δ in correspondence to three important phases of the evolution of the perturbation, for both linear theory and spherical collapse model.

Linear Theory	**Spherical collapse model**
$\delta_{\mathrm{non-linear,l}} = 0.568$	$\delta_{\mathrm{non-linear,sc}} = 1$
$\delta_{\mathrm{ta,l}} = 1.06$	$\delta_{\mathrm{ta,sc}} = 4.06$
$\delta_{\mathrm{vir,l}} = 1.686$	$\delta_{\mathrm{vir,sc}} = 177$

halo, δ_{vir}. Furthermore, as shown in Table 1.2, we can link those three fundamental values obtained in the spherical collapse model with those, incorrect, obtained extending the linear theory in the non-linear region. These relations allow us to characterise the dynamics of the perturbation using the linear theory. As an example, in order to have the collapse before a given redshift z, the over-density of the spherical perturbation must be:

$$\delta = \delta_{\mathrm{vir,l}}(1 + z), \tag{1.30}$$

where $\delta_{\mathrm{vir,l}} = 1.686$ is the value found in the linear regime.

The spherical collapse model is over-simplified: no density fluctuations collapse isolated in spherical symmetry. The collapse is generally followed by a relaxation process, called virialization, after which the DM halo satisfies the virial theorem. Thus, once virialized, halos can be described using the so-called virial properties (Barkana and Loeb, 2001), such as the virial radius R_{vir} and the virial temperature T_{vir}:

$$R_{\mathrm{vir}} = 0.784\left(\frac{M}{10^8 h^{-1} M_\odot}\right)^{1/3}\left[\frac{\Omega_m \Delta_c}{18\pi^2 \Omega_m(z)}\right]^{-1/3}\left(\frac{1+z}{10}\right)^{-1} h^{-1}\mathrm{kpc}, \tag{1.31}$$

$$T_{\mathrm{vir}} = 2\times 10^4\left(\frac{\mu}{0.6}\right)\left(\frac{M}{10^8 h^{-1} M_\odot}\right)^{2/3}\left(\frac{\Omega_m \Delta_c}{18\pi^2 \Omega_m(z)}\right)^{1/3}\left(\frac{1+z}{10}\right)^{-1} \mathrm{K}, \tag{1.32}$$

where μ is the mean molecular weight, $\Omega_m(z) = \Omega_m(1+z)^3/[\Omega_m(1+z)+\Omega_\Lambda+\Omega_k(1+z)^2]$ and Δ_c is the final overdensity relative to the critical density at the collapse z, which in a universe where $\Omega_r + \Omega_m + \Omega_\Lambda = 1$ can be written as (Bryan and Norman, 1998)

$$\Delta_c = 18\pi^2 + 82[\Omega_m(z) - 1] - 39[\Omega_m(z) - 1]^2. \tag{1.33}$$

In the bottom-up hierarchical structure formation scenario predicted by the CDM model, perturbations with the lowest mass are the first to undergo non-linear collapse, and thus form halos. These small-scale halos, following the redshift evolution, gradually merge to form higher mass halos. In this context, an interesting quantity to measure is the abundance of halos of a particular mass at a certain redshift. The process to derive such quantity has been described by Press and Schechter (1974). The main idea is that if we smooth the linear density field on some mass-scale M, the portion of space in which the density field exceeds a critical threshold δ_c, belongs to collapsed objects of mass M. The smoothing is analogous to filter on a scale R with a window function W_R. The critical density in the case of spherical collapse method is $\delta_c = 1.68$. If we assume a Gaussian random field of perturbations with a dispersion $\sigma(M, z)$, the probability distribution of density fluctuations can be written as:

$$p(\delta, \sigma) = \frac{1}{\sqrt{2\pi}\sigma} \exp\left(-\frac{1}{2}\frac{\delta^2}{\sigma^2}\right), \tag{1.34}$$

and the fraction of halos with mass M that has collapsed at redshift z is given by:

$$P(M, z) = \int_{\delta_c}^{\infty} p(\delta, \sigma) d\delta\,. \tag{1.35}$$

Finally, we can define the halo mass function, i.e. the number density of virialized halos in the mass range $M, M + dM$:

$$n(M, z)dM = \sqrt{\frac{2}{\pi}} \frac{\delta_c(t)}{\sigma_M^2(M)} \frac{\rho_0}{M} e^{-\frac{\delta_c^2(t)}{2\sigma_M^2(M)}} \left|\frac{d\sigma(M)}{dM}\right| dM, \tag{1.36}$$

where ρ_0 is the present-day unperturbed density and $\sigma(M)$ is the root mean square mass fluctuation on a comoving scale containing an amount of mass M.

With the Equation 1.36, we take into account only half of the mass of the Universe, so a factor 2 has to be included. This discrepancy is due to the so-called *cloud-in-cloud* problem, i.e. a miscount of low-mass object embedded within larger regions.

1.3.3 Gas infall and cooling

So far, we focused on the evolution of DM overdensities during the expansion of the Universe. However, we *observe* galaxies, i.e. the light emitted from the stars and gas present in them. Once dealing with gas, the treatment is not as easy as with non-collisional DM,

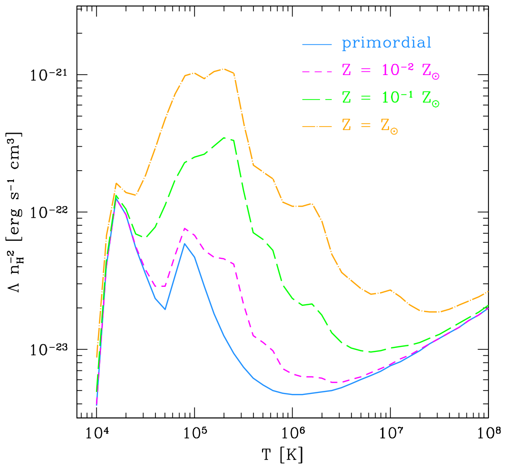

Figure 1.5. Cooling function multiplied by n_{H}^2 for different metallicities, as tabulated by Sutherland and Dopita (1993). The cooling rate increases with increasing metallicity (see text).

involving often dissipative and nonlinear processes. We can draw the following very raw scheme: during the matter-dominated phase, baryonic matter falls into the DM potential wells. The baryonic perturbations increase rapidly to the DM perturbations level, thereafter at the same rates. At the beginning of our picture, thus, the gas settles with the same spatial distribution as the DM. Once fluctuations in the DM turn around and collapse, the gas can be heated by shocks as it falls into the gravitational potential well of the dark halo, producing a hot gas halo that is pressure-supported against collapse, with a temperature T_{vir} described by Equation 1.32.

The gas can then cool - determining the reservoir from which the stars can form - through processes which strongly depend on its temperature and chemical composition. The temperature of the gas, in fact, determines the ionisation state, while the chemical composition is directly connected to the cross sections in play. The involved processes are basically 4 (Kauffmann et al., 1994): the first is the Inverse Compton scattering of CMB photons by hot electrons, which is important only at $z > 10$ (Rees and Ostriker, 1977); the second process, important for halos with $T_{\mathrm{vir}} \lesssim 10^4$ K, is the H_2 radiative cooling, occurring after the excitation (and subsequent decay) of rotational or roto-vibrational energy levels, which removes energy from the gas. The third process is the atomic-cooling, after the radiative decay due to a previous collision between partially ionised atoms and electrons, which excite atoms to higher energy levels. This cooling path is very important for halos with $T_{\rm vir} > 10^4$ K. Finally, the last process is Bremsstrahlung radiation, produced by the accelerated electrons in a ionized plasma. This process is dominant only in massive cluster ($T_{\rm vir} \sim 10^7$ K).

We can specify the cooling time $t_{\rm cool}$ by dividing the thermal energy density of the gas by the cooling rate per unit volume:

$$t_{\rm cool} = \left(\frac{3}{2}\frac{\rho_{\rm gas} k T_{\rm vir}}{\mu m_{\rm H}}\right) / [\rho_{\rm gas}^2 \Lambda(T_{\rm vir}, Z_{\rm gas})], \tag{1.37}$$

where $\rho_{\rm gas}$ is the gas density and Λ is the cooling function, shown in Figure 1.5 as tabulated by Sutherland and Dopita (1993).

For primordial gas, the cooling function shows two peaks, related to photoemission due to H and He recombination. For heavier elements the involved cooling processes for each temperature are more complex. However, increasing metallicity implies increasing channels available for cooling. As a results, metal-rich gas will cool much more efficiently than metal-poor gas.

As the gas cools, its pressure decreases and the gas falls toward the centre of the galaxy, settling on a disk structure once the angular momentum is conserved. The rate at which the cold reservoir forms depends on both the cooling timescale (i.e. how fast the gas can cool) and on the halo dynamical timescale (i.e. how rapid the cold gas falls in the galactic centre).

The simple picture described above can become more complicated if we account for additional physical processes. For instance, the presence of a photo-ionising radiation can suppress the cooling in low-mass halos (Haiman and Loeb, 1997; Gnedin, 2000; Omukai, 2001; Machacek et al., 2001; Valiante et al., 2016) and SN explosions or central BH feedback can reduce the cooling rate in massive halos by heating the hot halo gas (Bower et al., 2001, 2006; Croton et al., 2006).

1.3.4 Formation of stars

The theory of star formation (SF) is still far from being fully understood. Stars form from the collapse of dense interstellar gas, called molecular clouds (MCs), with sizes, densities and temperatures such that molecules are formed. These clouds are, in fact, composed mainly by H_2 and CO, with the presence of dust. The denser parts of the cloud can collapse under its self-gravity, and star formation begins. As the cores collapse, they fragment into clumps, which then form protostars, with the whole process taking $\sim 10^7$ yr.

Since 1944, with the seminal work of Walter Baade, it is possible to classify stars into two main populations, depending on their metallicity. The most metal-rich stars, Population I (Pop I) stars, have metallicities $Z > 0.1\,Z_\odot$, where $Z_\odot = 0.013$ (Asplund et al., 2009), and were found mainly in spiral arms of our Galaxy. The second population of stars (Pop II stars) are instead metal-poor ($Z \sim 10^{-4}, 10^{-3}$) with respect to Pop I stars, suggesting that they are formed in less metal-polluted environments, probably during an earlier time of the Universe, and found generally in the halo of MW. However, since the metallicity produced by the Big Bang Nucleosynthesis (BBN) is only $Z \sim 10^{-12} - 10^{-10}$, the gas from which Pop I and Pop II stars form must have been recycled by previous generations of stars. With this simple argument, a third population of stars, the so called Pop III stars, has been invoked. These stars should have formed from the (almost) metal-free gas, and polluted the surrounding gas through winds and supernova explosions. From these metal enriched regions, Pop II stars would have then formed. Indeed, this process cannot be explained by anything else but the chemical enrichment produced by the activity of these first, metal-free Pop-III stars (Heger and Woosley, 2002), which have never been directly detected so far.

The era between $z \sim 1100$ ($t_\mathrm{H} \sim 380000$), probed by the CMB, and $z \sim 11$ ($t_\mathrm{H} \sim 400$ Myr), where the farthest galaxy ever observed lies (Oesch et al., 2016), is called *Dark Ages*. This crucial phase ends when the first stars and accreting black holes turned on and shined, radiating copious amount of ionizing photons and starting the process called *Reionization* of the Universe. This non-instantaneously process (starting at $z \sim 20-30$), was the second[2] most important phase transition of the Universe, and consists in the reionization, on cosmic scale, of the hydrogen (H-Reionization) and helium (He-Reionization). These two phase transitions appear at different times in Cosmic history. Since the majority of matter is in the form of hydrogen, the term Reionization generally refers to the H-Reionization.

Pop III stars

The first generation of stars are thought to be very different from the one we observe nowadays. Due to the low presence (or absence) of metals in the early Universe, Pop III stars

---

[2] After the recombination - the first phase transition - the elements in the Universe were neutral.

are more massive and with hotter surface temperatures with respect to Pop I/ II stars.

In Pop III native clouds, radiative de-excitation of H_2 is the only coolant able to decrease the temperature down to $\sim$ few 100 K, allowing stars to form. After the formation of H_2 and for high enough gas densities ($\sim 10^{18}\,\mathrm{cm}^{-3}$), the gas becomes optically thick to H_2 cooling, and thermal evolution becomes adiabatic (Omukai, 2000; Yoshida et al., 2006). During an adiabatic collapse, temperature, which is related to density ($T \propto \rho^{2/3}$ for atomic gas) increases. In this case, the Jeans mass $M_J \propto T^{3/2}/\rho_0^{1/2}$ (i.e. the minimum cloud mass for becoming gravitational unstable, with subsequent collapse), would increase with increasing density. This implies that in metal-free condition, MCs are:

(*i*) initially hotter, and

(*ii*) no (or very limited) fragmentation occurs.

For these reasons, Pop III stars will be more massive than late type stars and more luminous, due to the higher surface temperature. While Pop III stellar masses suggested by the first simulations were $M \sim 100\,M_\odot$ (Abel et al. 2002; Bromm et al. 2002), models including UV radiation emitted by the protostar showed that the characteristic stellar mass is reduced to $\sim 40\,M_\odot$ (Hosokawa et al. 2011; Stacy et al. 2012). In more recent simulation, Hirano et al. 2014 found stellar masses in the range $10 - 10^3\,M_\odot$, with a dependence on their formation environment. Being massive, Pop III life-time τ is short ($\tau \sim M_\star^{-3}$), about few $\times 10^6$ yr. They end as SNe, enriching the interstellar medium (ISM) with metals and possibly leaving also a BH remnant.

For further details on Pop III properties and formation sites, see Section 3.3.1.

Chapter 2

Black holes

The first theorization of objects with gravity strong enough to prevent the light to escape were by John Michell and Pierre-Simon Laplace in the 18th century. After the development of the Einstein GR theory, and the first BH solution found by Karl Schwarzschild in the beginning of 20th century, BHs were set-aside as mathematical exoticism, and reconsidered as a part of GR only in 1960s. Their physical and mathematical peculiarities, drawing a very uncommon picture, make them above the most charming objects present in the Universe.

From a mathematical point of view, a BH is a particular solution of the Einstein Field Equation (EFE, Equation 1.6). Thanks to the no hair theorem emerged from the work done by W. Israel (Israel, 1967), B. Carter Carter (1971) and D. Robinson (Robinson, 1975), we know that stationary BHs are fully described by only three parameters: the mass M, the spin - the dimensionless ratio between the angular momentum and the mass of the BH $\mathbf{a} = \mathbf{J}/M$, and the charge Q. The description is even simpler for astrophysical BHs, which are neutral, so that the parameters reduce to $\mathbf{a}$ and M.

In the following, we will introduce some important concepts concerning BHs, such as their brief description in GR and an introduction to the gas accretion process.

2.1 Schwarzschild and Kerr solution

In GR, a non-rotating BH ($\mathbf{a} = 0$) is the solution of the EFE which describes the space-time outside a spherical mass, found by Schwarzschild in 1916 (Schwarzschild, 1916).

The peculiarity of this geometrical solution is that there is a spherical surface, called *event horizon*, where bizarre phenomena occur, among which the most important is that the escape velocity from this surface is equal to the speed of light. This means that nothing which, falling towards the BH, crosses the event horizon, is able to do it on the way around, remaining confined in a region causally disconnected from the rest of the Universe.

The line element (i.e. an infinitesimal displacement vector in a metric space) for the Schwarzschild metric takes the form:

$$ds^2 = -\left(1 - \frac{R_s}{r}\right)c^2 dt^2 + \left(\frac{1}{1 - \frac{R_s}{r}}\right)dr^2 + r^2(d\theta^2 + \sin^2\theta d\phi^2), \tag{2.1}$$

where

$$R_s = 2GM_\bullet/c^2, \tag{2.2}$$

is the Schwarzschild radius. For a non-rotating body, the Schwarzschild radius coincides with the event horizon.

When $R_s/r \ll 1$ the gravitational field is weak and the Newtonian approximation applies, while for $r \to \infty$ the metric reduces to Minkowski's metric (i.e. it is asymptotically flat).

The equation of motion of a massive test particle in the Schwarzschild space-time is a 2D-stable circular orbit, and the radius of the Innermost Stable Circular Orbit (ISCO) is,

$$R_{\rm ISCO} = \frac{6GM_\bullet}{c^2} = 3R_s. \tag{2.3}$$

while the maximum efficiency with which energy is extracted (see Section 2.2) occurs at $R_{\rm ISCO}$, and is

$$\epsilon_{r,ISCO} = 0.057. \tag{2.4}$$

The case of rotating, uncharged axially-symmetric BH with a spherical event horizon is called Kerr BH, and the Kerr line element in the Boyer-Lindquist coordinates takes the form:

$$ds^2 = -dt^2 + \Sigma\left(\frac{dr^2}{\Delta} + d\theta^2\right) + (r^2 + a^2)\sin^2\theta d\phi^2 + \frac{2Mr}{\Sigma}(a\sin^2\theta d\phi - dt)^2 \tag{2.5}$$

where

$$\Delta(r) \equiv r^2 - 2Mr + a^2, \tag{2.6}$$

$$\Sigma(r, \theta) \equiv r^2 + a^2 \cos^2 \theta, \tag{2.7}$$

where M, by comparing it with the asymptotically flat limit, represents the BH mass, while Ma its angular momentum.

The Kerr metric is stationary, axisymmetric but not static. Furthermore, for $a \to 0$, it reduces to the Schwarzschild metric while for $r \to \infty$ to the Minkowski's space-time in polar coordinates.

The event horizon of a Kerr BH corresponds to the surface for which $\Delta = 0$, i.e.

$$r_+ = M + \sqrt{M^2 - a^2}. \tag{2.8}$$

For $M = a$, the event horizon disappears. This condition is excluded by the Roger Penrose's *cosmic censorship hypothesis* in 1969 (Penrose, 1969): no "naked" singularity - except the Big Bang - exists in the Universe. On the other hand, $a^2 > M^2$ has no real solution. Despite this possibility is still debated, numerical simulations on astrophysical processes leading to BH formation suggest that $a < M$, and the condition $a > M$ is generally considered non-physical. Thus, it is generally assumed

$$a^2 \leq M^2, \tag{2.9}$$

where $a^2 = M^2$ is called *extremal* or *maximally rotating* BH.

In Kerr space-time, the radius of the ISCO depends on the spin of BH, and on the rotational direction of the orbiting particle with respect to the spinning BHs. In general, it can be expressed as (Bardeen et al., 1972):

$$R_{\text{ISCO}} = \frac{1}{2} R_s \left[3 + Z_2(a) \pm \sqrt{(3 - Z_1(a))(3 + Z_1(a) + 2Z_2(a))} \right], \tag{2.10}$$

where $Z_{1,2}(a)$ are functions of the spin parameter only and the sign ± refers to the co- (counter-) rotating case. For two extreme BHs with $a = M$, we find

$$R_{\mathrm{ISCO-}} = \frac{GM}{c^2}, \tag{2.11}$$

$$R_{\mathrm{ISCO+}} = \frac{9GM}{c^2}, \tag{2.12}$$

where − refers to the direct motion, while + to the retrograde one.

The last stable circular orbit in the equatorial plane corresponds to a maximum efficiency of energy extraction, which is a function ranging from

$$\epsilon_{\mathrm{r,ISCO}} = 0.057, \tag{2.13}$$

for non rotating BHs, while for maximally rotating BHs with co-rotating gas accretion flow it will be,

$$\epsilon_{\mathrm{r,ISCO}} = 0.423. \tag{2.14}$$

2.2 Accretion onto a BH

Accretion onto massive objects is a very important physical process. Massive bodies can accrete matter, generally gas, from the surrounding. The infall of matter, from less to more bound orbits, produces an extraction of gravitational energy, approximately proportional to the ratio M/R between the mass of the central object M and its radius R: the more the object is compact and massive, the larger is the amount of energy that can be released during accretion. This energy can be converted into radiation. In fact, together with gravity, viscosity can heat up the orbiting gas, causing thermal emission from the accreting material.

The detection of binary BHs merging pairs (Abbott et al., 2016a,b) opened the way to gravitational astronomy, which offers a new observational window to the "dark" Universe. So far, however, accretion has been the main physical process who made possible observational study of BHs. In fact, non-accreting BHs are indirectly detectable for dynamical perturbation produced on the motion of stars orbiting around them, but this is possible only for $M_{\mathrm{BH}} \gtrsim 10^7\ M_{\odot}$ and nearby galaxies (Gültekin et al., 2009; Greene et al., 2010).

To understand the radiative power generated through accretion, let us consider a particle mass m at an infinite distance from a central BH with mass M_{BH}. Its gravitational energy will be $E_i = 0$. Once this particle joins the ISCO, its energy becomes

$$E_f = \frac{1}{2}\frac{GM_{\rm BH}m}{R_{\rm ISCO}}, \tag{2.15}$$

and for a varying mass rate approaching the BH we find

$$\frac{dE}{dt} \equiv L = \frac{1}{2}\frac{GM_{\rm BH}}{R_{\rm ISCO}}\frac{dm}{dt}, \tag{2.16}$$

where L is, by definition, the luminosity. Rewriting the radius $R_{\rm ISCO}$ as $R_{\rm ISCO} = 2\beta GM_{\rm BH}/c^2 = \beta R_s$, the energy released per unit second of accreting material from infinity to the inner orbit is

$$\frac{dE}{dt} = \frac{1}{4\beta}\frac{dm}{dt}c^2, \tag{2.17}$$

defining $dx/dt = \dot{x}$ and $\epsilon_r = 1/4\beta$, the luminosity can be written as

$$L = \epsilon_r \dot{m} c^2. \tag{2.18}$$

The net output from the accretion process can, thus, be summarized in the radiative efficiency ϵ_r, which is the radiative energy generated per unit rest-mass accreted.

Radiative efficiencies found for BHs can be $\epsilon_r \gtrsim 0.4$ (see Equation 2.14) for maximally spinning BH. This means that more than 40% of the accreting material is converted in radiation. To better understand the order of magnitude of such emission, let us compute the radiative efficiency of proton-proton (pp) chain reaction. The pp chain reaction, which is a channel of stellar nucleosynthesis, consists in the conversion of 4 protons in one helium nucleus α, i.e. $4{\rm p} \rightarrow \alpha^2 + 2{\rm e}^+ + 2\nu_{\rm e} + 4.3\times10^{-12}$ J, with the side production of two positrons, two neutrinos and energy. The radiative efficiency of this process is:

$$\epsilon_r = \frac{4m_p - m_\alpha}{4m_p} \sim 0.007, \tag{2.19}$$

where m_p is the proton mass and m_α is the mass of the α particle.

The efficiency of accretion is $\sim$ 50 times larger than nuclear fusion, and it is involved in most of the high-luminosity phenomena in the Universe. The emerging light makes possible the detection of these luminous objects also very far from us, driving the study of BHs and distant massive BHs for the last few decades.

In general, the geometry of the flow can be simplified as spherical or disk-like, depending, inter alia, on the intrinsic angular momentum of the gas.

In the following Sections we discuss some properties of the two main geometries in very idealized accretion models.

2.3 Spherical flows: the Bondi accretion

The pioneer of the study of spherical accretion onto compact objects was Hermann Bondi in the fifties. He formalized the problem of spherical accretion and gas dynamics in a gravitational field.

Consider a central compact object of mass M surrounded by a spherically symmetric gas reservoir. Far from the accreting object, the gas has a uniform pressure P_∞ and density ρ_∞, while the sound speed will be $c_{s,\infty} = (\gamma P_\infty/\rho_\infty)^{1/2}$, where γ is the adiabatic index.

Assuming a steady accretion, and combining the equations of mass and momentum conservation, it is possible to write the so-called Bondi equation (Bondi, 1952):

$$\frac{1}{2}\left(1-\frac{c_s^2}{u^2}\right)\frac{du^2}{dr} = -\frac{GM}{r^2}\left[1-\frac{2c_s^2 r}{GM}\right]. \tag{2.20}$$

Let us assume a radius, defined as the Bondi radius

$$r_B = \frac{2GM}{c_s^2}, \tag{2.21}$$

which represents the approximated radius of influence of an accreting body. For $r = r_B$ the right side of Equation 2.20 vanishes, thus the left side translates into

$$u(r_B)^2 = c_s(r_B)^2 \rightarrow \left.\frac{d(u^2)}{dr}\right|_{r=r_B} = 0. \tag{2.22}$$

Bondi equation admits six solutions, which describe their behaviours at r_B, $r \rightarrow \infty$ and $r \rightarrow 0$.

For our purpose, we focus on the so-called *type 1* solution - one of the two transonic solutions

$$u(r_B)^2 = c_s(r_B)^2\,,\;\; u^2 \rightarrow 0 \text{ as } r \rightarrow \infty, \tag{2.23}$$

which represents an subsonic accretion flow at $r > r_B$ and supersonic at $r < r_B$. Under the assumption of an adiabatic infall, it is possible to uniquely determine the mass accretion rate $\dot{M}_B$:

$$\dot{M}_B = 4\pi q_s \frac{G^2 M^2 \rho_\infty}{c_{s,\infty}^3}, \tag{2.24}$$

where

$$q_s(\gamma) = \frac{1}{4}\left(\frac{2}{5-3\gamma}\right)^{(5-3\gamma)/(2\gamma-2)}, \tag{2.25}$$

and ranges from $q_s(\gamma = 5/3) = 1/4$ to $q_s(\gamma = 1) = 1.12$.

Spherical, steady accretion, thus, depends on the square of the central compact object's mass and the physical conditions of the surrounding gas at large distances from it.

2.4 Eddington Limit

As already introduced, the accretion process produces a huge amount of radiation. There will be a maximum luminosity, called the Eddington luminosity, $L_{\rm Edd}$, beyond which radiation pressure overcomes gravity, blowing out the gas and inhibiting the accretion process itself.

Let us consider a non rotating, spherically symmetric gas of ionized hydrogen around a central source M. Emitted photons couple with free electrons[1] due to Thomson scattering, producing an outward force of radiation pressure, whit a energy flux $F = L/4\pi r^2$ at a radius r from the source, where L is luminosity. Remembering that the photon momentum is $p = E/c$, the outward momentum will thus be

$$P_{\rm r} = \frac{F}{c} = \frac{L}{4\pi r^2 c}. \tag{2.26}$$

The (radial) radiative force on a single electron is

$$F_{\rm r} = P_r \sigma_T = \frac{L}{4\pi r^2 c}\sigma_T, \tag{2.27}$$

where $\sigma_T \sim 6.6 \times 10^{-25}{\rm cm}^2$ is the electron Thomson-scattering cross section.

On the other hand, protons[2] are attracted inward due to gravity, through a (radial) force

---

[1] Pressure on protons is neglected due to their higher inertia, which reduces the gradient of pressure on protons of a factor $(m_p/m_e)^2 \sim 10^6$.

[2] gravitational force acting on electrons is $m_p/m_e \sim 10^3$ times lower than that on protons. Thus, it is possible to neglect this term.

$$F_g = \frac{-GMm_p}{r^2}. \tag{2.28}$$

To keep the gas bound, it must be

$$|F_r| \leq |F_g|, \tag{2.29}$$

which translates into a condition on the luminosity

$$L \leq \frac{4\pi G c m_p}{\sigma_T} M \equiv L_{\mathrm{Edd}}, \tag{2.30}$$

where L_{Edd} is the Eddington luminosity, and that can be conveniently expressed as:

$$L_{\mathrm{Edd}} \approx 3.3 \times 10^4 \left(\frac{M}{M_\odot}\right)\left(\frac{L}{L_\odot}\right) \approx 1.26 \times 10^{38} \left(\frac{M}{M_\odot}\right) \mathrm{erg\,s^{-1}}. \tag{2.31}$$

It is possible to define also the Eddington mass accretion rate $\dot{M}_{\mathrm{Edd}}$, i.e. the accretion rate producing an Eddington luminosity

$$\dot{M}_{\mathrm{Edd}} = \frac{L_{\mathrm{Edd}}}{\epsilon_{r,E} c^2}. \tag{2.32}$$

Adopting the general assumption for $\dot{M}_{\mathrm{Edd}}$ of $\epsilon_{r,E} = 1/16$, the above relation can be rewritten as

$$\dot{M}_{\mathrm{Edd}} = 3.54 \times 10^{-8} \left(\frac{M}{M_\odot}\right) \frac{M_\odot}{\mathrm{yr}}. \tag{2.33}$$

In the previous section, we have seen that the conversion factor between the physical cause, $\dot{M}$, and the physical consequence, L, is the radiative efficiency ϵ_r.

Indeed, in principle, it is possible to exceed the Eddington mass accretion rate, still under the condition $L < L_{\mathrm{Edd}}$, if the radiative efficiency is *sufficiently* small. This would produce a super-Eddington flow (and a super-Eddington growth) without a blow-out of the gas reservoir from which the central object accretes. The Eddington luminosity can be exceeded also when the accretion flow is not spherical, i.e. in presence of accretion disks. In the latter case, accretion would mostly take plane in the equatorial place, while the radiation is emitted in the vertical direction, and it is not capable to stop the gas inflow.

2.5 Accretion from a disk

The accretion process can be far from spherically symmetric. In fact, matter generally has non-zero angular momentum.

During the collapse triggered by the gravity of the central object, the gas cloud will conserve its angular momentum, producing increasing angular velocity. This rotation is responsible for the flattening of the cloud, which will form a disk-structure. But as long as a particle, orbiting around a BH, should conserve its angular momentum, no accretion process and, thus, no energy emission would occur. It is necessary to transport angular momentum from inner to outer radii. In this way, inner particles are able to fall into smaller orbits, producing a luminous accretion disk and flowing onto the BH. The key-process that is able to transport outward angular momentum and dissipate energy is viscosity. Let us assume two parallel shear flows, one with velocity v_1 and the second with v_2, where $v_1 > v_2$. Viscosity acts tending to uniform the layers, with a momentum transferred from the faster to the slower one. Through this mechanism, in viscous disks mass accretes inward, while angular momentum is transferred outward.

Dynamical timescale of accretion disks are generally much shorter than the timescales of thermal and viscous processes (Abramowicz et al., 1988). For this reason, it is possible to restrict the treatment only to the dynamical structure. The relative importance of gravity, pressure and rotation gives rise to different types of accretion disks, and the most known structures are shown in Figure 2.1.

Accretion disk models generally assume stationary, axially symmetric distribution of matter accreting onto the BH. All physical quantities, thus, are assumed to depend only on the distance from the central body, r, and half thickness of the disk, z. In the following, we briefly outline three well studied case: first, the *thin* model, (Shakura and Sunyaev, 1973), for which $z/r \ll 1$ in every point of the structure. The second one is the *slim* disk model (Abramowicz et al., 1988), where $z/r \leq 1$, while the third model is the advection dominated accretion flow (ADAF), which is characterized by very low accretion rates with respect to the Eddington one, and for which $z/r \sim 1$.

Accretion rates in thin disks are sub-Eddington, and flows go down into the BHs with almost circular, Keplerian geodesic orbits. They have high luminosities, due to high radiative efficiencies (i.e. all the heat generated by viscosity at a given radius is immedi-

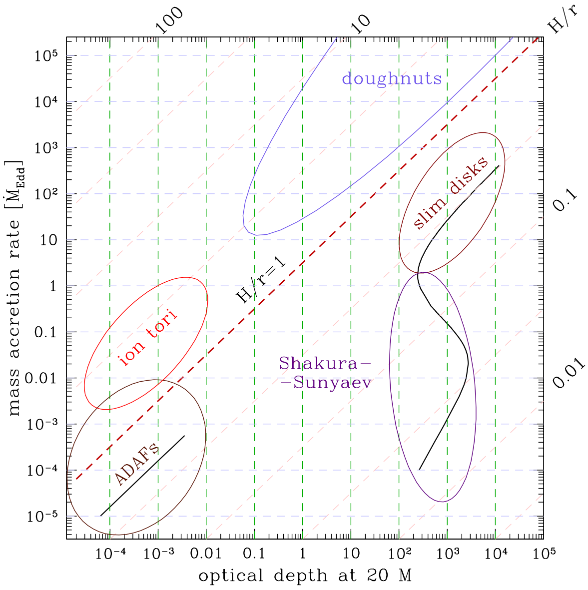

Figure 2.1. Some of the known analytic and semi-analytic solutions of stationary BH accretion disks. Adapted from Sądowski (2011)

ately radiated away): $\epsilon_r = 0.057$ for non rotating BH, while $\epsilon_r = 0.420$ for $a = 1$, and the mechanisms responsible for the outward transportation of angular momentum are both magneto-rotational instability effects, together with gas viscosity (Chandrasekhar, 1960).

The spectral energy distribution (SED) emerging from thin disks is the sum of the black body emission (due to the large opacities) related to different part of the disk with different temperatures:

$$T(r) = \left[\frac{3GM\dot{M}}{8\pi\sigma r^3}\left(1 - \sqrt{\frac{R_{\rm inner}}{r}}\right)\right]^{\frac{1}{4}} \tag{2.34}$$

where G is the gravitational constant, σ is the Stefan–Boltzmann constant, M is the mass of the central object, $\dot{M}$ is the mass rate of accretion onto the body, and $R_{\rm inner}$ is the inner radius of the disk, and it can be conveniently rewritten as:

$$T \sim 10^5 \left(\frac{M}{10^8 M_\odot}\right)^{-1/4} \left(\frac{\dot{M}}{0.1\dot{M}_{\rm Edd}}\right)^{1/4} \left(\frac{r}{10R_S}\right)^{-3/4} \left[1 - \left(\frac{r}{R_{\rm ISCO}}\right)^{1/2}\right] \text{K}. \tag{2.35}$$

The corresponding emerging spectrum will be

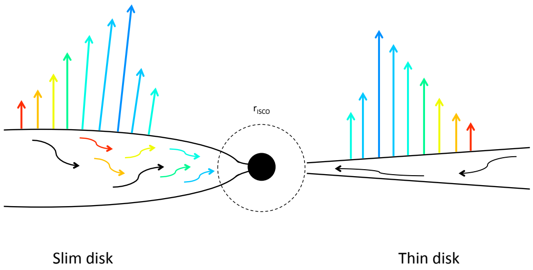

Figure 2.2. A scheme of the standard thin (right) and slim (left) accretion discs.

$$L_\nu = \int_{R_{\text{inner}}}^{\infty} 2\pi^2 r P(\nu, T(r)) dr, \tag{2.36}$$

where

$$P(\nu, T(r)) = \pi \frac{2h\nu^3}{c^2} \frac{1}{\exp(h\nu/\kappa T(r)) - 1}, \tag{2.37}$$

while the total luminosity is then

$$L = \frac{1}{2} \frac{GM\dot{M}}{R_{\text{inner}}}. \tag{2.38}$$

The Equations 2.35 and 2.36 imply that supermassive BHs (SMBHs), with masses of order $10^9\, M_\odot$, have the maximum of the emission in the optical/UV band, while stellar mass BHs have accretion disks that emit mainly in the X-ray band.

For very sub-Eddington accretion rates and very small opacities, the structure formed around a BH is an advection-dominated accretion flow (ADAF), whose analytic description is more complicated than the thin disk one. From a geometrical point of view, they are thick, with a shape more similar to a sphere rather than a disk. As a typical characteristic of thick flows, ADAF are radiatively inefficient (the cooling mechanism is advection instead of radiation), and their emission is a non-thermal power law, generally with the presence of a Compton component.

For nearly and super-Eddington accretion rates, when $L \sim L_{\text{Edd}}$, the disk structure is better described by the slim disk solution. They have large opacities, and radiative efficiencies lower than the typical values associated to the thin geometry (Madau et al., 2014). Slim disks are geometrically inflated in the inner regions, so that they are described by a set of ordinary differential equations where the vertical dimension is not neglected. Due to their thickness, the viscosity-generated heat and, subsequently the photons, have not enough time to escape. In fact, it is possible to define a radius, called *trapping radius*, within which the radiation is advected, instead of radiating away (see Section 5.1.3). For this reason, despite highly super-Eddington accretion rates, the luminosities can remain only mildly super-Eddington, departing from the linear relation $L \propto \dot{M}$ and becoming $L \propto \log \dot{M}$.

Slim disks are a generalization of the thin disk model. In fact, for low accretion rates, the solution converges to the thin disk solution. Moreover, while thin disk model formally ends at $R_{\rm ISCO}$, slim disks extend down to the BH horizon, as shown in Figure 2.2.

A better description of the slim disk solution, and its radiative properties, are discussed in Chapters 4 and 6. For a complete description of the state-of-art of stationary BH accretion disks and numerical simulations, we refer the reader to the review by Abramowicz and Fragile (2013).

Part II

The first black holes

Chapter 3

On the formation of the first quasars

Up to ~ 40 SMBHs of $> 10^9\ M_\odot$ have been observed till date, which are believed to power the optically bright quasars ($> 10^{47}$ erg s^{-1}) at $z > 5$ (e.g. Mortlock et al. 2011; Wu et al. 2015). How these BHs formed in a relatively short time scale, already 12 Gyr ago in the early Universe ($\lesssim 700 - 800$ Myr; e.g. Fan et al. 2001, 2004; De Rosa et al. 2011, 2014) is still an open question (e.g. Volonteri 2010; Natarajan 2011).

Luminous (optically selected) quasars at high redshift, thus offer the most direct constraint on the evolution of the first SMBHs and serve a unique laboratory to study the earliest phases of galaxy formation and evolution as well as the properties of the early Universe. In the left panel of Figure 3.1 we show a collection of high redshift ($z > 3$) SMBHs reported to date. Note that at $z > 6$, they are already as massive as the BHs observed at lower redshifts ($z = 3 - 5$) and in the local Universe (see e.g. Sani et al. 2011; Kormendy and Ho 2013).

The two noteworthy record holders are ULAS J1120+0641 (J1120) and SDSS J0100+2802 (J0100), hosting the most distant ($z \sim 7.1$, Mortlock et al. 2011), and the most massive (1.2×10^{10}M$_\odot$, Wu et al. 2015) SMBHs ever observed respectively.

In the right panel of Figure 3.1 we show the bolometric luminosity as a function of the BH mass for the collection of $z \geq 6$ quasars presented by Wu et al. (2015). The nuclei of these objects are actively accreting massive BHs, shining close to or above the Eddington luminosity (green dashed line). Coloured points show three of the most interesting objects observed to date: the two record holders introduced above, J1120 (magenta triangle) and J0100 (blue square) and quasar SDSS J1148+5251 (red circle, hereafter J1148) which is

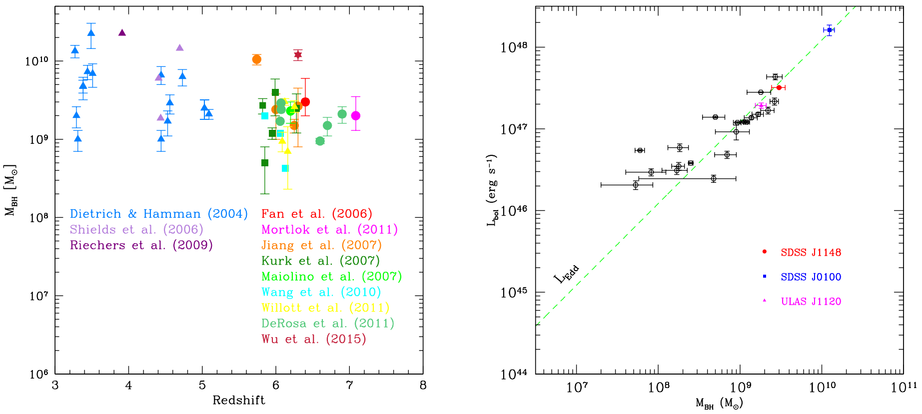

Figure 3.1. *Left panel*: BH mass as a function of redshift for $M_{\rm BH} \gtrsim 10^9\, M_\odot$ quasars at $z > 3$. References to the data are labelled and color coded in the figure. *Right panel*: Bolometric luminosity as a function of the BH mass for $z > 6$ quasars. Black data points are taken from high-z quasars from Wu et al. (2015). The green dashed line show Eddington luminosity (Valiante et al., 2017).

one of the best studied quasar, discovered at $z = 6.4$ (Fan et al., 2001). As it can be seen from the figure, J0100 is the most luminous quasar known at $z > 6$, with bolometric luminosity $L_{\rm Bol} = L_{\rm Edd} \sim 4 \times 10^{14}$ L$_\odot$(Wu et al., 2015), making it 4 times brighter than J1148 (red circle), and 7 times brighter than J1120 (magenta triangle).

In this Chapter, we will present state-of-the-art theoretical models for the formation and evolution of high redshift SMBHs and their host galaxies. The first part is dedicated to the description of the environmental conditions required for the formation of different populations of seed BHs. We then will briefly discuss different pathways for the fast growth of these seeds up to $> 10^9\, M_\odot$ BHs at $z \sim 6$, as well as their co-evolution with the host galaxies.

3.1 Open questions

A SMBH is born first as a much smaller *seed* BH, which then grows by accreting matter and merging with other BHs. Numerous studies have been devoted to explaining how and when these seed BHs and their host galaxies form. Here we briefly discuss the mostly debated issues related to the discovery and formation of distant quasars and their observed properties (see Gallerani et al. 2017 for a recent review on the first quasars observed physical properties).

How and when did the $z > 6$ SMBHs form & the nature of their progenitors

The formation mechanism and properties of the first seed BHs are the subject of several studies which focus on three distinct scenarios (see e.g. Volonteri 2010; Natarajan 2011; Latif and Ferrara 2016 for complete reviews).

The first scenario relies on low-mass seeds, namely BHs of few tens to few hundreds solar masses, formed as remnants of Population III (Pop III) stars in the mass range $[40 - 140]$ and $> 260\,M_{\odot}$ (e.g. Madau and Rees 2001; Abel et al. 2002; Heger et al. 2003; Volonteri et al. 2003; Yoshida et al. 2008) up to $\sim$ 1000 $\mathrm{M}_{\odot}$ stars that may form at $z > 20$ (Hirano et al., 2015).

On the other hand, intermediate mass, $10^3 - 10^4\,M_{\odot}$, BHs may arise from stars and stellar-mass BHs collisions in dense clusters (e.g. Omukai et al. 2008; Devecchi and Volonteri 2009; Katz et al. 2015; Davies et al. 2011; Lupi et al. 2014; Yajima and Khochfar 2016).

Finally, a third SMBH formation channel has been proposed: high-mass seeds, forming in $T_{\mathrm{vir}} \geq 10^4$ K halos, exposed to an intense H_2 photo-dissociating ultra-violet (UV) flux (but see e.g. Spaans and Silk, 2006, for a different scenario), via direct collapse (DC) of low metallicity gas clouds into $10^4 - 10^6\,M_{\odot}$ BHs. Such a scenario has been explored in details by means of both analytic works (e.g. Loeb and Rasio 1994; Bromm and Loeb 2003a; Eisenstein and Loeb 1995; Volonteri and Rees 2005; Begelman et al. 2006; Lodato and Natarajan 2006; Spaans and Silk 2006; Ferrara et al. 2014 and simulations (e.g. Wise and Abel 2008; Regan and Haehnelt 2009a,b; Shang et al. 2010 Inayoshi and Omukai 2012; Regan et al. 2014; Inayoshi et al. 2014; Becerra et al. 2015).

Another debated issue is related to the seed BH growth mechanism that is needed in order to explain $z > 6$ SMBHs.

Alvarez et al. (2009) pointed out that Pop III star remnants forming in mini halos at $z > 15$ do not grow efficiently in mass to become miniquasars (BHs with mass$\sim 10^6\,M_{\odot}$). However, after merging with atomic cooling halos (i.e. halos with virial temperatures of $\geq 10^4$ K), the BH feedback may be able to inhibit star formation, thus leading to efficient accretion and growth of the BH.

In addition, if Pop III stars are less massive than expected, i.e. not exceeding $100\,M_\odot$ (e.g. O'Shea and Norman 2007; Hosokawa et al. 2011; Greif et al. 2011; Stacy et al. 2012; Hirano et al. 2015), the resulting BHs of $\sim 20-60\,M_\odot$ may receive a kick during their formation, ejecting them out of their host halos and thus preventing their subsequent growth (Whalen and Fryer, 2012). Moreover, because of their low mass, such BHs are not expected to settle in the galaxy center. They would rather wander in the halo, without accreting gas (see e.g. Volonteri, 2010, for a discussion)

Various studies suggest that BHs may evolve via uninterrupted gas accretion at the Eddington rate and/or episodic super-Eddington accretion phases, to grow up to billion solar masses, especially in the case of low-mass seeds (Haiman 2004; Yoo and Miralda-Escudé 2004; Shapiro 2005; Volonteri and Rees 2005, 2006; Pelupessy et al. 2007; Tanaka and Haiman 2009; Johnson et al. 2013; Madau et al. 2014; Volonteri, Silk, and Dubus 2015).

We refer the interested reader to reviews by Volonteri (2010); Natarajan (2011), Volonteri and Bellovary (2012), Volonteri et al. (2016a), Latif and Ferrara (2016), Johnson and Haardt (2016) and references therein for details on the first seed BHs formation and feeding mechanisms.

The seeds of the first SMBHs are still elusive even to the most sensitive instruments that exist today, thus preventing us from putting observational constraints on their nature. A good example is the bright Lyα emitter CR7 observed at $z \sim 6.6$ (Matthee et al., 2015; Sobral et al., 2015; Bowler et al., 2016) where either Pop III stars (Sobral et al., 2015; Visbal et al., 2016; Dijkstra et al., 2016) or an accreting DCBH (Pallottini et al., 2015; Hartwig et al., 2016; Agarwal et al., 2016a; Smith et al., 2016; Smidt et al., 2016; Agarwal et al., 2017) has been suggested as the primary constituent of its metal poor component.

Although the observational signatures of seed BHs still remain unexplored, Pacucci et al. (2016) suggest a promising method to search for DCBH candidates in deep multi-wavelength surveys, based on photometric observations. By modelling the spectral energy distribution and colors of objects selected from the CANDELS/GOODS-S field catalogues (Guo et al., 2013) they identify two X-ray detected faint active galactic nuclei (AGN), 33160 and 29323 (Giallongo et al., 2015) (but see also (Weigel et al., 2015; Cappelluti et al., 2016; Vito et al., 2016)) as DCBHs prototypes at $z \sim 6$ and ~ 9.7, respectively.

The existence of such low-luminosity AGN at very high redshift, together with the recent reduction in the optical depth due to free electrons, τ_e reported by the Planck Collaboration et al. (2016) has renewed the interest in the role of the first quasars in cosmological reionization. Although the idea of quasars substantially contributing to, or even being the main responsible for, reionization (e.g. Madau and Haardt 2015) is still highly debated (see e.g. D'Aloisio et al. 2016) the recent discoveries strengthen the motivation for a better understanding of their demographics and origin.

What are the properties of high-z SMBHs hosts?

High-z quasars are predicted to be hosted in the most massive dark matter halos residing in over-dense environments (e.g. Overzier et al., 2009; Di Matteo et al., 2012; Angulo et al., 2013) However, clear observational evidences of such a scenario are still missing, as observations provide controversial results (e.g. Stiavelli et al., 2005; Willott et al., 2005; Wang et al., 2005; Zheng et al., 2006; Kim et al., 2009; Utsumi et al., 2010; Husband et al., 2013; Simpson et al., 2014; Morselli et al., 2014; McGreer et al., 2016; Mazzucchelli et al., 2017; Balmaverde et al., 2017).

The quasar hosts are chemically evolved, metal and dust-rich, galaxies. Although their metallicity is quite difficult to trace, constraints on the gas-phase elemental abundances in the interstellar medium (ISM) come from the detection of emission line ratios in broad- and the narrow-line regions (BLRs and NLRs, respectively)

Although BLRs are representative of a small fraction of the gas content, concentrated within the central region ($10^4\,M_\odot$ on parsec scales, close to the AGN), the observed emission line ratios, such as FeII/MgII (e.g. Barth et al. 2003), NV/CIV (e.g. Pentericci et al. 2002), (Si IV+OIV)/CIV (Nagao et al., 2006; Juarez et al., 2009), and metal lines like CII and OI (e.g. Maiolino et al., 2005; Becker et al., 2006) trace up to $\sim$ 7 $Z_\odot$ metallicities (Nagao et al., 2006; Juarez et al., 2009) suggesting a fast evolution of the ISM chemical properties. By using emission line ratios as tracers, Jiang et al. (2007) estimated gas metallicity of a sample of $5.8 < z < 6.3$ quasars, powered by $10^9 - 10^{10}\,M_\odot$ SMBHs, finding values as high as $\sim 4\,Z_\odot$.

A better proxy of the host galaxy ISM metallicity, on larger scales (comparable to the host galaxy size), is provided by NLRs. A mean gas-phase metallicity $Z_{\rm NLR} = 1.32^{+0.25}_{-0.22} Z_\odot$

is inferred from CIV/He II and C III/C IV flux ratios in quasar, with no significant evolution up to $z \sim 4$ (Nagao et al., 2006; Matsuoka et al., 2009). Such super-solar metallicities are reminiscent of the star formation history (SFH) of the system (see e.g. Matsuoka et al. 2009 and references therein) and can serve as a lower limit for the $z \sim 6$ quasar host galaxies.

Constraints on the cool/warm dust content come from the observations of far-infrared (FIR) and sub-millimetre (sub-mm) continuum radiation, while NIR and MIR observations may provide indications of the hot dust component (e.g. Jiang et al. 2007).

The observed $\geq 10^{13}$ $L_{\odot}$ quasar FIR luminosities are consistent with emission from dust with temperatures of the order of 30-60 K and masses $> 10^{8}$ $M_{\odot}$ (Bertoldi et al., 2003; Priddey et al., 2003; Robson et al., 2004; Beelen et al., 2006; Wang et al., 2008; Valiante et al., 2011, 2014; Michałowski et al., 2010). From the same FIR luminosities, high star formation rates (SFRs), ≥ 1000 $M_{\odot}$/yr, can be inferred, suggesting that a large fraction of these systems has ongoing, highly efficient, star-formation activity (see e.g. Table 1 in Valiante et al. 2014 and references therein)[1].

Is there a stellar mass crisis?

The rapid enrichment by metals and dust at very high redshift discussed above suggests that quasar host galaxies could have undergone intense episodes of star formation. Similar chemical abundances are typically found in local galaxies which, however, evolved on longer time scales.

The estimated mean BH-stellar bulge mass ratio, M_{BH}/M_{star}, of $z \sim 6$ quasars is about 10 times higher than the one observed in the local Universe (e.g. Wang et al. 2010; 2013), suggesting that high redshift BHs may have formed or assembled earlier than their host galaxies (e.g. Lamastra et al. 2010; Venemans et al. 2016). Although this result could be strongly affected by observational selection effects (Lauer et al., 2007; Volonteri and Stark,

---

[1] Note that the SFR is usually inferred using the FIR Luminosity-SFR scaling relation (Kennicutt, 1998) which relies on the assumption that all FIR radiation comes from dust heated by stellar optical-UV emission. A factor of $2-3$ lower SFRs are found taking into account that in luminous quasars, like the ones observed at $z > 6$, $30-60\%$ of the dust heating may be due to the AGN emission itself (Wang et al., 2010; Schneider et al., 2015). Indeed, Schneider et al. (2015) show that the optically bright quasar J1148 may contribute $30-70\%$ of the observed FIR luminosity ($> 20\mu$m) heating the large amount of dust ($\sim 3 \times 10^{8}$ $M_{\odot}$) in the host galaxy ISM. We refer the reader to Valiante et al. (2014) and Schneider et al. (2015) for a discussion.

2011) and large uncertainties in the estimation of the mass and size of the stellar bulge (Valiante et al. 2014; Pezzulli et al. 2016), it is difficult to explain how the ISM has been enriched to chemical abundances similar to that of local galaxies, albeit with $\lesssim 10\%$ of the stars (Valiante et al., 2011; Calura et al., 2014; Valiante et al., 2014).

What is the role of BH feedback?

It is expected that galaxy-scale winds, triggered by the large amount of energy released in the BH accretion process, play a crucial role in regulating the BH-host galaxy co-evolution, shaping the SFH and BH accretion history itself (e.g. Silk and Rees 1998; Granato et al. 2004; Di Matteo et al. 2005; Springel et al. 2005 Ciotti et al. 2009; 2010; Hopkins and Elvis 2010; Zubovas and King 2012).

Indeed, massive and fast large scale gas outflows, associated to quasar activity, have been observed in local and high redshift quasars (Feruglio et al. 2010; 2015; Alatalo et al. 2011; Aalto et al. 2012; Alexander et al. 2010 Nesvadba et al., 2010; 2011, Maiolino et al. 2012; Cano-Díaz et al. 2012; Farrah et al. 2012; Trichas et al. 2012; Carniani et al. 2016). At $z > 6$ a massive gas outflow has been inferred from observations of [CII] emission line in J1148, revealing an outflow rate $\geq 2000 - 3000\ M_{\odot}/yr$ (Maiolino et al., 2012; Cicone et al., 2015).

However there are still open issues like: what is the outflow powering mechanism, what are the effects of BH feedback on the host galaxy, how can the observed strong outflows and starbursts be simultaneously sustained? Although there are hints of star formation being quenched by quasar feedback at high redshift (Cano-Díaz et al., 2012; Farrah et al., 2012; Trichas et al., 2012; Carniani et al., 2016), it is unclear if such feedback is able to completely suppress star formation in galaxies (Peng et al., 2015). On the other hand, it has been pointed out that AGN-driven positive feedback (Zinn et al., 2013; Cresci et al., 2015) which triggers or enhances star formation, may be as important as quenching mechanisms in galaxy formation (e.g. Gaibler et al. 2012; Wagner et al. 2013; Silk 2013; Bieri et al. 2015).

3.2 Theoretical models

In the following sections we review the results of state-of-the art theoretical models for the formation of the first BHs, the properties of the environment in which they form and the evolution of their host galaxies. We focus on models in which the evolution of the baryonic component of galaxies is followed by means of analytic prescriptions linked to their host DM halo properties. In particular, we discuss two complementary approaches adopted to describe DM halos,

- *pure semi-analytic models (pSAMs)*: that use analytic algorithms (e.g. Monte Carlo) usually based on the extended Press-Schechter (EPS, (Press and Schechter, 1974; Lacey and Cole, 1993)) or similar, formalism (see e.g. Parkinson, Cole, and Helly 2008; Somerville and Kolatt 1999; Zhang, Woosley, and Heger 2008)

- *hybrid semi-analytic models (hSAMs)*: that use cosmological N-body simulations (e.g. Springel et al. 2005) to extract DM halo properties (e.g. mass and spatial distribution) and build their models on top of them.

Pure semi-analytic techniques are commonly adopted to shed light either on the early gas enrichment with metals and dust in the high redshift ISM (Hirashita and Ferrara 2002; Morgan and Edmunds 2003; Dwek, Galliano, and Jones 2007; Valiante et al. 2009; Gall et al. 2011b; 2011a, Dwek and Cherchneff 2011, Mattsson 2011; Pipino et al. 2011; Calura et al. 2014) or on the origin of the first SMBHs and the resulting BH-host galaxy scaling relations (e.g. Volonteri et al. 2003; 2005; Madau et al. 2004; Volonteri and Rees 2006, Dijkstra et al. 2008; Tanaka and Haiman 2009; Devecchi et al. 2010; 2012; Petri et al. 2012; Dijkstra et al. 2014; Volonteri, Silk, and Dubus 2015).

However, in order to interpret the observed properties of high redshift quasars discussed in the previous section it is important to connect all the physical processes regulating the formation of SMBHs and the host galaxies' chemical evolution history in a self-consistent cosmological framework.

A first attempt to link the chemical evolution of the ISM (metals and dust) to the SMBH formation in $z > 6$ quasar by means of a pSAM has been made by Valiante et al. (2011;

2014; 2016) and Pezzulli et al. (2016) employing the cosmological data-constrained model GAMETE/QSODUST. The model successfully reproduces the observed properties of a sample of $z > 5$ quasars such as the mass of molecular gas, metals, dust and BHs (Valiante et al., 2014) and has been recently improved to investigate different SMBHs formation scenarios. The relative role of low-mass and high-mass seeds is investigated in Valiante et al. (2016), while Pezzulli et al. (2016) study the effect of different gas accretion modes/regimes by including new, physically motivated, prescriptions for gas cooling, disk and bulge formation in progenitor galaxies.

These models are targeted to highly biased regions of the Universe, where a SMBH is expected to form (e.g. Stiavelli et al. 2005; Kim et al. 2009; Utsumi et al. 2010; Morselli et al. 2014), namely single DM halos of $10^{12} - 10^{13}\ M_{\odot}$, which represent the highest density fluctuations at $z \sim 6$ (e.g. Fan et al. 2004; Volonteri and Rees 2006). In other words, all the halos in the merger trees of high-z pSAMs are the ancestors of a single quasar host. In particular, the observed/inferred properties of the best (observationally) studied quasar, J1148 at $z = 6.4$, are often adopted as a reference data set to constrain/explore model parameters (e.g. Dwek et al. 2007; Valiante et al. 2009, 2011; Dwek and Cherchneff 2011; Valiante et al. 2016; Pezzulli et al. 2016) in the above mentioned studies.

The importance of several physical processes has emerged from both pSAMs and hSAMs, such as metal enrichment of the medium from galactic winds (Dijkstra et al., 2014; Habouzit et al., 2016c) and the clustering radiation sources (Dijkstra et al., 2008; Agarwal et al., 2012). The dependence of these physical aspects on the spatial halo distribution is better described by hSAMs as cosmological simulations: either DM only or hydrodynamical, directly provide the spatial distribution of halos. In general, hSAMs are designed to describe average volumes of the Universe that are able to probe smaller scales, exploring in detail the environmental conditions required for the formation of the high redshift BH population.

The population of SDSS quasars presents an observational limit of 1 cGpc^{-3} for $10^{9}\ M_{\odot}$ BHs (e.g. Fan et al. 2006; Venemans et al. 2013). Much larger volumes, and thus large scale N-body simulations are required to produce one such billion solar mass BH in a statistically significant manner, from either a Pop III or a DCBH seed. On the other hand, small scale N–body simulations (i.e. much smaller volumes $\sim$ 100 cMpc^{-3}) are instead best suited for studying the environment in which the first stars and seed BHs form. Either way, hSAMs operating on either of these volumes present complementary insights into the problem of forming BHs at $z > 6$.

So far, hSAMs have mostly been used to study the formation of high-mass seeds. For example, Agarwal et al. (2012); Habouzit et al. (2016c) use hSAMs in which DM only simulations permit one to account for effects that are critical to the first galaxy formation paradigm. Local feedback mechanisms such as the net radiation flux and metal pollution can be folded into the construct of hSAMs, along with other recipes such as self–consistent star formation and tracking halo histories across cosmic time.

The first part of this review is dedicated to the description of the environmental conditions required for the formation of different populations of seed BHs in both average volumes, simulated by hSAMs, and biased regions described in pSAMs. We then will briefly discuss different pathways for the fast growth of these seeds up to $> 10^9\, M_\odot$ BHs at $z \sim 6$, as well as their co-evolution with the host galaxies.

3.3 The first seed BHs: how, where and when

In the following sections we discuss the environmental conditions that enable and regulate the formation of the first seed BHs in a cosmological context, as explored by both pSAMs and hSAMs. We focus our attention on the formation of low-mass (Pop III remnants) and high-mass (DCBHs) seeds.

3.3.1 Seeds formation sites

As they are the end products of massive Pop III stars, low-mass seed formation is enabled by nearly primordial conditions: metal and dust poor gas fragmenting into one or few massive stars at redshift $z \sim 20$ (e.g. Abel et al. 2002; Heger et al. 2003; Madau and Rees 2001; Yoshida et al. 2008; Hosokawa et al. 2011; Latif et al. 2013b; Hirano et al. 2014; 2015). Gas enriched up to metallicity $Z_{\rm cr} \geq 10^{-4}\, Z_\odot$, or dust-to-gas ratios $\mathcal{D} > 4 \times 10^{-9}$, fragments more efficiently (thanks to metal lines cooling and dust continuum radiation), to form instead lower mass, population II (Pop II) stars (Schneider et al. 2002, 2003; Omukai et al. 2005; Schneider et al. 2012a). Such conditions are expected to be easily met in the first virialised structures at early times, the so-called minihalos, characterize by virial temperatures of $1.2 \times 10^3 < T_{\rm vir} < 10^4$ K and masses $M_{\rm h} \sim 10^{5-6}\,M_{\odot}$ (see e.g. Bromm 2013 for a review).

Although early studies suggest that Pop III star formation in these halos is characterized by high-mass stars ($\geq 100\,M_{\odot}$, e.g. Abel et al. 2002; Bromm et al. 2002; Bromm and Loeb 2004; Yoshida et al. 2008), more recent simulations have shown that Pop III stars forming under different minihalo environmental conditions (e.g. determined by the presence or absence of photo-dissociating and ionizing feedback) may span a wider range of masses, from few tens up to $\sim 1000\,M_{\odot}$ (e.g. Hirano et al. 2014; 2015; Hosokawa et al. 2016. In these works only one star per halo is formed. However, a number of studies, resolving protostellar scales ($\sim 100\,{\rm R}_{\odot}$), show that fragmentation of protostellar disks may lead to the formation of multiple stars, with a wide mass spectrum (down to few solar masses), in small clusters (e.g. Clark et al. 2008; 2011; Turk et al. 2009; Stacy et al. 2010; 2016, Greif et al. 2011; 2012; Susa et al. 2014).

Pop III stars also represent the first sources of light and heavy elements (including dust, e.g. Nozawa et al. 2007; Heger and Woosley 2010; Marassi et al. 2015), setting the stage for all subsequent structure formation in their neighbourhood. Therefore, it is imperative that their formation is captured in the models for a consistent identification of the seed BH hosts. Resolving minihalos, in which these stars form, is thus crucial for models, at least at $z > 20$. Unfortunately, the mass/size resolution limit in both hSAMs (i.e. the box size and DM particle mass) and the pSAMs (i.e. the minimum DM halo mass) is often determined by the inherent computational costs.

Depending on the aim of the model, different scale/mass resolutions are suited for different studies. Resolving arbitrarily small halos is computationally prohibitive even for analytic binary Monte Carlo algorithms. In pSAMs the resolution of the merger tree is thus defined by the minimum halo mass, which, together with the adaptive redshift interval (Δz) are chosen to maintain manageable computational times, simultaneously matching the EPS predictions at different redshifts (e.g. Volonteri et al. 2003; Tanaka and Haiman 2009).

In N-body simulations, the need to resolve a minihalo sets an upper limit on the box-size that can be simulated in a reasonable time frame. N-body simulations with volumes $\sim 100\,{\rm cMpc}^3$ allow one to resolve minihalos, capturing the small-scale sub-grid physics.

These simulations offer insights on the formation sites of the first stars and seed BHs but lack statistical significance in terms of SMBH abundance for which larger volumes are required as discussed in section 3.2.

The formation of a DCBH requires the absence of star formation and of efficient coolants (metals and dust) in order to maintain isothermal collapse of gas clouds in Lyman$-\alpha$- cooling halos (Lyα, $T_{\rm vir} \sim 10^4$ K), leading to a Jeans halo mass (which scales as $T^{3/2}$) which is high enough to avoid fragmentation. Thus, high-mass seed BHs are expected to form out of poorly enriched gas ($Z < Z_{\rm cr}$) if star formation is somehow inhibited. Colliding cold accretion flows (e.g. Inayoshi and Omukai 2012) or high relative velocity galaxy mergers ($\geq$ 200km/s) can shock-heat the gas in the dense central regions of galaxies, collisionally dissociating the H_2 molecules (e.g. Inayoshi et al. 2015), thus preventing the gas from forming stars. Alternatively, the presence of H_2 photo-dissociating flux, i.e. photons in the Lyman Werner (LW) band ($11.2 - 13.6$ eV) emitted by nearby external sources, may suppress star formation in Lyα cooling halos (e.g. Bromm and Loeb 2003b; Begelman et al. 2006; Spaans and Silk 2006; Inayoshi et al. 2014; Ferrara et al. 2014). These conditions indeed enable the formation of a supermassive star (SMS) of $10^{4-5}\,M_\odot$ that may eventually lead to a massive seed BH by accreting the surrounding material (e.g. Bromm and Loeb 2003b; Begelman et al. 2006; Lodato and Natarajan 2006, 2007; Inayoshi and Omukai 2012; Inayoshi et al. 2014; Ferrara et al. 2014; Haemmerlé et al. 2017). Another pathway to create massive BHs in the presence of an external LW radiation field is via a *quasi-star* system. A massive star rapidly forms a $10 - 100\,M_\odot$ BH embedded in a radiation pressure supported dense gas cloud which then experiences high gas infall (and therefore accretion) rates $\sim 1\,M_\odot/yr$, eventually resulting in a more massive $10^{4-5}\,M_\odot$ DCBH seed (Spaans and Silk, 2006; Begelman et al., 2008). This peculiarity of the environmental conditions, and the frequency of their occurrence is still under debate (Agarwal et al. 2012; 2014; Habouzit et al. 2016c; Dijkstra et al. 2014; Yue et al. 2014; Chon et al. 2016) . The conditions are sensitive to galaxies' assembly histories and on the interplay between the effect of chemical, radiative and mechanical feedback, driven by star formation and BH growth itself.

3.3.2 Forming the first stars

In star forming halos both Pop III or Pop II stars form depending on the chemical enrichment (metallicity) of the gas. Pop III stars form out of metal-free/poor gas ($Z < Z_{\rm cr}$) while metal/dust-rich gas clouds instead lead to Pop II star formation.

The metallicity of a galaxy is usually the result of the interplay between in-situ and external metal pollution, i.e. stellar nucleosynthetic products injected in the galaxy interstellar medium (ISM), and in-falling metal rich (and dusty) gas ejected from nearby galaxies via supernovae (SNe) and AGN-driven winds.

Most hSAMs allow Pop III stars to form in metal-free halos, i.e. the ones that have never hosted a star in their past and/or pass the critical mass threshold (Agarwal et al., 2012). The mass threshold can be understood as a negative feedback effect of LW photons that delay Pop III SF by a fraction of dissociating H_2 molecules in a minihalo. While exposed to LW radiation, $J_{\rm LW}$[2], the halo must grow (or accrete more gas) in order to replenish the H_2 content, thereby becoming suitable for Pop III SF (e.g. Machacek et al. 2001; Wise and Abel 2007; O'Shea and Norman 2008). We show this $M_{\rm crit} - J_{\rm LW}$ curve expressed as Eq. 3.1 (Agarwal et al. 2012), in Figure 3.2 (from O'Shea and Norman 2008), where

$$M_{\rm crit} \approx 4\left(1.25 \times 10^5 + 8.7 \times 10^5 \,(4\pi J_{\rm LW})^{0.47}\right). \tag{3.1}$$

In their recent pSAMs, Valiante et al. (2016) and de Bennassuti et al. (2017) compute the fraction of gas that can cool down and form stars in minihalos as a function of halo virial temperature, redshift, gas metallicity and level of LW flux $J_{\rm LW}$ at which the halo is exposed. At a given redshift, the halo mass threshold increases with $J_{\rm LW}$. Progressively more massive minihalos are expected to form stars at lower redshifts, at a fixed $J_{\rm LW}$. A value $J_{\rm LW} \leq 0.1$ is already high enough to suppress star formation in the less massive minihalos ($< (3-4) \times 10^6\, M_\odot$) at $z > 20$. In good agreement with the gas collapse simulations of O'Shea and Norman (2008), Pop III star formation is inhibited in $\leq 10^7\, M_\odot$ pristine ($Z = 0$) minihalos exposed to a LW flux $J_{\rm LW} \geq 1$, at redshift $z < 17$. Stronger $J_{\rm LW}$ levels (e.g. > 10) sterilize all pristine minihalos already at redshift $z = 20$.[3]

To date, observations do not provide strong enough constraints on the Pop III IMF.

---

[2] Note that we use the term flux and specific intensity interchangeably in this Chapter where both refer to a

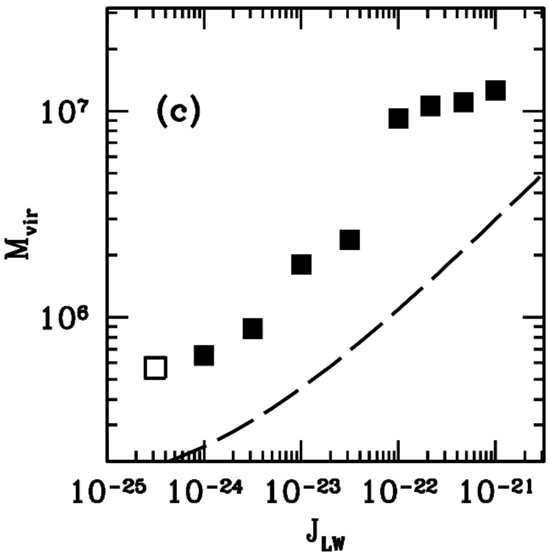

Figure 3.2. The $M_{\rm crit}$ – $J_{\rm LW}$ relation from O'Shea and Norman (2008), Figure 3. The squares represent their updated calculations while the Machacek et al. 2001 relation is depicted by the dashed line. The empty square represent the case with $J_{\rm LW} = 0$. If the mass of a pristine minihalo exposed to a given $J_{\rm LW}$, lies above the curve formed by the squares, it is considered Pop III star forming.

On the other hand, theoretical studies provide predictions on the mass distribution of these stars, that varies among different study (see e.g. the reviews by Bromm 2013; Glover 2013).

The most commonly adopted scenario in hSAMs (e.g. Agarwal et al. 2012, 2013; Chon et al. 2016) is to form 1 Pop III star in a minihalo, randomly picked from a top–heavy IMF that ranges from 100 – 1000 $M_\odot$. For atomic cooling pristine halos, where molecular hydrogen is still present in the central region, generally a cluster of 10 – 100 Pop III stars are allowed to form (e.g. Greif and Bromm 2006; Greif et al. 2011; 2012; Clark et al. 2011), following the same IMF.

Regardless of the DM halo mass, massive Pop III stars with an average mass of ~ 100 – 200 $M_\odot$ are allowed to form in high-z pSAMs (e.g. Valiante et al. 2011, 2014;

---

specific intensity in the LW band in units of 10^{-21}erg^{-1}s^{-1}cm^{-2}Hz^{-1}sr^{-1}

[3] Note that Valiante et al. (2016) and de Bennassuti et al. (2017) also investigate the dependence of the $M_{\rm crit} - J_{\rm LW}$ relation on metallicity. They show that the presence of a small amout of metals does not significantly affect the results as long as $Z \leq 10^{-1.5} Z_\odot$. At higher metallicities, gas cooling and thus star formation can occur in progressively smaller halos so that ~ 10^6 $M_\odot$ minihalos are able to form stars already at $z \lesssim 20$ (we refer the readers to the original papers for more details).

Pezzulli et al. 2016). The number of stars depends on the total stellar mass formed in each star formation episode, and thus on the star formation efficiency and available gas mass. An alternative scenario for Pop III star formation in pSAMs has been proposed by Valiante et al. (2016): Pop III stars form with an intrinsic top-heavy IMF in the mass range $[10-300]\ M_{\odot}$. Then, this IMF is stochastically sampled, on the fly, according to the time-dependent total mass of newly formed stars. We will discuss the effect of these two different assumptions for Pop III stars formation on the low-mass seed BHs distribution, later (in Figure 3.6).

In metal-rich halos, Pop II star formation is generally accounted for by converting a fixed fraction of the available gas into stars. The time/redshift evolution of the gas content is modelled either by scaling the DM halo mass with the universal baryon fraction (e.g. Dijkstra et al. 2008, 2014; Habouzit et al. 2016c) or solving a set of differential equations (e.g. Valiante et al. 2011, 2014, 2016; Agarwal et al. 2012; Pezzulli et al. 2016). In hSAMs the star formation recipes are usually calibrated to reproduce the cosmic star formation rate density (CSFRD) observed at $z > 6$ (Hopkins, 2004; Mannucci et al., 2007; Bouwens et al., 2008; Laporte et al., 2012). Since pSAMs are generally targeted to explain the existence of a single quasar, the models are designed to match the observables of the quasar in question.

3.3.3 Conditions for direct collapse

The treatment of the DC scenario is now taking advantage of hybrid models where instead of Press-Schechter merger trees, one uses a fully cosmological N-body simulation as a playground for the various recipes critical to DCBH formation. One of the main advantages of using hSAMs to study the formation of SMBHs at early times is the spatial information that enables one to study the dependence of various processes on the halos' physical distribution within the simulated volume. Nearby star-forming halos emit LW photons that are able to photo-dissociate H_2 (Omukai, 2001; Omukai et al., 2008; Shang et al., 2010; Latif et al., 2013a)and thus the spatial distance between halos is a crucial ingredient as it controls the strength of the irradiation flux (e.g. Agarwal et al. 2016b). Anisotropies (fluctuations) in the LW background , due to source clustering and/or proximity to the DCBH host candidate, are indeed the key of the radiation-driven DCBH formation scenario (e.g. Dijkstra et al. 2008; 2014; Sugimura et al. 2014; Agarwal et al. 2016b; Regan et al. 2016; 2014)When a proto-galaxy is located nearby an emitting source, spatial correlation makes the difference. Far from the emitting source the LW photons flux seen by the target halo is too low to affect the fraction of molecular gas which remains high. On the hand, the halo is photo-evaporated, by ionizing radiation, if it is too close to the illuminating source (e.g. Regan et al. 2016). Time synchronization matters too. The time elapsed between the starburst onset in the primary halo and the gas collapse in the companions must be short in order to avoid halo photo-evaporation or pollution by heavy elements (e.g. Visbal et al. 2014; Regan et al. 2017; Agarwal et al. 2017).

We provide here an overview of the large scale feasibility of the DC model, i.e. we do not consider studies related to the formation of individual DCBHs (see e.g. Latif and Ferrara 2016 for a review), and rather discuss studies which aim at deriving statistical properties, such as the number density of DCBH sites that form in the early Universe and the conditions leading to them.

In order to identify a DCBH formation site within an average volume of the Universe, one must account for the entire LW and metal pollution history of the atomic cooling halo in question, especially taking into consideration the effects of the local environment. This is one of the biggest strengths of hSAMs as painting galaxies on N–body simulations allows us to compute spatial locations.

Critical LW flux

We have discussed above how (low level) LW flux can delay Pop III star formation in pristine minihaloes. Once the halo becomes atomic cooling, i.e. when it attains a virial temperature of $T_{\rm vir} > 10^4$ K and the primary coolant becomes atomic hydrogen (Omukai, 2000), an extremely high level of flux can completely shut down H_2 cooling by dissociating these molecules in the most dense (thus efficiently self–shielded) regions (Omukai, 2001; Omukai et al., 2008; Shang et al., 2010; Latif et al., 2013a).

The critical level $J_{\rm cr}$, above which direct collapse of gas clouds into massive seeds is enabled, is still a matter of debate and remains a free parameter for models. Assuming that Pop III stellar populations mimic a $T = 10^5$ K and Pop II stellar populations a $T = 10^4$ K blackbody, Omukai (2000) computed the critical value of $J_{\rm crit}$ using their 1D spherically symmetric gas collapse model. Since the shape of the blackbody spectrum depends on its temperature, $J_{\rm crit}$ depends on the type of the stellar population externally irradiating the pristine atomic cooling halo. They found $J_{\rm cr}^{\rm III} \approx 10^4 - 10^5$ and $J_{\rm cr}^{\rm II} \approx 10^2 - 10^3$ is needed from Pop III and and Pop II populations to cause DCBH formation in a neighbouring pristine atomic cooling halo. Revisions in this estimate followed by employing high resolution 3D hydrodynamical simulations and better recipes for H_2 self–shielding, leading to an estimate of $J_{\rm cr}^{\rm III} \sim 1000$ and $J_{\rm crit}^{\rm II} \approx 10 - 100$ (Shang et al., 2010; Wolcott-Green et al., 2011; Latif et al., 2014; Hartwig et al., 2015).

In addition, ionizing photons and X-rays can both increase the free electron fraction promoting H_2 formation (Inayoshi and Omukai 2011; Yue et al. 2014; Johnson et al. 2014; Aykutalp et al. 2014; Inayoshi and Tanaka 2015). As a result a higher critical LW level, up to $J_{\rm cr} \sim 10^4 - 10^5$, is required (Latif et al. 2014; Regan et al. 2014; Latif and Volonteri 2015).

Besides H_2 molecules, H^- ions play a critical role in pristine gas collapse as they regulate H_2 formation at densities $n \lesssim 10^3$ cm^{-3} via the reactions

$$\mathrm{H} \quad + \mathrm{e} \rightarrow \mathrm{H}^- + \gamma \tag{3.2}$$

$$\mathrm{H}^- \quad + \mathrm{H} \rightarrow \mathrm{H}_2 + \mathrm{e}^- \tag{3.3}$$

The importance of this network is further understood by their corresponding photo–destruction channels

$$\mathrm{H}_2 \quad + \gamma_{\rm LW} \rightarrow \mathrm{H} + \mathrm{H} \tag{3.4}$$

$$\mathrm{H}^- \quad + \gamma_{0.76} \rightarrow \mathrm{H} + \mathrm{e}^- \tag{3.5}$$

where $\gamma_{\rm LW}$ and $\gamma_{0.76}$ represent the photons in the LW band and photons with energy greater than 0.76 eV respectively. Ignoring the role of 1eV photons can lead to a gross overestimation in the value of LW flux required to suppress H_2 cooling, as demonstrated by Wolcott-Green et al. (2011). Furthermore, Glover (2015a,b) showed that inconsistencies in the chemical networks and reaction rate coefficients can lead to a factor ~ 3 difference in the determination of $J_{\rm cr}$.

The assumption of representing Pop III and Pop II spectral energy distributions (SEDs) as blackbodies was questioned by Sugimura et al. (2014); Agarwal and Khochfar (2015);

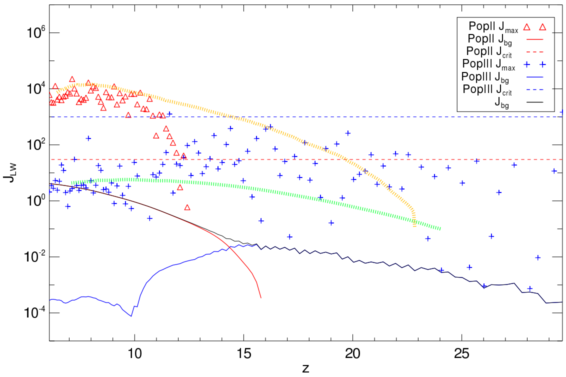

Figure 3.3. From Agarwal et al. (2012): The background and local level of LW radiation plotted for each redshift. “The red triangles ($J^{\mathrm{II}}_{\mathrm{local}}$) and blue crosses ($J^{\mathrm{III}}_{\mathrm{local}}$) indicate the maximum value of LW radiation to which a pristine halo is exposed at each redshift in their volume. The red and blue dashed lines represent $J^{\mathrm{II}}_{\mathrm{crit}}$ and $J^{\mathrm{III}}_{\mathrm{crit}}$ respectively. It is interesting to see that the maximum value of $J^{\mathrm{III}}_{\mathrm{local}}$ (blue crosses) falls short of $J^{\mathrm{III}}_{\mathrm{crit}}$ (blue dashed line). However, in the case of Pop II sources, the maximum value of $J^{\mathrm{II}}_{\mathrm{local}}$ (red triangles) is several orders of magnitude higher than the $J^{\mathrm{II}}_{\mathrm{crit}}$ (red dashed line)." The green dotted line is the specific intensity J_{bg} given by Dijkstra et al. (2014). Finally, the yellow dotted line shows the average LW emission from Valiante et al. (2016).

Agarwal et al. (2016b) who showed that using realistic SEDs to represent stellar populations instead drastically alters the paradigm. This is because the change in the slope of a SED with the age of a stellar population alters the rate of production of LW photons (e.g. Schaerer 2002) with respect to 1eV photons. Agarwal et al. (2016b); Wolcott-Green et al. (2017) demonstrated that indeed, one can not expect a single value of J_{cr} from a given stellar population, but that it is a value dependent on the underlying stellar population’s SFH and varies from 0.1 – 1000 in their 1D models. Needless to say, given that these studies are very recent, this variation in the nature of J_{cr} needs to be further explored.

In Figure 3.3 we show the global and spatial LW intensities from the Agarwal et al. (2012) hybrid fiducial model, and compare them to other studies. The averaged background LW intensity,J_{bg}, at a given redshift is computed as a function of the stellar mass density at that redshift.

$$J_{\mathrm{bg}}(z) = \frac{hc}{4\pi m_{\mathrm{H}}} \eta_{LW} \rho_{\star} (1+z)^3 \,,$$

where η_{LW} is the number of LW photons emitted per stellar baryon, and $\rho_{\star}$ is the stellar mass density at a given redshift, z. Both quantities are linked to the stellar population, so that $J_{\rm bg} = J^{\rm III}_{\rm bg} + J^{\rm II}_{bg}$ (see Greif and Bromm 2006; Agarwal et al. 2012 for more details). The green dotted line is instead the specific intensity $J_{\rm bg}$ given by Dijkstra et al. (2014). The yellow dotted line in Figure 3.3 shows the average LW emission computed in the pSAM of (Valiante et al., 2016) (similar values are also shown by Petri et al. (2012)).

As it can be seen from the figure, the global LW background radiation, $J_{\rm bg}$ is always far below the critical value for DC, $J_{\rm cr}$ (horizontal dashed red and blue lines). Thus, the study of the spatial variation of the photo-dissociating emission is fundamental to identify potential DCBH formation sites.

Ahn et al. (2009) presented the first study of the evolution of the inhomogeneous LW background, in which the local LW flux intensity is self-consistently computed in a cosmological N-body simulation, explaining its importance. Their study is based on a suite of runs that were originally aimed at understanding reionization (Iliev et al., 2007), but was modified to include a radiative–transfer module for LW photons. Ahn et al. (2009) find that the average intensity of the LW radiation exceeds the threshold value for H_2-cooling and star formation suppression in minihalos well before the reionization process is complete. In their scenario, both the average and local LW flux can be $\geq 10^{-2}$ already at $z < 20$ (see e.g. their figure 10). As a result, $Ly\alpha$-cooling halos are the dominant sources of reionzation while minihalos are sterilized before they can significantly contribute to the ionizing and LW background radiation. Following this study, several other models (pSAMs and hSAMs) pointed out the importance of LW flux fluctuations due to sources clustering in the formation of DCBHs (e.g. Dijkstra et al. 2008, 2014; Agarwal et al. 2012; Habouzit et al. 2016c; Chon et al. 2016; Pawlik et al. 2014).

In Figure 3.3 we also show the values of the local LW flux, $J_{\rm local}$, from single stellar populations as computed by Agarwal et al. (2012) in their hSAM volume at each redshift. They show that while Pop III stars are never able to produce the $J^{\rm III}_{\rm crit}$ in their vicinity, Pop II stars are able to produce $J^{\rm II}_{\rm crit}$ quite easily (see Agarwal et al. 2012 for details). This result was later confirmed by Agarwal et al. (2014); Habouzit et al. (2016b) in their suite of hydrodynamical runs, and by Chon et al. (2016).

Due to the lack of spatial information, pSAMs instead can not capture the spatial variations of $J_{\rm LW}$ with respect to the background flux as hSAMs do. However, the LW emission from Pop III/II stars and accreting BHs is self-consistently computed, according to their SED, as a function of stellar age and metallicity and of BH accretion rate (e.g. Petri et al. 2012; Valiante et al. 2016). An important difference with respect to hSAMs is that in pSAMs the star formation and BH accretion efficiency are usually calibrated to match the observed SFR and BH mass of specific, single, objects (e.g. quasar J1148 in Valiante et al. 2016). Within the biased region occupied by the progenitors of a 10^{13} DM halo, the computed LW flux can be interpreted as a mean value for the local fluctuations exceeding the background level, as expected by several models (e.g. Dijkstra et al. 2008; Tanaka and Haiman 2009; Agarwal et al. 2012; Dijkstra et al. 2014). In addition, Petri et al. (2012) and Valiante et al. (2016) show that stellar emission provides the dominant contribution to the photo-dissociating flux with respect to accreting BHs. For example, the global LW emission from stellar populations in Valiante et al. (2016), taken as a proxy of the local flux in their biased region (orange dotted line Figure 3.3), is in good agreement with the maximum local Pop II LW flux, at $z < 11$ (red triangles), and with the large scatter in the maximum local Pop III flux, at larger redshifts (blue crosses), from Agarwal et al. (2012).

The role of metal enrichment

As the first generation of stars form in the Universe they also create the first wave of metals that provide the conditions for Pop II star formation (e.g. Mackey et al. 2003; Greif et al. 2007; Whalen et al. 2008; Joggerst et al. 2010; Ritter et al. 2012). Thus, it is critical to understand metal pollution in terms of both in–situ and external effects. The chemical enrichment of a given halo is indeed the result of the ongoing and past star formation (i.e. metals and dust produced by stars in the parent galaxy and/or its progenitors) as well as contamination by infalling material from outside the halo (galactic winds). Both self-enrichment and winds play a role in setting the conditions for seed BH formation.

As we have seen above, several models (both pSAMs and hSAMs) point out that DCBH regions are expected to be close to star-forming galaxies, in order to maintain a low abundance of H_2. These are also the first regions which are exposed to metal-pollution from galactic winds driven by SNe and AGN.

Although Agarwal et al. (2012) do not explicitly consider galactic winds in their model, their results on the number and environment of DCBH sites were in good agreement with the FiBY suite of hydrodynamical simulations (Agarwal et al., 2014) that did include external metal pollution. This suggests that, for the assumed $J_{\rm cr} = 30$, the DCBH population is not significantly affected by winds. Using their analytic approach Agarwal et al. (2017) find that even with instantaneous metal mixing, the metal outflows (e.g. due to SN winds) from the irradiating galaxy are unable to prevent the advent of isothermal collapse in the neighbouring DCBH halo. The external atomic cooling site has sufficient time to undergo isothermal collapse in the presence of the LW radiation field before being polluted to $Z > Z_{cr}$.

Dijkstra et al. (2014) explore the effect of metal pollution by both SN-driven galactic outflows and genetic enrichment on the DCBH formation probability by computing the size of regions that can be enriched with metals transported by galactic SN-driven winds and the probability that a halo remains metal free (i.e. it do not inherit metals from its progenitor halos). They show that external metal pollution sterilizes DCBH host candidates on a scale of ≤ 10 kpc. The results suffer from the lack of spatial information in their pSAM.

The effect of galactic winds has been recently confirmed by Habouzit et al. (2016c). In their model, DC is enabled in the vicinity of $\sim 10^{11}$ $M_\odot$ star-forming halos, that can provide a high enough radiation intensity ($J_{\rm LW} > J_{\rm cr} = 100$, see their Figure 3) to halos at a distance of $\sim 15 - 20$ kpc at $z > 15$, without polluting them. In other words when the expanding metal rich bubbles created by SN explosions are still smaller than the regions irradiated by a strong intensity.

By means of a set of differential equations Valiante et al. 2011, 2014, 2016 self-consistently follow the global life cycle of the mass of metals and dust in the ISM of J1148 progenitor galaxies taking into account the metal pollution (infalls) of the external medium due to both SN- and AGN-driven winds. They find that a more efficient self-enrichment of galaxies within a merger tree, with the respect to the average genetic pollution history, may prevent the formation of DCBHs progenitors before the LW flux exceeds the critical threshold, while infalling metals are responsible for the super-critical enrichment of newly virialised halos (see e.g. Valiante et al. 2016).

It is worth noting that, metal mixing is an extremely complicated topic. The time scale for metals escaping their host halo and mixing with the gas of the halo being polluted is not fully understood (e.g. Cen and Riquelme (2008); Wise and Abel (2008); Smith et al. (2015);

Chen et al. (2016)). Additionally, the escape of metals from their parent halo depends on the wind–escape–velocity and the potential well of the halo (Muratov et al., 2015; Smith et al., 2015).

Metal-enrichment is indeed predicted to be very disparate in the early Universe, but some halos could remain metal-free down to $z \sim 6$ (Tornatore et al., 2007; Fumagalli et al., 2011; Pallottini et al., 2014). The fraction of metal-free halos, or at least halos below the critical metallicity to avoid fragmentation, depends on chemical and mechanical processes (Schneider et al., 2006a,b). Detailed prescriptions of the effects of inhomogeneous enrichment as well as of the physical properties of metal winds escaping from star–forming halos can not be easily modelled in either pure or hybrid SAMs. However cosmological hydrodynamical simulations can self-consistently track the evolution of metal-enrichment over the entire simulated volumes (Latif et al., 2016; Agarwal et al., 2014; Habouzit et al., 2016b).

Summarizing, the combined effect of chemical and radiative feedback sets the condition for the formation of both low-mass and high-mass seeds as it regulates Pop III/II star formation in all halos and determines the fraction of atomic cooling (Lyα) halos that can potentially host DCBHs at later times. As long as the build up of a super-critical $J_{\rm LW}$ precedes the efficient metal pollution, DCBH formation can occur in atomic cooling halos.

3.3.4 DCBHs number density

Over the past few years, the question of the number density of DCBHs has become a topic of great interest, and has led to values that span several orders of magnitude, from $\sim 10^{-1}$ to 10^{-9} cMpc^{-3}.

Here we compare the results of both hSAMs Agarwal et al. (2012); Habouzit et al. (2016c) and pSAMs of Dijkstra et al. (2008, 2014); Valiante et al. (2016). We include DCBH number densities from the Agarwal et al. (2014) and Habouzit et al. (2016b) hydrodynamical simulations as they offer a direct comparison of semi-analytic and hydrodynamic approaches.

Dijkstra et al. (2008) compute the probability distribution function of the LW flux at which DM halos are exposed to at $z \sim 10$ taking into account their clustering properties. They find that only a small fraction, $< 10^{-6}$, of all atomic cooling halos are exposed to a LW flux exceeding the assumed critical threshold, $J_{\rm LW} > 10^3$ and thus derive a number density of $< 10^{-6}$ cMpc^{-3} potential DCBHs hosts.

In contrast, using a semi-analytic model on top of a cosmological N–body simulation, Agarwal et al. (2012) find a higher number density, in the range $10^{-2} - 10^{-1}$ cMpc^{-3} for $J_{\rm crit} = 30$ (their fiducial model), even accounting for in–situ metal pollution from previous star formation events.

In their fiducial model, Dijkstra et al. (2014) include star formation in atomic cooling halos (but do not include minihalos), metal pollution from progenitor halos and galactic outflows and estimate $n_{\rm DCBH} \sim 10^{-9} - 10^{-6}$ cMpc^{-3} between $z = 20$ and 7. They explore the dependence of their predictions on model assumptions, such as the value of LW photons escape fraction and critical flux for DC, underlying the important effect of galactic winds decreasing the number density by several orders of magnitudes. The fraction of LW photons escaping from galaxies, and contributing to the photodissociating background radiation, indeed plays a crucial role in this scenario. However the LW escape fraction is still highly uncertain (may increases from 0 to 1 depending on halo and stellar mass) and strongly dependent on the ionization front propagation (e.g. Kitayama et al. 2004; Schauer et al. 2015, 2017a)

More recently, Habouzit et al. (2016c) find a number density of DCBH regions in the range $10^{-7} - 5 \times 10^{-6}$ cMpc^{-3}, consistent with what found by Dijkstra et al. (2014). A factor of 2 higher number density can be found in cosmological N–body simulations in which primordial fluctuations are described by a non-Gaussian distribution. In addition they also estimate the Pop III remnant BHs number density, being about 2 order of magnitude higher than that of DCBHs, although they do not resolve minihalos in their simulations. Similar values are found in hydrodynamical simulations by Habouzit et al. (2016b) for different box sizes and resolutions.

In their pSAM aimed to study the role of Pop III remnant BHs and DCBHs in the formation of a $z \sim 6$ SMBH, Valiante et al. (2016) predict an average number density of $\sim 10^{-7}$ cMpc^{-3} DCBHs. These are the DCBHs expected to form in J1148 progenitor galaxies, along the hierarchical history of a $10^{13}\,M_\odot$ DM halo. As we will discuss later, only a fraction of these high-mass seeds eventually end in the final SMBH, driving its fast growth.

In Figure 3.4 we show a collection of DCBH number densities derived from some of the studies discussed above. Symbols represent different radiation intensity thresholds: squares refer to $J_{\rm LW,crit} = 30$, circles to $J_{\rm LW,crit} = 100$, and triangles to $J_{\rm LW,crit} = 300$. The figure is taken from Habouzit et al. (2016b) who compare the results of semi-analytic studies by Dijkstra et al. (2014) (dark gray symbols) with hydrodynamical simulations: one of the the FiBy simulations based on the smoothed particle hydrodynamics (SPH) code GADGET (e.g. Springel et al. 2005) presented by Agarwal et al. (2014) (light grey crossed square at $z = 10.5$); two runs of the 10 cMpc box Chunky simulation with a collapse times scale equal to 10 Myr (purple symbols) and to the halo free fall time, $t_{\rm ff}$ (orange square); the large-scale (142 cMpc side box) cosmological simulation Horizon-noAGN (cyan symbols, Dubois et al. 2014b; Peirani et al. 2016). We refer the reader to the original paper Habouzit et al. (2016b) for a detailed discussion. We have included in this figure the predictions by Agarwal et al. (2012) in the $z = 7 - 10$ redshift range (light gray squares) and Valiante et al. (2016) at $z = 18$ and 15 (black triangles). Finally, the horizontal blue solid line show the SMBH number density observed at $z \sim 6$ of 1 cGpc^{-3}.

Consensus between different studies

One of the most restrictive ingredient of the DC scenario is the absence of H_2 (through both H_2 destruction and prevention of H_2 formation) to keep the gas temperature and thus the Jeans mass high enough to avoid the fragmentation of gas clouds. This should favour the formation of only one massive object. As mentioned in Section 2, the exposure to a strong LW radiation is one of the possible way to strongly depress H_2 abundances (Omukai, 2000; Omukai et al., 2008; Shang et al., 2010). From Ahn et al. (2009), we have understood that the spatial variations of the radiation intensity, driven by LW photons able to photo-dissociate H_2, was certainly a key requirement of the scenario. Most of the models for the radiation intensity include now a spatial varying component based on local photo-dissociating sources. The radiation intensity is either computed directly from stellar particles according to their age, distance, and redshift (Agarwal et al., 2012, 2014; Habouzit et al., 2016b), or from the stellar mass painted on DM halos (Dijkstra et al., 2014; Habouzit et al., 2016c; Chon et al., 2016).

Moreover, the critical radiation flux needed to destroy H_2, seems to be driven mainly by

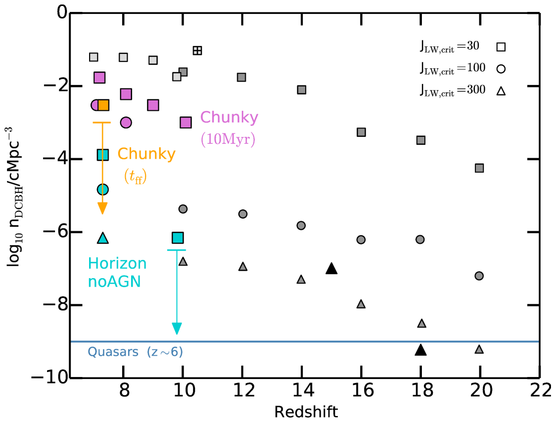

Figure 3.4. Comoving number density of halos that can host a DCBH, at a given redshift. Symbols represent different radiation intensity thresholds. Squares: $J_{\rm LW,crit} = 30$, circles: $J_{\rm LW,crit} = 100$, triangles: $J_{\rm LW,crit} = 300$. The horizontal solid blue line show the comoving number density of $z \sim 6$ SMBHs. The light gray crossed square at $z = 10.5$ is from the hydrodynamical simulation by Agarwal et al. (2014), the light gray squares in the range $z = 10 - 7$ are from Agarwal et al. (2012) (private communication), dark gray squares and black triangles are the results of Dijkstra et al. (2014) and Valiante et al. (2016), respectively. The orange square shows the number density for Habouzit et al. (2016b) (10 cMpc side box, $t_{\rm ff}$, see text). The purple squares and circles show the number density for Habouzit et al. (2016b) (10 cMpc side box, 10 Myr, see text). The cyan squares, circle and triangle represent the large-scale cosmological simulation Horizon-noAGN (Dubois et al., 2014b; Habouzit et al., 2016b, 142 cMpc side box).

Pop II stars. This is supported by three main ideas. First of all, the LW radiation background created by Pop III stars emission, impacts their surrounding by photo-dissociating molecular hydrogen. Cooling rate decreases, which delays the gas collapse, and this vicious circle lowers and delays the formation of new Pop III stars at later time (O'Shea and Norman, 2008; Johnson et al., 2012). The life time of Pop III stars is also thought to be short ($\sim$ 10 Myr), it could be too short for providing a high LW radiation intensity during the whole free-fall time of a dark matter halo. One can compute the redshift at which the free-fall time is approximately equal to $\sim$ 10 Myr, and finds $z \sim 45$. This means that a halo illuminated only by Pop III radiation, could form a BH only at very early times, around $z \sim 45$. Finally, the intensity of Pop III radiation itself may be not enough to provide the critical radiation intensity commonly assumed for the DC model (O'Shea and Norman, 2008; Agarwal et al., 2012). In Figure 3.5 (reproduced from Agarwal et al., 2012), we show the distribution of the local varying radiation intensity seen by pristine halos at $z = 16$, before the formation of the first Pop II stars, and $z \sim 9$, after their formation. Radiation intensity from Pop III stars is shown in blue, and from Pop II stars in red. Dashed lines indicate the critical radiation intensity expected for Pop III stars (in blue) and Pop II stars (in red). Pop III stars radiation intensity appears to be almost always below the critical intensity (below the corresponding red dashed line), whereas a majority of pristine halos under Pop II stars radiation flux can meet the critical radiation intensity condition. The distribution of radiation intensity to which halos are exposed to, is in good agreement between various studies, using similar methods and LW radiation modellings (Agarwal et al., 2012; Chon et al., 2016), or different approaches (Dijkstra et al., 2008).

Finally, all studies agree that metal-pollution from both heritages, previous episodes of star formation in halo progenitors and galactic winds from nearby halos, *could* play a fundamental role. Galactic winds could sterilize potential DCBH regions by enriching them in metals, on a scale of $\leqslant 10\,\mathrm{kpc}$, thereby reducing their number density (Dijkstra et al., 2014). The process is a complex interplay of metals mixing in a gas medium of varying density, the propagation of metals in the IGM, and the winds launching out from their host halo (Cen and Riquelme, 2008; Smith et al., 2015). Agarwal et al. (2017) recently devised a semi-analytical model working under worst case assumptions for DCBH formation under the influence of metals originating from neighbouring galaxies that provide the necessary LW flux. Even after assuming an extremely short (300 pc) separation between their DCBH candidate halo and external LW sources, and instantaneous metal mixing, they find that the metal mixing is insufficient to shut down DCBH formation. This is because during the time window when the target halo can form a DCBH, its metallicity remains well below the critical threshold above which SF is expected (Omukai et al., 2008; Latif and Ferrara, 2016).

Why do we have a spread in the number density

The large diversity of models (modelling of the photo-dissociating radiation intensity, and metal-enrichment, for example), methods (pSAMS, hybrid with DM only simulations, or hydrodynamical ones), set-up of simulations (star formation, SN feedback), used to esti-

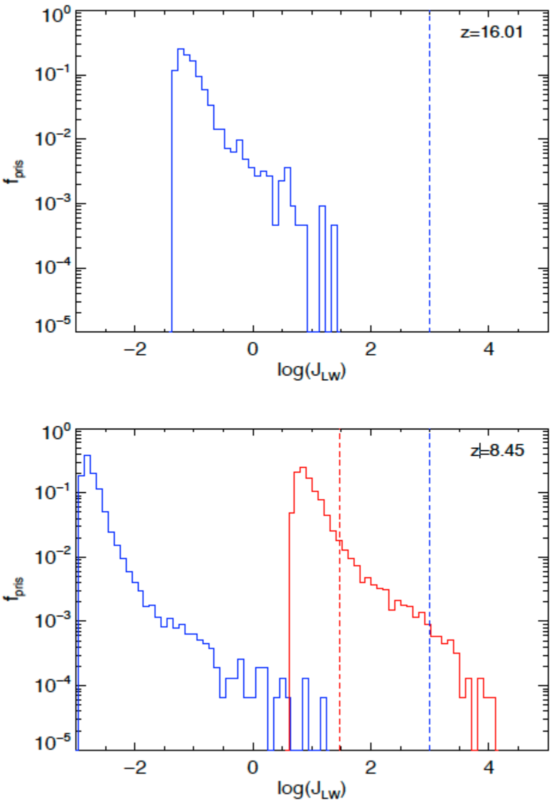

Figure 3.5. Distribution of local radiation intensity (Agarwal et al., 2012) seen by pristine halos at $z = 16$ (top panel), before the formation of Pop II begins, and later on at $z \sim 9$ (bottom panel) when Pop II is already in place. $f_{\rm pris}$ is the number fraction of pristine halos exposed to a given $J_{\rm LW}$. Radiation intensity from Pop III stars is shown in red, and radiation intensity from Pop II stars in blue. Dashed lines indicate the critical radiation intensity expected for Pop III stars (in red) and Pop II stars (in blue). Pop III stars radiation intensity appears to be almost always below the critical intensity (below the corresponding dashed line), whereas a fraction of pristine halo illuminated by Pop II stars radiation flux can meet the critical radiation intensity condition.

mate the number density of DCBH regions, complicate the task of comparing their results. Despite the fact that all the studies presented here seem to agree pretty well, several of the models use different assumptions. In this section, we identify the main differences between the different models.
Habouzit et al. (2016b) perform a comparison between the SAM model of Dijkstra et al. (2014) and the hybrid model of Agarwal et al. (2014), and find that compared to hydrodynamical simulations, Dijkstra et al. (2014) overestimates the stellar mass that form in halos. In the opposite, Dijkstra et al. (2014) underestimate the number of galaxies that contribute to radiation, and the extent of metal polluted bubbles (the latter can vary strongly depending on the stellar mass going SN, and the medium properties). In some cases, the different assumptions compensate each other, and lead to the same estimate of the number density of the potential DCBH host halos (Habouzit et al., 2016b).

Differences between models using dark matter only simulations and models from hydrodynamical simulations can be studied by comparing Agarwal et al. (2012) (distribution of halos from a dark matter simulation) and Agarwal et al. (2014) (hydrodynamical simulation). The number density derived by Agarwal et al. (2012) is shown in light gray squares in Figure 3.4, whereas the number density from Agarwal et al. (2014) is represented in crossed square point in Figure 3.4. Agarwal et al. (2014) is an improvement of Agarwal et al. (2012), because now, thanks to the hydrodynamical output, the model takes into account self-consistently cooling of halos, metal-enrichment through SN feedback, molecular dissociation and photo-ionization.

As discussed above hSAMs are largely adopted to study the feasibility of the DCBH formation scenario. However, one would eventually want to know whether these high-mass seed BHs, that formed at early times, can actually grow and form the population of quasar we see at $z = 6$, and under which conditions this is possible (accretion, galaxy-galaxy mergers, super-Eddington episode, and so on).

Most of the studies discussed in this review provide upper limits on the number density of DCBHs, because they are not able to follow all the physical processes from the selection of dark matter halos to the collapse of the gas to form a BH. However, they seem to all show that the DCBH number density is higher than the observed number density of quasars at high redshift, 10^{-9} cMpc^{-3}, horizontal blue line in Figure 3.4 (Fan et al. 2006; Mortlock et al. 2011). If a higher critical flux is required for DCBH formation ($J_{crit} > 100$), as it is actually found in 3D zoom–in simulations, then Dijkstra et al. (2014) (see also Habouzit et al., 2016b, with the large scale simulation Horizon-noAGN) show that the upper limit on the DCBH number density is sufficient to reproduce the population of quasars. However, such high critical values do not explain the population of less massive BHs that we observe today in more normal and low-mass galaxies (Greene, 2012; Reines et al., 2013).

On the other hand, smaller simulation boxes that resolve minihalos and include a more developed chemistry network, have lead to the derivation of higher DCBH region number density, particularly because they impose a lower critical radiation intensity ($J_{crit} = 30$) (Agarwal et al., 2012, 2014). Such low values of the critical intensity could suggest that the DC scenario may also be able to seed the more *normal* galaxies. Recently, Habouzit et al. (2016b) show that this also strongly depends on SN feedback implementation, and that to explain BHs in normal galaxies, a weak SN feedback is required.

Although large progress has been made, both in terms of pure SAMs and hybrid models to investigate the DC scenario, owing to the the large spread in the number density of DCBH regions derived, and the uncertainty in the nature of the critical LW radiation intensity, it is still unclear if the DC scenario can produce enough BHs to explain the population of high redshift quasars.

Regarding the target of this review, high redshift quasars, a natural follow up of these studies would be to follow the growth of the BHs, modelling the accretion and feedback as a function of host halo merger history. To this aim, a number of semi-analytic studies have been developed so far (see Section 3.2). In the following part of this Chapter we will review state-of-the-art results on the growth of $z \sim 6$ SMBHs and their host galaxies.

3.4 From seeds to the first quasars

Several studies have investigated the early growth of SMBHs starting from either low-mass or high-mass seeds (see reviews by e.g. Volonteri 2010; Natarajan 2011; Volonteri and Bellovary 2012; Haiman 2013; Johnson and Haardt 2016). In these models, SMBHs

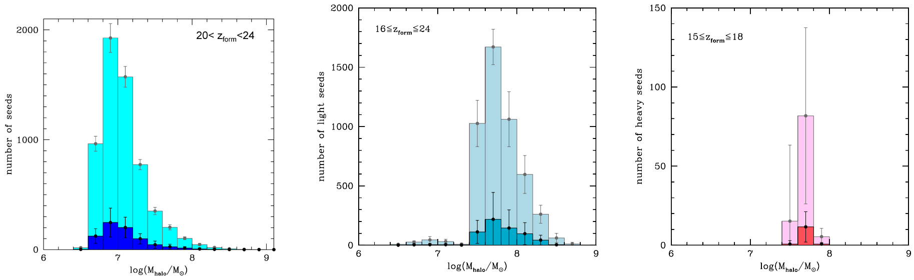

Figure 3.6. Distribution of the average number of seed BHs as function of the DM halo mass from different seeding prescriptions adopted in pSAMs: *(i)* equal-mass 100 $M_\odot$ low-mass seeds (left panel) and *(ii)* (10-140) and (260-300) $M_\odot$ Pop III remnant BHs (middle panel) plus $10^5\,M_\odot$ high-mass seeds (right panel). Histograms and data points show the number of total (in lighter colors) and real SMBH progenitors (darker histograms, see text). Error bars account for the 1σ dispersion. The figures are adapted from (Pezzulli et al., 2016) and (Valiante et al., 2016). The average redshift range in which seeds form, according these two models, is given in each panel.

growth is driven by both gas accretion and mergers with other BHs. In this section we briefly review the most recent studies of the hierarchical assembly of a quasar and its host galaxy, as described by pSAMs.

3.4.1 Low-Mass vs high-mass seeds

In Figure 3.6 we show the distribution of the number of seed BHs formed along the hierarchical build up of a $z \sim 6$ quasar (i.e. in its progenitor galaxies) as a function of the host DM halo mass. In the left panel we show the number of equal mass stellar BHs, low-mass seeds of $10^2\,M_\odot$, assumed to form in newly virialized halos, as long as they are metal poor, $Z < Z_{\rm cr} = 10^{-3.8}$, i.e. at $z \geq 20$, as predicted by Pezzulli et al. (2016). The other two panels instead are for a mixed-seed-based seeding prescription (Valiante et al., 2016): $(40 - 140)$ and $(260-300)\,M_\odot$ Pop III remnant BHs (middle panel) plus $10^5\,M_\odot$ high-mass seeds (right panel), forming along the same merger history. In this scenario the formation of low-mass and high-mass seeds is simultaneously explored thus, allowing to directly compare the role of the two channels in the formation of a SMBH. In all panels, histograms and data points are obtained by averaging over 29(10) different merger histories of the $10^{13}\,M_\odot$ DM halo in the low-mass-seed(mixed-seed) case, with error bars showing the 1σ dispersion. Both prescriptions have been adopted to model the quasar, J1148 at $z = 6.4$, with a SMBH of $(2-6) \times 10^9 \, M_\odot$ (Barth et al. 2003; Willott et al. 2003; De Rosa et al. 2011). As we discussed in the previous sections, the number, redshift and typical host halo mass of both low-mass and high-mass seeds is determined by the interplay between the early chemical enrichment – due to metal-rich infalling gas from the external medium, polluted by SN- and AGN-driven winds from other galaxies – and the intensity of the LW radiation (from both stars and accreting BHs) to which the halos are exposed.

The inclusion of radiative feedback effects results in a less efficient and slightly slower metal enrichment, enabling Pop III stars to form on average down to lower redshift, e.g. $z \sim 16$ in the model shown on Figure 3.6. As we see in the right panel of the Figure, DCBH form in $10^7 - 10^8 \, M_\odot$ progenitor halos (and in the narrow redshift range $15 - 18$, see Valiante et al. 2016 for details), consistent with what is expected from their formation theory and the findings of Bellovary et al. (2011); Agarwal et al. (2012); Habouzit et al. (2016a); Chon et al. (2016).

In their pSAM, Petri et al. (2012) combine both low-mass and high-mass seeds to investigate their relative role in the formation of SMBHs in a pSAM. They explore the dependence of the resulting SMBH evolutionary scenario on the fraction of halos (exposed to a LW flux $J_{\rm cr} > 10^3$) that can actually host DCBHs. A $10^9 - 10^{10} \, M_\odot$ BH is formed at $z \sim 6$ if at least $(1-10)\%$ of all the halos host a high-mass seed (see their Figs. 4 and 9).

For a critical LW threshold $J_{\rm cr} > 300$ Valiante et al. (2016) predict an average high-mass seeds occurrence ratio (the number of galaxies with $Z < Z_{\rm cr}$ when $J_{\rm LW} > J_{\rm cr}$ divided by the number of all the halos exposed to a flux $J_{\rm LW} > J_{\rm cr}$) of $\sim 5\%$ at $z > 15$. This suggests that chemical feedback plays a dominant role in determining of the birth environment[4].

Recently, Schauer et al. (2017b) explore the effects of baryonic streaming velocities on minihlaoes, offering an alternative pathway to inhibit Pop III star formation before the pristine halo reaches the atomic cooling limit. Chon et al. (2016) combined a semi-analytic model for galaxy formation with halo merger trees extracted from N-body DM simulations to select possible DCBH hosts among atomic cooling halos. By means of zoom–in cosmological hydrodynamical simulations of the selected halos, they explore the evolution of gas

---

[4] Indeed, if for example, a factor of ~ 4 higher $J_{\rm cr}$ is assumed in this model, the formation of high-mass seeds is completely suppressed by chemical feedback.

collapse in the DCBH sites. They mostly follow the approach of Agarwal et al. (2012) but bring a previously unexplored effect to light: tidal gravitational fields affecting gas collapse. They show that unless assembled via major–mergers, their DCBH sites do not survive the tidal fields and get disrupted before an isothermal collapse can ensue at gas densities of $n \geq 10\,\mathrm{cm}^{-3}$. A DCBH occupation fraction of $\sim 5\%$ (2 out of the selected 42) is found in this study, in good agreement with the pSAM of Valiante et al. (2016).

3.4.2 The role of mergers and BH dynamics

Merger events can serve as an important physical process that drives the growth of BHs. However, binary (or multiple) BH interactions, driven by dynamical friction, are quite complex, multi-scale processes. The physical scales of interest span from sub-pc scales of the Schwarzschild radius (e.g. $\sim 10^{-11}$ pc for $100 - 300\,M_{\odot}$ BHs and $\sim 10^{-8} - 10^{-7}$ pc for BHs of $10^{5} - 10^{6}\,M_{\odot}$) up to the Mpc scale of the host galaxy mergers. In addition, the mechanism leading to BH-BH mergers, the time it takes for BHs to coalesce via gravitational wave (GW) emission, and the relation between the end–state of the merger and the properties of the respective host galaxies, are still open questions.

However, SAMs aimed to study the formation and evolution of SMBHs trough cosmic time usually adopt simple prescriptions to account for the contribution of mergers to the BH growth (see e.g. Tanaka and Haiman 2009 and references therein).

In major mergers[5] BHs follow the fate of their host galaxies, coalescing to form a more massive BH. However, during this process, a large center-of-mass recoil (kick) can be imparted to the newly formed BH as a consequence of asymmetric gravitational wave emission (e.g. Campanelli et al. 2007; Schnittman et al. 2008; Baker et al. 2008). The acquired kick velocity can be as large as $\sim 100\,\mathrm{kms}^{-1}$, enough to eject the coalesced binary out of the host galaxy (see e.g. Yoo and Miralda-Escudé 2004; Volonteri and Rees 2006; Tanaka and Haiman 2009; Barausse 2012 and references therein for details). On the other hand, in minor mergers one of the two merging BHs, usually the least massive one, is assumed to remain as a satellite in low-density regions, without accreting or contributing

---

[5] Usually major and minor mergers are defined according to the mass ratio of the two merging DM halos (e.g. Tanaka and Haiman 2009 and reference therein). For example, a mass ratio higher than 1 : 10 is assumed by Volonteri and Rees 2006 to identify major merger events.

to the growth of the final BH.

The effective number of seed BHs from which a SMBH forms depends on these assumptions. Valiante et al. (2016) predict that only $\sim$ 13% of the low-mass and high-mass seeds in their model (darker histograms in middle and right panels in 3.6) contribute to the final mass of the SMBH of J1148, at $z = 6.4$, as a large fraction of BHs is lost due to minor mergers.

A similar fraction, $\sim$ 15% (indicated by the darker histogram in the left panel) is left by taking into account the combined effect of minor mergers and gravitational recoil on growing low-mass seeds. On average, $\sim$ 56% satellites BHs are lost along the entire merger tree in minor mergers while $\sim$ 32% of the coalescing BHs, in major merger events, gain a recoil velocity large enough to exceed the retention speed, being kicked out of the galaxies (Pezzulli et al. 2016; a much larger fraction, $\sim$ 99% is found by Volonteri et al. 2003).

The effect of BH recoil due to gravitational wave emission during BH mergers has been also studied by Sijacki et al. (2009). They resimulate the most massive $z = 6$ DM halo extracted from the Millennium simulation in order to study the effect of BH mergers (Blecha et al., 2016) in the growth of high redshift massive BHs. A SMBH of $10^9 - 10^{10}\ M_\odot$ is produced in an Eddington-limited scenario, by planting massive BH seeds of $10^5\ M_\odot$, in DM halos with masses $10^{9-10}\ M_\odot$ at z=15. They find that if the initial BH spin is high the growth of mostly isolated (only a small number of mergers occur) massive BHs is hampered. However, BH kicks substantially expel low-mass BHs, and thus do not affect the overall growth of the SMBHs.

BH mergers are found to play a minor role in the formation of the first SMBHs (at relatively lower redshifts), in pSAMs (e.g. Fig 6 in Pezzulli et al. 2016) and recently in hydrodynamical simulations like MassiveBlack and BlueTides (e.g. Feng et al. (2014); Di Matteo et al. (2016)).

Mergers between BHs drive the black hole mass assembly only at high redshifts (but see Petri et al. 2012). For example, although driving the BH growth process at $z > 11$, BH-BH coalescences contributes to less than 1% of the J1148 final BH mass at $z = 6.4$ (Valiante et al., 2011). Similarly, in Valiante et al. (2016), BH mergers (of mainly low-mass seeds) are predicted to drive the BH growth down to $z \sim 15$, before the gas accretion regime triggered by the formation of the first high-mass seeds, sets in.

Conversely, in the large-volume, cosmological hydrodynamical simulation Horizon–AGN (box size of 100 h^{-1} Mpc and resolution mass of 8×10^7 $M_\odot$) Dubois et al. (2014a) show an accretion-dominated BH growth at high redshift, while in the older Universe, the galactic centers tend to be less gas-rich, and, thus, the mass growth of the central BHs is mostly driven by mergers. In addition, a demographic study of BHs has been recently carried out by Volonteri et al. (2016b) within the same simulation. They show that the fraction of BH host galaxies is higher at higher stellar masses and that multiple BHs are hosted in the most massive halos as a consequence of merger events. A population of dual AGN, a central and an off–center accreting BH, is found in the simulated halos.

Recent ALMA observations presented by Trakhtenbrot et al. (2017a) have revealed a large number, $\sim 50\%$, of massive star forming galaxies interacting with quasar hosts (within < 50 kpc scales). The authors argue that this may support the idea of major merger-driven growth playing an important role in the formation of SMBHs in high redshift quasars, at least those showing sub-mm galaxy (SMG) companions. The $z \sim 5$ quasar in the sample shows similar properties in terms of BH mass and bolometric luminosity but varies in terms of host galaxy properties (see Netzer et al. 2014; Trakhtenbrot et al. 2017a for details on the sample), suggesting different accretion mechanisms may be operating in different environments.

3.4.3 The role of gas accretion

Semi-analytic techniques have been largely employed to study the role of different gas accretion regimes and/or the effect of dynamical processes in the early growth of SMBHs (e.g. Volonteri et al. 2003; 2005; Begelman et al. 2006 Volonteri and Rees 2005; 2006; Tanaka and Haiman 2009, Volonteri et al. 2015).

Volonteri and Rees (2006) show that the observed high-z SMBH masses can be reproduced starting from low-mass seeds ($\sim 100\,M_\odot$) if they accrete gas at super-Eddington rates, at early stages. Super-Eddington accretion is a selective and biased process, occurring only for a small fraction of BH seeds if they form in metal-free atomic cooling ($T_{\rm vir} \geq 10^4$K) halos (e.g. Volonteri and Rees, 2005; 2006).

Gas accretion rates that are 10^4 times higher than the Eddington rate can be reached by low-mass seeds in super-Eddington models (e.g. Volonteri and Rees 2005, Pezzulli et al.

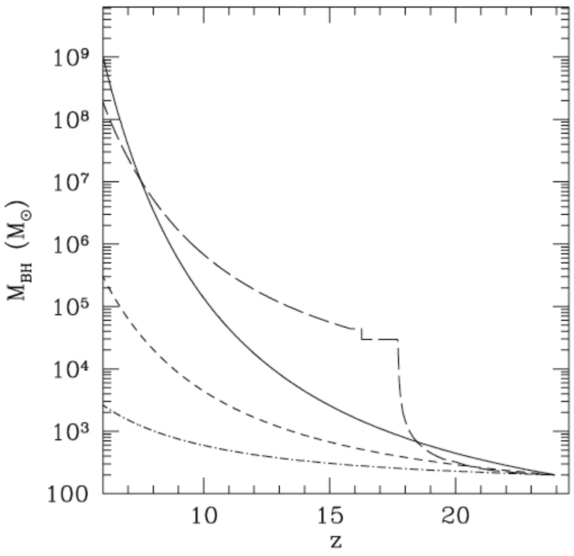

Figure 3.7. The growth of a low-mass seed BH mass as a function of redshift in different regimes: Eddington-limited gas accretion with radiative efficiencies $\epsilon = 0.1, 0.2, 0.4$ (solid, short-dashed and dot-dashed lines, respectively); super-critical accretion (long-dashed line). The figure is taken from Volonteri and Rees (2006).

.

2016 and references therein). However, mildly super-Eddington intermittent accretion at $\sim 3 - 4\,\dot{M}_{\rm Edd}$ (or in general $< 20\,\dot{M}_{\rm Edd}$) may be efficient enough to grow a SMBH in less than 800 Myr (at $z \sim 7$) starting from a single (e.g. Madau et al. 2014, see their Figure 2) or a population (e.g. Pezzulli et al. 2016, see their Figure 5) of $100\,M_\odot$ BH seeds.

In Figure 3.7 we show the plot presented by Volonteri and Rees (2006) to illustrate the SMBH mass growth along the merger tree of a $10^{13}\,M_\odot$ halo at $z = 6$. The figure depicts the effect of different accretion regimes and/or radiative efficiencies on the mass assembly of a $\sim 100\,M_\odot$ seed that starts accreting at $z = 24$: Eddington-limited with a radiative efficiency $\epsilon = 0.1, 0.2, 0.4$ (solid, short-dashed and dot-dashed lines, respectively) and super-Eddington (long-dashed line). Radiatively efficient gas accretion disks ($\epsilon > 0.1$) strongly limit the growth of their BH, even while accreting continuously at the Eddington rate.

The requirement for episodic, radiatively inefficient, super-critical gas accretion onto stellar mass seed of $20 - 100\,M_\odot$ is supported by sub-pc resolution hydrodynamical simulations presented by Lupi et al. (2016). They compare two different methods, the Adaptive Mesh Refinement technique used in the code RAMSES, and the Lagrangian Godunov-type method adopted in GIZMO. In addition, three-dimensional radiation magneto-hydrodynamic simulations suggest that super-Eddington accretion flows can drive the rapid growth of low-mass BHs simultaneously, enabling high levels of both radiative and mechanical feedback Jiang et al. (2014). On the other hand, super-critical accretion onto low-mass BH seeds is not supported by radiation hydrodynamic models for BH formation in HII regions, which instead suggest rather low rates of accretion, below (or at most close to) the Eddington limit (e.g. Milosavljević et al. 2009a,b; Park and Ricotti 2011; 2012; 2013).

Very recently, the analysis of a sample of 20 quasars, including ULAS J1120 and SDSS J0100 at $z \geq 5.8$ presented by Trakhtenbrot et al. (2017b) suggest that the inferred BH masses and luminosities can be naturally explained by means of a classical thin accretion disk model, with radiative efficiencies in the range [0.04-0.4] and sub-Eddington accretion rates. This support the idea that super-critical growth may have occurred at earlier cosmic epochs ($z > 10$, e.g. Pezzulli et al. 2016).

Super-Eddington gas accretion regime is not only adopted for low-mass seeds growth. In their recent analytic model, Volonteri et al. (2015) show that galactic inflow rates as high as $1 - 100\, M_{\odot}/yr$ may trigger a sequence of fast ($10^4 - 10^7$ yr) episodes of super-critical accretion, onto both low-mass or high-mass seeds, at rates which are $10^2 - 10^4$ times larger than in the Eddington-limited scenario (see their Figure 2). As a result of these intermittent phases of short super-Eddington gas accretion a SMBH can be produced.

In the super-Eddington scenarios, the radiatively inefficient slim disk model (Abramowicz et al., 1988) ensures that even in the presence of hyper-Eddington accretion ($>> 20\dot{M}_{\rm Edd}$) the bolometric luminosity of the accreting BH is only mildly super-Eddington, $L_{\rm bol}/L_{\rm Edd} \leq (2-4)$ (e.g. Mineshige et al. 2000; Volonteri and Rees 2006; Madau et al. 2014; Volonteri et al. 2015; Pezzulli et al. 2016).

In Eddington-limited gas accretion scenarios, in which the BH can accrete at most at the Eddington rate, the formation of high-mass seeds, enabled by the LW radiative feedback is crucial to explain the fast growth of $z \sim 6$ SMBHs (see e.g. Johnson et al. 2013, the recent pSAMs of Petri et al. 2012; Valiante et al. 2016 and the review by Johnson and Haardt 2016). In their mixed-seed-based model Valiante et al. (2016) determine the relative contribution of low-mass and high-mass seeds to the final BH mass of J1148. They report that efficient Eddington-limited growth relies on the formation of $\approx 1 - 10$ high-mass seeds in order to produce the expected SMBH mass at $z = 6.4$. If high-mass seed formation is prevented, the predicted final BH mass does not exceed $\sim 10^6$ $M_{\odot}$, thus warranting the need for super-Eddington accretion in the low-mass seeds scenario.

Finally, a new cosmological semi-analytic model for galaxy formation, including the growth of SMBHs within a large box size (1.12 cGpc h^{-1}) N–body simulation (hSAM), has been presented by Makiya et al. (2016). Their model is currently tuned to reproduce the properties of local galaxies. Using this simulation, Shirakata et al. (2016) suggest that stringent constraints on the seed BH mass, may come from less massive bulges observed at $z \sim 0$, rather than the high redshift BH-bulge mass relation. Their study suggests that the mass of BHs observed in $\sim 10^9$ $M_{\odot}$ bulges is overpredicted if only seeding by high-mass seeds (10^5 $M_{\odot}$) is considered. Such small stellar mass bulges instead favour seeding by smaller seed BHs (10^3 $M_{\odot}$) or a mixed population of seed BHs randomly distributed in the mass range $10^3 - 10^5$ $M_{\odot}$.

Numerical simulations of equal-mass protogalaxies encounters show that merger-driven gas inflows are able to trigger the formation (without requiring the suppression of star formation) and rapid growth of a massive BH Mayer et al. (2010) as well as of actively accreting SMBH binaries Mayer et al. (2007). Recently, a suite of high spatial resolution simulations ($\sim$ 10 pc) have been devoted to study the effect of galaxy mergers on BH accretion, as a function of the initial merging galaxies' mass ratio, orbital configuration and gas fraction. These different stages of galactic encounters is described in Capelo et al. (2015). They confirm that more efficient BH accretion is induced during galaxy mergers with the initial mass ratio being the most critical parameter affecting BH accretion and AGN activity.

In the simulations presented by Feng et al. (2014); Di Matteo et al. (2016) the rapid growth of BHs, occurring in bulge dominated galaxies, is driven by large scale filamentary cold gas accretion, rather than by major gas rich mergers. Feng et al. (2014) extract 3 DM halos from the cosmological hydrodynamical simulation MassiveBlack, hosting 10^9 $M_{\odot}$ BHs and re-simulate them with zoom-in techniques. They find that dense cold gas is able to sustain accretion. During the accretion phase at the Eddington rate, the cold gas directly feeds the BH, while in the sub-Eddington phase (that they find for $z \lesssim 6$), the accretion disc is disturbed and disrupted by feedback. A recent numerical simulation, including X-rays radiation transport, presented by Smidt et al. (2017) suggest that both the SMBH observed in ULAS J1120 and SDSS J0100 (at $z \sim 7$ and $z = 6.3$, respectively) can form from $10^5\ M_\odot$ BH seeds (planted at $z = 19.2$) growing via cold accretion streams. The models reproduce the observed properties of the two quasars, such as the host galaxy mass, SFR, metallicity, luminosity and ionized near zone, including the dynamical mass enclosed within the inner 1.5 kpc region of the ULAS J1120 host galaxy, inferred from recent ALMA observations (Venemans et al., 2017).

Although the numerous studies presented to date, we can not yet draw firm conclusions on which growth mechanism (via super- or sub- critical accretion disks, cold accretion streams, mergers) and/or seed formation channel (low-mass vs high-mass seeds) is to be preferred, or more viable than the others, for high redshift SMBH formation.

3.4.4 BH feedback

As discussed in Section 3.1, the physical processes involved in quasar formation and evolution are expected to be regulated by AGN and stellar feedback. During the quasar-dominated regime ($z \lesssim 8$, see Section 3.5.2) a strong, galaxy-scale wind is predicted to be driven by the energy released during both BH accretion and SN explosions. This feedback is expected to clear the ISM of gas and dust leaving a un-obscured line of sight toward the central emitting source. In addition, radiation emitted from the optically bright quasar J1148 may contribute to at least 30% of the observed FIR luminosity ($> 20\ \mu$m) heating the large amount of dust ($\sim 3 \times 10^8\ M_\odot$) in the host galaxy ISM, outside the un-obscured cone. Both stellar and quasar optical/UV emission are expected to be reprocessed by dust, thus contributing to the observed FIR luminosity (Schneider et al., 2015).

Adopting an energy-driven wind prescription similar to that usually adopted by numerical simulations (e.g. Di Matteo et al. 2005) pSAMs show that the AGN feedback is the main driver of the massive observed gas outflow rates at $z > 6$. This is predicted to have a dominant effect with respect to stellar feedback (energy-driven winds from SN explosions) in shaping the high-z BH-host galaxy co-evolutionary path. For example, a powerful quasar-driven gas outflow is launched during the latest stages of the evolution ($\sim 100 - 200$ Myr) in the best-fit models of Valiante et al., 2011; 2012 and Pezzulli et al. (2016), for J1148. The predicted outflow rates are in good agreement with the observations, $> 1000 - 3000$ $M_{\odot}$/yr (Maiolino et al., 2012; Cicone et al., 2015) and $\sim 10^3$ times more efficient than the sub-dominant SN-driven contribution.

However, it is worth noting that the prescription usually adopted in SAMs to describe the energy-driven wind effects can not provide insights on the physical processes determining the observed properties of the outflowing gas and its complex dynamics.

Although described by sub-grid prescriptions, the response of the gas to the energy released by the accreting BH is now well described by hydro-dynamical simulations. Costa et al. (2014) study AGN feedback using the moving-mesh code AREPO. They find that, despite the fact that momentum driven outflows predict a $M_{\rm BH} - \sigma$ relation similar to that observed, the energy-driven scenario better reproduces the observed, large scale anisotropic AGN-driven outflows. With the same code Costa et al. (2015) re-simulate a zoom-in region around the six most massive halos at $z \sim 6$ to study the brightest quasars. They show that the high-velocity extended cold gas observed out to ~ 30 kpc (Maiolino et al. 2012; Cicone et al. 2015) requires the combined effect of SN and AGN feedback. SN-driven winds are responsible for the pre-enrichment of the circumgalactic and intergalactic medium in which the massive, fast (> 1400 kms^{-1}) AGN-driven hot outflow is launched, ensuring efficient radiative cooling (see e.g. Figure 2 in Costa et al. 2015) to explain the presence of cold gas (see e.g. Cicone et al. 2015).

Finally, high velocity ($10^2 - 10^3$ km s^{-1}) energy-driven winds on large scales have been recently also studied by Bieri et al. (2017) by means of radiation-hydrodynamic simulations of isolated galactic discs. They suggest that outflow rates as high as $\sim 10^3$ $M_{\odot}/yr$ are sustained by IR radiation, with scattering on dust grains enabling efficient momentum transfer to the gas.

3.5 The host galaxy properties

3.5.1 The origin of high-z dust.

Several theoretical models have been devoted to the study of the rapid enrichment of the ISM in $z > 6$ galaxies and quasars, and in particular to the origin of the huge amount of dust ($> 10^8\, M_\odot$) inferred from the FIR and sub-mm observations (e.g. Hirashita and Ferrara 2002; Morgan and Edmunds 2003; Dwek, Galliano, and Jones 2007; Dwek and Cherchneff 2011; Valiante et al., 2009; 2011; 2014; Gall et al., 2011b; 2011a; Mattsson 2011, Valiante et al. 2014; Calura et al. 2014).

A SN origin for the dust observed in the early Universe has often been advocated because of the shorter evolutionary time scale of core collapse SNe progenitors ($10 - 40\, M_\odot$ stars, with an age < 10 Myr) with respect to that of AGB stars (e.g. Morgan and Edmunds 2003; Dwek, Galliano, and Jones 2007). This scenario was supported by the deviation of the dust extinction curves of $z > 4$ quasars and gamma ray bursts (GRB) from the Small Magellanic Cloud (SMC) extinction curve, typical of $z < 2$ quasars (Maiolino et al., 2004; Stratta et al., 2007; Perley et al., 2010; Gallerani et al., 2010). This suggests either a different dust production mechanism or dust processing into the ISM at high redshift.

However, subsequent studies pointed out that stellar sources alone can not account for the entire dust budget and grain growth in cold, dense gas clouds must also have a dominant role, even at $z > 6$ (e.g. Michałowski et al. 2010; Valiante et al. 2011; Pipino et al. 2011; Rowlands et al. 2014; but see Ferrara et al. 2016).

Moreover, in contrast to what was previously thought, AGB stars are able to significantly contribute to dust production in high redshift quasars, producing a dust mass at least similar to that of SNe, already at $z \sim 8 - 10$ depending on the host galaxies' SFH and IMF (see Valiante et al. 2009 and Figure 8 in Valiante et al. 2011).

Modelling the properties, and in particular the evolution of dust, in quasar host galaxies at $z > 6$ is still a major challenge. Li et al. 2007; 2008 carried out the first multi-scale simulation, using GADGET2 (Springel et al., 2005), aimed to follow the formation of quasar J1148 in a hierarchical scenario, accounting for self-regulated BH growth (starting from Pop III seeds), AGN feedback and the host galaxy properties evolution. They showed that the metallicity and dust mass of J1148 are produced through a series of efficient bursts of star formation (see Figure 7 in Li et al. 2007) resulting in a final stellar mass of $10^{12}\, M_\odot$, similar to what is expected from the local $M_{\rm BH} - M_\star$ relation. To date, this is the only attempt to study the high-z dust properties made with numerical approaches (Li et al., 2008). However, only a single plausible hierarchical build-up of the J1148 DM halo, extracted (and re-simulated) from the $1 h^{-1}$ Gpc^3 volume is explored in these works and thus, the resulting

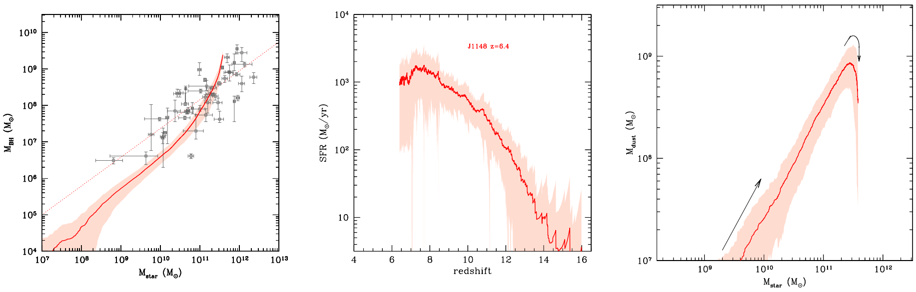

Figure 3.8. The cosmic cycle of a typical quasars at $z \sim 6$. Models reproduce the properties of J1148 (see text). Left panel: the build-up of the $M_{\rm BH} - M_{\rm star}$ relation through cosmic time as compared with data and empirical fit for local galaxies (Sani et al., 2011). Middle panel: the predicted star formation history via quiescent and merger-driven bursts (see e.g. Valiante et al. 2011). Left panel: the assembly of the dust mass into the ISM as a function of the stellar mass. In all panels the solid lines show the average over 50 different DM halo merger trees with shades representing the 1σ dispersion. These figures are adapted from Valiante et al. (2011).

SFH is unique. Semi-analytic models, which instead enable a statistical investigation of different SFHs, provide similar conclusions. The chemical properties of the host galaxy require an order of magnitude higher stellar mass with respect to the dynamical constraint, as discussed in the following sections.

3.5.2 The BH-host galaxy co-evolution

Observational campaigns at $z > 5$ show that quasars and their host galaxies are characterized by similar properties in terms of the BH, dynamical, dust and molecular gas masses, suggesting a common evolutionary scenario.

In Figure 3.8 we show the best-fit evolutionary scenario for the BH and host galaxy properties of J1148 as predicted by Valiante et al. (2011; 2014). Solid lines show the redshift evolution of the total masses[6] of BH and stars (on the left), the total SFR (in the middle) and dust and stars again (on the right) averaged over 50 different DM halo merger trees, with shaded areas representing the 1σ error.

As soon as efficient star formation starts, the BH grows in the buried AGN. At this

---

[6] At each redshift the total BH mass is given by the sum of the masses of all the existing nuclear BHs. In the same way the total stellar and dust masses represent the stellar and dust content summed over all the existing halos. See Valiante et al. (2011) for details.

stage its optical emission is outshined by the ongoing strong star burst, SFRs from 100 up to > 1000 $M_{\odot}$/ yr, at $z \sim 8$ (middle panel). The mass of dust (right panel) rapidly grows, reaching values as high as $10^9\, M_{\odot}$, when the bulk of the stellar mass, $\sim (2-4) \times 10^{11}\, M_{\odot}$, is already in place. During this dust-obscured phase, the total nuclear BH mass reaches $\sim 2 \times 10^8\, M_{\odot}$.

In this scenario, the progenitor galaxies of J1148 at $z \sim 8-10$ are predicted to have similar properties (e.g. BH, stellar and dust mass) as the observed SMGs at lower redshifts (e.g. Santini et al. 2010; Michałowski et al. 2010; Magnelli et al. 2012). These sub-mm galaxies are suggested to be the evolutionary stage preceding the active quasar phase.

The transition between the starburst-dominated regime and the quasar-dominated evolution, at $z < 8$, is triggered by powerful energy-driven winds which clear up the ISM of dust and gas (see e.g. the down turn indicated by the black arrow in the right panel of Fig 3.8), un-obscuring the line of sight toward the quasar and damping the SFR (we will discuss the AGN feedback in the following section).

SMBH evolution models suggest a steeper evolution of the BH-stellar bulge mass relation at high redshift, with the SMBH forming before/faster than the stellar bulge (e.g. Petri et al. 2012). In addition, the observed deviation of high redshift quasars from the local BH-stellar-mass ratio seems to be a natural outcome of SMBH growth driven by episodic super-Eddington accretion which leads to a BH accretion rate-to-SFR ratio of $> 10^2$ (Volonteri et al., 2015).

Agarwal et al. (2013) track the subsequent growth of DCBH seeds by using a modified version of the Agarwal et al. (2012) hSAM. In their simulated volume, they find that the merger of a DCBH host satellite with the neighbouring galaxy (source of the LW radiation field), leads to the resultant system lying above the local M_{BH}–M_{star} relation, already at these early stages of the evolution. The authors term this phase as 'obese black hole galaxies' or OBGs as the DCBH is able to outshine the stellar component, leading to unique observables that distinguish them from normal galaxies. The OBGs are expected to transition onto the local M_{BH}–M_{star} relation via mergers. However, they do not account for the formation and evolution of metals and dust in the ISM, which represent a strong constraint on the host galaxy SFH and final stellar mass.

Chemical evolution models instead point out that SFR, gas, metals and dust content of quasar host galaxies are well reproduced with standard assumptions of stellar IMF, star formation efficiency and dust grain growth, for galaxies with stellar masses $\geq 10^{11}\ M_\odot$ (see left panel of Figure 3.8). These are about one order of magnitude higher than the stellar masses inferred from the observations of high redshift quasars (e.g. Wang et al. 2010; 2013) and would bring the predicted $M_{\rm BH} - M_{\rm star}$ relation closer to the local value, suggesting that high redshift dynamical (and thus stellar) masses may be underestimated (Valiante et al., 2011; 2014, Calura et al. 2014).

Although a top-heavy IMF scenario (i.e. biased to more massive stars) can reproduce the observed dust mass and the deviation of J1148 from the local $M_{\rm BH} - M_{\rm star}$ relation, it requires a less-efficient SFH to do so. This results in a SFR at $z = 6.4$ that is more than 10 times smaller than the observed rate (Valiante et al. 2011), too small to provide the observed FIR luminosity even if the AGN contribution to dust heating (Schneider et al., 2015) is accounted for.

Instead, assuming a short evolutionary time scale does not solve the tension either. At the observed SFR $\sim 1000\ {\rm M_\odot/yr}$ the $\sim (3-4) \times 10^{10}\ M_\odot$ stellar mass estimated for quasars like J1148 would be produced in a quite short time interval, $\sim 10 - 20$ Myr. Such an evolutionary time scale is too short for stellar evolution to account for dust enrichment up to $> 10^{8}\ M_\odot$, even with a maximally efficient mode of dust formation by SNe (see Valiante et al. 2014 for a detailed discussion).

Following this discussion, it is important to note that, at $z > 6$, stellar masses can not be convincingly obtained via SED fitting as in local and lower redshift systems. A lower limit to the stellar mass (dynamical bulge) is usually obtained as $M_{\rm star} = M_{\rm dyn} - M_{\rm H_2}$ where dynamical and molecular gas masses, $M_{\rm dyn}$ and $M_{\rm H_2}$, respectively, are derived from CO observations.

Large uncertainties are introduced by the methods adopted to infer $M_{\rm dyn}$ and $M_{\rm H_2}$. A large scatter ($> 60\%$) in the estimated molecular gas mass is due to the adopted CO line luminosity−to−H_2 mass conversion factor, $\alpha_{\rm CO} = 0.8 \pm 0.5\ {\rm M_\odot/(K\ km\ s^{-1}\ pc^2)}$. This is typical of ultra luminous infrared galaxies (ULIRGs, Solomon et al. 1997, Downes and Solomon 1998) and usually adopted for high redshift quasars too. In addition, $M_{\rm dyn}$ strongly depends on geometrical assumptions for gas distribution which is usually considered to be disk-like, with given inclination angle i and radius R, which are difficult to infer from observations at such high redshifts. An uncertainty of more than 50% must be associated to the inferred values, $M_{\rm dyn} sin^2 i = (10^{10} - 10^{11})\, M_\odot$. A radius $R = 2.5$ kpc and an inclination angle $i = 65$ have been inferred for J1148, in which the CO emitting region is spatially resolved (Walter et al., 2004). For other quasars a similar radius and a mean inclination angle of 40 are usually assumed (see e.g. Maiolino et al. 2007; Wang et al. 2010).

Theoretical studies suggest that lower inclination angle ($i < 30$) and/or larger disk radius ($R \sim 5 - 30$) kpc may solve the so-called stellar mass crisis (see e.g. Figure 9 and discussion in Valiante et al. 2014).

Recent Atacama Large Millimeter and sub-millimetre Array (ALMA) observations of [CII] emission in quasars have suggested that a large fraction of the CO may be still undetected (Wang et al., 2013), supporting the idea that dynamical mass estimates could be missing some of the stars. Moreover, IRAM Plateau de Bure Interferometer (PdBI) follow-up observations of [CII] 158μm emission line and FIR continuum in J1148 host galaxy have revealed the presence of an extended cold gas component out to ~ 30 kpc which may be an indication of star formation activity on larger scales with respect to the size of the CO emission (Cicone et al., 2015).

Thus, stellar mass estimates from model predictions and observations may be reconciled by accounting for a more complex and/or more extended star and gas distribution, beyond the few kpc radius inferred from the CO emitting regions. Observations (Cicone et al., 2015), SAMs (Valiante et al., 2011; 2014 and Calura et al. 2014) and numerical simulations (e.g. Khandai et al. 2012) seem to agree with this scenario. Quasars at $z \sim 5$ resolved in the MassiveBlack simulation are predicted to be compact and gas rich systems with intense burst of star formation occurring in both the innermost and outer regions, out to the DM halo virial radius ($\sim 200h^{-1}$ kpc, Khandai et al. 2012).

In addition, Di Matteo et al. (2016) show that the most massive BHs ($> 10^8\, M_\odot$) at $z \sim 8$ reside in compact bulge-dominated galaxies (more than 80% of the stars are in the spheroidal component). The total stellar masses of these systems are already $> 10^{10}\, M_\odot$ (see e.g. Fig 1 and Table 1 of Di Matteo et al. 2016), bringing them well within the scatter of the observed local $M_{\rm BH} - M_{\rm star}$ relation. Pure SAMs provide very similar results [7].

---

[7] A mean BH and stellar mass of 4×10^8 and $3-4\times10^{10}\, M_\odot$ are predicted in both low-mass- and mixed-seeds

Finally, Lyu et al. (2016) derived a typical stellar mass of $(3-5)\times 10^{11}\ M_{\odot}$ on the basis of the IR SED analysis of about 100 quasars at $z > 5$, suggesting a BH-galaxy mass ratio of $10^{-3} - 10^{-2}$, consistent with local relations.

3.6 Discussion

In this review we have discussed the formation of the first quasars, and in particular the rapid growth of their SMBHs focusing on pure semi-analytic or hybrid (SAM plus N–body simulations) approaches.

For comparison, we have also mentioned the results of some of the state-of-the-art hydrodynamical simulations, providing deep insights on the dynamical evolution of galaxies. With respect to these simulations, semi-analytic (pure or hybrid) methods have the complementary role of enabling statistical studies and exploring different models and parameter space, on shorter computational time scales.

However, simplified geometries, models for the gas cycling and/or sub-grid prescriptions limit the scope of both pSAMs and hSAMs. Indeed, some physical aspects are still far from being taken into account in these models, such as the gas physics, feedback from stars and/or the accreting BH, or accretion rate in the inner part of the halo. This is where cosmological hydrodynamical simulations offer a laboratory to study the impact of physical processes related to the structure of collapsed objects.
Angular momentum, for example, is one such physical process. Gravitational systems, such as halos can possess a given degree of rotational support, which is described by the spin parameter $\lambda_{\rm spin} = {\rm J|E|^{1/2}/GM_h^{5/2}}$, with J the angular momentum of halos, E the total energy, and $M_{\rm h}$ the mass of halos. The angular momentum of a halo, or its baryonic central region, is thought to be the result of clustering/surrounding neighbors applying tidal torques on the given halo (Peebles, 1969).

Although, they have the advantage of directly tracking the cosmic evolution of the baryonic component of galaxies (where semi-analytic models need to use approximations), the main limitation of hydrodynamical simulations is that the physical processes, acting on different scales can not be described simultaneously, yet[8]. In other words, large and

---

scenarios presented in Valiante et al. (2016); Pezzulli et al. (2016).

[8] In addition, due to the higher computational costs required to run hydrodynamical simulations these mod-

small scales can not be resolved at the same time in simulations. This has been widely discussed by Habouzit et al. (2016b), in the case of DCBH formation. They use a small scale (1 cMpc), high resolution ($M_{\rm DM,res} \sim 2 \times 10^3\, M_\odot$) to study in detail the effect of expanding metal-rich bubbles around possible DC sites, while a larger box size (10 cMpc) with intermediate resolution ($M_{\rm DM,res} \sim 10^7\, M_\odot$) is adopted to statistically asses the impact of metal enrichment, SFR and SN-driven winds on the DCBH number density, in a significant volume of the Universe. Finally, the Horizon-noAGN large box (142 cMpc), low resolution ($8 \times 10^7\, M_\odot$) simulation is adopted to test whether DCBHs are able to explain the population of high redshift quasars.

Among the most recent hydrodynamical simulations devoted to study the rare, high density peaks DM halo hosting the first quasars, MassiveBlack (Di Matteo et al., 2012) and its high-resolutions zooms (Khandai et al., 2012; Feng et al., 2014), investigate the formation of SMBHs in the first galaxies, by covering a volume of 0.75 Gpc^3. A higher resolution is reached in the 0.5 Gpc^3 volume of the BlueTides simulation (Feng et al. 2015; 2016), enabling the study of the formation of the first SMBHs at early cosmic epochs ($z > 7$, Di Matteo et al. 2016).

Given the advancement in theoretical modelling techniques, all the different approaches can together be considered as a powerful tool to investigate different physical processes related to the formation and evolution of the first quasars at $z \sim 6$. Combined with observational constraints from current and future high-resolution instruments, these models can be further improved to provide definitive answers to the open questions discussed in Section 3.1.

---

els are often restricted to few realizations, small volumes and/or still require sub-grid prescriptions (just like SAMs).

Chapter 4

Growing the first supermassive black holes: the super-Eddington regime

4.1 Introduction

As discussed in Chapter 3, explaining the existence of high-z SMBHs is a challenge for theoretical models. In order to grow up to billion solar masses at $z \sim 6$, seed BHs must accrete gas at the Eddington rate almost uninterruptedly for several hundreds Myr, even if they start as heavy seeds of $[10^5 - 10^6]\,M_\odot$. Alternatively, short episodes of super-Eddington accretion have been suggested as a viable way to allow the efficient growth of SMBHs, especially if these start from light seeds of $\sim 100\,M_\odot$ (Haiman 2004; Yoo and Miralda-Escudé 2004; Shapiro 2005; Volonteri and Rees 2005, 2006; Pelupessy et al. 2007; Tanaka and Haiman 2009; Madau et al. 2014; Volonteri et al. 2015). In a recent numerical study, Lupi et al. (2016) show that, if a large reservoir of dense cold gas is available, a $M_{\rm BH} \sim 10^5 M_\odot$ can grow in a $\sim$ Myr timescale starting from a seed mass of $\sim 20 - 100\,M_\odot$, under the assumption of a slim accretion disk solution. The slim disk solution represents an advective, optically thick flows that generalise the standard Shakura & Sunyaev solution (see Section 2.5). In this model, the radiative efficiencies, that depend on the accretion rate, are low: the radiation is trapped and advected inward by the accretion flow (see however the recent simulations by Sądowski and Narayan 2016). In this scenario, the outflow has a negligible effect and the BH can accrete up to 80% − 100% of the gas mass available.

Indeed, there is observational evidence of mildly super-critical accretion (Kelly and

Shen, 2013; Page et al., 2014) in quasars at redshift up to ~ 7. In addition, recent numerical simulations aimed to study super-Eddington accretion onto a rapidly rotating BH (McKinney et al., 2014) and the energy, momentum and mass outflow rates from radiatively inefficient accretion discs (Sądowski et al., 2013) predict Eddington ratios $\eta_{\rm Edd} = L/L_{\rm Edd}$ up to 10. Such a high ratio has been also invoked to explain the nature of ultraluminous X-ray sources (e.g. Middleton et al., 2013).

In this Chapter, we investigate the role of super-Eddington accretion in the formation of the first SMBHs at redshift $z \sim 6$, with the aim to understand what are the environments where it can occur and discuss the implications for the coevolution of the SMBHs and their host galaxies at high redshifts. We base our analysis on the data-constrained semi-analytical model GAMETE/QSOdust that allows to simulate a large number of hierarchical histories of a quasar host dark matter halo, following the star formation history, chemical evolution and nuclear black hole growth in all its progenitor galaxies. The model has been first successfully used to investigate the properties of the $z = 6.4$ quasar SDSS J1148+5251 by Valiante et al. (2011, 2012), applied to a sample of quasars at $5 < z < 6.4$ by Valiante et al. (2014) and more recently used to investigate the relative importance of light and heavy seeds in the early growth of high-z SMBHs under the assumption of Eddington-limited accretion (Valiante et al., 2016). Here we present an improved version of the model, GAMETE/SuperQSOdust, that has been modified to follow gas cooling, disk and bulge formation, and BH gas accretion in all the progenitor systems of a $z = 6.4$ quasar, using SDSS J1148+5251 (hereafter J1148) as a prototype for the general class of luminous high-redshift quasars.

This Chapter is organized as follows. In Section 4.2 we briefly describe the hierarchical semi-analytic merger tree used to simulate the DM halo progenitors; in Section 4.3 we introduce the model, describing assumptions and physical prescriptions. In Section 4.4 we present the results. Finally, a discussion and the main conclusions are given in Section 4.5. In particular, we find that $\sim 80\%$ of $z \sim 6$ SMBH mass is grown by super-Eddington accretion, which can be sustained down to $z \sim 10$ in dense, gas-rich environments. The average BH mass at $z \sim 20$ is $M_{\rm BH} \gtrsim 10^4 \, M_\odot$, comparable to that of direct collapse BHs. At $z = 6.4$ the AGN-driven mass outflow rate is consistent with the observations and the BH-to-bulge mass ratio is compatible with the local scaling relation. However, the stellar

SDSS J1140+5251	
z	6.42
$M_{\rm BH}$ [$10^9 M_\odot$]	4.9 ± 2.5
$M_{\rm H2}$ [$10^{10} M_\odot$]	2.3 ± 1.9
$M_{\rm dyn} \sin^2 i$ [$10^{10} M_\odot$]	3.4 ± 1.3
$L_{\rm FIR}$ [$10^{13} L_\odot$]	2.2 ± 0.33
$L_{\rm bol}$ [$10^{14} L_\odot$]	1.36 ± 0.74
SFR [10^3M$_\odot$/yr]	2.0 ± 0.5
$M_{\rm dust}$ [$10^8 M_\odot$]	$3.4^{+1.38}_{-1.54}$

Table 4.1. Observed and inferred properties of the quasar SDSS J1148+5251. The black hole mass, $M_{\rm BH}$, is estimated from the Mg$_{\rm II}$ doublet and the $\lambda = 3000$ Å continuum (De Rosa et al., 2011). The mass of molecular gas, $M_{\rm H_2}$, and the dynamical mass, $M_{\rm dyn} \sin^2 i$, have been estimated from CO observations (see Valiante et al. 2014 for more details). The star formation rate, SFR, has been computed from the far-infrared (FIR) luminosity using the Kennicutt relation (see Section 4.4 fore further details). The value of $L_{\rm FIR}$ and $M_{\rm dust}$ have been computed by Valiante et al. (2011, 2014). The bolometric luminosity $L_{\rm bol}$ is estimated from the observed flux at 1450 Å (Fan et al., 2003) using the bolometric correction by Richards et al. (2006).

mass in the central 2.5 kpc is closer to the value inferred from CO observations. Finally, $\sim 20\%$ of J1148 progenitors at $z = 7.1$ have BH luminosities and masses comparable to ULAS J1120+0641, suggesting that this quasar may be one of the progenitors of J1148.

4.2 The hierarchical semi-analytic Merger Tree

The reconstruction of hierarchical merger histories for a M_h dark matter halo at redshift z is based on a binary Monte Carlo algorithm with mass accretion that applies the Extended Press-Schechter theory (see Section 1.3.1).

Rewriting Equation 1.36 in terms of progenitor mass M, we find

$$f(M, M_h)dM = \frac{1}{\sqrt{2\pi}} \frac{(\delta_c - \delta_{ch})}{(\sigma_M^2 - \sigma_{Mh}^2)^{3/2}} \exp\left[-\frac{(\delta_c - \delta_{ch})^2}{2(\sigma_M^2 - \sigma_{Mh}^2)^2} \right] \left| \frac{d\sigma_M^2}{dM} \right| dM, \tag{4.1}$$

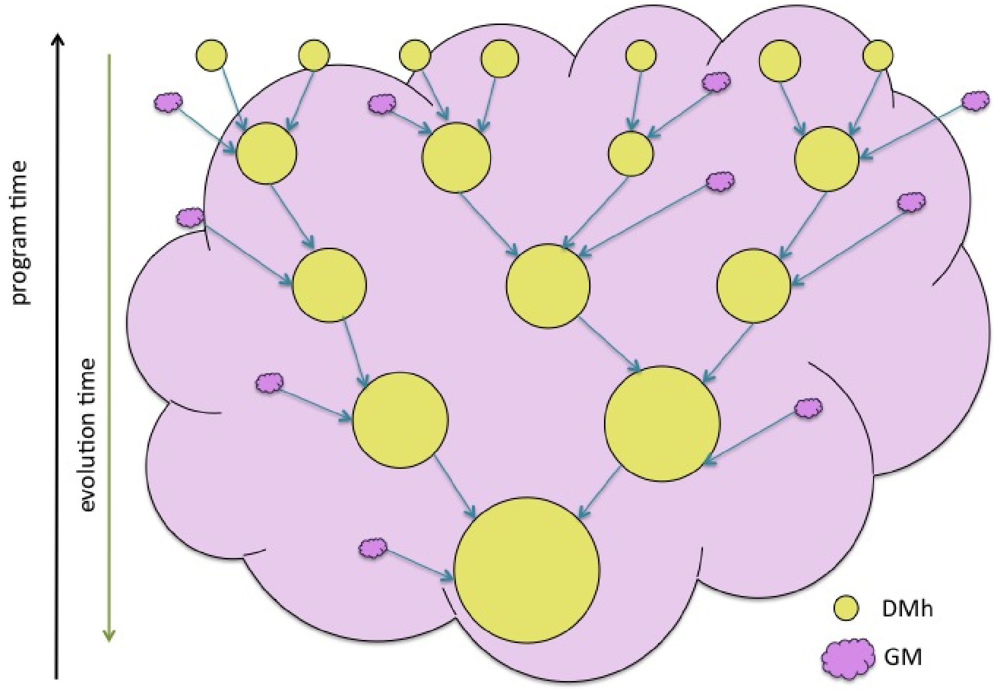

Figure 4.1. Illustration of a DM halos binary merger process as modelled in GAMETE/QSODUST. The cloud represents the Galactic Medium (GM) and the green circles the DM halos. Physical time flows in the diagram from top to bottom while viceversa for the code time.

where, following Chapter 1, we recall that: σ^2_M is the linear rms density fluctuation smoothed with a top-hat filter of mass M (σ^2_{Mh} is smoothed with a top-hat filter of mass M_h) and $\delta_c = \delta_c(z)$ is the critical linear overdensity threshold for collapse at redshift z (while $\delta_{ch} = \delta_c(z_h)$) defined as $\delta_c(z) = 1.686/D(z)$ where $D(z)$ is the linear growth factor (Carroll et al., 1992):

$$D(z) = \frac{5\Omega_m(z)}{2(1+z)}\left[\frac{1}{70} + \frac{209}{140}\Omega_m(z) - \frac{\Omega^2_m(z)}{140} + \Omega^{4/7}(z)\right]^{-1}, \tag{4.2}$$

and $\Omega_m(z) = \Omega_{m0}(1+z)^3[1 - \Omega_{m0} + (1+z)^3\Omega_0]^{-1}$.

This equation gives the fraction of mass in a halo of mass M_h at redshift z_h which, at an earlier time $z > z_h$, belongs to less-massive progenitors having mass in the range M to $M + dM$. Multiplying Equation 4.1 by the mass fraction, we find the number of halos per unit of mass

Figure 4.2. Number of progenitors of a halo $M_h = 10^{13} M_\odot$ at $z = 6.4$ as a function of the progenitor halo mass. Each panel shows the results for a single redshift, with histograms representing the averages over 10 independent merger tree realizations and errorbars indicating the Poissonian errors on the counts in each mass bin. Solid lines show the predictions of the Extended Press-Schechter theory while vertical lines mark the values of the resolution mass at the corresponding redshift.

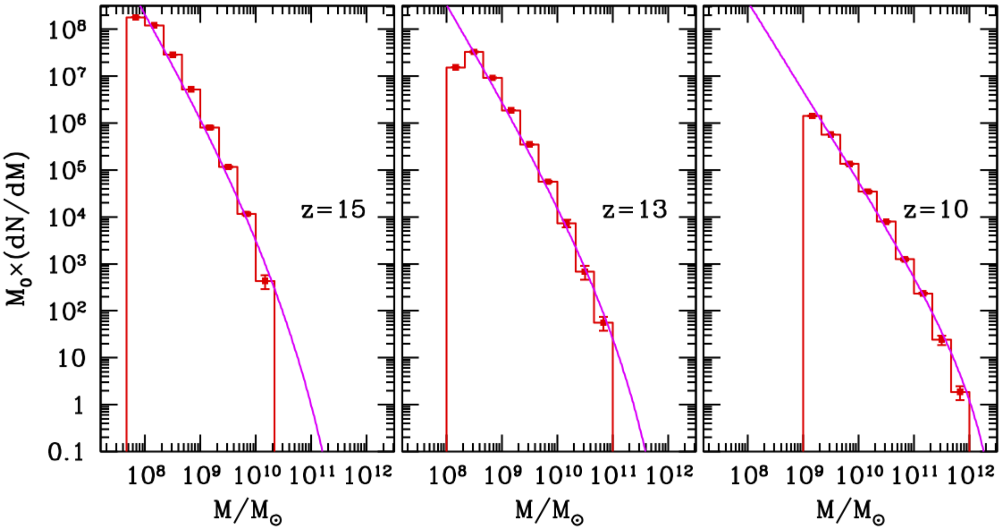

$$\frac{dN(M, M_h)}{dM} dM = f(M, M_h) \frac{M_h}{M} dM. \tag{4.3}$$

Writing the above equation in the limit $z \to z_h$ we find

$$\frac{dN}{dM} dM = \frac{1}{\sqrt{2\pi}} \frac{M/M_h}{(\sigma_M^2 - \sigma_{Mh}^2)^{3/2}} \frac{d\delta_c}{dz} \left| \frac{d\sigma_M^2}{dM} \right| dM dz, \tag{4.4}$$

where $z = z + dz$.

Using Equation 4.4, the code runs backward in time starting from a DM halo of fixed mass $M_h \in [10^{12}, 10^{13}] M_\odot$ in the redshift interval $z \in [5, 7]$, as outlined in Figure 4.1.

Fixing a cut-off resolution mass M_{res}, that separates the mass collapsed into progenitor halos, ($M_{\rm prog} > M_{\rm res}$) and the mass accretion M_{am} from the surrounding medium ($M_{am} < M_{\rm res}$), for each step the DM halo has two possibilities: to loose mass or to loose mass and to fragment in two progenitors, that have random masses smaller than $M_h/2$ and greater than $M_{\rm res}$.

The number of progenitors that the halo of mass M_h forms via fragmentation during a time step dz is

$$N_p = \int_{M_{res}}^{M_h/2} \frac{dN}{dM} dM. \tag{4.5}$$

In order to prevent multiple fragmentation (to avoid $N_p > 2$), since N_p decreases for decreasing dz, binary algorithms usually require small time steps.

The accreted mass fraction is:

$$F_a = \int_{M_0}^{M_{res}} \frac{dN}{dM} \frac{M}{M_0} dM. \tag{4.6}$$

To discriminate between accreted mass and progenitors, the code generates at each time step, and for each progenitor mass M_h, a random number $0 < C < 1$ and compares it with N_p. If $N_p < C$ the halo does not fragment at this step but just updates the new halo mass with $M_h(1 - F_a)$, while if $N_p \geq C$ the halo fragments. To ensure mass conservation, we proceed in two steps: first, a new random number in the mass range $M_{res} < M_1 < M_h/2$ is extracted from the distribution described by Eq 4.4; this identify the mass of the first progenitor halos. Then, the mass of the second progenitor is taken to be $M_2 = M_h(1 - F_a) - M_1$.

A high value of M_{res} prevents multiple fragmentation and controls the computational cost, but is important to find a good compromise between these advantages and the need to resolve low-mass halos. Indeed, hierarchical models predict less massive halos at high z, so that M_{res} should be a redshift dependent quantity, decreasing for increasing redshift.

Once virialized, the halo mass which, at a given redshift z correspond to a virial equilibrium temperature $T_{\rm vir}$ can be approximated as (Barkana and Loeb, 2001)

$$M(T_{\rm vir}, z) \sim 10^8 M_\odot \left(\frac{10}{1+z}\right)^{3/2} \left(\frac{T_{\rm vir}}{10^4 K}\right)^{3/2} \tag{4.7}$$

We take $M(T_{vir} = 10^4 K, z) \equiv M_4(z)$ to be the minimum mass of halos that can cool via the hydrogen Lyman-α line. In Figure 4.2 we show the mass function of progenitor halos of a $M_h = 10^{13} M_\odot$ at $z = 6.4$, at four different redshifts. Using the merger tree algorithm described above, we have run 10 independent merger histories of the final halo. The figure

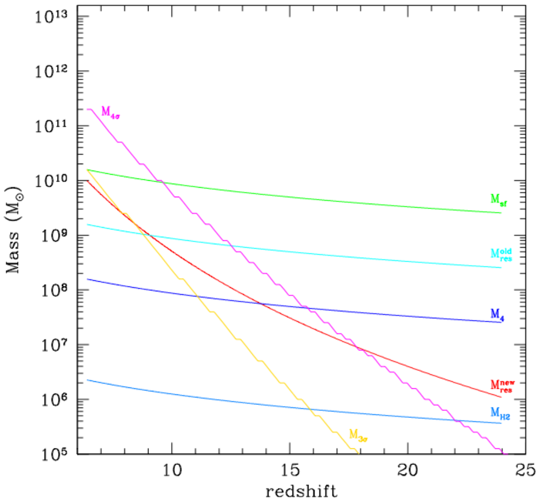

Figure 4.3. Redshift evolution of relevant timescales: $M_{\rm res}^{\rm old}$ (cyan) and $M_{\rm res}^{\rm new}$ (red) are the old and new resolution masses adopted in the merger tree; $M_{\rm H_2}$ (light blue) and M_4 (dark blue) are the minimum halo mass for H_2 and Lyman-alpha cooling; $M_{3\sigma}$ (yellow) and $M_{4\sigma}$ (purple) are the mass-scales that correspond to 3-sigma and 4-σ density fluctuations; finally, $M_{\rm sf}$ (green) is the threshold mass for star formation. All the mass-scales have been obtained assuming Planck cosmological model (see text).

shows that the results are in good agreement with the analytic predictions of the Extended Press-Schechter theory.

4.2.1 Mass resolution

We have chosen a value of the resolution mass shown in Figure 4.3, $M_{\rm res}^{\rm new}$, that we assume to have the following redshift dependence:

$$M_{\rm res}^{\rm new}(z_i) = 10^{-3} M_{\rm halo}(z_0) \left(\frac{1+z_i}{1+z_0} \right)^{-7.5}, \tag{4.8}$$

where $z_0 = 6.4$ and $M_{\rm halo}(z_0) = 10^{13}$ are the adopted redshift and halo mass for J1148. The redshift evolution of $M_{\rm res}^{\rm new}(z)$ is shown in Figure 4.3, where it is compared to the resolution mass used in (Valiante et al., 2011), $M_{\rm res}^{\rm old}(z)$, and to other relevant masses. It is clear from the figure that with this new choice, the merger tree is able to resolve a larger number of low-mass progenitors at high redshift. To compensate for this new choice of resolution mass, we also modify the time-step of the merger tree to ensure binarity. Hence we adopt logarithmically spaced redshift steps,

$$(1 + z_i) = (1 + z_{\mathrm{i+1}})10^{\mathrm{dz}}$$

with

$$dz = \frac{1}{i_{max}} \log(\frac{1 + z_n}{1 + z_0}), \tag{4.9}$$

where $i_{max} = 820$ is the total number of time step, $z_n = 24$ is the maximum considered redshift.

4.3 The model

In this section we provide a brief summary of the original GAMETE/QSODUST model and we present the new features for the upgrade version GAMETE/SUPERQSODUST, sketched in the Figure 4.4.

We reconstruct 30 independent merger histories of a dark matter halo at redshift 6.4 assumed to be the host of J1148. We adopt a Navarro Frenk & White (1995, NFW) density profile with a mass of $M_{\mathrm{h}} = 10^{13} M_{\odot}$, within the range supposed to host high-z bright quasars (Volonteri and Rees, 2006; Fan et al., 2004) and simulate its hierarchical history using a binary Monte Carlo merger tree algorithm based on the Extended Press-Schechter theory (Lacey and Cole, 1993).

The code follows the time evolution of the mass of gas, stars, metals and dust in a 2-phase ISM inside each progenitor galaxy (see also de Bennassuti et al., 2014), taking into account chemical enrichment from Asymptotic Giant Branch (AGB) stars and SNe, which inject dust and metals into the ISM, grain destruction by SN shocks and grain growth in dense molecular clouds.

Energy-driven outflows, powered by both AGN and SN feedback, are considered in the model: the energy released by the BH accretion process and SN explosions couples with the gas and can unbind a huge amount of interstellar gas (Silk and Rees, 1998). Although the physical mechanisms that trigger these galaxy-scale winds are still controversial, the model predicts mass ejection rates comparable to the observed ones (Maiolino et al., 2012; Valiante et al., 2012; Cicone et al., 2015).

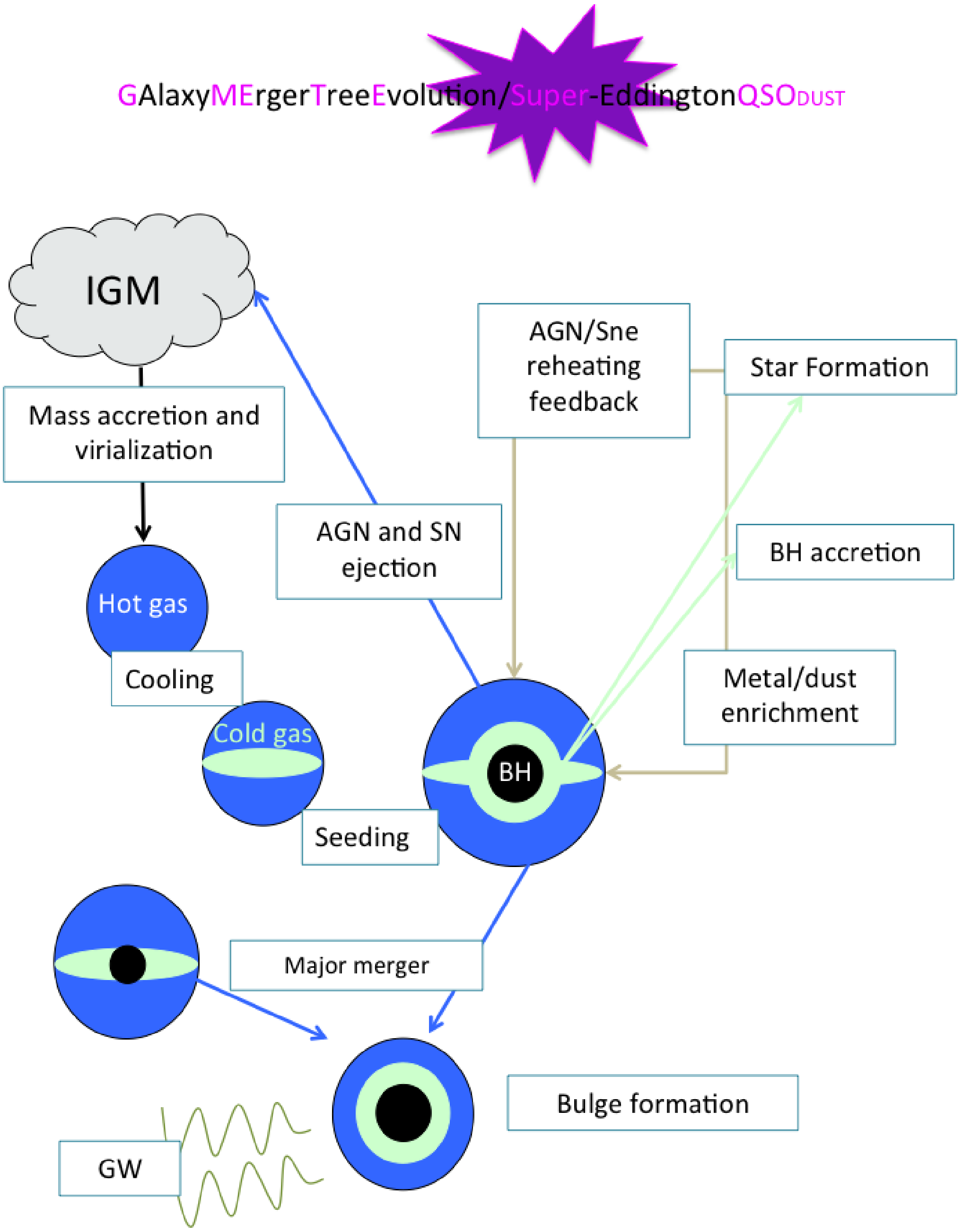

Figure 4.4. Sketch representing the operational scheme of GAMETE/SuperQSODust.

Following Valiante et al. (2011, 2016) we focus our study on one of the most distant and best studied quasar, J1148, discovered at redshift $z \simeq 6.4$ (Fan et al., 2003). The observationally inferred properties of this quasar are reported in Table 4.1. These are used to calibrate the model by fixing the adjustable free parameters shown in Table 4.2, as described below.

In what follows, we discuss the new features of the code, namely: (*a*) the formation of the disk via gas cooling; (*b*) the formation of the bulge via major mergers; (*c*) bursted and quiescent star formation both in the disk and in the bulge; (*d*) the BH seeding prescription; (*e*) the BH growth via accretion and coalescences, considering also the recoil velocities that can be generated by the product of the merging pair due to asymmetric gravitational wave emission; (*f*) SNe and AGN feedback, responsible of galactic-scale winds.

We adopt a ΛCDM cosmology with parameters $\Omega_m = 0.314$, $\Omega_\Lambda = 0.686$, $h = 0.674$ (Planck Collaboration et al., 2014), so that the Hubble time at redshift 6.4 is 851 Myr. The difference with the cosmological parameters adopted in previous works (Valiante et al., 2011, 2014) is mainly the larger value of σ_8 (Planck $\sigma_8 = 0.834$, WMAP7 $\sigma_8 = 0.761$), which implies an increased power at small scales, leading to a larger number of progenitor systems at high redshifts.

4.3.1 Gas cooling

In each newly virialized dark matter halo with mass M_h, the initial gas mass is assumed to be the cosmic baryon fraction $M_{\rm diff} = (\Omega_{\rm b}/\Omega_{\rm m})\, M_h$. We suppose this gas to be all in the diffuse phase, i.e. pressure-supported, and to follow an isothermal density profile ρ_g defined as:

$$\rho_g(r) = \frac{M_{\rm diff}}{4\pi R_{\rm vir} r^2}, \tag{4.10}$$

where $R_{\rm vir}$ is the virial radius of the dark matter halo. The hot diffuse gas gradually cools providing the reservoir of cold gas out of which stars form (see Section 1.3.3). The gas cooling processes strongly depend on the temperature and chemical composition of the gas.

In dark matter halos with virial temperature $T_{\rm vir} < 10^4\, K$, referred to as mini-halos, the primordial gas can cool only through H_2 roto-vibrational transitions (Haiman et al., 1996).

As the gas becomes progressively enriched in heavy elements, other molecular species can contribute to cooling and collisionally excited metal fine-structure lines, mostly OI, CII can provide additional cooling pathways. Here we only consider the contribution of H_2, OI and CII cooling using metallicity dependent tabulated cooling functions, $\Lambda(T_{\rm vir}, Z)$, computed as described in Appendix A of Valiante et al. (2016) but we neglect the effect of H_2 photo-dissociation by Lyman-Werner photons. We will return to this point in Section 4.4.

In dark matter halos with virial temperatures $T_{\rm vir} \geq 10^4$K (Lyα cooling halos), the temperature is high enough to excite atomic transitions, allowing the primordial gas to cool through hydrogen Lyman-α line emission. In this regime, we use metallicity-dependent tabulated cooling functions presented by Sutherland and Dopita (1993) and shown in Figure 1.5.

The time scale for gas cooling, $\tau_{\rm cool}$, is defined as:

$$\tau_{\rm cool} = \frac{3}{2}\frac{\mu m_p \kappa_B T_{\rm vir}}{\rho_g(r_{\rm cool})\Lambda(T_{\rm vir}, Z)}, \tag{4.11}$$

where κ_B is the Boltzmann constant, μ is the mean molecular weight and $r_{\rm cool}$ is the cooling radius and it is obtained by assuming that the cooling time is equal to the halo dynamical time $t_{\rm dyn} = R_{\rm vir}/v_{\rm DM}$, where $v_{\rm DM}$ is the dark matter (DM) halo circular velocity:

$$r_{\rm cool} = \left[\frac{t_{\rm dyn}\, M_{\rm diff}\, \Lambda(T_{\rm vir}, Z)}{6\pi\, \mu m_p\, \kappa_B T_{\rm vir}\, R^2_{\rm vir}}\right]^{1/2}. \tag{4.12}$$

Then, the gas cooling rate can be computed[1] as:

$$\dot{M}_{\rm cool} = 4\pi\rho_g(r_{\rm cool})r^2_{\rm cool}\frac{dr_{\rm cool}}{dt} = \frac{M_{\rm diff}}{2R_{\rm vir}}\frac{r_{\rm cool}}{t_{\rm dyn}}. \tag{4.13}$$

4.3.2 Disk and bulge formation

Along the hierarchical history of the final DM halo, we define major (minor) halo-halo merger events as those with halo mass ratio $\mu = M_{\rm halo,1}/M_{\rm halo,2}$ (with $M_{\rm halo,1} \leq M_{\rm halo,2}$) larger (lower) than $\mu_{\rm thr} = 1/4$ (Barausse, 2012). In quiescent evolution (i.e. no encounters with other galaxies), the cold gas settles on a rotationally-supported disk, because of the conservation of angular momentum, and can start to form stars. The disk, composed of gas

---

[1] Note that if $r_{\rm cool} > R_{\rm vir}$ we assume that the gas never reaches hydrostatic equilibrium and it is immediately available to star formation (De Lucia et al., 2010).

and stars, can be disrupted by a major merger and a spherical bulge is expected to form in this event. Minor mergers, instead, are not expected to destroy the disk but may help the growth of the bulge by disk instabilities (Naab and Burkert, 2003; Bournaud et al., 2005).

In our model, major mergers are supposed to destroy both the gaseous and stellar disk components of the newly-formed galaxy, adding the stars and gas to the central bulge. Minor mergers do not contribute to the transfer of matter between the disk and bulge, and thus lead to the formation of a new galaxy with disk and bulge masses that are the sum of the two progenitors ones.

We consider a self-gravitating disk, with an exponential gas surface density profile, $\Sigma_{\rm d}$, defined as (Mo et al., 1998):

$$\Sigma_{\rm d}(r) = \Sigma_{\rm d}(0)\, e^{-r/R_{\rm d}}, \tag{4.14}$$

where $R_{\rm d}$ is the scale radius of the gaseous disk and $\Sigma_{\rm d}(0)$ is the central surface densities of the gas. For the stellar component of the disk, we adopt the same density profile with the same scale radius $R_{\rm d}$. Following Mo et al. (1998) we define the scale radius as,

$$R_{\rm d} = \frac{1}{\sqrt{2}}\left(\frac{j_{\rm d}}{m_{\rm d}}\right)\lambda R_{\rm vir}\frac{1}{\sqrt{f_{\rm c}}} f_{\rm R}(\lambda, c, m_{\rm d}, j_{\rm d}), \tag{4.15}$$

where $j_{\rm d} = J_{\rm d}/J$ is the ratio between the disk angular momentum and that of the halo, $m_{\rm d} = M_{\rm d}/M_{\rm h}$ is the disk mass (stars+gas) fraction over the halo mass. From the conservation of the specific angular momentum we assume $j_{\rm d}/m_{\rm d} = 1$. The spin parameter λ is considered to be constant and equal to 0.05, the mean value adopted by Mo et al. (1998).

The factors $f_{\rm c}$ and $f_{\rm R}$ take into account the correction to the total energy of the halo resulting from the NFW density profile and the gravitational effect of the disk, and are computed following the prescription given by Mo et al. (1998). The factor $f_{\rm c}$ depends on the concentration parameter c, that we assume to be constant and equal to $c = 1$[2]:

---

[2] Unfortunately, numerical studies of the concentration parameter of dark matter halos spanning the mass and redshift range relevant for the present study are not available. Extrapolating the results of Muñoz-Cuartas et al. (2011), we adopt a constant value of $c = 1$. At a fixed halo mass, BH growth would be favoured in more concentrated halos, that are characterized by a larger mass and circular velocity in the inner regions (Mo et al., 1998).

$$f_{\rm c} = \frac{c}{2}\frac{1 - 1/(1+c)^2 - 2\ln(1+c)/(1+c)}{[c/(1+c) - \ln(1+c)]^2}. \tag{4.16}$$

The factor $f_{\rm R}$ is computed as,

$$f_{\rm R} = 2\left[\int_0^\infty e^{-u}u^2 \frac{v_c(R_{\rm d}u)}{v_c(R_{\rm vir})}\right]^{-1}, \tag{4.17}$$

where $v_c(r)$ is the total rotation velocity of the system,

$$v_c^2(r) = v_d^2(r) + v_b^2(r) + v_{\rm DM}^2(r). \tag{4.18}$$

Here v_b is the circular velocity of the bulge, $v_{\rm DM}$ is the circular velocity of the DM halo and v_d is the circular velocity of the thin, exponential disk,

$$v_d^2 = \pi G \Sigma_0\, x^2[I_0(x/2)K_0(x/2) - I_1(x/2)K_1(x/2)], \tag{4.19}$$

where $x = r/R_{\rm d}$ and I_α, K_α are the modified Bessel functions of the first and second type, respectively and $\Sigma_0 = \Sigma(0)_{\rm d} + \Sigma(0)_{\rm d}^\star$ is the sum of the gas and stellar central ($r = 0$) surface densities.

For the bulge component, we assume that the gas density profile $\rho_{\rm b}(r)$ is described as (Hernquist, 1990),

$$\rho_{\rm b}(r) = \frac{M_{\rm b}}{2\pi}\frac{r_{\rm b}}{r(r+r_{\rm b})^3}, \tag{4.20}$$

where the scale radius, $r_{\rm b}$, is computed as $r_{\rm b} = R_{\rm eff}/1.8153$ (Hernquist, 1990), and the effective radius $R_{\rm eff}$[3], depends on the gas and stellar masses in the bulge (Shen et al., 2003):

$$\log(R_{\rm eff}/{\rm kpc}) = 0.56\log(M_{\rm b} + M_{\rm b}^\star) - 5.54. \tag{4.21}$$

We adopt the same density profile for the stellar component in the bulge.

The velocity profile of the bulge, computed through the Poisson equation is

$$v_b^2 = \frac{Gr(M_{\rm b} + M_{\rm b}^\star)}{(r_{\rm b} + r)^2}. \tag{4.22}$$

---

[3] $R_{\rm eff}$ is the effective radius of the isophote enclosing half the light.

Table 4.2. The calibrated values of the adjustable parameters of the reference model.

Free parameters		**values**
$\epsilon_{\mathrm{d}}^{\star}$	quiescent star formation efficiency	0.083
β	BH accretion efficiency	0.03
ϵ_{AGN}	AGN-feedback efficiency	1.5×10^{-3}

We assume that the halo responds adiabatically to the gradual build up of the disk and bulge, maintaining the spherical symmetry during the contraction. Thus, the angular momentum is conserved during the collapse from a mean initial radius r_i to a radius r ($< r_i$), so that:

$$M_f(r)r = M(r_i)r_i, \tag{4.23}$$

where $M(r_i)$ is the mass of DM enclosed in r_i obtained integrating the NFW density profile and $M_f(r)$ is the total final mass within a radius r:

$$M_f(r) = M_{\mathrm{d,t}}(r) + M_{\mathrm{b,t}}(r) + (1 - f_{\mathrm{gal}})M(r_i), \tag{4.24}$$

where $M_{\mathrm{d,t}}(r)$ and $M_{\mathrm{b,t}}(r)$ are the total disk and bulge masses (star and gas) enclosed within a radius r, obtained by integrating eqs. (4.14) and (4.20), and $f_{\mathrm{gal}} = [M_{\mathrm{d,t}} + M_{\mathrm{b,t}}]/M_{\mathrm{h}}$ is the fraction of the total mass in the disk and bulge.

The velocity curve of the perturbed DM halo is then,

$$v_{\mathrm{DM}}^2(r) = [G(M_f(r) - M_{\mathrm{d,t}}(r) - M_{\mathrm{b,t}}(r)]/r. \tag{4.25}$$

Following these prescriptions we model the formation and evolution of disk and bulge components in each halo along the reconstructed merger histories.

Star formation rate

Hydrodynamical simulations suggest that merging events, major mergers in particular, can trigger bursts of star formation in the central regions as a consequence of the tidal forces produced by galaxy-galaxy interactions (Mihos and Hernquist, 1994; Springel, 2000; Cox et al., 2008).

Since starbursts are confined in the very central region of the galaxy, we assume a quiescent mode of star formation in the disk while bursts are triggered in the bulge when a major merger occurs. The star formation rate (SFR) in the disk is described as,

$$\dot{M}^{\star}_{\rm d} = \epsilon^{\star}_{\rm d} \frac{M_{\rm d},}{\tau_{\rm d}} \tag{4.26}$$

where $M_{\rm d}$ is the gas mass in the disk, $\tau_{\rm d} = 3R_{\rm d}/v_c(3R_{\rm d})$ is the dynamical time of the disk evaluated at the peak of the circular velocity profile (Mo et al., 1998), $R_{\rm d}$ is the disk scale radius defined in Equation 4.15 and $\epsilon^{\star}_{\rm d}$ is an adjustable free parameter representing the star formation efficiency in the disk. In our reference model, $\epsilon^{\star}_{\rm d} = 0.083$ (see Table 4.2).

Similarly, the SFR in the bulge is computed as,

$$\dot{M}^{\star}_{\rm b} = \epsilon^{\star}_{\rm b} \frac{M_{\rm b}}{\tau_{\rm b}}, \tag{4.27}$$

where $M_{\rm b}$ is the gas mass in the bulge, $\tau_{\rm b} = R_{\rm eff}/v_c(R_{\rm eff})$ is the dynamical time of the bulge and the effective radius $R_{\rm eff}$ is defined in Equation 4.21 above. We assume that in absence of merger events, the star formation efficiency in the bulge is equal to that of the disk, $\epsilon^{\star}_{\rm b} = \epsilon^{\star}_{\rm d}$. When a merger event occurs, the star formation efficiency increases as a consequence of the destabilizing effect of the interaction, and we adopt the following scaling relation:

$$\epsilon^{\star}_{\rm b} = \epsilon^{\star}_{\rm d}\, f(\mu), \tag{4.28}$$

with $f(\mu) = \max[1, 1 + 2.5\,(\mu - 0.1)]$, so that mergers with $\mu \leq 0.1$ do not trigger starbursts. With the adopted scaling relation, the starburst efficiency in the reference model is $0.083 \leq \epsilon^{\star}_{\rm b} \leq 0.27$, consistent with the range of values found by means of hydrodynamical simulations of merging galaxy pairs (Cox et al., 2008) and adopted by other studies (Menci et al., 2004; Valiante et al., 2011).

4.3.3 Black hole growth and feedback

BH seeds

We assume BH seeds to form only as remnants of first (Pop III) stars. In fact, our main aim is to investigate if SMBHs can form by super-Eddington accretion starting from light seeds at high redshift. Although the initial mass function of Pop III stars is still very uncertain, the most recent numerical simulations suggest a characteristic mass of a few hundreds of solar masses at $z \sim 25$, that progressively shifts to a few tens of solar masses at lower redshifts (Hirano et al., 2015). For simplicity, here we do not consider the redshift modulation of the characteristic mass and we plant a BH seed with a mass of $M_{\rm seed} = 100\,M_{\odot}$ in each newly-virialized halo with a metallicity $Z < Z_{\rm cr} = 10^{-4} Z_{\odot}$, above which the effects of dust and metal line cooling allow the gas to fragment, reducing the characteristic mass to values comparable to those found in local stellar populations (Schneider et al., 2002, 2003, 2012b; Omukai et al., 2005).

BH accretion

Once formed, the BH accretes gas from the surrounding medium. The correlation between the mass of central SMBH and the bulge mass or velocity dispersion (Magorrian et al. 1998; Richstone et al. 1998, see Kormendy and Ho 2013 and references therein) and the small scale on which the accretion takes place, suggest that the accretion onto the central black hole should be fuelled by the cold gas present in the bulge.

The collapse of material onto the central BH in a galaxy is triggered by both merger-driven infall of cold gas, which loses angular momentum due to galaxy encounters, and quiescent accretion, assuming that the accretion rate is proportional to the cold gas mass in the bulge,

$$\dot{M}_{\rm accr} = \frac{f_{\rm accr} M_{\rm b}}{\tau_{\rm b}}, \tag{4.29}$$

where, similarly to Equation (4.28), the accretion efficiency is expressed as,

$$f_{\rm accr} = \beta f(\mu), \tag{4.30}$$

where β is an adjustable free parameter. In our reference model, $\beta = 0.03$ (see Table 4.2), so that the efficiency of BH accretion is about $\sim 1/3$ of the efficiency of star formation in the bulge.

Thus, the mass growth rate is,

$$\dot{M}_{\rm BH} = (1 - \epsilon_r)\dot{M}_{\rm accr}, \tag{4.31}$$

where the radiative efficiency ϵ_r is defined as,

$$\epsilon_r = \frac{L_{\rm bol}}{\dot{M}_{\rm accr}\, c^2}, \tag{4.32}$$

with $L_{\rm bol}$ being the bolometric luminosity emitted by the accretion process. At high accretion rates, the Shakura and Sunyaev (1973) model of BH growth through a thin disk, where all the heat generated by viscosity is immediately radiated away, is incorrect. Instead, it is possible to use the optically thick, slim accretion disk solution, that is characterized by low radiative efficiencies (Abramowicz et al., 1988).

The bolometric luminosity, $L_{\rm bol}$, is computed starting from the numerical solutions of the relativistic slim accretion disk equations obtained by Sądowski (2009), adopting the fit presented by Madau et al. (2014):

$$\frac{L_{\rm bol}}{L_{\rm Edd}} = A(a)\left[\frac{0.985}{\dot{M}_{\rm Edd}/\dot{M}_{\rm accr} + B(a)} + \frac{0.015}{\dot{M}_{\rm Edd}/\dot{M}_{\rm accr} + C(a)}\right], \tag{4.33}$$

where the Eddington accretion rate is defined as $\dot{M}_{\rm Edd} \equiv 16\, L_{\rm Edd}/c^2$ and $A(a), B(a)$ and $C(a)$ are functions of the BH spin parameter a,

$$A(a) = (0.9663 - 0.9292a)^{-0.5639}, \tag{4.34}$$

$$B(a) = (4.627 - 4.445a)^{-0.5524}, \tag{4.35}$$

$$C(a) = (827.3 - 718.1a)^{-0.7060}. \tag{4.36}$$

The slim accretion disk model represented by Equation (4.33) predicts that even when the accretion rate is super-Eddington, with $1 \lesssim \dot{M}_{\rm accr}/\dot{M}_{\rm Edd} \lesssim 100$, the disk luminosity remains only mildy super-Eddington, with $L_{\rm bol} \lesssim (2-4)\, L_{\rm Edd}$. In fact, in this regime a large fraction of the energy generated by viscosity does not have the time to be radiated away and is instead advected into the black hole. As a result, the radiative efficiency is very small, with $0.002 \lesssim \epsilon_r \lesssim 0.05$, almost independently of the value of the BH spin parameter (see Figure 1 in Madau et al. 2014. Conversely, when the accretion rate is sub-Eddington, the radiative efficiency increases reaching an almost constant value which depends on the BH spin, as in the standard think disk solution, with $\epsilon_r \lesssim 0.05$ for $a = 0$ and $\epsilon_r \lesssim 0.3$ for $a = 0.98$.

Here we do not describe the time evolution of the BH spin parameter and we simply assume that the module of the spin vector a is randomly extracted from a uniform distribution

(Tanaka and Haiman, 2009; Barausse, 2012).

BH mergers

In halo merging events, we assume that the two nuclear BHs coalesce with the same timescale of their host halos. However, in minor mergers (with $\mu < \mu_{\rm thr} = 1/4$, see Section 4.3.2) only the largest of the two progenitors BHs can settle in the centre of the new halo potential well, surviving as a nuclear BH, while the smaller one ends up as a satellite.

During the BH merger, the newly formed BH receives a large center-of-mass recoil due to the net linear momentum carried by the asymmetric gravitational waves emission (Campanelli et al., 2007; Schnittman et al., 2008; Baker et al., 2008). The recoil (or kick) velocity of the coalesced binary depends on the mass ratio of the merging pair and on the amplitude and orientation of the spin vectors of the two BHs. Here we follow the parametrization presented by Tanaka and Haiman (2009) and - for each merger event - we compute the kick velocity as a function of the BH mass ratio assuming the spin vectors to be randomly oriented. The average kick velocities increase with the mass ratio of the merging pair, $q = M_{\rm BH,1}/M_{\rm BH,2}$ (with $M_{\rm BH,1} \leq M_{\rm BH,2}$). For strongly unequal mass mergers, with $0.01 \lesssim q \lesssim 0.1$, we find $\langle v_{\rm kick} \rangle = 1 - 100$ km/s, whereas for larger mass ratios, with $0.1 \lesssim q \lesssim 1$, the kicks can be very strong, with velocities $\langle v_{\rm kick} \rangle = 100 - 1000$ km/s.

We then compare the kick velocity with the circular velocity at the radius of influence of the BH, $R_{\rm BH} = GM_{\rm BH}/v_c^2(R_{\rm BH})$ with $v_c(r)$ given by Equation (4.18), and we retain the BH only when $v_{\rm kick} < v_c(R_{\rm BH})$. For $M_{\rm BH}/M_{\rm h} = 10^{-3}$, the retention velocity is $v_c(R_{\rm BH}) \sim 2v_{\rm vir}$, where $v_{\rm vir}$ is the escape velocity at the virial radius (Yoo and Miralda-Escudé, 2004).

BH feedback

There is now strong observational evidence that the energy released by the quasar can drive powerful galaxy-scale outflows (for recent works see Feruglio et al. 2015; Carniani et al. 2015; Cresci et al. 2015 and references therein). Outflowing gas at velocities up to $v \sim 1400$ km/s traced by [CII] emission has been detected in SDSS J1148 (Maiolino et al., 2012) with an estimated total mass outflow rate of $1400 \pm 300\, M_\odot$/yr that decreases with distance from the quasar, ranging from a peak value of $\sim 500\, M_\odot$/yr at ~ 3 kpc to $\lesssim 100\, M_\odot$/yr at ~ 20 kpc (Cicone et al., 2015).

In Valiante et al. (2012) we show that the quasar-driven mass outflow rate predicted by GAMETE/QSODUST, on the basis of a simple energy-driven wind, is in good agreement with the observations. Here we follow a similar approach, adopting the so-called "blast wave" model, in which the AGN radiation field can accelerate the gas generating fast supersonic winds which propagates outwards through an expanding blast wave, pushing out the surrounding medium (see e.g. Cavaliere et al. 2002; King 2003, 2005, 2010; Lapi et al. 2005; Menci et al. 2005, 2008; Zubovas and King 2012, 2014; Costa et al. 2014 and references therein).

In this framework, the energy released by the AGN that couples with the interstellar gas is estimated as,

$$\dot{E}_{\rm AGN} = \epsilon_{\rm AGN}\, \epsilon_r\, \dot{M}_{\rm accr} c^2, \tag{4.37}$$

where the coupling efficiency $\epsilon_{\rm AGN}$ is an adjustable free parameter. In our reference model $\epsilon_{\rm AGN} = 1.5 \times 10^{-3}$ (see Table 4.2).

If the post shock material does not cool efficiently, the bubble expands adiabatically and the outflow is energy-driven. As the blast wave propagates from the center of the halo, it first interacts with the gas of the disk and bulge, reheating a fraction of cold gas and transferring mass to the diffuse hot phase.

When the shock has propagated beyond the bulge and disk radius, part of the gas mass is ejected from the galaxy, if the binding energy is not enough to hold the material.

The mass outflow rate at a given radius r can be estimated as:

$$\dot{M}_{\rm w,AGN}(r) = 2\, \epsilon_{\rm AGN}\, \epsilon_r \left(\frac{c}{v_c(r)} \right)^2 \dot{M}_{\rm accr}, \tag{4.38}$$

where v_c is the circular velocity of the system given by Equation (4.18), and we evaluate the above equation at the bulge, disk and DM halo virial radius.

A similar description is used to describe the effects of SN-driven winds. The mass outflow rate beyond a given radius r is given by:

$$\dot{M}_{\rm w,SN}(r) = \frac{2\, \epsilon_{\rm SN}\, E_{\rm SN}}{v_c(r)^2} R_{\rm SN} \tag{4.39}$$

where $R_{\rm SN}$ is the rate of SN explosions, $E_{\rm SN}$ is the average SN explosion energy, and $\epsilon_{\rm SN} = 1.6 \times 10^{-3}$ is the SN wind efficiency (Valiante et al., 2012). The time-dependent SN rate and

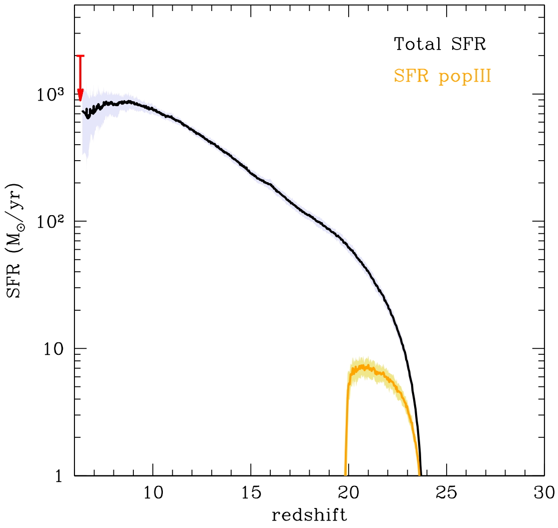

Figure 4.5. Redshift evolution of the total SFR (black line) and of Pop III stars (orange line), averaged over the 30 realizations. Shaded areas represent 1-σ dispersions and the red arrow indicates the upper limit on the SFR inferred from the IR luminosity (see in the text for further details).

explosion energy is computed for each galaxy along the merger tree according to formation rate, age and initial mass function of its stellar population. A detailed description of the chemical evolution model can be found in Valiante et al. (2011, 2014) and de Bennassuti et al. (2014).

4.4 Results

In this section, we present the predicted evolution of the hierarchical assembly of the SMBH and its host galaxy. To explore the dependence of the results on the population of progenitors and their merger rate, for the same model parameters we have run 30 independent merger trees. In one merger tree we find that a merger occurs at $z = 6.43$ between two black holes of $M_{1,\mathrm{BH}} = 1.7\times10^9 M_\odot$ and $M_{2,\mathrm{BH}} = 1.6\times10^9 M_\odot$, producing a recoil velocity $\sim$ 2 times higher than the retention speed, $v_c(R_{\mathrm{BH}})$. The newly formed BH is displaced from the center and it stops accreting gas. For this reason, we do not consider this to be a viable formation route for a bright quasar like J1148, and we exclude this merger tree from

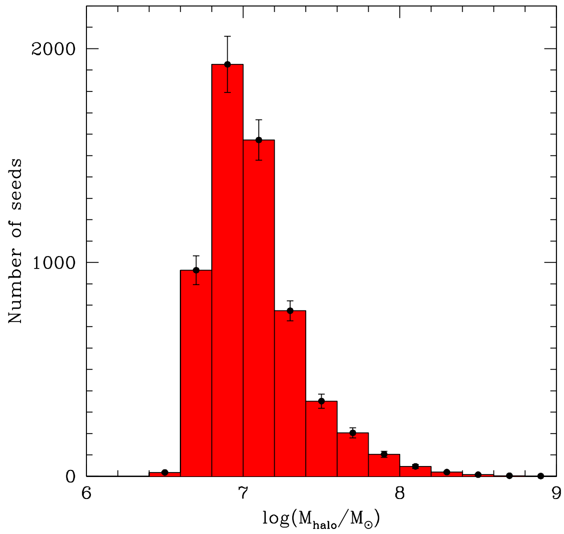

Figure 4.6. Mass distribution of halos hosting a newly formed 100 $M_{\odot}$ BH seed, averaged over the 30 realizations with 1-σ error bars.

the sample average.

4.4.1 The formation of stars and BH seeds

In Figure 4.5, we show the redshift evolution of the total SFR (summed over all the progenitor galaxies in each simulation) and the separate contribution of Pop III stars. We also show the upper limit on the SFR of $\sim 2000\, M_{\odot}$/yr (Table 4.1) inferred from the observed FIR luminosity using the relation $L_{\rm FIR}/L_{\odot} = 10.84 \times 10^9\,{\rm SFR}/(M_{\odot}/{\rm yr})$ (Valiante et al., 2014). This relation[4] is based on the assumption of starburst dominated dust heating and it provides only an upper limit to the real SFR, due to the non-negligible contribution from the AGN. According to a recent detailed radiative transfer analysis, the AGN can provide up to 60% of the total FIR luminosity (Schneider et al., 2015), decreasing the SFR by a factor 1.4 - 2.5, in agreement with the average value of $\sim 800\, M_{\odot}$/yr predicted by the reference model.

Due to efficient metal enrichment, Pop III star formation becomes negligible below z $\sim$ 20 and no more BH seeds are formed, consistent with other studies (Madau and Rees

---

[4] The conversion factor between the FIR luminosity and the SFR has been obtained assuming a 10 - 200 Myr burst of stars with solar metallicity and a Larson IMF with $m_{\rm ch} = 0.35 M_{\odot}$ (Valiante et al., 2014).

2001; Haiman and Loeb 2001; Heger et al. 2003; Volonteri et al. 2003; Madau et al. 2004; Valiante et al. 2016. The mass distribution of DM halos which host BH seeds ranges between $\sim 3 \times 10^6 M_\odot$ and $\sim 10^8 M_\odot$ with a peak at $M_\mathrm{h} \sim 10^7 M_\odot$, as shown in Figure 4.6. Thus, we find that a major fraction ($\sim$ 90%, on average) of BH seeds are formed in DM mini-halos, where gas cooling could be easily suppressed due to H_2 photo-dissociation by Lyman-Werner photons. The inclusion of this additional feedback effect slows down metal enrichment and extends BH seeds formation to lower redshifts ($z \geq 15$) and larger DM halos ($\sim 5 \times 10^7 - 10^9 M_\odot$). While the evolution of the total BH mass and BH accretion rate at $z < 15$ is only mildly affected, the birth environment of late-forming seed BHs (gas rich Ly-α cooling halos) may be more favourable to super-Eddington accretion. Here we do not consider the effect of H_2 photo-dissociation, which we defer to a future study, and we assume that the formation rate of Pop III stars is limited only by metal enrichment.

4.4.2 BH evolution

In Figure 4.7 we show the redshift evolution of the BH mass and black hole accretion rate (BHAR) predicted by our reference model. In the top panels, the values are obtained summing over all BH progenitors present at each redshift in each simulation and then averaged over the 30 realizations. The different lines allow to separate the contribution to the BH mass and accretion rate achieved by means of sub-Eddington ($\leq 16\, L_\mathrm{Edd}/c^2$) and super-Eddington ($> 16\, L_\mathrm{Edd}/c^2$) accretion events. By construction, the final BH mass predicted by the reference model is $\sim (3.6 \pm 1.6) \times 10^9 M_\odot$, in agreement with the value inferred from observations of J1148 (see Table 1). We find that, on average, $\sim$ 75% of the final SMBH mass grows by means of super-Eddington gas accretion. This provides the dominant contribution to the total BHAR at all but the smallest redshifts. Although the quantities shown in all panels have been averaged over 30 merger trees, the redshift evolution of the BHAR appears to be very intermittent, a consequence of rapid depletion/replenishment of the bulge gas reservoir out of which the BHs accrete.

To gain a better idea of the typical values of BH mass and BHAR predicted by the reference model, in the bottom panels of Figure 4.7 we also show the mean quantities, averaged over all BH progenitors present at each redshift in each simulation. It is clear that at $20 \lesssim z \lesssim 25$ the mean BH mass rapidly grows from $\sim 100\, M_\odot$ to $\sim 10^4\, M_\odot$ by means of

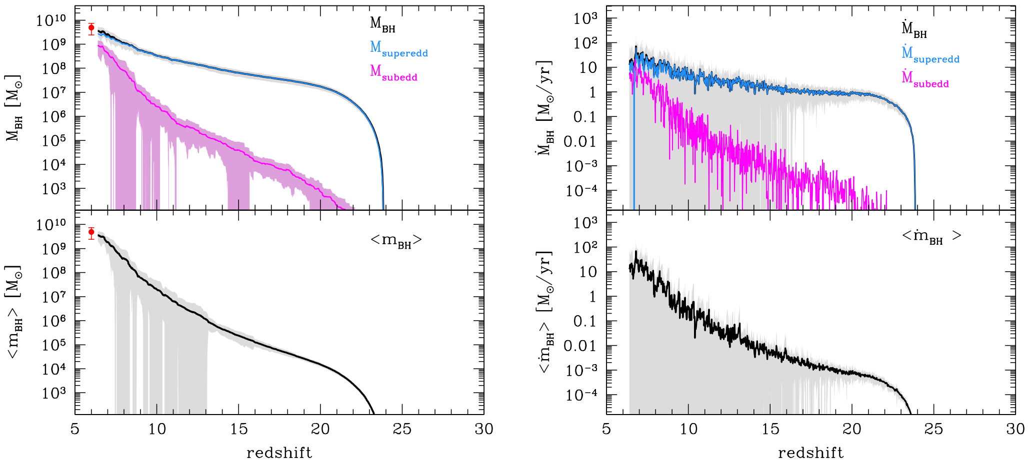

Figure 4.7. Redshift evolution of the total and mean BH masses and BHARs, averaged over 30 independent merger trees. Shaded areas are 1-σ dispersions. *Top, left panel*: total BH mass (summed over all BH progenitors at each redshift in each simulation, black line) and the BH mass grown by means of sub-Eddington (magenta line) and super-Eddington (cyan line) accretion events. *Top, right panel*: total BHAR (black line) and BHAR obtained considering only sub- (magenta line) and super- (cyan line) Eddington accreting BHs. The mean BH mass and BHAR (averaged over all BH progenitors at each redshift in each simulation) are shown in the bottom panels (left and right, respectively).

super-Eddington gas accretion rates of $10^{-5} M_\odot/\mathrm{yr} \lesssim \mathrm{BHAR} \lesssim 10^{-3} M_\odot/\mathrm{yr}$. Hence, due to early efficient super-Eddington accretion, the mean BH progenitors at $z \sim 20$ have already achieved a mass comparable to the BH mass predicted by the direct collapse scenario. This is consistent with what recently found by Lupi et al. (2016) by means of high-resolution numerical simulations, which show that stellar-mass black holes can increase their mass by 3 orders of magnitudes within a few million years while accreting gas at super-Eddington rates in the dense cores of high-z galaxies.

Figure 4.8 shows the average distribution of BHs accreting at super- and sub-Eddington rates as a function of the BH mass and Eddington accretion ratio for different redshift intervals. The reference model predicts that, at $15 \leq z \leq 25$, almost all BH progenitors accrete at super-Eddington rates. Since the BH masses are still relatively small, $10^2\, M_\odot \leq M_{\mathrm{BH}} \leq 10^6\, M_\odot$, BH accretion rates of $10^{-5} M_\odot/\mathrm{yr} \lesssim \mathrm{BHAR} \lesssim 5 \times 10^{-3} M_\odot/\mathrm{yr}$, which characterize the early mass growth (see the bottom right panel of Figure 4.7), correspond to

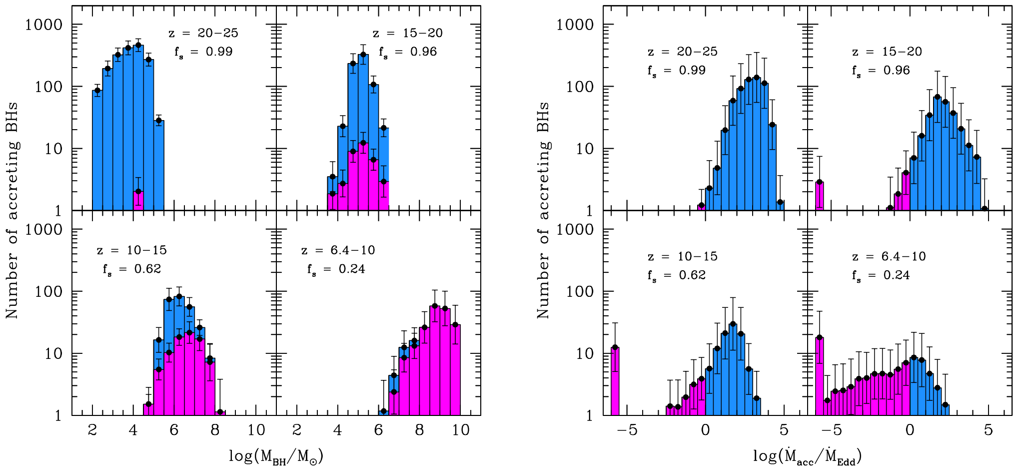

Figure 4.8. Number of accreting BHs as a function of the black hole mass (*left panel*) and the accretion ratio (*right panel*), averaged over 30 realizations with $1{-}\sigma$ error bars. The histograms show the number of super- (cyan) and sub- (magenta) Eddington accreting BHs. In each figure, we separately show 4 different redshift intervals and we give the corresponding number fraction of super-Eddington accreting BHs over the total, $f_{\rm s}$.

very large accretion ratios, $\dot{M}_{\rm accr}/\dot{M}_{\rm Edd} \sim 10^2 - 10^4$. The mass of BH progenitors increases with time and the fractional number of super-Eddington accreting BHs decreases, being $f_{\rm s} \sim 60\%$ at $z \sim 10 - 15$ and dropping to $f_{\rm s} \sim 20\%$ at $z < 10$. Because of the larger BH masses, the accretion ratios are smaller and $\dot{M}_{\rm accr}/\dot{M}_{\rm Edd} < 500$ at $z < 10$.

For most of the evolution, we find that BH progenitors accrete at highly super-Eddington rates, with $\dot{M}_{\rm accr}/\dot{M}_{\rm Edd} >> 10$. At these large Eddington accretion ratios the applicability of the adopted slim disk solution is highly debated. In fact, recent general-relativistic magneto-hydrodynamical simulations show that BHs accreting at $20 < \dot{M}_{\rm accr}/\dot{M}_{\rm Edd} < 200$ develop a disk structure that is still radiatively inefficient, with total luminosities that do not exceed $\sim 10\,L_{\rm Edd}$, but the total energy escaping the system can be very large, mostly in the form of thermal and kinetic energy of outflowing gas and Poyinting flux (McKinney et al., 2014; Sądowski et al., 2013). However, Inayoshi et al. (2015) have shown that there exist regimes where steady accretion rates larger than 3000 times the Eddington rate can be sustained.

To better assess the impact of these extreme hyper-Eddington accretion events on our results, we have run the same set of simulations discussed so far but artificially imposing

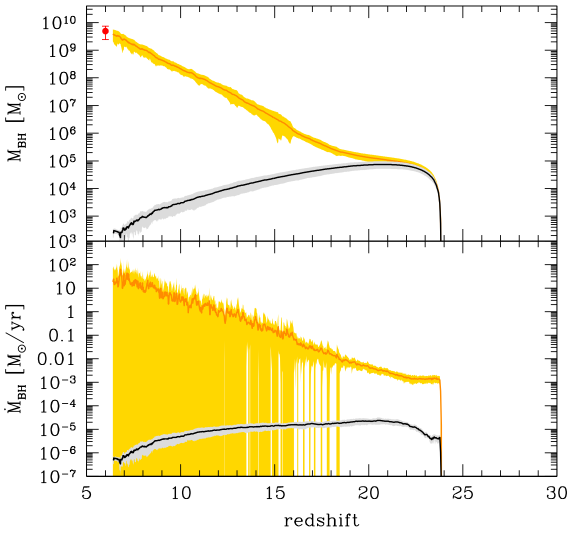

Figure 4.9. Redshift evolution of the total BH mass (*upper panel*) and BHAR (*lower panel*), averaged over 30 independent merger trees. Shaded areas are 1-σ dispersions. In each panel, the orange line indicates the predicted evolution assuming $\dot{M}_{\rm accr} \leq 20\,\dot{M}_{\rm Edd} = 320\,L_{\rm Edd}/c^2$ and the black line shows the evolution assuming the conventional Eddington limited accretion, $\dot{M}_{\rm accr} \leq L_{\rm Edd}/c^2$ (see text).

an upper limit of $\dot{M}_{\rm accr} \leq 20\,\dot{M}_{\rm Edd} = 320\,L_{\rm Edd}/c^2$ to the gas accretion rate. The results are shown in Figure 4.9. In the same figure, we also show, for comparison, the evolution predicted assuming Eddington-limited accretion. In order to better compare with previous results, this model has been run assuming $\dot{M}_{\rm accr} \leq L_{\rm Edd}/c^2$ (1/16 smaller than the definition adopted in the present study, see Equation 4.33), as conventionally adopted in the literature.

We find that, even when the Eddington accretion ratio is $\dot{M}_{\rm accr}/\dot{M}_{\rm Edd} \leq 20$, the final SMBH mass predicted by the reference model is in good agreement with the observations. The high-redshift evolution of both the total BH mass and the total BHAR, however, is markedly different from the results shown in Figure 4.7. At $z > 10$ the BHAR is several orders of magnitudes smaller and the BH mass is correspondingly affected, being $\sim 10^6\,M_\odot$ at $z \sim 15$ ($\sim 1/100$ of the total BH mass shown in Figure 4.7 at the same z). Due to the smaller gas accretion rates at high redshifts, a larger gas fraction is retained around nuclear BHs at $z < 10$. As a result, the BH mass has a steeper late growth rate, with short episodes of intense gas accretion reaching $\sim 10^2\,M_\odot$/yr at $z \sim 7$.

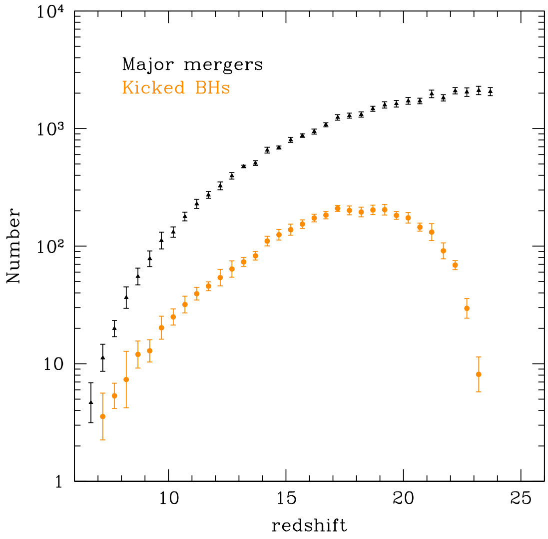

Figure 4.10. The average redshift distribution of major mergers (black triangles) and of kicked BHs during BH-BH coalescences in the model where $\dot{M}_{\rm accr} \leq L_{\rm Edd}/c^2$ (orange points). Each point has been obtained averaging over 30 different merger tree realizations and the errorbars correspond to the 1-σ dispersion.

On the contrary, when Eddington-limited gas accretion is assumed, the final BH mass can no longer be reproduced using the reference model. In this case, the gas accretion rates are too small to trigger fast BH growth at high redshifts. The total BH mass is dominated by the coalescence of BH seeds and its redshift evolution is strongly affected by lack of BH seeds at $z < 20$ (see the behaviour of the Pop III SFR in Figure 4.5) and by kicks received during BH-BH coalescences in major mergers. Figure 4.10 shows the evolution of the average number of major mergers and of kicked BHs predicted by the model. While the average number of major mergers decreases with time, the number of kicked BHs increases at $20 \lesssim z \lesssim 25$ and than decreases at lower z. This is due to the combination of the growing number of BH seeds formed at high z and of the shallow potential wells of their host mini-halos, which allow the kick velocity of the newly formed BH to easily exceed the retention speed.

Hence, we can conclude that super-Eddington accretion is fundamental for the formation of the first SMBHs at $z > 6$, even when extreme hyper-Eddington accretion events are not considered.

4.4.3 Environmental conditions for Super-Eddington accretion

Our model enables us to perform a statistical study of the physical properties of the environments where BH progenitors accrete at super-Eddington rates. The left panel of Figure 4.8 shows that when both sub- and super-Eddington accreting BHs are present, their BH masses are comparable, with a tendency of sub-Eddington accreting BHs to have larger masses at lower z. Similarly, the occurrence of super-Eddington accretion is not correlated with the mass of the host dark matter halo, nor with its gas content or metallicity. At each given value of any of these quantities, in fact, both sub- and super-Eddington accreting BHs are found in the simulations.

The different accretion regimes are more cleanly separated when we plot the Eddington gas accretion ratio as a function of the ratio between the gaseous bulge and the BH masses (see the left panel of Figure 4.11). Most of the BHs that accrete at sub-Eddington rates are characterized by $M_{\rm b}/M_{\rm BH} < 20$, whereas the number of super-Eddington accreting BHs is negligible when $M_{\rm b}/M_{\rm BH} < 0.1$. However, when $0.1 \leq M_{\rm b}/M_{\rm BH} \leq 20$ (the region between the two vertical lines in the plot), the BHs can be characterized by vastly different accretion ratios: a good fraction of the hyper-Eddington accreting BHs are found in this region of the plot. The larger accretion rate in these systems is due to the much shorter dynamical time of the bulge. This is shown in the right panel of Figure 4.11. A sequence of increasing bulge dynamical times is evident, with most of the BHs found in bulges with $0.01\,{\rm Myr} \lesssim \tau_{\rm b} < 1\,{\rm Myr}$ in hyper-Eddington, $0.1\,{\rm Myr} \lesssim \tau_{\rm b} < 20\,{\rm Myr}$ in mildly super-Eddington, and $5\,{\rm Myr} \lesssim \tau_{\rm b} < 20\,{\rm Myr}$ in sub-Eddington accretion regimes. Indeed, hyper-Eddington accreting BHs are predominantly found in high-z systems, with less massive and more compact bulges. The figure also shows that super-Eddington accretion requires gas-rich bulges and that, when $M_{\rm b}/M_{\rm BH} < 0.1$, only sub-Eddington accreting BHs in massive, gas poor bulges are found.

The environmental conditions for super-Eddington accretion that emerge from our statistical study are in good agreement with the results recently found by Lupi et al. (2016). By means of detailed hydro-dynamical simulations, these authors show that, in order to accrete at super-Eddington rates, BHs must be embedded in dense gas structures, with masses comparable or larger than the masses of the accreting BHs.

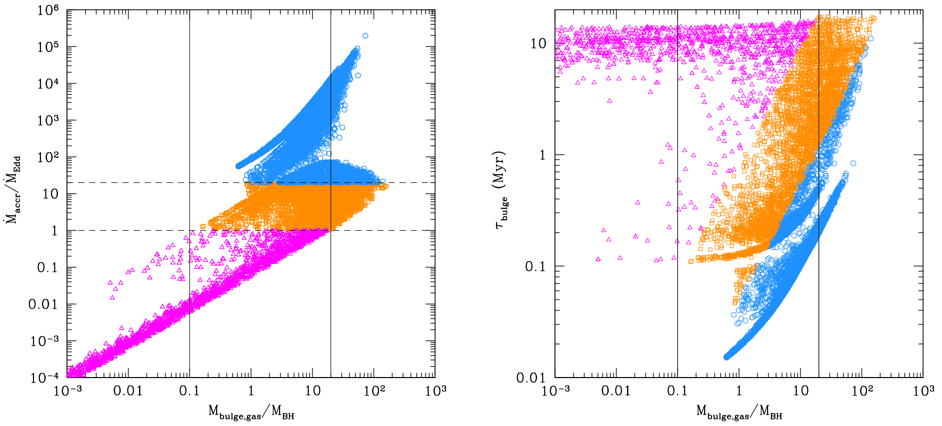

Figure 4.11. Eddington accretion ratio, $\dot{M}_{\rm accr}/\dot{M}_{\rm Edd}$, (*left panel*) and dynamical timescale of the bulge, $\tau_{\rm b}$, (*right panel*) as a function of the bulge gas - BH mass ratio, $M_{\rm b}/M_{\rm BH}$. Each point represents an accreting BH in any of the 30 merger histories. Sub-Eddington accreting BHs are shown by magenta triangles, and we separate mildly super-Eddington accreting BHs with $1 \leq \dot{M}_{\rm accr}/\dot{M}_{\rm Edd} \leq 20$ (orange squares) and hyper-Eddington accreting BHs with $\dot{M}_{\rm accr}/\dot{M}_{\rm Edd} > 20$ (cyan circles). The two horizontal dashed lines in the left panel allow to visually separate these regimes. The vertical lines in both panels give two reference values of $M_{\rm b}/M_{\rm BH} = 0.1$ and 20 (see text).

4.4.4 BH-driven outflow

Outflowing cold gas in J1148, traced by [C II] emission, was first detected by Maiolino et al. (2012) with the IRAM Plateau de Bure Interferometer, and then confirmed with high-resolution follow-up observations by Cicone et al. (2015). The outflow has a complex morphology and spatial extent, reaching a maximum projected radius of 30 kpc. The estimated mass outflow rate and velocity are shown in Figure 4.12 as a function of the projected distance from the nucleus. In the same figure, we also show the predictions of the reference model. Following Equation (4.38), the outflow velocity is computed as the circular velocity at the corresponding radius, $v_{\rm w,AGN}(r) = v_{\rm c}(r)$, and we estimate the mass outflow rate accounting for the delay $\tau_{\rm dyn} = r/v_{\rm w,AGN}$ between the BH energy release and the observation. Due to the large variability of the BH luminosity, the 1-σ dispersion among the different merger trees of the predicted average mass outflow rate (gray shaded region in the upper panel) is consistent with the data. However, the average values (black solid line) are larger than observed and show a different radial dependence, especially at $r > 20\,{\rm kpc}$.

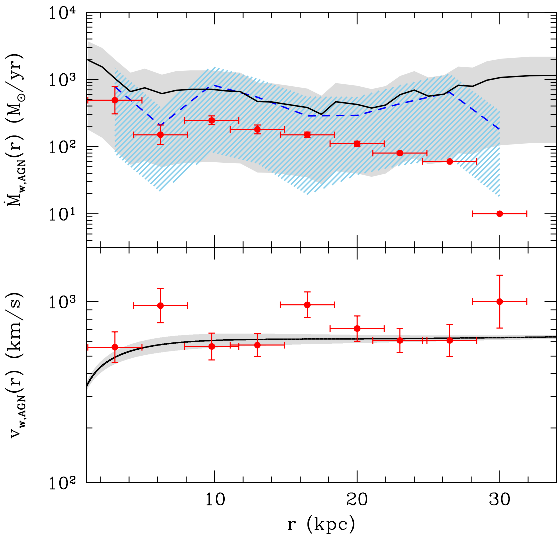

Figure 4.12. The mass outflow rate (*upper panel*) and velocity (*lower panel*) as a function of the projected distance from the nucleus. Cicone et al. (2015) observations are shown with red data points and the predictions of the reference model are shown by black solid lines with shaded gray regions. The blue dashed line in the upper panel (with the cyan dashed region) shows the predicted outflow rate that we would infer using the BH luminosity predicted by the reference model and the observed outflow velocities (see text). The lines show the average among the 30 merger trees and the shaded regions are the 1-σ dispersion.

The bottom panel shows that the observed outflow travels at a velocity consistent with the circular velocity of the host system. There are a few radii where the observed values are larger, probably reflecting a stronger coupling between the energy and momentum injected by the AGN and the surrounding gas. Yet, even if we take the observed values of outflow velocities at each radius to estimate $\tau_{\rm dyn}$ and $\dot{M}_{\rm w,AGN}$ (see the blue dashed line in the upper panel with the cyan shaded region), the resulting mean mass outflow rate is still larger than observed. Our description of an energy-driven wind with constant coupling efficiency may not be adequate to capture the complex dynamics of this massive outflow. However, Cicone et al. (2015) stress that the data should be considered as a lower limit on the total mass outflow rate, because it accounts only for the atomic gas phase of the outflow, while a significant amount of the outflowing mass may be in the molecular phase.

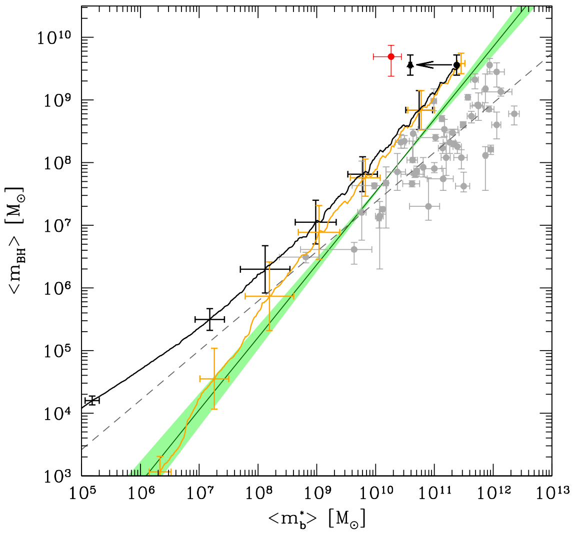

Figure 4.13. Redshift evolution of the mean black hole mass as a function of the mean bulge stellar mass in SMBH progenitors for the reference model (black solid line) and the model with $\dot{M}_{\rm accr} \leq 20\,\dot{M}_{\rm Edd}$ (orange solid line). Gray circles are data for local galaxies, with the empirical fit (gray dashed line) provided by Sani et al. (2011). The solid green line with shaded region is the scaling relation derived by Kormendy and Ho (2013). The red point represents the black hole and stellar mass within a region of 2.5 kpc inferred from observations of J1148 (Table 4.1). The model predictions are averaged over 30 merger tree realizations and the errorbars show the 1-σ dispersion for both mean BH and bulge stellar mass, at few selected redshift along the averaged merger histories. The arrow illustrates the reduction in stellar mass if we restrict to the central 2.5 kpc region (black data point, see text).

4.4.5 The coevolution of BHs and their host galaxies

It is interesting to explore the implications of our results for the co-evolution of nuclear BHs and their host galaxies. In Figure 4.13 we show the evolutionary path (from the bottom left to the top right) in the mean BH mass - stellar bulge mass ($\langle m_{\rm BH}\rangle$ - $\langle m_{\rm b}^{\star}\rangle$) plane predicted by the reference model (black solid line) and by the model with $\dot{M}_{\rm accr} \leq 20\,\dot{M}_{\rm Edd}$ (orange solid line). In each simulation, we consider the mean values among all the SMBH progenitors and their hosts present at each redshift, and then we average over the 30 merger trees. For comparison, we also show in the same figure the observational data and the empirical fit (gray data points and dashed line) for local galaxies provided by Sani et al. (2011), and the

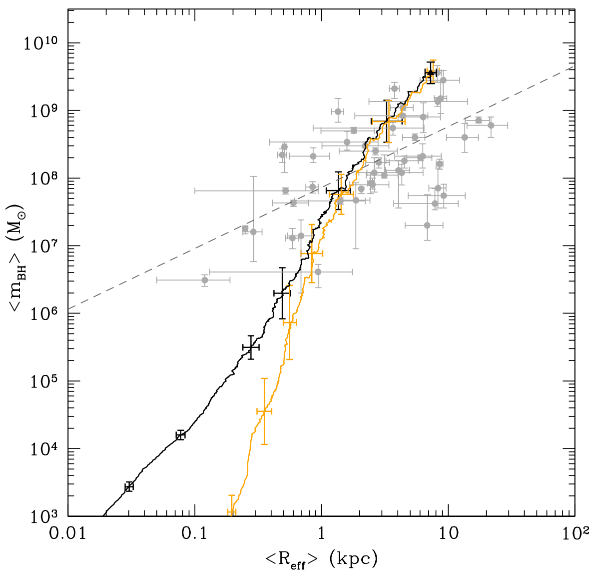

Figure 4.14. Redshift evolution of the mean black hole mass as a function of the mean bulge effective radius of the host galaxy, averaged over 30 merger tree realizations with 1-σ errorbars at few selected redshift, for the reference model (black solid line), and the model with $\dot{M}_{\rm accr} \leq 20\,\dot{M}_{\rm Edd}$ (orange solid line). Gray circles represent data for local galaxies, with the empirical fit (gray dashed line) given by Sani et al. (2011).

more recent scaling relation inferred for local ellipticals and classical bulges by Kormendy and Ho (2013, solid green line and shaded region).

In the reference model, BH progenitors of the first SMBHs at $z > 6$ follow a symbiotic evolution, with a small offset with respect to the observed local scaling relation. When $\dot{M}_{\rm accr} \leq 20\,\dot{M}_{\rm Edd}$, the different evolution at high-z is reflected in a steeper relation between the mean BH mass and the stellar bulge, very close to that predicted by Kormendy and Ho (2013). The difference between the models becomes negligible when $\langle m_{\rm BH}\rangle > 10^7\,M_\odot$ ($\langle m_{\rm b}^{\star}\rangle > 10^9\,M_\odot$), which occurs - on average - at $z \sim 10$.

When the average BH mass has reached its value of $(3.6 \pm 1.6) \times 10^9 M_\odot$ at $z = 6.4$, the host galaxy has already grown to a bulge (total) stellar mass of $2.7\,(3.2) \times 10^{11} M_\odot$. Hence, we predict a final average BH-to-bulge (total) stellar mass ratio of $M_{\rm BH}/M_{\rm star} = 0.013\,(0.011)$, well within the scatter of the relations inferred from various observational studies of massive local galaxies (Marconi and Hunt, 2003; Sani et al., 2011; Kormendy and Ho, 2013, and references therein). However, this ratio is ~ 25 times smaller than what is inferred from observations of J1148 (red data point). Following the procedure commonly applied to high-z bright QSOs, the stellar mass is computed as $M_{\rm star} = M_{\rm dyn} - M_{\rm H_2}$, with $M_{\rm dyn}$ and $M_{\rm H_2}$ inferred from CO observations (see Table 1, Walter et al. 2004; Wang et al. 2010). Similar results obtained for a larger sample of $z > 6$ QSOs have suggested the idea that the first SMBHs grow faster than their host galaxies (Wang et al. 2010, 2013; Venemans et al. 2015 see however Willott et al. 2015).

As suggested by Valiante et al. (2014), observations of high-z QSOs are sensitive to the innermost $2.5 - 3$ kpc and may be missing a significant fraction of the galaxy (Valiante et al., 2014). This is also supported by recent observations of J1148, which show extended [C II] 158 μm emission and far-infrared (FIR) continuum, likely associated with cold gas and star formation on scales of $\sim 10 - 20$ kpc (Cicone et al., 2015).

Indeed, the mean bulge effective radius at $z = 6.4$ predicted by the model is $R_{\rm eff} = 7.3 \pm 0.8$ kpc, in good agreement with observations of local galaxies hosting the largest BHs (see Figure 4.14). When we restrict to the innermost 2.5 kpc, we find a mean bulge stellar mass of $(3.9 \pm 0.2) \times 10^{10} M_{\odot}$, much closer to the observation (see the arrow and black data point in Figure 4.13). The same is true if we consider the mean gas mass within 2.5 kpc, that we predict to be $M_{\rm H_2} = (2.0 \pm 0.9) \times 10^{10}\, M_{\odot}$, that well reproduce the observed value (see Table 1).

Finally, the reference model predicts a mean dust mass at $z = 6.4$ of $M_{\rm dust} = (3.6 \pm 0.9) \times 10^{8}\, M_{\odot}$, in good agreement with the value inferred from the FIR luminosity. This result has been obtained using the chemical evolution module, which includes dust processing in a 2-phase ISM, that has been developed by Valiante et al. (2011, 2014) and de Bennassuti et al. (2014). Hence, consistent with previous findings (Valiante et al., 2011, 2014), we find that the large dust mass that has enriched the ISM of the host galaxy is the result of a large stellar component, and that the apparent tension with the observed dynamical mass - the so-called *stellar mass crisis* - is at least partly due to the small spatial extent of the observations. We refer the interested readers to Valiante et al. (2014) for an extended discussion on this point.

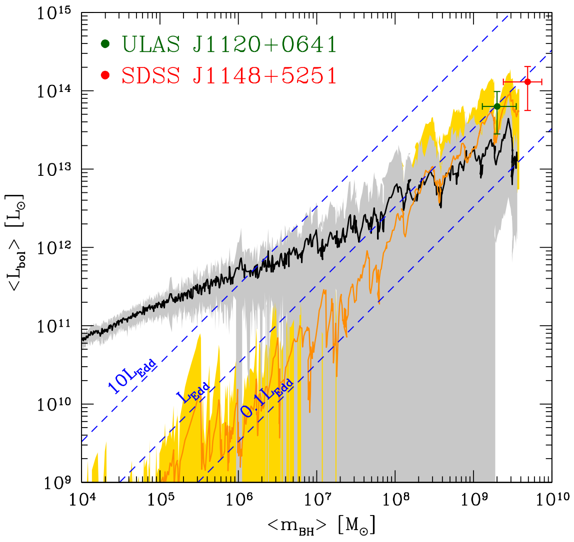

Figure 4.15. Mean bolometric luminosity of BH progenitors as a function of the mean BH mass predicted by the reference model (black solid line) and by the model with $\dot{M}_{\rm accr} \leq 20\,\dot{M}_{\rm Edd}$ (yellow solid line). For each model, the lines show the average among the 30 merger trees and the shaded regions are the 1-σ dispersion. The data points show the observational values of the two quasars SDSS J1149 (red circle) and ULAS J1120 (green square). The diagonal dashed lines show some reference values of the luminosity in units of the Eddington luminosity.

4.5 Discussion and conclusions

The data-constrained model GAMETE/SuperQSODust allows us to explore a large number of formation histories of a given quasar, in the present case J1148 at $z = 6.4$, reproducing the observations of the quasar and its host galaxy. With the adjustable free parameters that we have selected, described in Table 2, the model reproduces the physical quantities listed in Table 1. Hence, the properties that we predict for the host galaxy of J1148 (SFR, dust mass, gas and stellar masses) are consistent with previous results obtained by (Valiante et al. 2014, 2016) for the same quasar.

With respect to (Valiante et al., 2011, 2014, 2016), the current version of GAMETE/SuperQSODust enables to (*i*) follow the formation and evolution of the disk and bulge in each progenitor galaxy, and (*ii*) remove the constraint of Eddington-limited BH accretion.

In particular, Valiante et al. (2016) find that the formation of a few (between 3 and 30 in the reference model) heavy BH seeds with masses $M_{\rm BH} = 10^5\, M_\odot$ enables the Eddington-limited growth of a SMBH by $z = 6.4$. This conclusion heavily depends on the occurrence - among the progenitors - of Lyman-α cooling halos where gas cooling is suppressed by the low-metallicity and strong Lyman-Werner background (Valiante et al., 2016). This "head start" requires favourable conditions, that are easily erased by the joint interplay of chemical, radiative and mechanical feedback effects.

Here we have explored the alternative scenario where the BHs can grow through a radiatively inefficient slim disk at super-Eddington rates. This condition is easily met by light BH seeds formed in gas-rich systems at high redshifts.

In the model presented in this work, we plant light BH seeds in newly virialized halos above redshift $z \sim 20$, before the effects of chemical feedback inhibit the formation of metal poor ($Z < Z_{\rm cr}$) stars. With this seeding prescription, we find that:

- On average, $\sim 80\%$ of the SMBH mass of J1148 is provided by super-Eddington gas accretion ($> 16\, L_{\rm Edd}/c^2$). This represents the dominant contribution to BH growth down to $z \sim 10$;

- Due to fast and efficient super-critical accretion, the mean BH mass at redshift $z \sim 20$ is $\gtrsim 10^4\, M_\odot$, comparable that predicted for heavy BH seeds formed by direct collapse;

- More than 90% of BH progenitors accrete at super-Eddington rates at $15 < z < 25$ in dense, gas-rich environments. At these redshifts, hyper-Eddington accretion events, with $\dot{M}_{\rm accr}/\dot{M}_{\rm Edd} \sim 10^2 - 10^4$, are common;

- The observed SMBH mass of J1148 at $z = 6.4$ can be reproduced even adopting a maximum super-Eddington accretion rate of $\dot{M}_{\rm accr} \leq 20\, \dot{M}_{\rm Edd}$, showing that hyper-critical accretion is not required;

- BH progenitors of the final SMBH evolve in symbiosis with their host galaxies. The predicted AGN-driven mass outflow rate at $z = 6.4$ shows a radial profile that is broadly consistent with the lower limits inferred from CII observations by (Cicone et al., 2015);

- The predicted final BH-to-bulge (total) stellar mass ratio, $M_{\rm BH}/M_{\rm star} = 0.013$, (0.011), is within the scatter of the observed local relation and a factor of ~ 25 lower than inferred from dynamical mass observations of J1148. The discrepancy is significantly reduced if we account for the mass within 2.5 kpc from the nucleus, the region targeted by CO data. At this radius, the mean bulge stellar mass is $(3.9 \pm 0.2) \times 10^{10}\, M_{\odot}$, much closer to the observational value.

As a consequence of the lower gas accretion rates, the average BH mass predicted by Valiante et al. (2016) is much smaller than in our reference model, at all but the latest redshifts (see their Figure 3). This difference is reduced when we impose that $\dot{M}_{\rm accr} \leq 20\, \dot{M}_{\rm Edd}$. In this case, the average BH progenitor mass at $z \sim 15$ is comparable in the two models. However, while in Valiante et al. (2016) the mass growth is triggered by the formation of heavy seeds, in our model this is achieved by mildly super-Eddington accretion on light BH seeds.

The progenitors of SMBHs at $z > 6$ experience the *strong* form of coevolution defined by Kormendy and Ho (2013), where galaxies affect BH growth by controlling BH feeding and merging, and BHs control galaxy properties via AGN feedback. In fact, while the small radiative efficiencies of super-Eddington accreting BHs is indispensable to limit the effects of AGN feedback (Lupi et al., 2016), at $z > 10$ the BHs shine at a few Eddington luminosities with a noticeable effect on the cold gas content of their host galaxies. At lower z, an increasing fraction of BH progenitors accrete at sub-Eddington rates, but with larger radiative efficiencies. As a result of the larger BH mass and BH accretion rates, AGN-driven winds at $z < 10$ power strong galaxy-scale outflows and suppress star formation, leading to the down-turn of the total SFR shown in Figure 4.5.

In Figure 4.15 we show the average bolometric luminosity as a function of the average BH mass of SMBH progenitors for the reference model (black solid line) and for the model with $\dot{M}_{\rm accr} \leq 20\, \dot{M}_{\rm Edd}$ (yellow solid line). The model predictions are compared with observations of SDSS J1148 ($z = 6.4$) and of the most distant quasar currently known, ULAS J1120 at $z = 7.1$ (Mortlock et al., 2011). The errorbars on the bolometric luminosities account for the observational uncertainties on the flux at 1450 Å and on the bolometric corrections (Richards et al., 2006). Some reference values of the luminosity in units of the Eddington luminosity are shown by the diagonal dashed lines. The difference among the two models reflects the different BH accretion history: in the model with $\dot{M}_{\rm accr} \leq 20\,\dot{M}_{\rm Edd}$ the first BH progenitors accrete at a lower rate, saving cold gas for the latest evolutionary phases. As a result, for BH progenitors with $M_{\rm BH} \lesssim 10^8\,M_\odot$, the mean luminosity predicted by the reference model is always super-Eddington (with $L_{\rm bol} > 10\,L_{\rm Edd}$ when $M_{\rm BH} \lesssim 10^6\,M_\odot$), whereas in the model with $\dot{M}_{\rm accr} \leq 20\,\dot{M}_{\rm Edd}$ the mean luminosity is always $0.1\,L_{\rm Edd} < L_{\rm bol} < L_{\rm Edd}$. However, in the latest evolutionary phases, when $M_{\rm BH} > 10^8\,M_\odot$, this trend is reversed. Given the observational uncertainties and the large variability among different merger trees, the luminosity of J1148 is consistent with the model predictions. Interestingly, the data point of ULAS J1120 is also lying within the 1-σ dispersion. Indeed, we find that $\sim 20\%$ of BH progenitors at $z = 7.1$ have luminosities and masses compatible with the observed values of ULAS J1120, indicating that this quasar may be one of the progenitors of SDSS J1148 at $z = 6.4$.

Chapter 5

The sustainable growth of the first black holes

In Chapter 4, it has been shown that $\sim 80\%$ of the mass of $z \sim 6$ SMBH with $M_{\rm BH} \sim 10^9\, M_\odot$ is grown via super-critical accretion events, which represent the dominant contribution at $z \gtrsim 10$. In fact, such accretion regime is favoured in dense, gas-rich environments characterized by high column densities, which are common at high redshift. On the contrary, the assumption of Eddington-limited accretion makes it impossible to reproduce the final SMBH mass starting from light seeds.

There are some physical processes that can suppress super-Eddington accretion in a cosmological context. First of all, the rate at which seed BHs can grow, immediately following their formation, strongly depends on the feedback effects of their stellar progenitors. This may create gas poor environment surrounding the BH, giving rise to a delay on the early growth of the first seeds (Johnson and Bromm, 2007; Alvarez et al., 2009; Johnson and Haardt, 2016). Moreover, an important factor which limits the duration of super-Eddington accretion is the feedback produced by the accretion process on the disk itself. In fact, a large fraction of the super-critical accretion power can drive disk winds, with a consequent loss of matter and, thus, a drop of the accretion rate (Bisnovatyi-Kogan and Blinnikov, 1977; Icke, 1980; Poutanen et al., 2007).

In this Chapter, we investigate the impact that the above mechanisms have on the early growth of the first BHs, assessing the feasibility of super-Eddington accretion as a channel for the formation of the first SMBHs. To this aim, we study the relative impact of these hampering mechanisms for super-Eddington growth using the cosmological semi-analytic model presented in Chapter 4 (hearafter P16), GAMETE/SuperQSOdust. In particular, we find that the feedback produced by the first stellar progenitors on the surrounding does not play a relevant role in preventing SMBHs formation. In order to grow the $z \gtrsim 6$ SMBHs, the accreted gas must efficiently loose angular momentum. Moreover disk winds, easily originated in super-Eddington accretion regime, can strongly reduce duty cycles. This produces a decrease in the active fraction among the progenitors of $z \sim 6$ bright quasars, reducing the probability to observe them.

5.1 Super-critical accretion flows

In the following paragraphs, we discuss the new features introduced in the model GAMETE/SuperQSOdust, i.e. the inclusion of the first stellar BH progenitors feedback on the surrounding gas, and a time-scale for the duration of a super-Eddington accretion event.

5.1.1 Seeding prescription

For each newly formed galaxy, we compute the star formation rate in the disk and in the bulge as $\dot{M}^{\star}_{\rm d,b} \propto M_{\rm d,b}/\tau_{\rm d,b}$, where $M_{\rm d,b}$ and $\tau_{\rm d,b}$ are the gas mass and the dynamical time of the disk (labelled 'd') and bulge ('b'), respectively (see Section 4.3.2 for further details).

Following Valiante et al. (2016), we assume Pop III stars to form when $Z < Z_{\rm cr} = 10^{-4}\, Z_{\odot}$ in the mass range $[10 - 300]\, M_{\odot}$ according to a Larson IMF (Larson, 1998):

$$\Phi(m_{\star}) = \frac{dN(m_{\star})}{dm_{\star}} \propto m_{\star}^{\alpha-1} e^{-m_{\star}/m_{ch}}, \tag{5.1}$$

with $\alpha = -1.35$, $m_{ch} = 20\, M_{\odot}$ (de Bennassuti et al. 2014; Valiante et al. 2016).

For non-rotating stars with $Z = 0$, a $M_{\rm seed} \sim 100\, M_{\odot}$ BH is expected to form from $M_{\star} \gtrsim 260\, M_{\odot}$ (Valiante et al., 2016). We do not consider as light seeds BHs forming from $[40 - 140]\, M_{\odot}$ progenitors because lighter BHs are not expected to settle steadily in the minimum of the potential well, due to stellar interactions (Volonteri 2010). Moreover, we do not take into account stars with masses of $M_{\star} = [140 - 260]\, M_{\odot}$, that are expected to explode as pair instability supernovae, leaving no remnants (Heger et al., 2003; Takahashi et al., 2016).

The probability to find a BH seed with, *at least*, $\sim 100\,M_\odot$, after a single star formation episode is,

$$f_{\rm seed} = \frac{\int_{260}^{300} m_\star \Phi(m_\star)\, dm_\star}{\int_{10}^{300} m_\star \Phi(m_\star)\, dm_\star}. \tag{5.2}$$

Based on results obtained by Valiante et al. (2016) through random sampling of the IMF, the condition $f_{\rm seed} \sim 1$ requires a minimum stellar mass formed in a single burst of $1000\,M_\odot$. Thus, conservatively, we assume that one $100\,M_\odot$ BH seed forms after a star-formation episode only if the total stellar mass formed $\Delta M_\star$ is $\geq 10^3\,M_\odot$.

5.1.2 Stellar progenitors feedback

The stellar progenitors of the first BHs are massive primordial stars, expected to form in minihalos. Their large luminosities, with a huge production of ionizing radiation for few Myr before their collapse (e.g. Schaerer 2002), can couple with the surrounding gas and heat it above the virial temperature of the host dark matter halo. As a result, BH seeds likely form in low-density HII region (e.g. Whalen et al. 2004; Alvarez et al. 2006), with consequent low gas accretion rates (Alvarez et al. 2009; Johnson et al. 2013; Johnson and Haardt 2016). Due to this radiative feedback in minihalos, the newborn BH may wait up to 100 Myr before starting to accrete efficiently.

Another important impact on the early BH growth is produced by SN explosions of massive primordial stars, which can provide a strong limit to the gas reservoir from which Pop III relic BHs can accrete.

To take into account these negative feedback effects, we assume that, following each Pop III star formation burst, all the gas is blown out of the galaxy, in the IGM. In addition, to mimic the impact of photo-ionization and heating, which affect the large-scale inflow, we assume that gas accretion from the IGM is inhibited as long as the virial temperature of the host halo remains $T_{\rm vir} < 10^4$ K. Furthermore, feedback produced by the first stars is strong enough to prevent further cooling and star formation within its host minihalo for the subsequent 200 Myr (Alvarez et al. 2009). For this reason, we suppress gas cooling in minihalos after the first star formation event, and relax this constraint only for halos with virial temperature $T_{\rm vir} \geq 10^4$ K.

5.1.3 The duration of super-Eddington accretion events

Idealistic slim accretion disk model predicts that a large fraction of the radiation produced by the accretion process can be advected into the BH instead of escaping. In fact, it is possible to define a radius $R_{\rm pt}$ within which the trapping of radiation becomes relevant. Trapping of radiation occurs in regions of the accretion disk for which the diffuse time scales $t_{\rm diff}(r)$ is larger than the accretion time $t_{\rm accr}(r)$. Imposing $t_{\rm diff} = t_{\rm accr}$ it is possible define the photon trapping radius $R_{\rm pt}$ (Ohsuga et al., 2002) :

$$R_{\rm pt} = \frac{3}{2}\dot{m}\, h\, R_s, \tag{5.3}$$

where $R_s = 2GM_{\rm BH}/c^2$ is the Schwarzschild radius, $\dot{m} = \dot{M}_{\rm accr}/\dot{M}_{\rm Edd}$ is the Eddington accretion ratio and $h = H/r$ is the ratio between the half disk-thickness H and the disk radius r. Since $h \approx 1$ in radiation pressure dominated regions, we assume $h = 2/3$ so that $R_{\rm pt} = R_s\dot{m}$.

In realistic cases, however, the accretion process can be suppressed. The outward angular momentum transport, necessary for accretion, also involves a transport of energy. This produces unbounding of gas far from the BH, thus less gas has the possibility to reach it. Moreover, a significant fraction of the accretion power in super-critical flows may drive disk winds. In fact, at large luminosities, flows are supported by radiation pressure, which is likely to induce outflows (Shakura and Sunyaev, 1973; Bisnovatyi-Kogan and Blinnikov, 1977; Icke, 1980; Ohsuga et al., 2005; Poutanen et al., 2007). Results of recent simulations suggest that the mass lost due to disk winds becomes relevant only as photon trapping becomes less important, i.e. in the outer region of the disk (Ohsuga and Mineshige, 2007; Takeuchi et al., 2009; Begelman, 2012; Sądowski et al., 2014). As already discussed in Volonteri et al. (2015), it is thus possible to assume that a significant disk wind is produced only after the disk radius has reached some significant fraction of the trapping radius. When this occurs, the mass lost to the outflow reduces the gas accretion rate, which can drop to $10-20\%$ of the inflow rate (e.g. Ohsuga and Mineshige 2007), decelerating the BH growth. In addition, the mass outflow increases with the disk radius (Volonteri et al. 2015), so that both effects can eventually quench black hole growth once the trapping radius is reached (see also Volonteri and Rees 2005; Volonteri et al. 2015).

Following Volonteri et al. (2015), we assume that once the disk radius $R_{\rm d}$ reaches $R_{\rm pt}$, the disk is blown away, and the accretion process is no longer sustained. This reflects into a condition on the maximum time for which super-Eddington accretion can be sustained[1] (Volonteri et al., 2015):

$$t_{\rm accr} = 2\lambda^{-2}\left(\frac{\sigma}{c}\right)^2 t_{\rm Edd}, \tag{5.4}$$

where $t_{\rm Edd} = 0.45$ Gyr is the Eddington time, $\lambda \leq 1$ is the fraction of angular momentum retained by the gas and σ is the gas velocity dispersion.

Since $R_{\rm d} \propto \lambda^2$, smaller values of λ lead to smaller disk sizes and hence to a prolonged phase of super-Eddington accretion, $t_{\rm accr}$.

For the present study we investigate two different values, $\lambda = 0.01$ and $\lambda = 0.1$. The latter is suggested by studies of angular momentum losses for gas feeding SMBHs during galaxy mergers. Capelo et al. (2015) find $\lambda < 0.5$ (with mean and median values of 0.28 and 0.27, respectively), in simulations with gas softening length of 20 pc. The former represent a more optimistic, but not extreme, case (see Begelman and Volonteri, 2017, for a discussion).

5.2 Results

In this section, we explore the impact of stellar feedback and of the disk outflow comparing the results of the new models with those found in P16 where the above effects were not considered. Models with stellar feedback and $\lambda = 0.1$ and 0.01 have been labelled as L01 and L001, respectively. The model described in Chapter 4, including stellar feedback and no disk outflow has been labelled NL. This implies that the only difference between L01 (or L001) and NL resides in accounting or not for disk winds effects. For each model, the results must be intended as averaged over $N_r = 5$ simulations.

5.2.1 The impact of Stellar feedback

Figure 5.1 shows the redshift distribution of newly formed BH seeds with (green histograms, NL model) and without (black histograms, P16 model) the effect of stellar feed-

---

[1] Being the disk radius $R_{\rm d} = \lambda^2 R_{\rm g} = \lambda^2 G M_{\rm BH}/\sigma^2$, and the Eddington luminosity $L_{\rm Edd} = t_{\rm Edd}/(M_{\rm BH}c^2)$, approximating $M_{\rm BH} = \dot{M}_{\rm BH}t$, the condition $R_{\rm d} \leq R_{\rm pt}$ turns into the inequality $(\lambda c/\sigma)^2(M_{\rm BH}/2t_{\rm Edd}\dot{M}_{\rm BH}) \leq 1$.

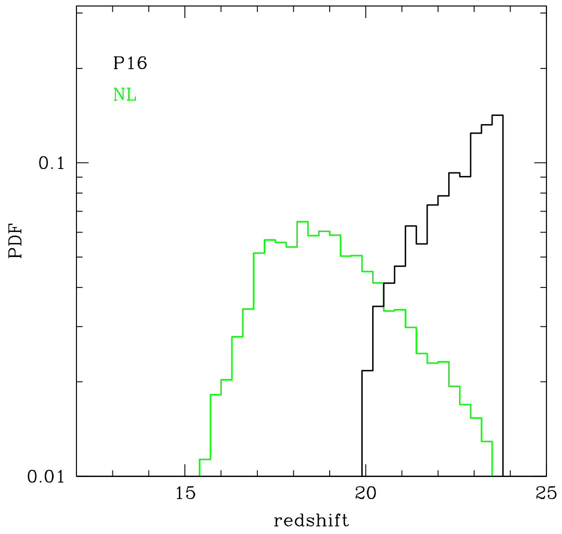

Figure 5.1. Probability distribution function of $100\,M_\odot$ BH seeds formation redshifts. PDF are averaged over 5 realizations. Green (black) histograms represent models with (NL) and without (P16) stellar feedback onto BH formation sites.

back. In the no-feedback case, due to efficient metal enrichment, Pop III star formation becomes negligible below $z \sim 20$. The inclusion of stellar feedback causes a shift of BH seed formation to lower redshift. Moreover, while in the no-feedback model we find $\sim 90\%$ of BH-seeds hosts are minihalos, once feedback is considered native galaxies are mostly Lyα-cooling halos. This stems from the condition that a $100\,M_\odot$ BH remnant requires a minimum Pop III stellar mass of $\Delta M_\star \sim 10^3\,M_\odot$ formed in a single burst, which can be hardly accomplished in minihalos, due to the low-efficiency feedback-limited star formation. The effect is that Pop III stars sterilize minihalos, without giving birth to a BH seed (Ferrara et al., 2014). Once minihalos have grown enough mass to exceed $T_{\rm vir} = 10^4\,$K, gas cooling is more efficient and $100\,M_\odot$ BH seeds have a larger probability to form. As a result, BH seeds continue to form down to $z \sim 15$ in the NL model, in good agreement with what found in Valiante et al. (2016).

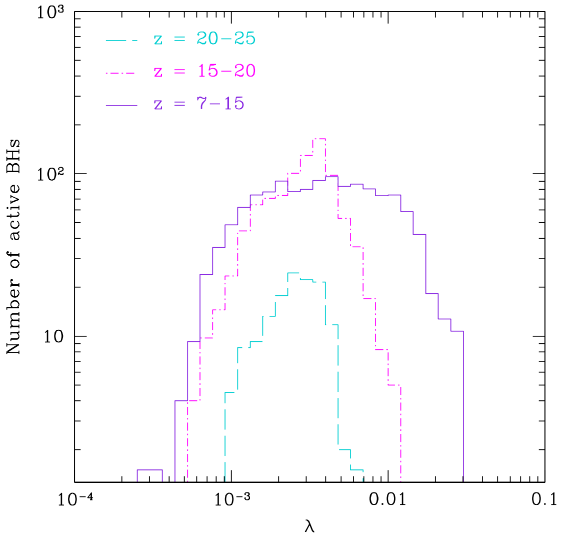

Figure 5.2. Distribution of the parameter λ in the redshift intervals $z = 20 - 25$ (turquoise, dashed), $z = 15 - 20$ (magenta, dashed-dotted), and $z = 7 - 15$ (violet, solid) for NL model.

5.2.2 Super-Eddington duration

To understand the impact of the duration of super-Eddington accretion episodes on high-z SMBHs growth, we have compared the L01 and L001 cases with the NL model. In the NL model, disk winds effects are not considered. Thus, the accreting event - and its lifetime - depends only on the presence, in a galaxy, of a BH surrounded by a gas reservoir. Since there is no apriori constraint on the accretion time-scale, it is possible to invert Equation 5.4 and obtain the distribution of λ values shown in Figure 5.2.

Model NL results in values of λ smaller than assumed in models L01 and L001, with $10^{-4} \lesssim \lambda \lesssim 10^{-1}$. We find slightly increasing values of λ for decreasing redshift, with wider distributions at lower z. This effect is dominated by an increasing dispersion in the values of σ for decreasing redshift. In fact, the duration of super-Eddington accretion, $t_{\rm accr}$, follows a narrow distribution around the time resolution $\Delta \rm t_r$ of the simulation at the corresponding redshift, with BHs accreting at most $\sim$ few times $\Delta t_{\rm r}$ (see the top row of Figure 5.3). These short durations are consequence of the rapid depletion of gas produced by efficient super-Eddington accretion, which represents the dominant contribution at all but the latest redshift of the SMBH evolution (see P16 for details). Conversely, in models

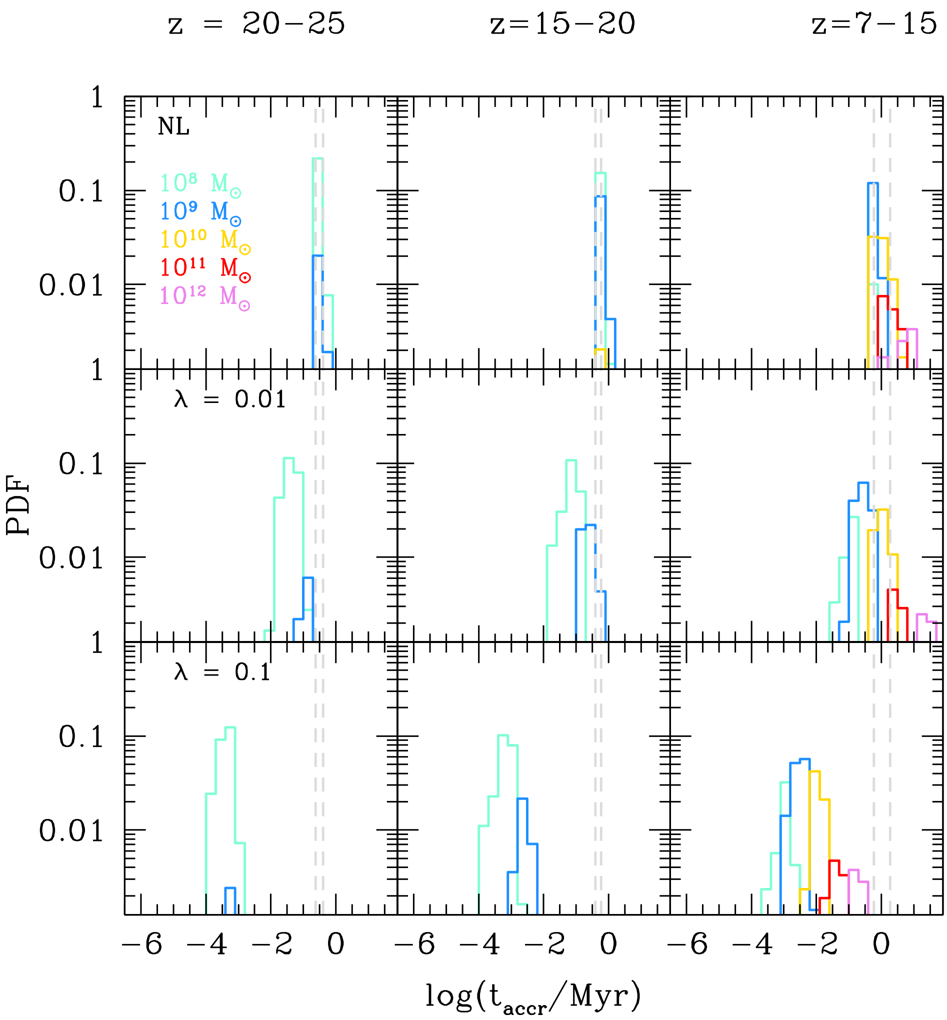

Figure 5.3. Probability distribution function of the time duration of single super-Eddington accretion events for NL (top panels), L001 (middle panels) and L01 (bottom panels) models. Columns refer to different redshift intervals, $z = 20 - 25$ (left), $z = 15 - 20$ (center) and $z = 7 - 15$ (right), while colours indicate different mass of the BHs' DM host halos, as labelled in the top-left panel. Vertical dotted lines represent the maximum and minimum values of time resolution Δt_r of the simulation, in the related redshift interval.

L001 and L01 we have limited super-Eddington accretion to t_{accr} as obtained from Equation 5.4, with resulting distributions shown in the middle (L001) and bottom (L01) panels of Figure 5.3. It is interesting to note that, under the assumption of $\lambda = 0.01$ or $\lambda = 0.1$, the accretion time-scales at $z > 15$ are shorter than adopted in P16 (hence in the NL model). In fact, larger values of λ implies less compact objects and, thus, larger values of R_d. This gives rise to shorter super-Eddington accretion episodes. For $z = 20 - 25$, where the entire population of active BHs is accreting at super-critical regimes, the L01 model predicts an accretion-time distribution peaking around $t_{accr} \sim 100\,\mathrm{yr}$, to be compared with $t_{accr} \sim 0.01$ (~ 1) Myr in L001 (NL) model, respectively. For lower z, the contribution of active galaxies with large gas velocity dispersion σ becomes relevant, and the accretion times t_{accr} become larger. For instance, in the L001 model it is possible to find BHs accreting for longer times (up to $\sim 30\,\mathrm{Myr}$) with respect to the NL model, where $t_{accr} \sim 1\,\mathrm{Myr}$.

The distribution of t_{accr} shows an increasing trend with increasing dark matter halo mass. This effect is negligible in the narrow distribution predicted by model NL. In models L01 and L001, instead, one order of magnitude increase in dark matter halo masses corresponds to increasing $\gtrsim$ half order of magnitude accretion time-scales t_{accr}.

It is interesting to compare how different assumptions on λ affect the BH mass growth. In the left panel of Figure 5.4 we show the evolution of the total (solid) BH mass, summing over all the progenitors present in the simulation at a given redshift. Dashed lines represent the time evolution of the most massive BH that powers the $z \sim 6$ quasar. At high-z, the difference in the total BH mass between NL and L001 models is about one order of magnitude, as a consequence of different total black hole accretion rates (Hanning smoothed), shown in the right panel of Figure 5.4. This quantity is computed as $\dot{M}_{BH} = \Delta M_{BH}/\Delta t_r$, i.e. as the average BH mass increase in the simulation time-step Δt_r, even if $t_{accr} < \Delta t_r$. Hence, lower BH accretion rates are a consequence of the lower t_{accr}. More gas is retained by dark matter halos due to reduced AGN feedback effects, leading to larger BH accretion rates at later times. As a results, in model L001 the total BH mass follows a steeper evolution at $z < 10$ compared to model NL, reaching a factor 2 larger value at $z = 6.4$.

Conversely, the accretion time-scales, t_{accr}, in the L01 model are too small to allow an efficient BH mass growth. Almost all the BHs present in model L01 accrete at super-Eddington rates for $t_{accr} \sim 100 - 1000\,\mathrm{yr}$. This leads to a BH mass growth from $\sim 10^5\,M_\odot$

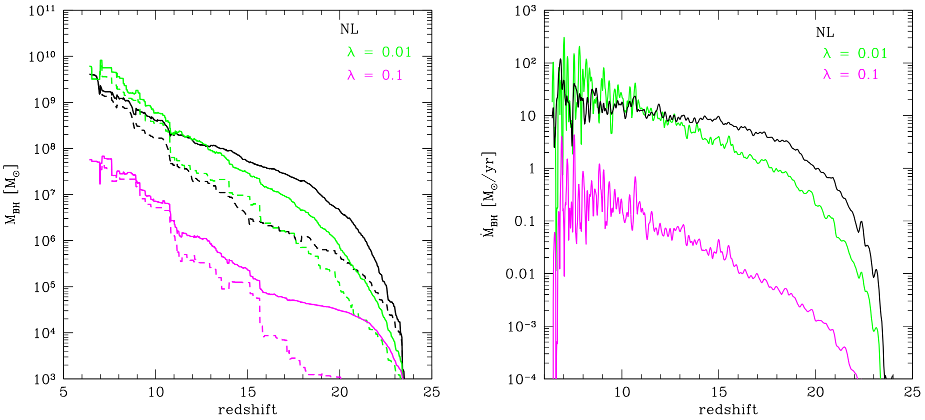

Figure 5.4. Time evolution of the more massive (dashed lines) and total (solid lines) black hole mass (left panel) and black hole accretion rate (right panel) evolution for NL (black line), L001 (green line) and L01 (magenta line) models.

to $10^6\,M_\odot$ between $z = 15 - 22$ and to a final BH mass $\sim$ 2 orders of magnitude lower than predicted by L001 and NL models.

5.3 Conclusions

Many models invoke super-Eddington accretion onto the first black holes as a possible route to form high-z SMBHs (Volonteri and Rees, 2005; Wyithe and Loeb, 2012; Madau et al., 2014; Alexander and Natarajan, 2014; Volonteri et al., 2015; Inayoshi et al., 2015; Sakurai et al., 2016; Ryu et al., 2016; Begelman and Volonteri, 2017). In P16, we have shown that super-Eddington accretion is required to form a $\sim 10^9\,M_\odot$ SMBH at $z \sim 6$ starting from $\sim 100\,M_\odot$ BH remnants of very massive Pop III stars. However, there are different mechanisms which can suppress early super-critical accretion. Feedback effects from the stellar progenitors can strongly affect the gas density around the newborn black holes, reducing the efficiency of gas accretion. In addition, the onset of disk winds can suppress BH growth, setting a maximum time-scale for sustainable super-Eddington accretion.

In this Chapter, we used the cosmological, data-constrained semi-analytic model GAMETE/SuperQSOdust, described in Chapter 4, to estimate the impact of these two physical processes on SMBHs formation at $z > 6$.

We find that the influence of stellar feedback on the surroundings produce a delay on

BH seeds formation, shifting their redshift distribution from $z \gtrsim 20$ to $z \gtrsim 15$. However, despite the very conservative assumptions made to maximize stellar feedback effects, we find that this delay does not prevent neither the growth of high-z SMBHs, nor the possibility of their BH progenitors to accrete at super-Eddington rates.

The impact of disk outflows, and the associated reduction of the duration of super-Eddington accretion episodes, strongly depends on the angular momentum of gas joining the accretion disk. Assuming that disk winds suppress BH accretion when the disk radius becomes comparable to the photon trapping radius, the result relies on the value of λ, which represents the fraction of angular momentum retained by the gas. For $\lambda = 0.1$, $t_{\rm accr} \sim 100 - 10^4$ yr at $z > 15$, too short to allow the SMBH to grow efficiently, and at $z \sim 6$ the final SMBH mass is ~ 2 orders of magnitude lower than what obtained in the model where disk winds are neglected. For $\lambda = 0.01$, instead, super-critical accretion events are sustained for time-scales $\sim 10^4 - 10^6$ yr. This suppresses the early growth phase, but the larger gas mass retained allows a steeper growth of the SMBH mass at later times.

The implication of this study is that the accreted gas must efficiently loose angular momentum to enable super-Eddington growth of the first SMBHs from light BH seeds. If $\lambda < 0.01$, super-Eddington accretion has a very short duty cycle, with $t_{\rm accr} \ll$ Myr at $z > 15$ and for ~ 0.1 Myr for $z = 7 - 15$. This decreases the active fraction of high-z BHs and further strengthens the conclusions of Pezzulli et al. (2017), discussed in the next chapter, that the higher-redshift progenitors of $z \sim 6$ quasars are difficult to observe "in the act", as the short and intermittent super-critical accretion events imply a low fraction of active black holes.

Chapter 6

Faint progenitors of luminous quasar

The detection and characterization of $z > 6$ quasars fainter than the ones currently observed would be extremely helpful to improve our understanding of the high-z SMBHs formation process. Several observational campaigns in the X-ray band have been made to discover the faint progenitors of SMBHs at $z \gtrsim 5$. Weigel et al. (2015) searched for active galactic nuclei (AGNs) in the *Chandra* Deep Field South (CDF-S) starting their analysis from already X-ray selected sources within the *Chandra* 4 Ms catalogue (Xue et al., 2011). They combined GOODS, CANDELS and *Spitzer* data to estimate the photometric redshift of their sources but no convincing AGN candidates was found at $z \gtrsim 5$. This result has been confirmed by the independent analysis of Georgakakis et al. (2015), who combined deep Chandra and wide-area/shallow XMM—Newton survey fields to infer the evolution of the X-ray luminosity function at $3 \lesssim z \lesssim 5$. They find a strong evolution at the faint-end and extrapolating this trend to $z \gtrsim 5$ they predict < 1 AGN in the CDF-S. A complementary approach was followed by Treister et al. (2013), who started from a sample of photometrically selected galaxies at $z \sim 6$, 7, and 8 from the *Hubble Space Telescope* Ultra Deep Field (HUDF) and CANDELS, and then combined these data with the 4 Ms CDF-S. None of the sources was detected in X-ray either individually or via stacking, placing tight constraints on black hole growth at these redshifts[1].

However, by improving the multi-dimensional source detection technique developed by Fiore et al. (2012), Giallongo et al. (2015) identified three faint AGN candidates in the GOODS-S field, with photometric redshifts $z > 6$. Very faint $z > 4$ galaxies are selected

---

[1] These authors estimate an accreted mass density $< 1000\,\mathrm{M}_\odot\,\mathrm{Mpc}^{-3}$ at $z \sim 6$.

in the sample from the near infrared (NIR) H band luminosity, down to $H \leq 27$ (which at these redshifts corresponds to a UV rest-frame selection). Then, AGN candidates with soft X-ray ($[0.5-2]$ KeV) fluxes above $F_{\rm X} \sim 1.5 \times 10^{-17} {\rm erg cm^{-2} s^{-1}}$, are extracted from the sub-sample. NIR-based selection methods allow to reach fainter X-ray fluxes than direct blind X-ray selections.

In contrast, none of the $z > 6$ NIR-selected sources identified by Giallongo et al. (2015) are found by Cappelluti et al. (2016) in the same area, using a similar approach as in Giallongo et al. (2015) but different thresholds and energy bands.

Beside the poor statistics and the large uncertainties related to photometric redshift estimates[2], the authors underline that the actual number of high redshift AGN candidates is very sensitive to the adopted selection procedure (see also Vito et al. 2016). The analysis of the ultra-deep 7 Ms Chandra observations in the CDF-S as well as future surveys carried out with the next generation X-ray observatory *ATHENA+*, will enlarge the systematic search of high redshift AGN to lower luminosity sources.

For this reason, several authors have proposed to search for SMBH progenitors through far-infrared emission lines that are unaffected by dust obscuration (e.g. Spaans and Meijerink 2008, Schleicher et al. 2010, Gallerani et al. 2014). Additionally, short episodes of mildly super-Eddington growth, followed by longer periods of quiescence, with duty cycles of $20-50\%$ (Madau et al., 2014), may further decrease the probability of observing accreting BHs, resulting in a low *active* BH occupation fraction. It should be noted that BHs cannot be detected by X-ray observations if their growth is driven by mergers, rather than mass accretion. Indeed, the accretion process is directly related to the emission in this band (see the detailed discussion by Treister et al. 2013).

In this Chapter, we will discuss which of these explanations is the most plausible to interpret the shortage of detections of faint progenitors of luminous quasars. To this aim, we use the semi-analytical model GAMETE/SUPERQSODUST, introduced in Chapter 4, that allows to simulate a statistically meaningful number of hierarchical histories of $z \sim 6$ quasars, following the star formation history, chemical evolution and nuclear black hole growth in all their progenitor galaxies. In the following Sections, we investigate the detectability of

---

[2] An example is the source 29323 with the highest photo-z=9.7 selected by Giallongo et al. (2015) but excluded from the Cappelluti et al. (2016) sample because of artifacts in the spectral energy distribution.

the faint progenitors of $z \sim 6$ BHs in the super-critical growth scenario, by constructing a model for the optical/UV and X-ray emission of the active BH progenitors. We consider the dependence of the X-ray spectrum on the Eddington ratio $\lambda_{\rm Edd} = L_{\rm bol}/L_{\rm Edd}$ (i.e. the bolometric-to-Eddington luminosity ratio).

By computing the spectral energy distribution for the sample of active galaxies simulated in a cosmological context. We find an average Compton thick fraction of $\sim 45\%$ and large typical column densities ($N_H \gtrsim 10^{23}\,{\rm cm}^2$). However, faint progenitors are still luminous enough to be detected in the X-ray band of current surveys. Even accounting for a maximum obscuration effect, the number of detectable BHs is reduced at most by a factor 2. In our simulated sample, observations of faint quasars are mainly limited by their very low active fraction ($f_{\rm act} \sim 1\%$), which is the result of short, super-critical growth episodes. We suggest that to detect high-z SMBHs progenitors, large area surveys with shallower sensitivities, such as *Cosmos Legacy* and XMM-LSS+XXL, are to be preferred with respect to deep surveys probing smaller fields, such as CDF-S.

6.1 The Spectral Energy Distribution of accreting BHs

The spectral energy distribution (SED) of AGNs has been modelled in the literature using empirical models inferred from observations (e.g. Marconi et al. 2004; Lusso et al. 2010) or calibrating physically motivated prescriptions with observations (Yue et al., 2013). These models have been also applied, when necessary, to super-critical growth regimes (Pacucci et al., 2015). Simulations of *slim* discs have been also developed, taking into account the vertical disc structure and predicting the SED of the emitted radiation (Wang et al., 1999; Watarai et al., 2000; Ohsuga et al., 2003; Shimura and Manmoto, 2003).

The typical spectrum of a radio quiet AGN can be approximately divided into three major components: the Infrared Bump (IB), the Big Blue Bump (BBB), and the X-ray region. Under the assumption of an optically thick disc, a large fraction, up to $\gtrsim 50\%$, of the bolometric emission is expected to be in the form of optical/UV thermal disc photons, producing the BBB continuum that extends from the NIR at $1\mu m$ to the UV ~ 1000 Å or the soft X-ray wavelengths, in some cases. In the hard X-ray band the AGN flux per unit frequency F_ν is well described by a power law with spectral index ~ 0.9 (Piconcelli

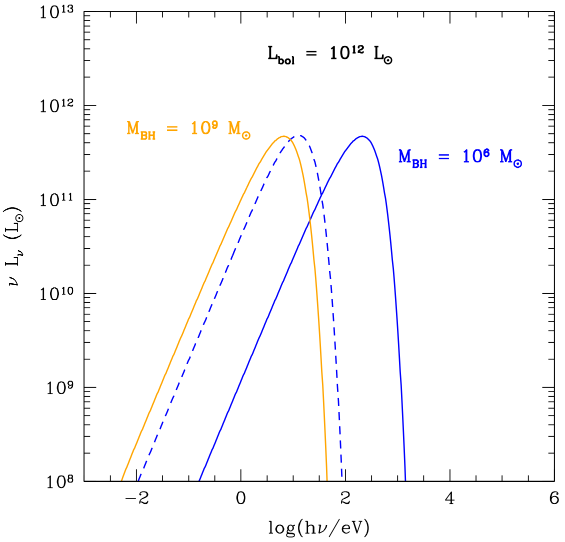

Figure 6.1. Examples of thermal emission spectra for BHs with masses of $10^6 M_\odot$ (blue lines) and $10^9 M_\odot$ (orange line) normalized to a common bolometric luminosity of $L_{\rm bol} = 10^{12} L_\odot$. Standard thin disc and slim disc models are shown with solid and dashed lines, respectively. For this luminosity, we find that $r_0 > r_{\rm pt}$ for the $10^9 M_\odot$ BH so that the slim and the thin disc models lead to the same emission spectrum.

et al., 2005; Just et al., 2007). This emission is due to Compton up-scattering of optical/UV photons by hot electrons in the corona above the disc. Overlapped to the continuum, there is also a strong emission line at 6.4 keV, a noticeable narrow feature corresponding to the Kα transition of iron, and a reflection component, usually referred to as *Compton hump*, around 30 keV (Ghisellini et al., 1994; Fiocchi et al., 2007). The Fe-Kα line is attributed to fluorescence in the inner part of the accretion disc, $\sim$ few Schwarzschild radii from the central BH, while the Compton hump is due to Compton-down scattering of high energy photons by high column density reflector $N_{\rm H} \gtrsim 10^{24}\,{\rm cm}^{-2}$. Finally, the IB extends from $\sim 1\,\mu m$ to $\sim 100\,\mu$m, and it is thought to arise from reprocessed BBB emission by dust.

In this section, we will focus on the emission in the optical/UV and X-ray bands[3].

6.1.1 Modeling the primary emission

We parametrize the emission from the hot corona as a power law

$$L_\nu \propto \nu^{-\Gamma+1} e^{-h\nu/E_c}, \tag{6.1}$$

where $E_c = 300\,\mathrm{keV}$ is the exponential cut-off energy (Sazonov et al., 2004; Yue et al., 2013) and Γ is the photon index. We include the reflection component using the PEXRAV model (Magdziarz and Zdziarski, 1995) in the XSPEC package, assuming an isotropic source located above the disc, fixing the reflection solid angle to 2π, and the inclination angle to 60°. Observations show evidence of a dependence of the photon index Γ of the X-ray spectrum on the Eddington ratio $\lambda_{\rm Edd} = L_{\rm bol}/L_{\rm Edd}$ (Grupe, 2004; Shemmer et al., 2008; Zhou and Zhao, 2010; Lusso et al., 2010; Brightman et al., 2013). Despite this correlation seems to be found in both the soft and hard bands, the measures of $\Gamma_{0.5-2\rm keV}$ can be contaminated by the presence of the soft excess, hampering any strong claim of a correlation between the primary emission in this band and $\lambda_{\rm Edd}$. Instead, this contamination is less important in the hard band [2−10]keV. Brightman et al. (2013) measured the spectral index $\Gamma_{2-10\rm keV}$ of radio-quiet AGNs with $\lambda_{\rm Edd} \lesssim 1$ up to $z \sim 2$, finding that:

$$\Gamma_{2-10\rm keV} = (0.32 \pm 0.05) \log \lambda_{\rm Edd} + (2.27 \pm 0.06). \tag{6.2}$$

Here we adopt the above relation to model the dependence of the X-ray spectrum on $\lambda_{\rm Edd}$.

We assume the primary emission in the optical/UV bands to be described as the sum of a multicolour black body spectrum $L_\nu^{\rm BB}$, emitted by different parts at different disc temperatures T:

$$L_\nu^{\rm BB} = L_0 \int_0^{T_{\rm max}} B_\nu(T) \left(\frac{T}{T_{\rm max}}\right)^{-11/3} \frac{dT}{T_{\rm max}}, \tag{6.3}$$

where $B_\nu(T)$ is the Planck function and L_0 is a normalization factor. The temperature profile of a steady-state, optically thick, geometrically thin accretion disc is (Shakura and Sunyaev, 1973):

$$T(r) = \left(\frac{3GM_{\rm BH}\dot{M}}{8\pi\sigma r^3}\right)^{1/4} \left(1 - \sqrt{\frac{r_0}{r}}\right)^{1/4}, \tag{6.4}$$

---

[3] The normalization of the final SED is $L_{\rm bol}$, computed for each active galaxy simulated in GAMETE/QSODUST (see P16 for details).

where $M_{\rm BH}$ is the mass of the compact object, $\dot{M}$ the gas accretion rate, σ is the Stefan-Boltzman constant and r_0 is the Innermost Stable Circular Orbit (ISCO), that we assume to be the ISCO for a non-rotating BH. The maximum temperature $T_{\rm max}$ is achieved at a radius $r(T_{\rm max}) = \frac{49}{36} r_0$.

Hence, the SED depends both on $\lambda_{\rm Edd}$ and $M_{\rm BH}$. In fact, for a given luminosity, the peak of the SED is shifted towards higher energies for lower $M_{\rm BH}$ (see Figure 6.1). However, the assumption of a standard *thin* disc model is valid when the disc is geometrically thin, i.e. for luminosities below $\sim 30\%$ of Eddington luminosity. Above this value, the radiation pressure causes an inflation of the disc (McClintock et al., 2006). Optically thick disc with high accretion rates are better described by *slim* accretion disc models (Abramowicz et al., 1988; Sądowski, 2009; Sądowski et al., 2011), where the photon trapping effect has an important role. In fact, photons produced in the innermost region of the disc are trapped within it, due to large Thompson optical depth, and advected inward. The typical radius within which photons are trapped, $r_{\rm pt}$, can be obtained by imposing that the photon diffusion time scale is equal to the accretion time scale, so that (Ohsuga et al., 2002):

$$r_{\rm pt} = \frac{3}{2} R_s (\dot{M}/\dot{M}_{\rm Edd,1}) {\rm h}, \tag{6.5}$$

where $R_s = 2GM_{\rm BH}/c^2$ is the Schwarzschild radius, $\dot{M}_{\rm Edd,1}$ is the Eddington accretion rate and ${\rm h} = {\rm H/r}$ is the ratio between the half disc-thickness H and the disc radius r. Since ${\rm h} \approx 1$ in radiation pressure dominated regions, we assume ${\rm h} = 2/3$ so that $r_{\rm pt} = R_s(\dot{M}/\dot{M}_{\rm Edd,1})$. Photon trapping causes a cut-off of the emission at higher temperatures and, thus, a shift of the spectrum towards lower energies. To consider this feature of super-critical, advection-dominated energy flows, we assume that the radiative emission contributing to the spectrum is that emerging from $r > r_{\rm pt}$. Under this assumption, the difference between *thin* and *slim-like* discs will appear for $L \gtrsim 0.3 L_{\rm Edd}$.

In Figure 6.1 we show the thermal emission corresponding to a bolometric luminosity of $L_{\rm bol} = 10^{12} L_\odot$ and two BH masses $M_{\rm BH} = 10^9 M_\odot$ (orange) and $M_{\rm BH} = 10^6 M_\odot$ (blue). We compare the classical *thin* disc (solid lines) to that of *slim* disc (dashed line). If we consider *thin* discs, for a given $L_{\rm bol}$, BHs with higher masses have a SED which peaks at lower energies. As a result of photon trapping, a comparable shift towards lower energies is obtained by a $\sim 10^6\, M_\odot$ BH with a super-critical accretion disc, for which $r_{\rm pt} > r_0$.

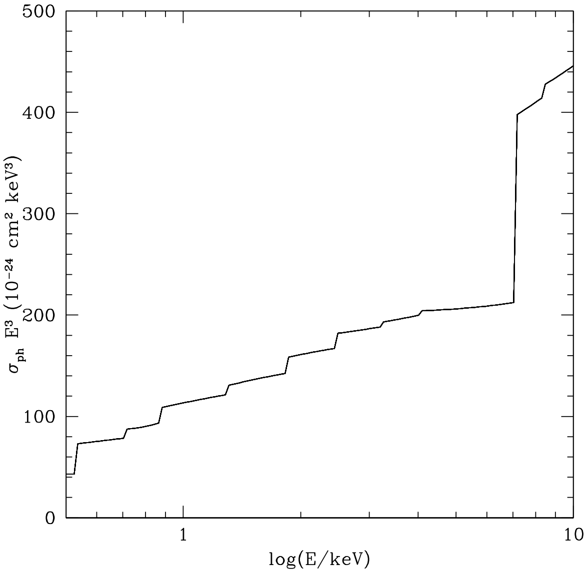

Figure 6.2. Photoelectric cross section as a function of energy for $Z = Z_\odot$.

The relative amplitude of the spectrum in the UV and X-ray bands is usually quantified by the the optical to X-ray spectral index $\alpha_{\rm OX}$, defined as $\alpha_{\rm OX} = -0.384 \log(L_{\rm 2keV}/L_{2500\text{Å}})$. Observations (Steffen et al., 2006; Just et al., 2007; Young et al., 2009; Lusso et al., 2010; Lusso and Risaliti, 2016) suggest that $\alpha_{\rm OX}$ increases with L_{2500}, implying that the higher is the emission in the UV/optical band, the weaker is the X-ray component per unit of UV luminosity. In a recent study, based on a sample of AGNs with multiple X-ray observations at $0 \lesssim z \lesssim 5$, Lusso and Risaliti (2016) found that $\log L_{\rm 2keV} = 0.638 \log L_{2500\text{Å}} + 7.074$, which implies,

$$\alpha_{\rm OX,2016} = 0.14 \log L_{2500\text{Å}} - 2.72. \tag{6.6}$$

In what follows, we adopt this relation to quantify the relative contribution of the optical/UV and X-ray spectrum, and truncate the emission from the hot corona at energies below $\sim 3T_{\rm max}$.

6.1.2 Absorbed spectrum

The radiation produced from the accreting process can interact with the gas and dust in the immediate surroundings of the BH. For the purpose of this study, we consider only the absorption in the X-ray band. The two main attenuation processes are photoelectric absorption and Compton scattering of photons against free electrons. The effect of these physical processes is to attenuate the intrinsic flux, F_ν, by:

$$F_\nu^{\rm obs} = F_\nu e^{-\tau_\nu}. \tag{6.7}$$

At $h\nu \gtrsim 0.1$ keV and under the assumption of a fully-ionized H-He mixture, the optical depth τ_ν can be written as $\tau_\nu = (1.2\sigma_T + \sigma_{ph})N_H$ (Yaqoob, 1997) where N_H is the hydrogen column density and σ_T and σ_{ph} are the Thomson and the photoelectric cross section, respectively.

Morrison and McCammon (1983) computed an interstellar photoelectric absorption cross section $\sigma_{ph}^{Z_\odot}$ as a function of energy in the range [0.03-10] keV, for solar metallicity $Z_\odot$[4].

In our simulations, the gas metallicities of high-z BH host galaxies span a wide range of values, with $0 \lesssim Z \lesssim Z_\odot$. To account of the metallicity dependence of the absorbing material, we separate the photoelectric cross section into its components

$$\sigma_{ph} = \sigma_H + \sigma_{He} + \sigma_{met}, \tag{6.8}$$

where σ_H and σ_{He} represent the contribution of hydrogen and helium.

The hydrogen ionization energy $\sim$ 13.6eV and helium second ionization energy $\sim$ 54.4eV are much lower than the energy in the X-ray band ($\sim$ keV), hence σ_H and σ_{He} can be safely evaluated in Born approximation. Following Shu (1991), the cross section in Born approximation for a hydrogen atom is

$$\sigma_{\rm X} = \frac{8\pi}{3\sqrt{3}}\frac{Z_{\rm X}^4 m_e e^{10}}{c\hbar^3(\hbar\omega)}\sqrt{\frac{48 Z_{\rm X} e^2}{2a_Z\hbar\omega}}, \tag{6.9}$$

where $Z_{\rm X}$ is the atomic number for the X-th element (1 for H, 2 for He), m_e and e are the electron mass and charge, c is the speed of light, $\hbar$ the reduced Plank constant and $a_Z = \hbar/Z_{\rm X} m_e e^2$.

In Figure 6.2 we can see the photoelectric cross section for $Z = Z_\odot$. For energies $\gtrsim$ 0.2keV, $\sigma_{\rm ph}$ is dominated by metals, in particular C and N. The cross section presents

---

[4] We have renormalized $\sigma_{\rm ph}$ that Morrison and McCammon 1983 originally computed for $Z = 0.0263$ to a solar metallicity value of $Z_\odot = 0.013$ (Asplund et al., 2009).

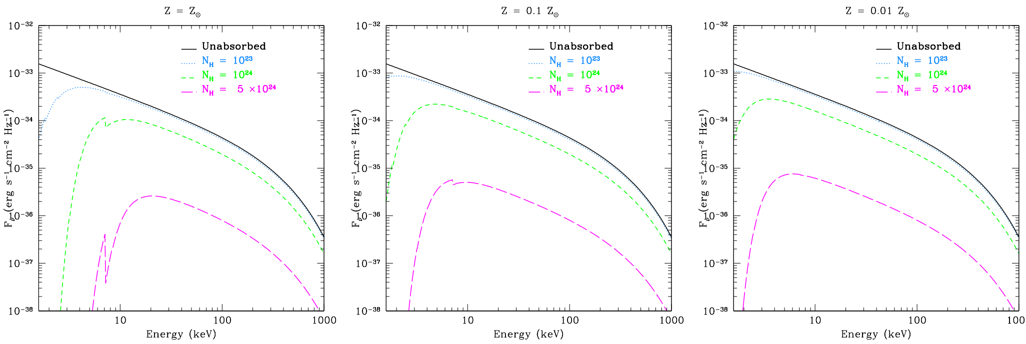

Figure 6.3. Primary (black solid line) and reprocessed emissions (dashed lines) of accreting BHs for column densities $N_{\rm H}$ = (10^{23}, 10^{24}, 5×10^{24}) cm^{-2}. Different panels refer to different metallicities: $Z = Z_\odot$ (left), $Z = 0.1Z_\odot$ (middle) and $Z = 0.01Z_\odot$ (right).

several gaps that correspond to the K-shell energies of different elements. In fact, in the evaluation of $\sigma_{\rm ph}$ it has been taken into account that an element X contributes to the absorption only if the photon energy is greater than the K-shell energy, with the highest energy gap corresponding to Fe. The photoelectric cross section decreases for increasing energy, when the Thomson cross section $\sigma_{\rm T}$ becomes dominant (for $E \gtrsim 10$ keV at $Z = Z_\odot$). Thus, softer X-ray photons are expected to be more absorbed than harder ones. This feature is well visible in Figure 6.3, where the intrinsic spectrum for $L_{\rm bol} = 10^{12} L_\odot$ and $M_{\rm BH} = 10^9 M_\odot$ (black line) is compared to the spectra attenuated by gas with $Z = Z_\odot$, $0.1\,Z_\odot$ and $0.01\,Z_\odot$ (from left to right respectively) and different values of hydrogen column density $N_{\rm H}$ (dashed lines), that have been computed consistently with the diffuse and cold gas density profiles (see Section 6.2). The effect of metallicity is relevant only at lower energies, where the photoelectric cross section is dominant. As already discussed, in fact, at energies $E \gtrsim 10$ keV the Thomson cross section becomes dominant, removing the absorption dependence on metallicity.

Compton thick AGNs, which are usually characterized by $N_{\rm H} \gtrsim 1.5 \times 10^{24}\,{\rm cm}^{-2}$, are completely absorbed in the soft band. The emission peak moves to $\sim 20\,$keV, and the corresponding magnitudes is ~ 2 orders of magnitude lower than in the intrinsic spectrum. For $N_{\rm H} \lesssim 10^{25}\,{\rm cm}^{-2}$, the direct emission is visible at energies $E \gtrsim 10\,$keV, and they are labelled as *transmission-dominated* AGNs. For even larger column densities ($N_{\rm H} > 10^{25}\,{\rm cm}^{-2}$) direct X-ray emission is strongly affected by Compton scattering and fully obscured, and only the faint reflection component can be detected (*reflection-dominated* AGNs). We note, however, that X-ray observations of $z \gtrsim 4$ quasars typically sample the rest-frame hard X-ray band.

The condensation of the absorbing material into grains reduces the value of $\sigma_{\rm ph}$. Morrison and McCammon (1983) estimate the importance of this effect, evaluating the photoelectric cross section in the case that all the elements but H, He, Ne and Ar are depleted in grains, with the exception of O, for which the condensation efficiency is assumed to be 0.25. The variation in the photoelectric cross section is relatively modest, $\sim 11\%$ at $E \sim 0.3$ keV and $\sim 4\%$ at 1 keV. Hence, hereafter we neglect this effect.

Despite we are restricting our analysis to the X-ray part of the emission spectrum, it is important to note that the absorbed radiation will be re-emitted at lower energies. Yue et al. (2013) find that for Compton-thick systems, secondary photons emitted by free-free, free-bound and two-photon processes can increase the luminosity by a factor of ~ 10 in the rest-frame $[3-10]$ eV, which will be redshifted in the near IR at $z = 0$. As a result, most of the energy emitted is expected to be observed in the IR and soft-X-ray bands (Pacucci et al., 2015, 2016; Natarajan et al., 2016).

6.2 The sample

In Section 6.1 we have introduced our emission model for accreting BHs. Physical inputs required to compute the spectrum are the BH mass, $M_{\rm BH}$, the bolometric luminosity, $\rm L_{bol}$, the Eddington accretion ratio, $\dot{M}/\dot{M}_{\rm Edd,1}$, the metallicity, Z, and the column density, $N_{\rm H}$. We adopt the semi-analytic model GAMETE/SuperQSOdust, in the version described by P16, to simulate these properties for a sample of BH progenitors of $z \gtrsim 6$ SMBHs. In this section, we first summarize the main properties of the model and then we describe the physical properties of the simulated sample.

6.2.1 Simulating SMBH progenitors with GAMETE/SuperQSOdust

The code allows to reconstruct several independent merger histories of a $10^{13} M_{\odot}$ DM halo assumed to host a typical $z \sim 6$ SMBH, like J1148 (e.g. Fan et al. 2004). The time evolution of the mass of gas, stars, metals and dust in a two-phase interstellar medium (ISM) is self-consistently followed inside each progenitor galaxy. The hot diffuse gas, that

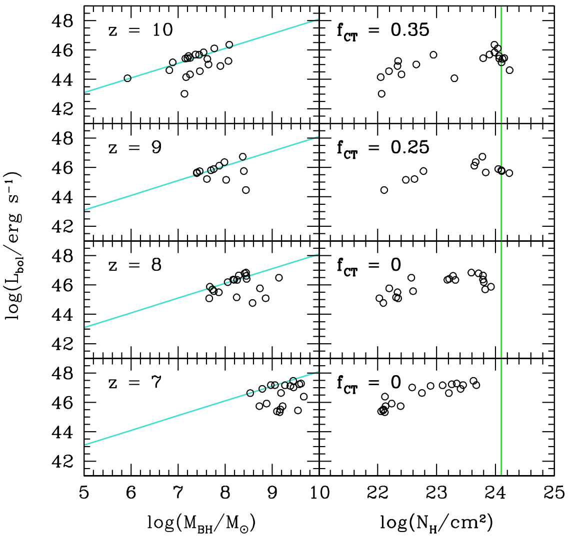

Figure 6.4. Properties of BH progenitors extracted from 30 simulations at $z = 7, 8, 9$ and 10. Bolometric luminosities are shown as a function of BH masses (*left panel*) and hydrogen column density in the host galaxy $N_{\rm H}$ (*right panels*). Cyan lines represent $L_{\rm Edd}(M_{\rm BH})$. The green vertical line represents the $N_{\rm H}$ corresponding to a Compton-thick system, while $f_{\rm CT}$ is the fraction of Compton-thick BHs present at that redshift.

we assume to fill each newly virialized DM halo, can gradually cool through processes that strongly depend on the temperature and chemical composition of the gas. For DM halos with virial temperature $T_{\rm vir} < 10^4$ K, defined as *minihalos*, we consider the contribution of H_2, OI and CII cooling (Valiante et al., 2016), while for Lyα-halos ($T_{\rm vir} \geq 10^4$ K) the main cooling path is represented by atomic transitions. In quiescent evolution, the gas settles on a rotationally-supported disc, that can be disrupted when a major merger occurs, forming a bulge structure. The hydrogen column density $N_{\rm H}$ has been computed taking into account the gas distribution in the diffuse and cold phases. We assumed a spherically-symmetric Hernquist density profile for the gaseous bulge (Hernquist, 1990),

$$\rho_b(r) = \frac{M_b}{2\pi}\frac{r_b}{r(r+r_b)^3}, \tag{6.10}$$

where M_b is the bulge mass of the gas, r_b is the scale radius $r_b = R_{\rm eff}/1.8153$ (Hernquist, 1990), and the effective radius, $R_{\rm eff}$, has been computed as $\log(R_{\rm eff}/{\rm kpc}) = 0.56\log(M_b + M_b^\star) - 5.54$, where $M_b^\star$ is the stellar mass of the bulge (Shen et al., 2003). For the diffuse gas, we adopt an isothermal density profile (see Section 2.1 and 2.2 in P16) and we do not consider the contribution of the galaxy disc to the absorbing column density.

We assume BH seeds to form with a constant mass of $100\,M_\odot$ as remnants of Pop III stars in halos with $Z \leq Z_{\rm cr} = 10^{-4}\,Z_\odot$. As a result of metal enrichment, BH seeds are planted in halos with a mass distribution peaking around $M_{\rm h} \sim 10^7\,M_\odot$, at $z > 20$, below which no Pop III stars is formed.

The BH grows via gas accretion from the surrounding medium and through mergers with other BHs. Our prescription allows to consider quiescent and enhanced accretion following merger-driven infall of cold gas, which loses angular momentum due to torque interactions between galaxies. We model the accretion rate to be proportional to the cold gas mass in the bulge $M_{\rm b}$, and inversely proportional to the bulge dynamical time-scale $\tau_{\rm b}$:

$$\dot{M}_{\rm accr} = \frac{f_{\rm accr} M_{\rm b}}{\tau_{\rm b}}, \tag{6.11}$$

where $f_{\rm accr} = \beta f(\mu)$, with $\beta = 0.03$ in the reference model and $f(\mu) = \max[1, 1 + 2.5(\mu - 0.1)]$, so that mergers with $\mu \leq 0.1$ do not trigger bursts of accretion.

As discussed in Section 6.1.1, once the accretion rates become high, the standard *thin* disc model is no longer valid. Therefore, the bolometric luminosity $L_{\rm bol}$ produced by the accretion process has been computed starting from the numerical solution of the relativistic slim accretion disc obtained by Sądowski (2009), adopting the fit presented in Madau et al. (2014). This model predicts mildly super-Eddington luminosities even when the accretion rate is highly super-critical.

The energy released by the AGN can couple with the interstellar gas. We consider energy-driven feedback, which drives powerful galactic-scale outflows, and SN-driven winds, computing the SN rate explosion for each galaxy according to formation rate, age and initial mass function of its stellar population (de Bennassuti et al., 2014; Valiante et al., 2014).

Finally, in BH merging events, the newly formed BH can receive a large center-of-mass recoil due to the net linear momentum carried by the asymmetric gravitational wave (Campanelli et al., 2007; Baker et al., 2008) and we compute the *kick* velocities following Tanaka and Haiman (2009).

We refer the reader to P16 for a more detailed description of the model.

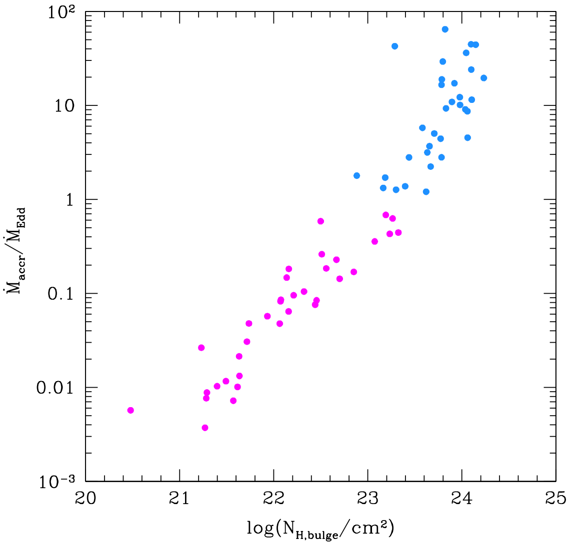

Figure 6.5. Column density of the bulge and Eddington accretion ratio for each of the active BHs found at $z = 7, 8, 9, 10$. Azure (magenta) represents super- (sub-) critical accreting BHs, i.e. those for which $\dot{M}/\dot{M}_{\rm Edd} > 1$

6.2.2 Physical properties of the sample

We run N_r independent merger trees and reproduce all the observed properties of one of the best studied quasars, SDSS J1148+5152 (hereafter J1148) at $z = 6.4$ that we consider as a prototype of luminous $z \gtrsim 6$ quasars. We choose $N_r = 30$ to match the statistics of the currently known sample of $z \gtrsim 6$ quasars with robust BH mass measurements and $M_{\rm BH} \gtrsim 10^9 M_\odot$ (Fan et al., 2001, 2003, 2004, 2006).

Figure 6.4 shows the bolometric luminosity as a function of the BH mass (left panel) and hydrogen column density (right panel) for *active* BH progenitors (i.e. with $\lambda_{\rm Edd} \geq 5 \times 10^{-3}$) of SMBHs extracted from the simulations at $z = 7, 8, 9, 10$. All BH progenitors have masses $M_{\rm BH} \gtrsim 10^6 M_\odot$ and bolometric luminosities $L_{\rm bol} \gtrsim 10^{42}$ erg/s. As it can be seen from the figure, luminosities never exceed $\sim$ few $L_{\rm Edd}$ (cyan lines), also for super-critical accreting BHs. This is a result of the low radiative efficiencies of the *slim* disc solution: only a small fraction of the viscosity-generated heat can propagate, while the larger fraction is advected inward. In the right panel of the figure, we show the relation between hydrogen column density $N_{\rm H}$ and bolometric luminosity. At all redshifts, our sample is composed only by *transmission-dominated* AGNs. The vertical lines indicate the

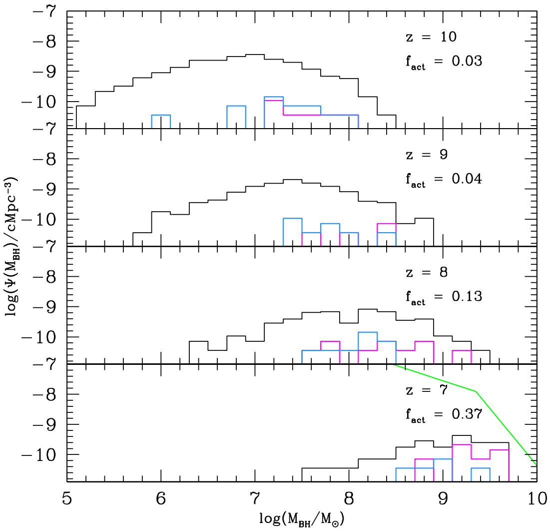

Figure 6.6. The mass function of BH progenitors at four different snapshots (z = 10, 9, 8 and 7 from top to bottom). The black line shows the total while the azure solid and magenta dotted lines indicate active BHs accreting at super and sub-Eddington rates, respectively. The fraction of active BHs at each redshift, $f_{\rm act}$, is also reported. The green solid line in the bottom panel represents the BH mass function inferred from observations by Willott et al. (2010) at $z = 6$.

column density above which the systems are classified as Compton-thick. The fraction of Compton-thick AGNs, $f_{\rm CT}$, is also shown. We find that $f_{\rm CT}$ increases with redshift, ranging between 35% at $z = 10$ to ~ 0 at $z = 7$ and that $f_{\rm CT} \sim 45\%$ for all the simulated sample at all redshifts. These numbers are consistent with the loose limits inferred from the analysis of the cosmic X-ray background (CXB) with AGN population synthesis models, which generally find $f_{\rm CT} = 5-50\%$ (Ueda et al., 2003; Gilli et al., 2007; Akylas et al., 2012), and with indications of growing obscuration with redshift (La Franca et al., 2005; Treister et al., 2009; Brightman and Ueda, 2012) and luminosity (Vito et al. 2013, see however Buchner et al. 2015).

The environmental conditions in which these BHs grow play an important role in determining the accretion regime. Figure 6.5 shows the Eddington accretion ratio $\dot{M}/\dot{M}_{\rm Edd}$, where $\dot{M}_{\rm Edd} = 16 L_{\rm Edd}/c^2$, as a function of the hydrogen column density of the bulge, which provides the gas reservoir to BH accretion. We find a positive correlation of the ratio with $N_{\rm H,bulge}$, showing that, when $N_{\rm H,bulge} \gtrsim 10^{23} {\rm cm}^2$, BHs accrete at super-critical rates.

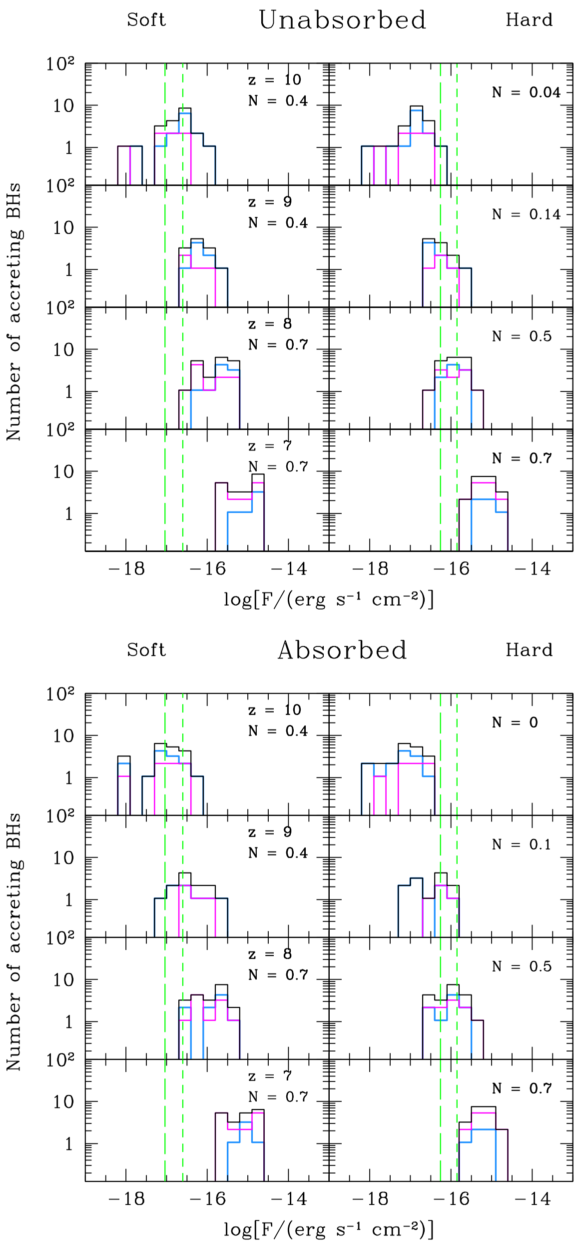

Figure 6.7. Flux distribution for each snapshot (black solid lines), divided in super- (azure) and sub- (magenta) Eddington accreting BH progenitors. We report both the *unabsorbed* model (*top panel*) and the *absorbed* model (*bottom panel*), for the soft (left panels) and hard (right panels) *Chandra* bands. Vertical dashed green lines represent different *Chandra* flux limits: CDF-S 4 Ms (long-dashed, Xue et al. 2011), $F_{\rm CDF-S} = 9.1 \times 10^{-18}$ (5.5×10^{-17}) erg s^{-1} cm^{-2} and CDF-N 2 Ms (short-dashed, Alexander et al. 2003), $F_{\rm CDF-N} = 2.5 \times 10^{-17}$ (1.4×10^{-16}) erg s^{-1} cm^{-2} in the soft (hard) band. In each panel, we also show the average number N of active progenitors with flux larger than CDF 4 Ms flux limit.

In the current model we do not take into account possible anisotropy of the AGN structure, such as the presence of a cleaned (dust and gas free) region from which the nucleus can be visible. For this reason we will investigate two extreme scenarios: the first assumes that there is no important absorption and that the observed X-ray emission is the intrinsic one (*unabsorbed* case), while in the second we compute the absorption as explained in Section 6.1.2 (*absorbed* case).

The first important quantity that we can compute is the BH mass function $\Psi(M_{\rm BH})$ of BH progenitors of $z \sim 6$, luminous quasars. Figure 6.6 shows $\Psi(M_{\rm BH})$ (black line) at different redshifts. The contribution of super- (azure solid) and sub- (magenta dotted) Eddington accreting BHs is also shown. Here the lines represent the averages over 30 merger tree simulations and the comoving volume V of the Universe in which BHs are distributed is $1\,{\rm Gpc}^3$, as the observed comoving number density of quasars at $z \sim 6$ is $n = 1\,{\rm Gpc}^{-3}$ (Fan et al., 2004). In the the bottom panel of Figure 6.6, we compare our results with the BH mass function inferred from observations of SMBHs by Willott et al. (2010) at $z = 6$ (shown with the green solid line). As expected, our predictions are below the observed distribution. In fact, our calculations describe the mass functions of BH progenitors of $z = 6$ SMBHs, namely a sub-population of existing BHs. This comparison is meant to show that our model predictions do not exceed the observed BH mass function.

At each redshift we consider the whole population of BH progenitors (active and inactive) along the simulated hierarchical merger histories (black solid histogram), with the exclusion of possible satellite BHs and kicked out BHs. These are assumed to never settle (or return) to the galaxy center, remaining always inactive (i.e. they do not accrete gas) and do not contribute to the assembly of the final SMBH (see P16 for details). The black solid histogram shows that the majority of BHs are temporarily non accreting BHs, due to the reduced gas content in the bulge. The fraction of active BHs in also reported in Figure 6.6 for the 4 snapshots. It increases by a factor ~ 1.3 from $z = 10$ to $z = 9$, ~ 3.2 from $z = 9$ to $z = 8$ and ~ 2.8 from $z = 8$ to $z = 7$. This is due to the increasing fraction of BHs that accrete at sub-Eddington rates (see also Fig. 4 in P16).

While the progenitors mass function is relatively flat at $z = 7$, a pronounced peak in the distribution becomes visible at higher redshifts, around $M_{\rm BH,peak} \sim 10^7\,(2.5 \times 10^6)\,{\rm M}_\odot$ at $z = 8\,(10)$. The mass density, particularly at the low mass end, is shifted towards more massive BHs at $z \leq 8$, as a consequence of BH growth due to mergers and gas accretion. Our simulations are constrained to reproduce the final BH mass of J1148 at $z_0 = 6.4$, thus the total number of progenitors naturally decreases as an effect of merging (major and minor) and gravitational recoil processes, implying a lower/poorer statistics as redshift approaches $\sim z_0$. Finally, the decreasing trend in the number density of $M_{\rm BH} < M_{\rm BH,peak}$ BHs, reflects the effects of chemical feedback. Efficient metal enrichment at $Z \geq Z_{\rm cr} = 10^{-4}\,Z_\odot$ inhibits the formation of Pop III stars and BHs already at $z < 20$. At lower redshifts the effects of dust and metal line cooling allows the gas to fragment more efficiently, inducing the formation of lower mass (Pop II) stars (Schneider et al., 2002, 2003, 2012b). As BH seeds grow in mass, the number density at the low-mass end decreases with time. By $z \sim 7$ the population of $< 10^6\,\mathrm{M}_\odot$ active progenitors is fully-evolved into more massive objects. The number and redshift distribution of accreting BHs in the two different accretion regimes have been widely investigated and discussed in P16. The resulting active BH mass functions reflect these properties. Super-Eddington accreting BHs are the dominant component (> 60%) down to $z \sim 10$ as indicated by the azure histogram in the upper panel of Figure 6.6. At lower z, super-critical accretion becomes progressively less frequent (< 24%), and sub-Eddington accretion dominates BH growth down to $z \sim 6-7$.

6.3 Results and discussion

In this section we analyse the X-ray luminosity of the BH sample introduced in the previous section and we discuss the best observational strategies to detect them by critically assessing the main reasons which have, so far, limited their observability.

Black hole occupation fraction. The black hole occupation fraction $f_{\rm BH}$ represents the number fraction of galaxies seeded with a BH, regardless the nuclear BHs are active or not. This quantity, not to be confused with the *AGN* fraction, is directly related to the seeding efficiency. In the work discussed in this Chapter, we assume that a BH seed is planted once a burst of Pop III stars occurs in a metal poor, newly virialized halo, as explained in Section 6.2. As already mentioned above, in the model we account for the possibility that a galaxy may lose its central BH during a major merger with another galaxy, due to

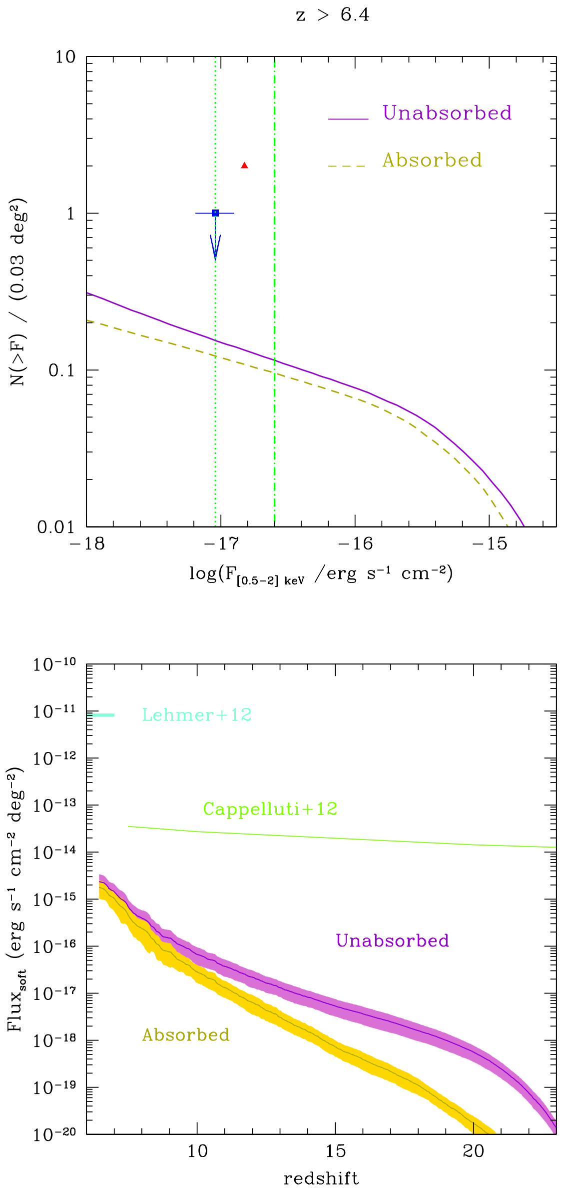

Figure 6.8. *Left panel:*Number of active BH progenitors, per unit area of 0.03 deg^2, with a flux larger than F in the *Chandra* soft band, as a function of F. Predictions for the *unabsorbed* (solid violet) and *absorbed* (dashed ochre) models are shown. Vertical green lines represent two different *Chandra* flux limits: CDF-S 4 Ms (dotted lines) and CDF-N 2 Ms (dashed-dotted lines). Red triangle and blue square represent, respectively, the observations obtained by Giallongo et al. (2015) and the upper limit of Weigel et al. (2015). *Right panel:* Cosmic X-ray Background in the soft band [0.5 - 2] keV predicted by the absorbed and unabsorbed models. The solid lines show the average among 30 independent simulations and the shaded region is the 1-σ scatter. We also show the soft CXB measured by Lehmer et al. (2012) in the 4Ms CDF-S and the upper limit on $z > 7.5$ accreting BHs placed by Cappelluti et al. (2012, see text).

large center-of-mass recoil velocity resulting from net-momentum carrying gravitational wave emission produced by the merging BH pair. As a result of this effect, the occupation fraction depends not only on the seeding efficiency, but also on the merger histories of SMBHs.

Alexander and Natarajan (2014) developed a model in which super-exponential accretion in dense star clusters is able to build a $\sim 10^4\, M_\odot$ BH in $\sim 10^7$ yr, starting from light seeds. The subsequent growth of this BH, up to $\sim 10^9\, M_\odot$, is driven by Eddington-limited accretion. They show that with this mechanism even a low occupation fraction of $f_{\rm BH} \sim 1-5\%$ can be enough to reproduce the observed distribution of $z > 6$ luminous quasars.

However, despite the local BH occupation fraction approaches unity, there are no strong constraints on the value of $f_{\rm BH}$ at high-z. In fact, the observed SMBHs number density at $z = 0$ could be reproduced even if $f_{\rm BH} \sim 0.1$ at $z \sim 5$, as a result of multiple mergers experienced by DM halos in the hierarchical formation history of local structures (Menou et al., 2001).

By averaging over 30 different merger trees, we predict that $f_{\rm BH}$ increases with z, finding an occupation fraction of $f_{\rm BH} = 0.95$, 0.84, 0.76, 0.70, at $z = 7, 8, 9, 10$, respectively[5]. Hence, more than 70% of the final SMBH progenitors host a BH in their centre at $z < 10$. Indeed, our simulated $f_{\rm BH}$ is higher than those predicted for average volumes of the Universe, as mentioned above, suggesting that the low occupation fraction is not the main limiting process for the X-ray detectability of BHs at $z > 6$.

Active fraction and obscuration. We report the *active* fraction $f_{\rm act}$ of SMBH progenitors, averaged over 30 simulations, in the labels of Figure 6.6. As it can be seen, $f_{\rm act}$ decreases with increasing redshift, from $f_{\rm act} = 37\%$ at $z = 7$ to 3% at $z = 10$. On average, the total active fraction (at all redshifts) is $f_{\rm act} = 1.17\%$. These values reflect the fact that BH growth is dominated by short, super-Eddington accreting episodes, particularly at high redshifts (P16), drastically reducing the fraction of active BHs, and thus the probability to observe them. A similar conclusion has been drawn by Page (2001), linking the observations of the local optical luminosity function of galaxies with the X-ray luminosity function

---

[5] Considering all the simulated galaxies in our sample, at all redshift, we find an occupation fraction of $f_{\rm BH} = 0.35$.

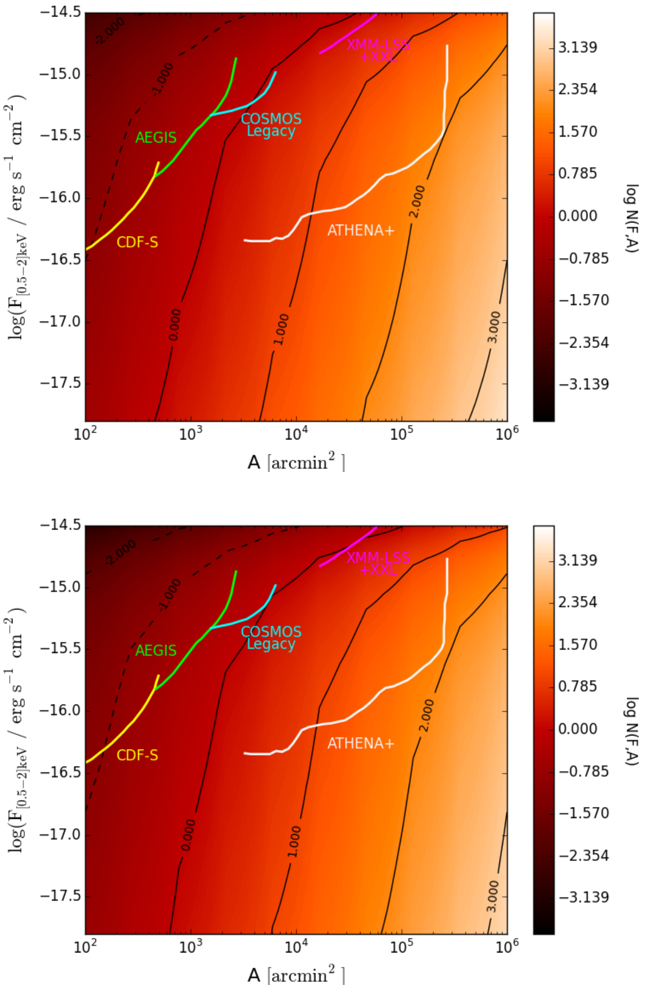

Figure 6.9. Number of progenitors potentially observable in a survey with sensitivity $F_{[0.5-2]\mathrm{keV}}$ and probing an area A for the *unabsorbed* (top panel) and *absorbed* (bottom panel) models. Black lines represent the values of $\log N(F, A) = -2, -1$ (dashed lines) and $\log N(F, A) = 0, 1, 2$ and 3 (solid lines). We also show the area/flux coverage achieved by current surveys and *ATHENA*+.

of Seyfert 1. They find an active BH occupation fraction of $f_{\rm act} \sim 1\%$. Comparable values have been also reported by Haggard et al. (2010) who combined *Chandra* and SDSS data up to $z \sim 0.7$, and Silverman et al. (2009) for the 10k catalogue of the zCOSMOS survey up to $z \sim 1$. While our predictions for $f_{\rm act}$ are consistent with the above studies, a larger fraction of active BHs is to be expected in models where SMBH growth at $z > 6$ is Eddington-limited ($\sim 40-50\%$ between $z \sim 7-10$, Valiante et al. 2016).

Figure 6.7 shows the total number of active progenitors as a function of flux in the *Chandra* soft (0.5-2 keV) and hard (2-8 keV) bands. We also distinguish super- (sub-) Eddington accreting BHs. As a reference, we report the flux limits of *Chandra* Deep Field South 4 Ms, $\rm F_{CDF-S} = 9.1 \times 10^{-18}\, erg\, s^{-1}\, cm^{-2}$ (dotted line, Xue et al. 2011) and *Chandra* Deep Field North (CDF-N) 2 Ms, $\rm F_{CDF-N} = 2.5 \times 10^{-17}\, erg\, s^{-1}\, cm^{-2}$ (dot-dashed line, Alexander et al. 2003), showing for each panel and each band the average number N of active BHs with a flux larger than the limit of the CDF-S 4 Ms. In the upper panel we show the *unabsorbed* model and the difference between the soft and hard X-ray band reflects the intrinsic SED. Moreover, since the flux limit of *Chandra* is deeper in the soft band, this energy range is to be preferred for the detectability of high-z progenitors.

The effect of an isotropic absorption on the flux is shown in the bottom panel of Figure 6.7. It does not appear to be as severe as it could be inferred from the large $N_{\rm H}$ shown in Figure 6.5. In fact, the soft (hard) *Chandra* bands at $z = 7, 8, 9, 10$ sample the rest frame energy bands $[4, 16]$keV, $[4.5, 18]$keV, $[5, 20]$keV, $[5.5, 22]$keV ($[16, 64]$keV, $[18, 72]$keV, $[20, 80]$keV, $[22, 88]$keV), respectively. As discussed in Section 6.1.2, in the range $[0.2-100]$keV, the harder is the photon energy, the lower is the photoelectric absorption. As a result, the average number N of detectable BHs in the *absorbed* model is close to that of *unabsorbed* model at redshift $z \sim 7-8$, while it becomes much lower at larger z, reaching N = 0 in the hard band at $z = 10$. This is a consequence of the larger fractions of Compton-thick BHs $f_{\rm CT}$ and, more generally, of the larger column densities. As already discussed, higher values of $N_{\rm H}$ correspond to super-Eddington accreting BHs. As a result, the shift towards lower fluxes in the *absorbed* model mainly affects super-Eddington accreting BHs.

In the left panel of Fig. 6.8 we show the cumulative number of BHs per unit area in the *unabsorbed* (solid line) and *absorbed* (dashed line) models with a flux $> F$ in the soft X-ray band. We have assumed here an area of $\hat{\rm A} = 0.03\,{\rm deg}^2$ and show the flux limits of

CDF-S 4 Ms and CDF-N 2 Ms as reference values[6].

For comparison, we report the number of AGN candidates selected with the same effective area coverage ($A_{obs} \sim$ Â) by Giallongo et al. (2015) with a flux threshold of $F_{\hat{X}} = 1.5 \times 10^{-17} \mathrm{erg\,s^{-1}\,cm^{-2}}$ (red circle). We also include the upper limit $N < 1$ resulted from the analysis by Weigel et al. (2015) of the CDF-S.

In the *unabsorbed* (*absorbed*) model we find $N(> F_{CDF-S}) = 0.15$ (0.12) and $N(> F_{\hat{X}}) = 0.13$ (0.1). The effect of absorption decreases the number N, also by a factor 2 for lower flux limits (< -17), but it is not the main limiting factor preventing the observations of BH progenitors. In fact, we find that $N < 1$ also in the *unabsorbed* model, for both F_{CDF-S} and $F_{\hat{X}}$. Our result is consistent with the non-detection reported by Weigel et al. (2015) and suggests that if the AGN candidates reported by Giallongo et al. (2015) are at $z > 6$, they are likely not SMBH progenitors of $z \sim 6$ quasars. If we rescale linearly with f_{act} the relation in Figure 6.8, for $f_{act} = 1$ we would find an average number of observable active progenitors of $N(> F_{CDF-S}) \sim 13$ (10) and $N(> F_{\hat{X}}) \sim 11$ (9). Thus, an active fraction of $f_{act} < 10\%$ is required in order to obtain a number of observed objects $N \lesssim 1$.

Interesting constraints on the activity of an early BH population have recently come from the measurement of the cross correlation signal between the fluctuations of the source-subtracted cosmic infrared background (CIB) maps at 3.6 and 4.5 micron on angular scales $> 20''$ and the unresolved CXB at [0.5 - 2] keV by Cappelluti et al. (2013). The authors argue that the cross-power is of extragalactic origin, although it is not possible to determine if the signal is produced by a single population of sources (accreting BHs) or by different populations in the same area. Indeed, theoretical models show that highly obscured accreting black holes with mass $[10^4 - 10^6]\, M_\odot$ at $z > 13$ provide a natural explanation for the observed signal (Yue et al., 2013, 2014), requiring a number density of active BHs of $[2.7 - 4] \times 10^{-5}\, M_\odot\,\mathrm{Mpc}^{-3}$ at $z \sim 13$ (Yue et al., 2016). While a detailed calculation of the cross-correlation between CXB and CIB is beyond the scope of the present analysis, in the right panel of Fig. 6.8 we compare the CXB in the soft band predicted by our models with the upper limit of $3 \times 10^{-13}/(1+z)\,\mathrm{erg\,cm^{-2}\,s^{-1}\,deg^{-2}}$ placed by (Cappelluti et al., 2012) on the contribution of early black holes at $z > 7.5$ under the assumption that they produce

---

[6] We assume BH progenitors to be distributed within a cube of 1 Gpc^3, corresponding to an angular size of $A_{box} \sim 390 \times 390\,\mathrm{arcmin}^2$ at $z \sim 7$ and $\sim 350 \times 350\,\mathrm{arcmin}^2$ at $z \sim 10$.

the observed large scale CIB excess fluctuations (Kashlinsky et al., 2012). For comparison, we also show the measured CXB in the soft band reported by Lehmer et al. (2012) from the analysis of the 4Ms CDF-S. The predictions for the absorbed and unabsorbed models are more than a factor 10 below the upper limit by Cappelluti et al. (2012), showing that the cross-correlation signal can not be reproduced by accreting SMBHs progenitors only.

Best observational strategy. In order to understand which survey maximizes the probability to observe faint progenitors of $z \sim 6$ quasars, we define the number of BHs expected to be observed in a survey with sensitivity F and probing an area A of the sky:

$$N(F, A) = N(> F) \frac{A}{A_{\rm box}}, \tag{6.12}$$

where $N(> F)$ is the number of progenitors with flux $\geq F$.

In Figures 6.9 we show $N(F, A)$ for the *unabsorbed* (top panel) and *absorbed* (bottom panel) models, in the *observed* soft band. We report the contours corresponding to $N(F, A) = 10^{-2}, 10^{-1}$ (black dashed lines) and $N(F, A) = 1, 10, 10^2$ and 10^3 (black solid lines). For fluxes $F_{[0.5-2]\rm keV} \gtrsim 10^{-14}\,\rm erg\,s^{-1}\,cm^{-2}$, we find $N(F, A) \lesssim 1$ for every possible area coverage. We also show the sensitivity curves in the soft band of current surveys: CDF-S in yellow, *AEGIS* in green (Laird et al., 2009), *COSMOS Legacy* in cyan (Civano et al., 2016), XMM-LSS (Gandhi et al., 2006) + XXL (Pierre et al., 2016) in magenta. In white we show the predicted curve for *ATHENA*+ with 5” PSF and multi-tiered survey strategy, for a total observing time of 25 Ms (for details see Aird et al., 2013), and note that a survey can observe the integrated number $N(F, A)$ over its curve. The difference between the *unabsorbed* and the *absorbed* models is almost negligible, reaching at most a factor of 2. In fact, the *observed* soft-band corresponds, for high-z progenitors, to rest-frame energies hard enough to be almost unobscured, despite the large $N_{\rm H}$ and Compton-thick fraction (see Section 6.3). The position occupied by the curve of the most sensitive survey performed nowadays, CDF-S, exploring a solid angle of $465\,\rm arcmin^2$, is observationally disadvantaged with respect to the *COSMOS Legacy*, less sensitive but covering a wider region of the sky. This survey, in fact, should observe at least one progenitor. Similarly, XMM-LSS+XXL, despite having an even lower sensitivity, represent the current survey that maximizes the probability of SMBH progenitors detections. A huge improvement in the detection will be obtained with *ATHENA*+. According to our simulations, for a total observing time of 25 Ms more than 100 SMBH progenitors will be detected.

The progenitors of $M_{\rm BH} \sim 10^9$ high-z quasars are luminous enough to be detected in the X-ray soft band of current surveys. The real limit to their observability is that these objects are extremely rare, as a result of their low *active* fraction. None of the surveys performed so far probes a region of the sky large enough for their detection to be meaningful, limiting the potentially observable systems to a few.

The above conclusion applies to a scenario where SMBH at z = 6 grow by short super-Eddington accretion episodes onto $100 M_\odot$ BH seeds formed at $z > 20$ as remnants of Pop III stars. In Valiante et al. (2016) we have investigated the alternative scenario where BH growth is Eddington limited and starts from BH seeds whose properties are set by their birth environment. According to this scenario, the formation of a few heavy seeds with mass $\sim 10^5 M_\odot$ (between 3 and 30 in our reference model) enables the Eddington-limited growth of SMBHs at $z > 6$.

6.4 Conclusions

The main aim of the work presented in this Chapter, was to interpret the lack of detections of $z \gtrsim 6$ AGNs in the X-ray band. Three are the most likely possibilities: *i*) large gas obscuration, *ii*) low BH occupation fraction or *iii*) low *active* fraction.

We developed a model for the emission of accreting BHs, taking into account the super-critical accretion process, which can be very common in high-z, gas-rich systems. We compute the spectrum of active BHs simulated by P16 with an improved version of the cosmological semi-analytical code GAMETE/SuperQSOdust. In P16, we have investigated the importance of super-Eddington accretion in the early growth of $z \sim 6$ SMBHs. Here we model the emission spectrum of all the simulated SMBH progenitors at $z > 6$ and study their observability with current and future surveys. Hence the sample of BHs that we have investigated does not necessarily represent a fair sample of *all* BHs at $z > 6$ but only the sub-sample of those which contribute to the early build-up of the observed number of $z \sim 6$ quasars with mass $M_{\rm BH} \gtrsim 10^9\, M_\odot$.

We find that:

- the mean occupation fraction, averaged over 30 independent merger tree realizations and over the whole evolution, is $f_{\rm BH} = 35\%$. It increases with z, being $f_{\rm BH} = 0.95$, 0.84, 0.76, 0.70, at $z = 7, 8, 9, 10$, suggesting that the occupation fraction is not the main limitation for the observability of $z > 6$ BHs.

- We find a mean Compton thick fraction of $f_{\rm CT} \sim 45\%$. Absorption mostly affect the super-Eddington accreting BHs at $z > 10$, where the surrounding gas reaches large values of $N_{\rm H}$;
- Despite the large column densities, absorption does not significantly affect the *observed* soft X-ray fluxes. In fact, at $z > 6$ the observed soft X-ray band samples the rest-frame hard energy band, where obscuration is less important. The absorption can reduce the number of observed progenitors at most by a factor 2;
- The main limiting factor to the observation of faint progenitors is a very low *active* fraction, the mean value of which is $f_{\rm act} = 1.17\%$. This is due to short, super-Eddington accreting episodes, particularly at high z. In fact, $f_{\rm act} = 3\%$ at $z = 10$ and grows to $f_{\rm act} = 37\%$ at $z = 7$ due to longer sub-Eddington accretion events.

  As a result, surveys with larger fields at shallower sensitivities maximize the probability of detection. Our simulations suggest that the probability of detecting at least 1 SMBH progenitor at $z > 6$ is larger in the *Cosmos Legacy* surveys than in the CDF-S.

Better selection strategies of SMBH progenitors at $z > 6$ will be possible using future multi-wavelength searches. Large area surveys in the X-ray band (e.g. *ATHENA*+) complemented with deep, high-sensitivity opt/IR observations (e.g. *James Webb Space Telescope*) and radio detection may provide a powerful tool to study faint progenitors of $z \sim 6$ SMBHs.

Part III

Black holes in the local Universe

Chapter 7

From the first black holes to the Local Universe

There are many evidences that almost all the galaxies in the Local Universe (LU) are hosting a massive (or supermassive) BH in their centres, and to date more than ~ 90 local MBH masses have been measured through direct methods (Kormendy and Ho, 2013). A representative picture is drawn in Figure 7.1, where we show a sample of galaxies at $z < 0.055$ hosting central BHs as provided by Reines and Volonteri (2015), with BH masses spanning several orders of magnitudes, from $5 \times 10^4\,M_\odot$ (RGG 118, Reines et al. 2013; Baldassare et al. 2015) to $\sim 2 \times 10^{10}\,M_\odot$ (NGC 4889, McConnell et al. 2012). This wide range is much larger than the one obtained for the $z \gtrsim 6$ sample detected so far. In the latter case, we are able to identify only the most massive SMBHs, with masses $M > 10^8\,M_\odot$ (see Figure 3.1) due to the large distances, and these objects are supposed to be only the tip of the iceberg of the entire nuclear BH population at that time. This limitation hampers our ability to put direct constraints on the nature of the first BH seeds, but can be partly overcome by searching for the smallest nuclear BHs, with masses $M_{\rm BH} \lesssim 10^5 - 10^6\,M_\odot$, in local dwarf galaxies. In fact, dwarf galaxies and their central BHs are supposed to experience a limited growth during cosmic time, due to quiet evolutionary history with a small number of accretion and merger events. The BH population in low-mass galaxies, thus, should not differ much from its initial distribution, suggesting that these nuclear BHs provide important constraints on different BH seeds formation models (Volonteri et al., 2008; Volonteri and Natarajan, 2009; Bellovary et al., 2011; Reines et al., 2013; Reines and Volonteri, 2015).

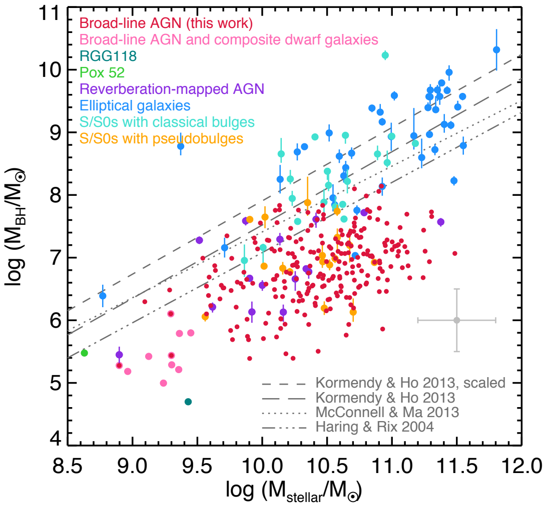

Figure 7.1. Black hole mass as a function of the total stellar mass in local galaxies, with an error showed with the grey errorbar. Red points represent 224 broad-line AGN from which virial BH masses are inferred from the single-epoch virial mass estimator (Reines and Volonteri, 2015), pink points show 10 broad-line AGN and composite dwarf galaxies (Reines et al., 2013). The two green points are for two individual objects: the dwarf galaxy RGG 118 (dark green, Reines et al. 2013; Baldassare et al. 2015 and Pox 52 (light green, Thornton et al. 2008. The other set of points represent 15 reverberation-mapped AGN (purple, Bentz and Katz 2015), dynamical BH mass measurements taken from Kormendy and Ho (2013) for elliptical galaxies (blue), S/S0 galaxies with classical bulges (turquoise) and S/S0 galaxies with pseudo-bulges (orange). Grey lines represent different BH-bulge mass scaling relations based on dynamical BH mass measurements. Adapted from Reines and Volonteri (2015).

A fundamental diagnostic for this study is the local BH occupation fraction (BHOF), introduced in Chapter 6, which represents the fraction of galaxies hosting a central BH, regardless of whether these are active or not. Theoretical models predict that different seeding mechanisms should produce different BHOF. Volonteri et al. (2008) and van Wassenhove et al. (2010) show that a high BHOF would be better explained by the Pop III remnants scenario for seed formation, since lower BHOF is expected if seeds are formed by direct collapse BHs. In addition, these authors suggest that the distribution of dwarf galaxies on the $M_{\mathrm{BH}} - \sigma$ relation is also important: while there are no relevant differences between the two seeding mechanisms at high velocity dispersion, for lower values of σ and BH masses, model predictions are distinct.

Unfortunately, constraints on the local BHOF in low-mass galaxies are based on X-ray observations, which are not strictly related to the BHOF but rather to a sub-sample of the entire BH population, i.e. the active ones. Therefore X-ray detections can put only a lower limit on the BHOF. Furthermore, the implications obtained so far from the observations in this band are still incomplete (Miller et al., 2015).

Our aim is to revisit this problem by comparing different BH seeding scenarios with their consequences at $z = 0$, focusing in particular on the expected properties of BHs in dwarf systems, with stellar masses down to $M_\star = 10^2\, M_\odot$. In the preliminary study that we present in this Chapter, we have used the output of a simulation of a well resolved Local Group (LG) with a Milky-Way like halo at its center. The simulation has been done with the new galaxy formation pipeline GAMESH (Graziani et al., 2015, 2017) that allows to reconstruct a MW-like galaxy and the LG structure, predicting the properties of their progenitors from $z \sim 20$ to $z = 0$.

In Section 7.1, we introduce the properties of dwarf galaxies in the LU, with a specific discussion on the low-mass BH population. GAMESH, the cosmological pipeline reproducing a LG-like structure, is described in Section 7.2. In Section 7.3 we review the main assumptions of our post-processing analysis. Preliminary results are presented in Section 7.4.

7.1 Local BH seeds relics in dwarf galaxies

The dwarf galaxies of the LG provide a statistically useful sample, since they are the most numerous galaxies of the present-day Universe (Marzke and da Costa, 1997). Due to their faint emission, however, their characterization may be challenging. In addition, observing low-mass BHs in dwarves is even more difficult. In fact, for these objects it is not expected a very active merger history, which could produce efficient BH growth. The result is that dwarf galaxies host low-mass BHs, with a weaker gravitational force and a subsequent weak effect on the motion of gas and stars around them.

7.1.1 Measuring BH masses

The most reliable way of estimating the nuclear BH mass is a direct measurement of the stellar and gas motion around it. A quantity related to the dynamical searches is the rotational velocity of the stars, which depends on the mass enclosed into their orbit, and the presence of a central BH will lead to a higher peak in the velocity curve. A similar approach can be adopted for estimating the central BH mass by using the gas instead of the stars. However, this technique is at the limits of what can be done with current instrumentation. For this kind of observations, in fact, it would be necessary to resolve the BH sphere of influence, defined as $r_{si} = GM_{\rm BH}/\sigma^2$. For $M_{\rm BH} = 10^5$ and $\sigma = 15$ km/s, this radius is only 2pc. As a result, searches with current facilities are restricted to galaxies within ~ 1 Mpc. Future large ground-based telescope, such as the Extremely Large Telescope (ELT), will increase the volume accessible to dynamical measurements (Reines and Comastri, 2016). In the meantime, observations will be mainly restricted to active BHs. In fact, BH measurements can be done through features directly produced by the accretion process, and many local dwarf active galaxies are optically-selected through narrow and broad emission lines (Greene and Ho, 2005, 2007; Barth et al., 2008; Reines et al., 2013). The BH mass is generally estimated through the virial method, for which $M_{\rm BH} = fv^2R_{\rm BLR}/G$, where v is the BLR velocity dispersion and f is a geometrical factor whose value depends on the shape of the BLR, whose radius is $R_{\rm BLR}$. These observational samples, however, can be biased toward the most powerful accreting BHs, those with a luminosity $L_{\rm bol} \sim L_{\rm Edd}$. In fact, local dwarf galaxies are generally dust and gas rich objects (Greene, 2012), and the nuclear emission, which already tends to be weak, can be affected by obscuration. On the contrary, X-ray observations can identify the fainter BHs, reaching sensitivity limits of $L_X \sim 2\times10^{38}$ erg/s (Miller et al., 2015) detecting sources down to $L_{\rm bol}/L_{\rm Edd} \lesssim 10^{-5}$. Since dwarves are generally characterized by ongoing star formation (Greene, 2012), at these low luminosities the contamination from X-ray binary emission could be important. For this reason, X-ray observations should be combined with sensitive, high-resolution radio ones (Gallo et al., 2008, 2010; Miller et al., 2012; Reines et al., 2014).

7.1.2 The local low-mass BH population

As already discussed in Section 7.1.1, the determination of BH masses through dynamical measurements is very difficult to achieve. However, few estimates are provided for nearby dwarf galaxies. NGC 4395, a dwarf Sd galaxy harbouring one of the nearest ($d \sim 4.4$ Mpc) known type 1 Seyfert nuclei, hosts a MBH with rapid X-ray variability (Shih et al., 2003) and the presence of radio jets (Wrobel and Ho, 2006). For this optically-selected AGN, studies of the kinematics of the molecular hydrogen have allowed to estimate its mass, $M_{\rm BH} \sim 4 \times 10^5\, M_{\odot}$ (den Brok et al., 2015). In the closer ($d \sim 3$ Mpc) S0 dwarf NCG 404, a stellar dynamical study showed the presence of a central BH mass of $M_{\rm BH} \sim 4.5 \times 10^5\, M_{\odot}$ (Seth et al., 2010).

Thanks to dynamical methods, we have also upper limits for a set of nearby objects, such as for the two spheroidal dwarves, Ursa Minor ($M_{\rm BH} \leq (2-3) \times 10^4\, M_{\odot}$, Lora et al. 2009) and Fornax ($M_{\rm BH} \leq 2.3 \times 10^4\, M_{\odot}$, Jardel and Gebhardt 2012), both MW satellites. A BH mass upper limit of $M_{\rm BH} = 2.2 \times 10^4\, M_{\odot}$ has been put on the nuclear BH of the elliptical dwarf galaxy, NGC 205, a M31 satellite (Valluri et al., 2005).

Although not a dwarf, it is interesting to note that M33, the third brightest galaxy of the LG and the closest to our MW ($M_{\rm BH,MW} = 4 \times 10^6\, M_{\odot}$, Boehle et al. 2016) after M31 ($M_{\rm BH,M31} = (1-2) \times 10^8\, M_{\odot}$ Bender et al. 2005) not show any evidence of the presence of a nuclear BH. Current best fit of the light profile for resolved stellar kinematic observations are able to put only an upper limit of $M_{\rm BH} < 1500\, M_{\odot}$ (Gebhardt et al., 2001) and $M_{\rm BH} < 3000\, M_{\odot}$ (Merritt et al., 2001).

The list of low-mass BHs in low-mass galaxies gets longer once we include also optically-selected AGNs. Barth et al. (2004) show that the dwarf Seyfert 1 galaxy Pox 52 host a MBH with a mass estimated from the broad H_{β} emission line of $M_{\rm BH} \sim 10^5\, M_{\odot}$. Together with NGC 4395, Pox 52 has been for long time the only MBH observed in dwarf galaxies. Systematic searches of low-mass BHs have been carried out with the advent of SDSS: a sample of ~ 200 broad-line AGN with $M_{\rm BH} \lesssim 3 \times 10^6\, M_{\odot}$ have been discovered by Greene and Ho (2004, 2007), while Barth et al. (2008) selected 29 Seyfert 2 galaxies with low luminosities, corresponding to a magnitude threshold of $M_g = -20$. However, those two searches are not probing the dwarf regime, since the stellar masses are much larger than the value of $M_{\star} \sim 10^9\, M_{\odot}$ typically found in dwarves such as Pox 52 and NGC 4395.

The first systematic search for MBHs in dwarf galaxies has been developed by Reines et al. (2013) by selecting 136 galaxies with a stellar content $< 3 \times 10^9\, M_\odot$ showing nuclear activity. However, only 10 of these systems showed a broad H_α emission, allowing a virial BH mass estimation of $10^5 - 10^6\, M_\odot$. The mass range has been pushed to lower values by Moran et al. (2014) through the detection of 28 AGN at $d \leq 80$ Mpc in low-mass, low-luminosity dwarf galaxies. These authors mostly find narrow-line objects, with a minimum BH mass of $\sim 10^3 - 10^4\, M_\odot$.

The current record-holder for the least-massive BH observed in the centre of a local galaxy is the one settled in the potential well of RGG 118, a dwarf at distance $d \sim 100$ Mpc. The presence of a $50000\, M_\odot$ MBH (Baldassare et al., 2015), estimated through a broad H_α emission, has also been confirmed by a Chandra X-ray detection.

Information on the BH seeding mechanisms may be inferred by extending the sample presented in Figure 7.1 down to lower stellar and BH masses. In fact, the slope of the low-mass end in the $M_{\mathrm{BH}} - M_\star$ plane can be used as a diagnostic: if the relation shows a flat trend, with a $M_{\mathrm{BH}} \sim 10^4 - 10^5\, M_\odot$ independently of the stellar mass, this may be interpreted as a trace of DCBH formation channel. On the contrary, Pop III BH remnants would show no flattening, because the observational limits would not allow to probe the $M_{\mathrm{BH}} \sim 100\, M_\odot$ asymptotic value of the relation (Volonteri and Natarajan, 2009; van Wassenhove et al., 2010). As we will discuss in Section 7.4, our high-resolution simulation is able to probe $z = 0$ galaxies down to $M_\star \sim 10^2\, M_\odot$. This allows us to make predictions on the low-mass end of the $M_{\mathrm{BH}} - M_\star$ relation.

7.2 Building up the Local Group: GAMESH

GAMESH is a new pipeline integrating the radiative transfer (RT) code CRASH (Graziani et al., 2013) with the version of the semi-analytic model GAMETE described in de Bennassuti et al. (2014, 2017). These two codes run on the top of an N-body simulation reproducing a LG-like structure (Kawata and Gibson, 2003). An illustration of the operative scheme, for a fixed time-step, is shown in Figure 7.2, where the transparent elements are planned to be included in the next future.

Along the time evolution, the feedback between star formation and RT is managed by

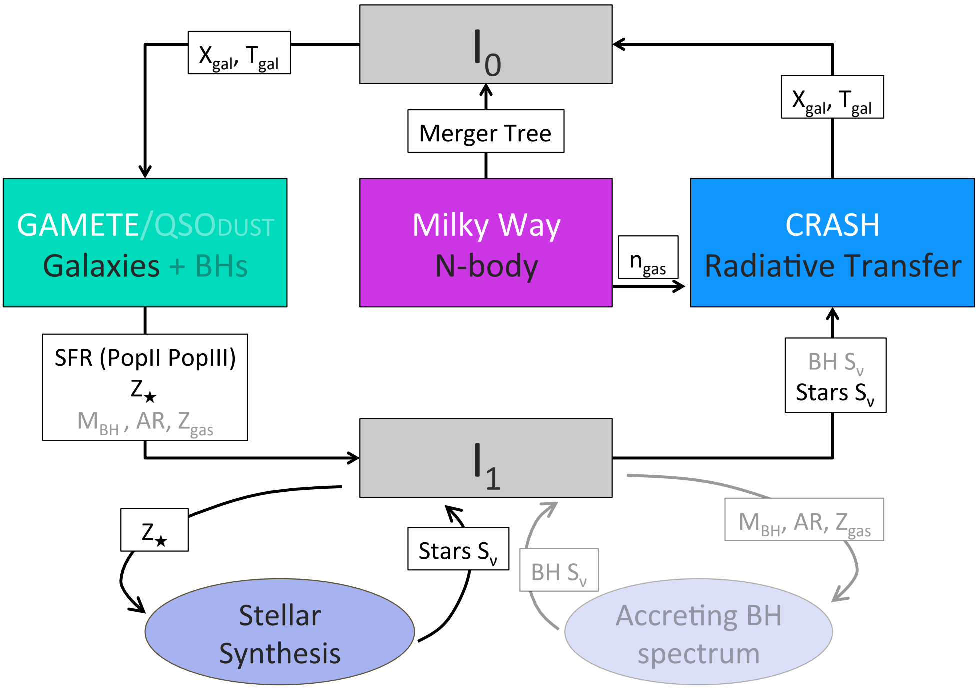

Figure 7.2. Sketch representing the operational scheme of GAMESH (Graziani et al., 2015, 2017). The transparent part of the diagram, regarding the radiative emission of BHs, is still to be included, and the running version of GAMETE is without BHs (see text).

two software modules called interactors: I_0 transforms the SFR predicted by GAMETE into a list of ionizing sources for CRASH, and I_1 uses the gas ionization and temperature determined by the RT to establish a SF in GAMETE.

The model reconstructs the formation and evolution of the MW-like halo and its neighbour through a series of snapshots provided by the N-body simulation at redshift z_i, using the physical condition obtained at z_i as initial conditions for the successive computation at z_{i+1}. Focusing on a fixed redshift z_i, the initial conditions are provided by the N-body simulation, which assigns z_i to all the components, sets-up the N-body merger tree into I_1 and the gas number density $n_{\rm gas}$ in the grid used by CRASH to map the physical domain. Once the initial conditions are set up, I_1 starts the simulation by creating a list of galaxies found in the merger tree. Each galaxy is characterized by the ionization fraction $x_{\rm gas}$ and the temperature $T_{\rm gal}$ found in the cell of the grid containing the galaxy center of mass. This list is then processed by GAMETE to establish which galaxy can form stars, self-consistently with the metallicity, temperature and ionization fraction of the accreting gas. The output of GAMETE, which is the subsample of star forming galaxies together with their SFR, stellar metallicity and population type, is converted by I_0 into a list of CRASH sources. It is done through a stellar synthesis database present in I_0 which evaluates the galaxy positions on the grid, their spectrum integrated ionization rate $\dot{N}_\gamma$ and the spectral shape S_ν. The RT code then propagate photons for a simulation duration corresponding to the Hubble time separating two snapshots, and it obtains the gas ionization $x_{\rm gas}$ and temperature $T_{\rm gas}$ at redshift z_i. These quantities are finally used for the subsequent redshift z_{i+1}, by repeating the same algorithm.

The preliminary results presented in this Chapter have been obtained without enabling the CRASH side of the pipeline.

7.2.1 N-body

To study the formation and evolution of a volume resembling the LG with a MW-like halo at its center, we adopt a N-body simulation carried with GDC+ (Kawata and Gibson, 2003), with periodic-boundary conditions. The simulation evolves for 155 snapshots, with a time-step of $\Delta t_{\rm res} = 15$ Myr in the redshift range $z = 20 - 10$, and with longer time-steps of $\Delta t_{\rm res} = 100$ at $z < 10$. Initial conditions are created with MUSIC (Hahn and Abel, 2011) with Planck cosmology (Planck Collaboration et al., 2014), and have not been selected in order to reproduce the observed propertied of the LG, but rather to simulate a candidate MW-like halo at high-resolution. Once identified it, zoom-in initial conditions are created. The total number of particles is 62421192 (55012200 in the inner high-resolution region) with the highest-resolved mass of $3.4 \times 10^5\ M_\odot$, while the virial mass of the simulated MW-halo is $1.7 \times 10^{12}\ M_\odot$. Hereafter, we will refer to the innermost 4 cMpc side volume centred on the MW-like halo as the LG, and to the 8cMpc box surrounding it as the Local Universe (LU).

In order to identify virialized structures, we use a standard friend-of-friend (FoF) algorithm with a linking parameter $b = 0.2$ and a threshold number of particles of 100. We have built the merger tree for each halo found at redshift $z = 0$, following its particles back to initial redshift. Once reconstructed the merger tree, it is possible to follow all the dynamical

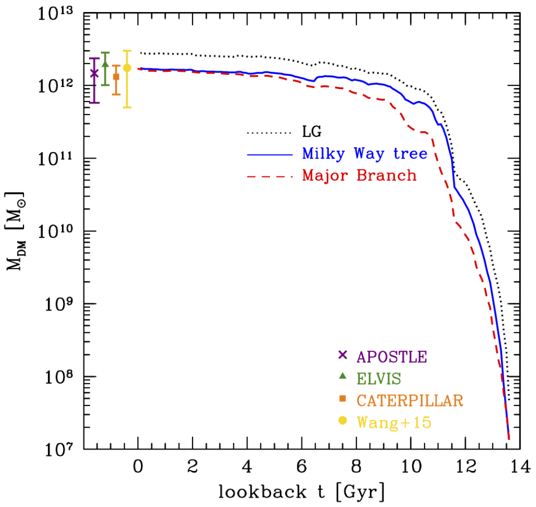

Figure 7.3. Build up history of the MW-like halo and the LG in the N-Body simulation. We show the total collapsed DM mass enclosed in the LG volume (the dotted black line) and the total mass of all the MW progenitors (solid blue line). The dashed red line represents the MW merger tree obtained following only the major branch. For reference, the mass of MW-sized halos taken from different DM simulations or independent methods is also shown. Adapted from Graziani et al. (2017).

processes involved in the evolution of a DM halo: accretion, mergers, tidal stripping and disruption.

A DM halo can grow through accretion of DM particles by acquiring particles from the IGM. In combination to this, the halo can evolve through merger events and tidal stripping, when at z_{i+1} results as a combination of two or many halos (referred as ancestors) at z_i . The categorization between merger and tidal interaction is based on the fraction of the mass transferred: if a halo transfers more than 20% of its mass to the descendant, the event is referred as merger, otherwise it is considered as mass accreted by tidal interaction.

Furthermore, a DM halo can also miss part of its mass by tidal interaction with nearby halos, and we refer to this event as halo stripping. For the same process, it can be even destructed, losing its identity at the next snapshot and returning its particles to the IGM.

The assembly history of the MW halo is shown in Figure 7.3 as a function of time (Graziani et al., 2017). The blue solid line accounts for the entire population of halos

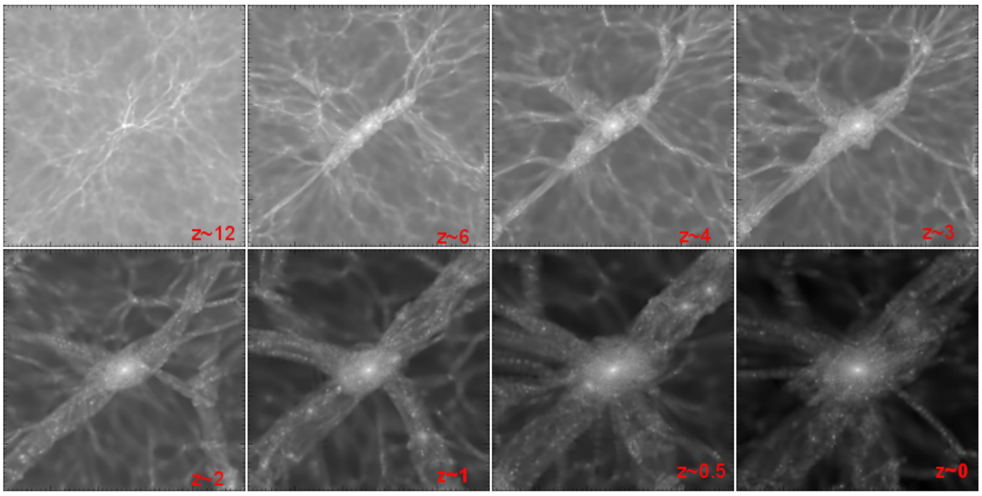

Figure 7.4. Slice cuts of the LG evolution at various redshifts with a spatial resolution of $r \sim 7.8$ kpc. The panels show the gas number density distribution obtained by scaling the DM mass in each cell of the spatial grid by the universal baryon fraction. Adapted from Graziani et al. (2017).

which will collapse in the MW at $z = 0$, while the red dotted line is the result obtained considering only the most massive halo. As visible, following the MW formation along the major branch is incorrect, and the difference is greater for higher z, where the MW mass is distributed in a larger number of progenitors. For $z \lesssim 0.3$, instead, the two curves converge to the same value.

It is also possible to visualize the formation of our simulated Galaxy in Figure 7.4, which represents the gas number density for a series of slice cuts illustrating, for different z, the LG and the central MW-like galaxy. Here the gas is only rescaled with the DM mass, assuming the universal baryon fraction. We can see that below $z \sim 2$ many structures start to collapse, also entering in the LG from the larger scale. While at high-z the evolution proceeds by assembling collapsed structures along filaments, for $z \lesssim 3$ the central halo dynamically dominates the LG evolution, attracting material from larger scales. This is an indication of multi-scale, multi-environment processes: galaxies grow by assembling material formed in different environments

7.2.2 GAMETE

In this Section, we will briefly introduce the main features of the basic version of GAMETE present in GAMESH. The natural improvement to this preliminary work will be accounting for BH formation and evolution by including the full version of GAMETE/SuperQSODust in GAMESH. To date, GAMETE assumes (Graziani et al., 2017):

- A star formation rate in Lyα-cooling halos for each time step SFR $= \epsilon_\star M_{\rm gas}/t_{\rm dyn}$, where $\epsilon_\star$ is the SF efficiency, $M_{\rm gas}$ is the total gas mass, and $t_{\rm dyn}$ is the dynamical time-scale of the DM halo.

- The SF efficiency in minihalos is assumed to be $\epsilon_{\rm mini} = a(T_{\rm vir})\epsilon_\star$, where $a(T_{\rm vir} = 2 \times [1 + (T_{\rm vir}/(2 \times 10^4{\rm K}))^{-3}]^{-1}$ (Salvadori and Ferrara, 2009, 2012);

- After Reionization, that is assumed to occur instantaneously at $z_{\rm reio} = 6$, SF can occur only in galaxies with $T_{\rm vir} > 2 \times 10^4$K. This is done in order to consider photo-heating and photo-evaporation;

- Stellar evolution is followed with the Instantaneous Recycling Approximation (IRA). For gas metallicity $Z < 10^{-4}\,{\rm Z}_\odot$, Pop III stars are assumed to form with a constant mass of 200 $M_\odot$, otherwise Pop II stars form with a Larson IMF (Larson, 1998) with a characteristic mass of $m_{\rm ch} = 0.35\,M_\odot$;

- The SN-driven mass outflow rate is $\dot{M}_{ej} = 2\epsilon_{\rm w}\dot{E}_{\rm SN}/v_{\rm c}^2$, where $\epsilon_{\rm w}$ is the wind efficiency, $v_{\rm c}$ the halo circular velocity and $\dot{E}_{\rm SN}$ is the energy rate released by SN explosions.

  The free parameters $\epsilon_{\rm w} = 0.0016$ and $\epsilon_\star = 0.09$ have been fixed in order to reproduce the MW and LG observed properties. In particular, the stellar, gas and metals masses of the simulated central halo at $z = 0$ are consistent with those of the MW (Bovy and Rix, 2013; Peeples et al., 2014; Kubryk et al., 2015), and the predicted SFR is in agreement with the value inferred from observations within the uncertainties (Smith et al., 1978; Diehl et al., 2006; Kubryk et al., 2015). Furthermore, the model predicts physical properties of the simulated MW progenitors compatible with observed scaling relations. For instance, GAMESH reproduces the SFR-$M_\star$ empirical fits for $z = [0 - 2.5]$ (Schreiber et al., 2015), and the observed mass-metallicity and

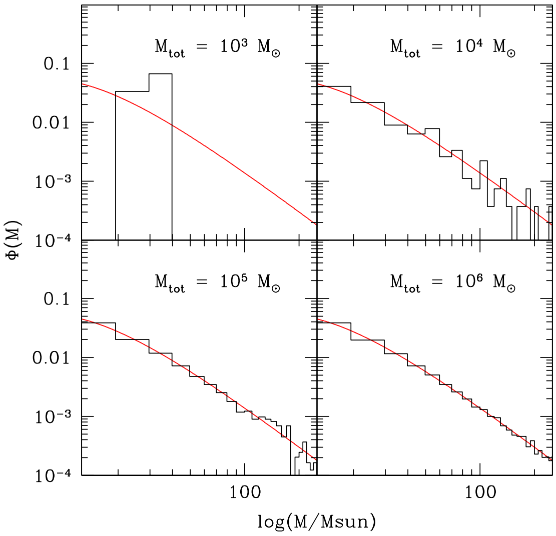

Figure 7.5. Comparison between the assumed Larson IMF (red lines) and the effective mass distribution resulting from the random sampling procedure (black histograms) for $M_{\rm tot}/M_\odot$ = 10^3, 10^4, 10^5, 10^6, as reported on each panel.

the fundamental plane of metallicity relations at $0 \leq z \leq 4$ (Mannucci et al., 2010; Hunt et al., 2012, 2016). For further details, we refer the readers to the original paper (Graziani et al., 2017)

7.3 The post-processed BH evolution

In this preliminary work, the inclusion of BHs has been done in post-processing. Moreover, once formed, we follow BH growth only through mergers, assuming no gas accretion. In this way, we are able to investigate the BHOF and the importance of BH-BH mergers for the formation of $z \sim 0$ BH population in the simulated LG.

Planting BH seeds

As already introduced in Chapter 4, Chapter 5 and Chapter 6, we assume BH seeds to form only as remnants of Pop III stars. In halos with subcritical gas metallicity ($Z < 10^4\,Z_\odot$), Pop III stars can form. In the post-processing analysis we assume the first generation of stars to form according to a Larson IMF with $m_{\rm ch} = 20\,M_\odot$ (see Equation 5.1). During each

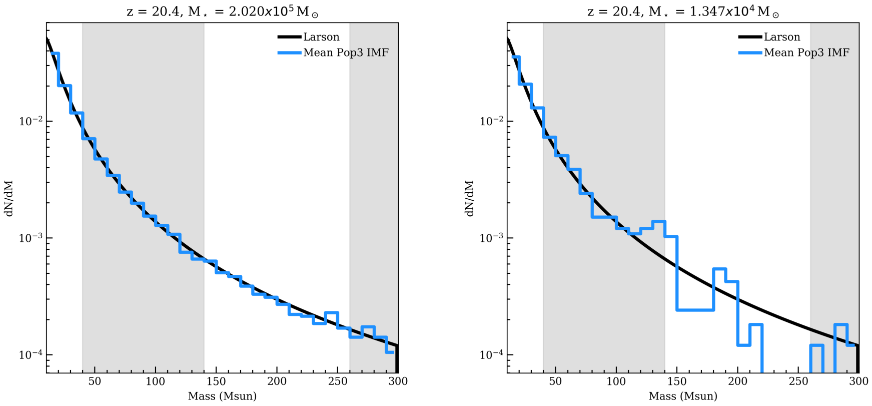

Figure 7.6. Pop III IMF obtained averaging over the galaxies present at $z = 20.4$. Left panel represents the sampled IMF as obtained assuming a SF episode lasting for the simulation time-step, i.e. $\Delta t_{\mathrm{res}} = 15$ Myr, while the right panels show the mass distribution for $\Delta t_{\mathrm{SF}} = 1$ Myr. Grey shaded regions indicate the mass ranges in which Pop III BH seeds form.

star formation episode, we stochastically sample the IMF with stars $M_\star = [10 - 300]\, M_\odot$ until we reach the total stellar mass formed. Figure 7.5 shows the mass distribution resulting from this procedure, respectively, when a mass of $10^3 - 10^6 M_\odot$ of stars is formed in a single Pop III burst. It is possible to see that there is a convergence between the theoretical and sampled IMF only when $M_{\mathrm{tot}} \gtrsim 10^6\, M_\odot$ (Valiante et al., 2016; de Bennassuti et al., 2017).

We then assume that stars with masses in the range $[40 - 140]\, M_\odot$ and $\leq 260\, M_\odot$ do not explode as SNe and directly collapse to BHs (Heger and Woosley, 2002). The most massive BH will be labelled as *nuclear*, and settled in the centre of the halo potential well. The rest of the population, referred as *satellite* BHs, are considered to be dislocated with respect to the galactic centre (Valiante et al., 2016).

Evolving the BH population through cosmic time

Once formed, we follow the evolution of the nuclear BHs and satellites separately.

We analyse, for each progenitor present at z_i, the interaction with each of its j-th ancestor at z_{i-1}. This depends on the merger history of the simulated LG, and in particular, given a halo, we distinguish between four possible connection between the j-th ancestor and its descendant:

Tidal interaction If the total mass transferred to the descendant, $f_{\rm transf}$, is less than 20 % the ancestor's mass, we assume that it is a tidal interaction. In this case, satellites and the nuclear BH are not transferred to the descendant.

Minor merger If the condition $f_{\rm transf} \geq 20$ % is satisfied for at least two progenitors, we classify the event as a merger. In this case, we must take into account the mass ratio $\mu_j = M_j/M_1$ between M_1, the most massive merging ancestor, and M_j, the mass of the j-th ancestor we are considering. Following Valiante et al. (2012, 2014); Pezzulli et al. (2016), we adopt a threshold of $\mu_{\rm thr} = 0.25$ to discriminate between major and minor mergers. If $\mu_j < \mu_{\rm thr}$, we classify the interaction as a minor merger. In this case, we assume that the two nuclear BHs do not merge and we transfer all the BHs of the ancestors to the satellite population of the j-th descendant.

Major merger If $\mu_j \geq \mu_{\rm thr}$, the interaction is classified as a major merger. In this case, the nuclear BHs are assumed to merge, forming a larger nuclear BH. In addition, the descendant inherits all the satellite BHs from its progenitors.

Quiescent evolution In this case, satellites and nuclear BHs are conserved between the two snapshots.

In summary, under the assumption that BHs do not accrete gas, when a galaxy evolves passively, both the central BH and the satellites do not undergo changes. When mergers occur, and the formation of a galaxy results from the interaction between different ancestors, we must consider the contribution of every single progenitor to its descendant. Hence, nuclear and satellite BHs at $z = 0$ will be the result of all these processes occurring along the merger history of all their ancestors.

We expect that our conclusions will be very sensitive to the assumed value of $\mu_{\rm thr}$. The value of $\mu_{\rm thr} = 0.25$ has been adopted in recent studies aimed at reproducing the properties of high-z SMBHs. A smaller threshold value of $\mu_{\rm thr} = 0.05$ has been used by Tanaka and Haiman (2009). Based on merger times inferred from numerical simulations (Boylan-Kolchin et al., 2008), they show that below this value the BH in the smaller halo never merges with the central BH of the most massive halo. However, these studies refer to BH-BH binary mergers at high redshift. Here, we are describing the build-up of nuclear BHs

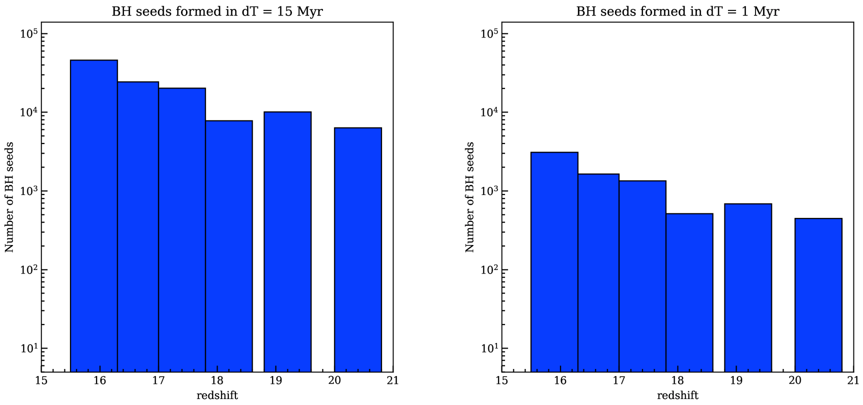

Figure 7.7. BH distribution at $z \gtrsim 16$ for $\Delta t_{\rm res}$ = 15 Myr (left panel) and $\Delta t_{\rm SF}$ = 1 Myr (right panel).

of spiral and dwarf galaxies in the LG, which are likely to have experienced a much more quite evolution. We will discuss the implications of the adopted $\mu_{\rm thr}$ in Section 7.5.

7.4 Preliminary results

In this Section, we explore the predictions, obtained with the post-processing procedure discussed above, for black hole seed formation and BH occupation fraction. The results that we will present refer to galaxies in the whole 8 cMpc simulation box, unless specified otherwise.

7.4.1 BH seeds formation

Starting from the SFR, the stellar mass is computed by GAMESH in the resolution time-step $\Delta t_{\rm res}$, i.e. $\Delta M_\star$ = SFR $\times \Delta t_{\rm res}$. However, simulations suggest that the birth of the first Pop III stars, and their explosions, inhibit subsequent star formation events (see Chapter 5 for a discussion). Since the lifetime of a massive Pop III star is only $\sim$ 1 Myr, we have tested also a case in which the duration of the star formation event is $\Delta t_{\rm SF}$ = 1 Myr, much smaller than the resolution time-step at high-z, $\Delta t_{\rm res} \sim$ 15 Myr. In Figure 7.6 we show the mass distribution of Pop III stars at z = 20.4, averaging over all the galaxies present at that time in the simulation ($N_{\rm gal}$ = 5), when the mass of stars formed in individual Pop III bursts is computed according to $\Delta t_{\rm res}$ (left panel) or $\Delta t_{\rm SF}$ (right panel). When the SF is interrupted

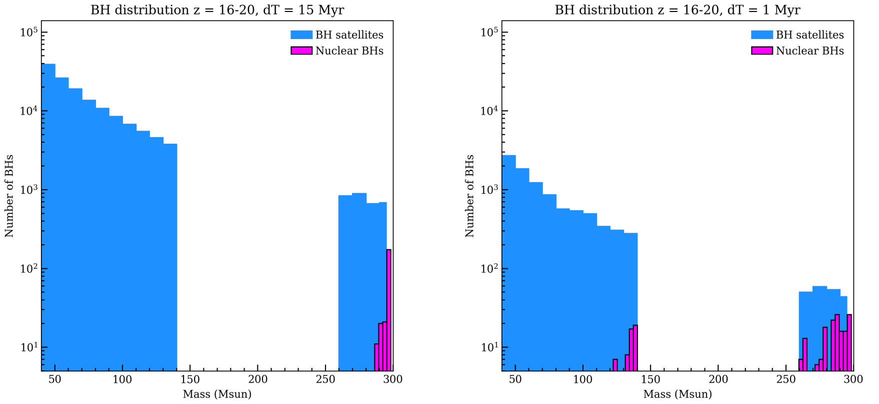

Figure 7.8. Mass distribution of nuclear BHs (magenta) and BH satellites (blue) at $z \gtrsim 16$ for $\Delta t_{\rm res} = 15$ Myr (left panel) and $\Delta t_{\rm SF} = 1$ Myr (right panel).

after 1 Myr, the mass of Pop III stars formed in each burst is reduced and hence the effect of the incomplete sampling of the IMF is apparent, even when multiple Pop III halos are combined. Indeed, the number of stars with masses > 150 $M_{\odot}$ is smaller, and this will be reflected in the mass distribution of Pop III BH remnants.

Figure 7.7 illustrates the redshift distribution of Pop III BH remnants considering all the simulated galaxies in the redshift range 16 - 20, for $\Delta t = 15$ and 1 Myr. While the shape of the distribution is similar, the total number of planted seeds reflects the difference in the mass out of which stars (and seeds) are formed.

The stochasticity especially affects the high-mass tail of the BH mass distribution. In Figure 7.8 we show the mass distribution of satellites (blue) and nuclear (magenta) BHs for all the simulated galaxies at $z \geq 16$. This redshift threshold is chosen because metal enrichment is sufficient to inhibit the formation of Pop III stars and of BH seeds at $z < 16$ (Graziani et al., 2017). The BH satellite population is dominated by BHs with masses < 140 $M_{\odot}$. Their relative frequency in this mass range is not strongly affected by the random sampling procedure, and the resulting shape of the mass spectrum is independent of Δt. On the contrary, the nuclear BH distribution mass sensitively depends on the stochasticity of Pop III star formation. In fact, for $\Delta t = \Delta t_{\rm res}$, the stellar mass produced in a SF burst is large enough ($10^4 - 10^5\ M_{\odot}$) to allow a full sampling of the IMF. Therefore the nuclear BH, i.e. the most massive found in the population of BH seeds, will be more likely close to the

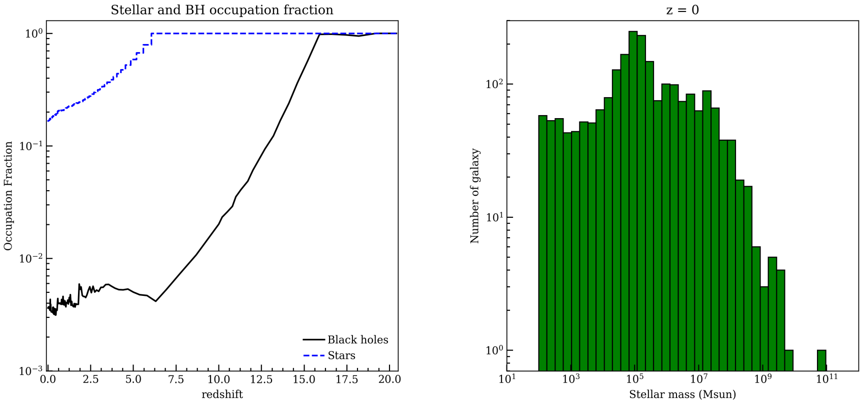

Figure 7.9. *Left panel*: Redshift evolution of the fraction of luminous halos (i.e. hosting $M_\star > 100\,M_\odot$, blue dotted line). The black, solid line represents the fraction of galaxies hosting a nuclear BH. *Right panel*: Stellar mass distribution of simulated $z = 0$ galaxies.

upper limit mass, $M_{\rm seed} \sim 300\,M_\odot$. Instead, when $\Delta t = 1$ Myr the nuclear BHs distribution is more spread, with masses reaching $130\,M_\odot$.

It is important to note that the duration of each Pop III star formation burst does not affect the black hole occupation fraction. In fact, the total number of nuclear BHs found at redshift $z \sim 16$ is the same for $\Delta t_{\rm res}$ and $\Delta t_{\rm SF}$, with BHOF($z = 16$) = 0.98. Since for $z < 16$ the physical conditions do not allow more seeds to be planted, we can safely adopt an integration time of $\Delta t_{\rm res}$.

7.4.2 BH occupation fraction

Due to feedback effects, a virialized DM halo is not necessarily a luminous halo. Under the assumptions discussed in Section 7.2.2, for $z < z_{\rm reio}$ we inhibit SF in halos with $T_{\rm vir} < 10^4$ K. As a result, at $z = 0$, only ~ 20 % of the simulated sample is a luminous galaxy, while the rest would not be visible through stellar radiative emission. In the left panel of Figure 7.9, the blue, dotted line shows the redshift evolution of the fraction of DM halos hosting stars with $M_\star > 100\,M_\odot$. We choose this lower limit because Ultra-Faint Dwarf (UFD) satellites of the MW are considered to extend to stellar masses as small as $10^2\,M_\odot$ (Weisz and Boylan-Kolchin, 2017; Jeon et al., 2017). The right panel of Figure 7.9 shows that, at the end of the simulation, the distribution of the stellar component spans a wide range of

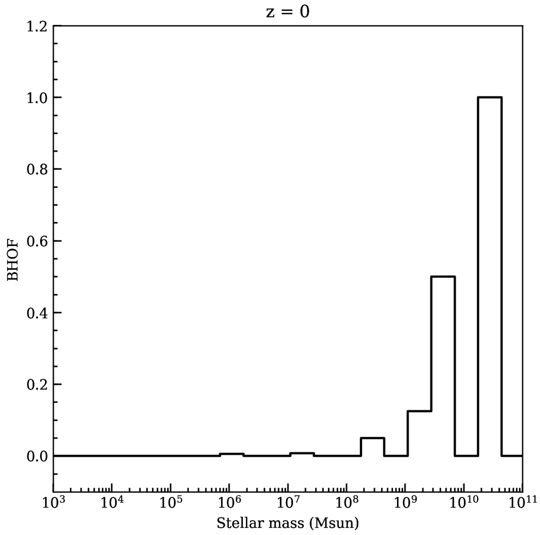

Figure 7.10. Black hole occupation fraction for galaxies with different stellar masses found in the simulated Local Universe.

masses, especially probing the dwarf and UFD regime, with a peak of the mass distribution $M_\star \sim 10^5 - 10^6\,M_\odot$.

Since we define the BHOF as the fraction of galaxies hosting a nuclear BH, we exclude from this estimate the contribution of dark halos with $M_\star \leq 100\,M_\odot$. The evolution of the BHOF is shown with a black, solid line in Figure 7.9. At $z = 16$, the last redshift where BH seeds form, the BHOF is ~ 1 (101 out of 103 luminous galaxies host a nuclear BH). Under the assumption made so far, N = 101 is the maximum number of nuclear BHs that can be found in the simulation box at each given time. During their subsequent evolution, these BHs can be preserved as nuclear BHs or can be transformed in a BH satellite, depending on the nature of merger events that will be encountered.

During the evolution, the number of nascent galaxies increases, while the available nuclear BHs, at most, remains the ones already formed. For this reason, the BHOF decreases with time, and at z = 0 we find a BHOF much smaller than 1 (BHOF(z=0) $\sim 3.6 \times 10^{-3}$). It is important to note that this value depends on the adopted $\mu_{\rm thr}$. Assuming that all nuclear BHs seeded at $z \geq 16$ survive and populate the centres of $z = 0$ luminous galaxies, we can estimate an upper limit on the BHOF of $\sim 3.8 \times 10^{-2}$, about a factor of 10 larger. Hence,

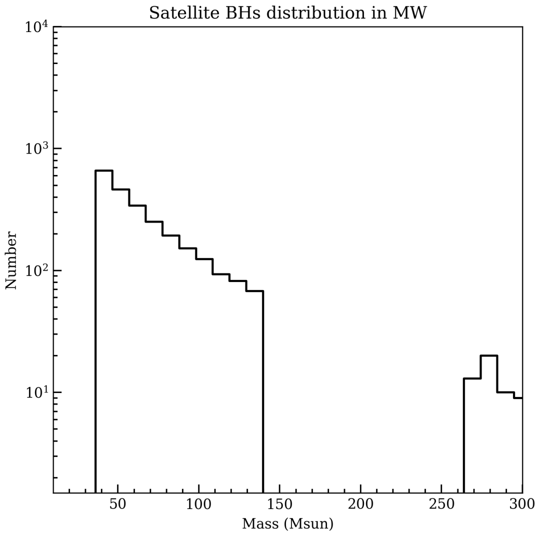

Figure 7.11. Mass distribution of the Milky Way BH satellites as predicted by the simulation at $z = 0$.

exploring the implications of lower values of $\mu_{\rm thr}$ is important (see Section 7.4.3).

Since structure formation proceeds in a hierarchical manner, we do not expect the distribution of nuclear BHs to be uniform between galaxies. In Figure 7.10, we show the $z = 0$ BHOF for galaxies with different stellar mass. Low mass galaxies, with $M_\star \lesssim 10^8\,M_\odot$, have BHOF $\sim$ 0. This is because some of low-mass galaxies are born at $z < 16$, when Pop III star formation has already been suppressed by metal enrichment and BH seeds from Pop III remnants can no longer form. Furthermore, low-mass galaxies generally experience a quiescent evolution, and this makes it difficult to inherit a BH through major mergers. For $M_\odot \gtrsim 10^8\,M_\odot$, instead, the interactions experienced by the galaxies increase, and the BHOF rises up to 1 for $M_\star \sim 5\times10^{10}\,M_\odot$. In this mass bin falls only the MW-like halo, which indeed hosts a BH.

7.4.3 The BH masses in the LG

With the assumption made in this preliminary work, i.e. turning off BH gas accretion, our model can only provide a strict lower limit on the nuclear BH mass distribution at $z = 0$ (see the discussion below). However, since BH satellites are dislocated with respect to the galactic center, it is reasonable to assume that once formed, they do not accrete from the nuclear gas reservoir. In Figure 7.11 we show the mass distribution of BH satellites from Pop III remnants in the MW-like halo at $z = 0$. Assuming that these BHs are not in binary systems and do not merge, we expect ~ 2500 Pop III BH remnant satellites, mostly with masses in the range $M \sim 40 - 100\,M_{\odot}$, comparable to the limits inferred for some of the recently observed gravitational wave events (Abbott et al., 2016a, 2017; The LIGO Scientific Collaboration et al., 2017).

The limitation of null BH accretion and the assumption of $\mu_{\rm thr} = 0.25$ as the minimum mass ratio to allow efficient BH-BH mergers lead to a very small predicted nuclear BH masses in the LG. In particular, we find that only 8 out of the original sample of 101 BH seeds survive as nuclear BHs. Their mass distribution is biased toward very small values, including the nuclear BH of the MW-like galaxy that is predicted to have a mass of only $M_{\rm BH} \sim 300\,M_{\odot}$. This is due to the fact that the MW halo grows mostly through smooth accretion and mergers with small satellites and the mass of its nuclear BH depends on the adopted seeding prescription and on the value of $\mu_{\rm thr}$. It is useful to compare our findings with recent results obtained through detailed numerical simulations of the MW galaxy. Marinacci et al. (2014) present cosmological hydrodynamic simulations of 8 MW-sized halos that are able to reproduce realistic properties of disc galaxies by $z = 0$. They predict final nuclear BH masses in the range $[2\times10^{7}-2\times10^{8}]\,M_{\odot}$. These values are obtained under the assumption that BH seeds have masses of the order of $\sim 10^{5}\,M_{\odot}$, and grow by mergers and Eddington-limited accretion. More recently, Bonoli et al. (2016) discuss the results of a zoom-in hydrodynamical simulation of a MW-type galaxy and follow the evolution of the nuclear BH. They find that the central BH grows mainly through mergers with other BHs from infalling satellites and that growth by gas accretion is negligible. The difference with respect to the results of Marinacci et al. (2014) is attributed to the different resolution of the simulations. The final BH mass predicted by Bonoli et al. (2016) is about $2.6\times10^{6}\,M_{\odot}$, and grows from a seed of $8.7 \times 10^{5}\,M_{\odot}$, formed at $z = 8.5$, by merging with 3 additional BHs with masses ranging between $(0.8 - 7.6) \times 10^{5}\,M_{\odot}$.

The above studies suggest that, in order to grow a nuclear BH with mass comparable to the observed one in the MW galaxy, massive BH seeds have to be in place by $z \sim 8$. Hence, it is not surprising that with our adopted seeding prescription and no gas accretion, we find a very small final nuclear BH mass for the MW-like halo. Our preliminary results suggest that either Pop III BH remnants are able to rapidly grow their masses through super-Eddington accretion, following their formation, or that heavier BH seed masses have characterized the progenitors of the MW nuclear BH.

In order to test the two possibilities presented above, we can assume that all Pop III BH remnants planted at $z \geq 16$ contribute to the final MW nuclear BH. Under this extreme assumption, we find a final BH mass of $M_{\rm BH} \sim 4 \times 10^4\, M_\odot$. This value is still two orders of magnitude smaller than the estimated BH mass of the MW, $4 \times 10^6\, M_\odot$ (Boehle et al., 2016). Hence, an early epoch of rapid BH growth is required if Pop III BH remnants are the seed progenitors of the MW nuclear BH. Conversely, we can estimate how many potential DCBH formation sites are found in the simulation. As an upper limit, we consider only those Lyα-cooling halos with metallicities $Z < Z_{\rm cr}$, regardless of the value of the LW flux at which they are exposed to. At $z = 16$, we find 26 Lyα-cooling halos with subcritical metallicities. If all these systems were MW progenitors, and were able to suppress H_2 cooling and form a DCBH with mass $\sim 10^5\, M_\odot$, we would have a final BH mass of $2.6 \times 10^6\, M_\odot$, consistent with the observations. We plan to further investigate which of these two possibilities is able to reproduce the MW central BH mass, and then we will extend the analysis to other galaxies in the LG.

7.5 Conclusions

In this Chapter we presented a preliminary study based on a post-processing analysis of a GAMESH simulation, run on a high-resolution N-body realization of a LG region with a well-resolved MW-like halo at its centre. We have followed the properties of individual Pop III star forming sites, and we have planted in each of these a nuclear BH selected to be the most massive among BH remnants. Given the low cooling efficiency of the primordial gas, and the short lifetimes of massive Pop III stars, we have accounted for the incomplete sampling of the IMF, and we have computed the emerging mass spectrum of Pop III stars and of their BH remnants. Assuming short duration of Pop III bursts, $\Delta t_{\rm SF} \sim 1$ Myr, causes an undersampling of the high-mass tail of the Pop III IMF. As a result, the masses of nuclear BHs range between 130 and 300 $M_\odot$.

In addition, we find that all BH seeds are planted at $z \geq 16$, below which metal enrichment prevents further episodes of Pop III star formation. At $z = 16$, we find a very high BH occupation fraction, ~ 98 %, independently of the adopted duration of Pop III bursts. Below this redshift, the hierarchical evolution of the simulated galaxies causes a continuous decrease of the BHOF, that becomes less than 5 % at $z \lesssim 6$ and reaches a value of 3.6×10^{-3} by $z = 0$. Furthermore, the BHOF is not constant with the stellar mass of the host galaxies: at $z = 0$, we find a negligible occupation fraction below $M_{\star} \sim 10^{8}\, M_{\odot}$, and that BHOF $\sim$ 20 %, 50 %, 100 % for $M_{\star} \sim 10^{9}, 10^{10}, 5 \times 10^{10}\, M_{\odot}$.

Overall, however, the number of central BHs found at $z = 0$ is very small (8), ~ 8 % of the original number of nuclear BH seeds formed at $z = 16$ (101). Among these nuclear survivors, the BH of the MW galaxy has a mass that is largely underestimated (300 $M_{\odot}$) compared to the observed value.

These results largely depend on (*i*) the adopted threshold value that classify major and minor mergers, and, consequently, nuclear and satellite BHs, and on (*ii*) the assumption that mass growth by gas accretion is negligible. Comparing our predictions with previous analyses (Marinacci et al., 2014; Bonoli et al., 2016), we conclude that either light BH remnants of Pop III stars are able to rapidly grow their masses soon after their formation, or that the Milky Way nuclear BH originates from more massive BH seeds, with masses comparable to the ones that characterize direct collapse BHs.

In the future, we will investigate each of these two possibilities, implementing BH formation and evolution in GAMESH. This will allow us to predict the properties of the birth environments of BH seeds (Pop III remnants and DCBHs) that result from a complex interplay of radiative and chemical feedback effects.

Part IV

Conclusions

The technological advances of recent years provided powerful tools and more sophisticated instruments, which allowed the human eyes to overcome previous limits. In particular, the observable Universe[1] has grown sensitively in its extent in the last decades, pushing its edges up to few hundred Myr after the birth of the Universe. At this observational limit, we find the first cosmic structures formed, marking the end of the Cosmic Dark Ages. So far, the most distant object ever observed is the GN-z11 galaxy, settled at $z = 11.09$, ~ 400 Myr after the Big Bang (Oesch et al., 2016). Despite its youth, the large densities of the early Universe led to efficient galaxy formation and evolution. Furthermore, observations also show the presence of galaxies hosting SMBHs with $M_{\rm BH} \sim 10^9\, M_\odot$ already at $z \gtrsim 6$. For instance, the redshift of farthest observed quasar, ULAS J1120, is $z = 7.08$ (Mortlock et al., 2011). The exploration of the distant Universe enabled us to identify more than 100 quasars at $z \sim 6$, born and grown in less than 700 Myr. However, within the hierarchical scenario of structure formation, the sample of luminous AGN at high redshift observed so far is supposed to be only the tip of the iceberg of the entire high-z BH population. In fact, the bulk of the $z \gtrsim 6$ MBH distribution is believed to consist of less massive BHs, too faint for being currently detected.

High-z quasars are still extremely intriguing, as they allow to test different theoretical models aimed at understanding the formation, growth and properties of the first black holes in the Universe. Such arguments represent the main research topics of my Ph.D. work. In particular, the questions we have tried to answer are the following.

Is super-Eddington accretion important for the formation of the first quasars?

The short period available to build SMBHs of $10^{10}\, M_\odot$ in the early Universe suggests that the gas accretion rate onto the first BHs may have been very high. We investigated the relevance of different growth regimes by developing an upgraded version of a model for cosmological structure formation to reconstruct the evolution of the first quasars in the Universe together with the properties of the host galaxies. This was done by making testable predictions on many observed quantities, such as the central BH mass, the luminosity, the outflow rate and the mass of stars, gas, metals and dust in the galaxy. Under the assumption

---

[1] Excluding the CMB radiation.

of the most natural seeding channel, i.e. Pop III BH remnants, we find that super-critical accretion is fundamental for the formation of the high-z AGN, which represents the dominant contribution to the MBH mass growth. Additionally, we notice that, once limiting the BH accretion rate to Eddington, the $10^9\ M_\odot$ SMBH mass at $z \sim 6$ is no longer reproduced.

How do the nuclear BH and the host galaxy of high-z AGN (co)evolve?

With our semi-analytic model, we can follow the evolution of the SMBH progenitors and the host galaxies until the final formation of the $z \sim 6$ quasars. The simulated growth in the $M_{\rm BH} - M_\star$ plane shows a symbiotic trend, with only a small offset with respect to the observed local scaling relation. Such a build-up ends its race within the scatter of the local observed BH-stellar mass data points. Interestingly, we find a *strong* form of coevolution, where galaxies affect BH growth by controlling BH feeding and merging, and BHs control galaxy properties via AGN feedback.

Is super-Eddington sustained in a cosmological context?

Super-Eddington accretion seems to be a "natural" regime in the distant Universe. In fact, this process is favoured in dense, highly-obscured environments where photon trapping is efficient, as structures in the early Universe are suggested to be. However, since there exist some processes which could reduce the duration of a single super-critical accretion event, this regime may appear more rarely than what supposed to be, and with shorter duty cycles. Furthermore, this time reduction could affect its capability of building high-z SMBH masses. We investigated the feasibility of super-Eddington accretion in a cosmological context by including a model for the maximum duration of a single super-critical accretion episode. As a result, we find that this regime still drives an efficient growth of the $z \sim 6$ nuclear SMBH, which finally reaches the mass observed in the high-z sample. This happens if the gas accreting onto the compact object efficiently loses its angular momentum.

What is the main driver for the lack of faint AGN detections at $z \gtrsim 5$?

To discriminate between different high-z SMBH growth scenarios, it is necessary to put observational constraints on the properties of their faint progenitors at $z \gtrsim 7$. However, to date, no convincing faint AGN candidate at $z \gtrsim 5$ has been selected in the X-rays.

Understanding the cause of such a lack of detections is mandatory. By developing an emission model for early accreting BHs which takes into account spectral features caused by the photon trapping effect, we estimate the X-ray flux distribution of $z \sim 6$ luminous quasar progenitors. With this study, it has been possible to foresee the properties, in terms of observability, of this BH population. In detail, such objects are luminous enough for being detected by current facilities, but they are rare. Short, intermittent super-Eddington accretion episodes strongly reduce the duty cycle of their active and luminous phase, and, as a consequence, the probability of observing them. Consequently, we suggest surveys with larger fields at shallower sensitivities in order to optimise this type of searches.

We conclude that the super-critical regime may help in giving some explanations to many open problems related to the properties of distant quasars, such as the presence of SMBHs already at $z \sim 7$, or the missing observations of their faint progenitors.

Is it possible to constrain the early black hole growth by observing the local dwarf galaxies?

All the theoretical models agree on predicting the BH seed formation to statistically end at $z > 10$. For this reason, the MBH population that we observe in the centres of local galaxies must have been formed at early times. Therefore, it is possible to study the characteristics of the first BHs by analysing their final fate, i.e. their descendants in the local Universe. The best targets for this study are dwarf galaxies. In fact, their quiescent merger evolution suggests that they are the objects which better preserve the "memory" of BH seed properties. In order to exploit the feasibility of constraining the early BH growth by observing the properties of local dwarf galaxies, we started to analyse the output of a N-body simulation reproducing a Local Group-like structure, coupled with a semi-analytic code for the baryonic evolution. Working in post-processing, we studied the formation of the first BH seeds, and followed their evolutionary paths from z ~ 20 to z = 0.

We find seed BHs with masses ranging from 130 to 300 $M_{\odot}$, depending on the efficiency and duration of Pop III bursts, which limit the formation of the most massive Pop III progenitors. Their formation epoch extends from $z \sim 20$ down to $z \sim 16$, below which metal enrichment prevents further Pop III SF. At $z = 16$ the black hole occupation fraction is nearly 1, but decreases thereafter as a consequence of the hierarchical evolution of galaxies and their nuclear BHs. At $z = 0$ the total black hole occupation fraction is only $\sim 3.6\times10^{-3}$, with a strong dependence on the stellar masses of the host galaxies. Out of the original 101 BH seeds that are formed at $z = 16$, only 8 survive at $z = 0$, and all of them in galaxies with $M_\star \gtrsim 10^8\,M_\odot$. Among these, we find that the MW-like galaxy hosts a nuclear BH of only $\sim 300\,M_\odot$, much smaller than observed. This depends on our assumption that mass growth by gas accretion is negligible, and on the adopted value of the halo mass ratio that classify major and minor mergers and, consequently, nuclear and satellite BHs. Future developments of GAMESH will allow us to overcome these two limitations, and to explore different BH seeding and accretion models in a self-consistent way. Ultimately, we hope to constrain early BH growth using a local perspective.

An outlook to the future

The first natural development of this work is to produce a self-consistent analysis of early BH formation and evolution, and to compare the results with the properties of local dwarf galaxies. This will be done by integrating the current N-body model with the semi-analytic code GAMETE/SuperQSOdust, introduced in this thesis. In this way, we will be able to put constraints on the BH mass distribution and occupation fractions of the galaxies surrounding the Milky Way.

Another possible follow-up may be the inclusion of other BH seed formation mechanisms. It is in fact interesting to improve and expand the previous answers by including also seeds produced by the direct collapse of cold gas into massive BHs, or by the merging of dense star clusters into very massive stars eventually forming a BH.

Moreover, an important improvement of the previous conclusions will be achieved once we extend our analysis to *mean* cosmological volumes. In fact, the results discussed in Chapter 4, Chapter 5 and Chapter 6 pertain to a subsample of the entire BH population, i.e. the progenitors of $z \sim 6$ quasars. Including the evolution at higher redshift of the entire $z \sim 6$ MBH population would in fact allow to foresee possible observational tests to be conducted on average sky areas.

Part V

Appendix

List of pubblications

Edwige Pezzulli, Rosa Valiante, Raffaella Schneider

Super-Eddington growth of the first black holes

2016, MNRAS, 458 3047

Edwige Pezzulli, Rosa Valiante , Maria C. Orofino, Raffaella Schneider, SImona Gallerani, Tullia Sbarrato

Faint progenitors of luminous quasars: why don't we see them?

2017, MNRAS, 466 2131

Rosa Valiante, Bhaskar Agarwal, Melanie Habouzit, **Edwige Pezzulli**

On the formation of the first quasar

2017, PASA, 34 31

Edwige Pezzulli, Marta Volonteri, Raffaella Schneider, Rosa Valiante

The sustainable growth of the first black holes

2017, MNRAS, 471 589

Rosa Valiante, Raffaella Schneider, Luca Zappacosta, Luca Graziani, **Edwige Pezzulli**

Chasing the observational signatures of seed black holes at $z > 7$*: candidate observability*

MNRAS, submitted

Francesco G. Saturni, Mattia Mancini, **Edwige Pezzulli**, F. Tombesi

"Zombie" or active? An alternative explanation to the properties of high-z galaxies

MNRAS, submitted

Edwige Pezzulli, Raffaella Schneider, Luca Graziani, Matteo de Bennassuti, Rosa Valiante

Constraining the first black holes growth through properties of the local dwarf galaxies

In prep.

Cometa, Beatriz Aurora.

Bibliography

S. Aalto, S. Garcia-Burillo, S. Muller, J. M. Winters, P. van der Werf, C. Henkel, F. Costagliola, and R. Neri. Detection of HCN, HCO^+, and HNC in the Mrk 231 molecular outflow. Dense molecular gas in the AGN wind. A&A, 537:A44, January 2012. doi: 10.1051/0004-6361/201117919.

B. P. Abbott, R. Abbott, T. D. Abbott, M. R. Abernathy, F. Acernese, K. Ackley, C. Adams, T. Adams, P. Addesso, R. X. Adhikari, and et al. Observation of Gravitational Waves from a Binary Black Hole Merger. *Physical Review Letters*, 116(6):061102, February 2016a. doi: 10.1103/PhysRevLett.116.061102.

B. P. Abbott, R. Abbott, T. D. Abbott, M. R. Abernathy, F. Acernese, K. Ackley, C. Adams, T. Adams, P. Addesso, R. X. Adhikari, and et al. GW151226: Observation of Gravitational Waves from a 22-Solar-Mass Binary Black Hole Coalescence. *Physical Review Letters*, 116(24):241103, June 2016b. doi: 10.1103/PhysRevLett.116.241103.

B. P. Abbott, R. Abbott, T. D. Abbott, F. Acernese, K. Ackley, C. Adams, T. Adams, P. Addesso, R. X. Adhikari, V. B. Adya, and et al. GW170104: Observation of a 50-Solar-Mass Binary Black Hole Coalescence at Redshift 0.2. *Physical Review Letters*, 118(22):221101, June 2017. doi: 10.1103/PhysRevLett.118.221101.

T. Abel, G. L. Bryan, and M. L. Norman. The Formation of the First Star in the Universe. *Science*, 295:93–98, January 2002. doi: 10.1126/science.295.5552.93.

M. A. Abramowicz and P. C. Fragile. Foundations of Black Hole Accretion Disk Theory. *Living Reviews in Relativity*, 16:1, January 2013. doi: 10.12942/lrr-2013-1.

M. A. Abramowicz, B. Czerny, J. P. Lasota, and E. Szuszkiewicz. Slim accretion disks. ApJ, 332:646–658, September 1988. doi: 10.1086/166683.

B. Agarwal and S. Khochfar. Revised rate coefficients for H_2 and H^- destruction by realistic stellar spectra. MNRAS, 446:160–168, January 2015. doi: 10.1093/mnras/stu1973.

B. Agarwal, S. Khochfar, J. L. Johnson, E. Neistein, C. Dalla Vecchia, and M. Livio. Ubiquitous seeding of supermassive black holes by direct collapse. MNRAS, 425:2854–2871, October 2012. doi: 10.1111/j.1365-2966.2012.21651.x.

B. Agarwal, A. J. Davis, S. Khochfar, P. Natarajan, and J. S. Dunlop. Unravelling obese black holes in the first galaxies. MNRAS, 432:3438–3444, July 2013. doi: 10.1093/mnras/stt696.

B. Agarwal, C. Dalla Vecchia, J. L. Johnson, S. Khochfar, and J.-P. Paardekooper. The First Billion Years project: birthplaces of direct collapse black holes. MNRAS, 443:648–657, September 2014. doi: 10.1093/mnras/stu1112.

B. Agarwal, J. L. Johnson, E. Zackrisson, I. Labbe, F. C. van den Bosch, P. Natarajan, and S. Khochfar. Detecting direct collapse black holes: making the case for CR7. MNRAS, 460:4003–4010, August 2016a. doi: 10.1093/mnras/stw1173.

B. Agarwal, B. Smith, S. Glover, P. Natarajan, and S. Khochfar. New constraints on direct collapse black hole formation in the early Universe. MNRAS, 459:4209–4217, July 2016b. doi: 10.1093/mnras/stw929.

Bhaskar Agarwal, Jarrett L Johnson, Sadegh Khochfar, Eric Pellegrini, Claes-Erik Rydberg, Ralf S Klessen, and Pascal Oesch. Metallicity evolution of direct collapse black hole hosts: CR7 as a case study. *arXiv.org*, page arXiv:1702.00407, February 2017.

K. Ahn, P. R. Shapiro, I. T. Iliev, G. Mellema, and U.-L. Pen. The Inhomogeneous Background Of H_2-Dissociating Radiation During Cosmic Reionization. ApJ, 695:1430–1445, April 2009. doi: 10.1088/0004-637X/695/2/1430.

J. Aird, A. Comastri, M. Brusa, N. Cappelluti, A. Moretti, E. Vanzella, M. Volonteri, D. Alexander, J. M. Afonso, F. Fiore, I. Georgantopoulos, K. Iwasawa, A. Merloni,

K. Nandra, R. Salvaterra, M. Salvato, P. Severgnini, K. Schawinski, F. Shankar, C. Vignali, and F. Vito. The Hot and Energetic Universe: The formation and growth of the earliest supermassive black holes. *ArXiv e-prints*, June 2013.

A. Akylas, A. Georgakakis, I. Georgantopoulos, M. Brightman, and K. Nandra. Constraining the fraction of Compton-thick AGN in the Universe by modelling the diffuse X-ray background spectrum. A&A, 546:A98, October 2012. doi: 10.1051/0004-6361/201219387.

K. Alatalo, L. Blitz, L. M. Young, T. A. Davis, M. Bureau, L. A. Lopez, M. Cappellari, N. Scott, K. L. Shapiro, A. F. Crocker, S. Martín, M. Bois, F. Bournaud, R. L. Davies, P. T. de Zeeuw, P.-A. Duc, E. Emsellem, J. Falcón-Barroso, S. Khochfar, D. Krajnović, H. Kuntschner, P.-Y. Lablanche, R. M. McDermid, R. Morganti, T. Naab, T. Oosterloo, M. Sarzi, P. Serra, and A. Weijmans. Discovery of an Active Galactic Nucleus Driven Molecular Outflow in the Local Early-type Galaxy NGC 1266. ApJ, 735:88, July 2011. doi: 10.1088/0004-637X/735/2/88.

D. M. Alexander, F. E. Bauer, W. N. Brandt, D. P. Schneider, A. E. Hornschemeier, C. Vignali, A. J. Barger, P. S. Broos, L. L. Cowie, G. P. Garmire, L. K. Townsley, M. W. Bautz, G. Chartas, and W. L. W. Sargent. The Chandra Deep Field North Survey. XIII. 2 Ms Point-Source Catalogs. AJ, 126:539–574, August 2003. doi: 10.1086/376473.

D. M. Alexander, A. M. Swinbank, I. Smail, R. McDermid, and N. P. H. Nesvadba. Searching for evidence of energetic feedback in distant galaxies: a galaxy wide outflow in a z $\sim$ 2 ultraluminous infrared galaxy. MNRAS, 402:2211–2220, March 2010. doi: 10.1111/j.1365-2966.2009.16046.x.

T. Alexander and P. Natarajan. Rapid growth of seed black holes in the early universe by supra-exponential accretion. *Science*, 345:1330–1333, September 2014. doi: 10.1126/science.1251053.

M. A. Alvarez, V. Bromm, and P. R. Shapiro. The H II Region of the First Star. ApJ, 639:621–632, March 2006. doi: 10.1086/499578.

M. A. Alvarez, J. H. Wise, and T. Abel. Accretion onto the First Stellar-Mass Black Holes. ApJ, 701:L133–L137, August 2009. doi: 10.1088/0004-637X/701/2/L133.

R. E. Angulo, O. Hahn, and T. Abel. How closely do baryons follow dark matter on large scales? MNRAS, 434:1756–1764, September 2013. doi: 10.1093/mnras/stt1135.

M. Asplund, N. Grevesse, A. J. Sauval, and P. Scott. The Chemical Composition of the Sun. ARA&A, 47:481–522, September 2009. doi: 10.1146/annurev.astro.46.060407.145222.

A. Aykutalp, J. H. Wise, M. Spaans, and R. Meijerink. Songlines from Direct Collapse Seed Black Holes: Effects of X-Rays on Black Hole Growth and Stellar Populations. ApJ, 797:139, December 2014. doi: 10.1088/0004-637X/797/2/139.

J. G. Baker, W. D. Boggs, J. Centrella, B. J. Kelly, S. T. McWilliams, M. C. Miller, and J. R. van Meter. Modeling Kicks from the Merger of Generic Black Hole Binaries. ApJ, 682:L29–L32, July 2008. doi: 10.1086/590927.

V. F. Baldassare, A. E. Reines, E. Gallo, and J. E. Greene. A $\sim$ 50,000 $M_\odot$ Solar Mass Black Hole in the Nucleus of RGG 118. ApJ, 809:L14, August 2015. doi: 10.1088/2041-8205/809/1/L14.

B. Balmaverde, R. Gilli, M. Mignoli, M. Bolzonella, M. Brusa, N. Cappelluti, A. Comastri, E. Sani, E. Vanzella, C. Vignali, F. Vito, and G. Zamorani. The primordial environment of supermassive black holes (II): deep Y and J band images around the z=6.3 quasar SDSS J1030+0524. *ArXiv e-prints*, June 2017.

E. Barausse. The evolution of massive black holes and their spins in their galactic hosts. MNRAS, 423:2533–2557, July 2012. doi: 10.1111/j.1365-2966.2012.21057.x.

J. M. Bardeen, W. H. Press, and S. A. Teukolsky. Rotating Black Holes: Locally Nonrotating Frames, Energy Extraction, and Scalar Synchrotron Radiation. ApJ, 178:347–370, December 1972. doi: 10.1086/151796.

R. Barkana and A. Loeb. In the beginning: the first sources of light and the reionization of the universe. Phys. Rep., 349:125–238, July 2001. doi: 10.1016/S0370-1573(01)00019-9.

A. J. Barth, P. Martini, C. H. Nelson, and L. C. Ho. Iron Emission in the z = 6.4 Quasar SDSS J114816.64+525150.3. ApJ, 594:L95–L98, September 2003. doi: 10.1086/378735.

A. J. Barth, L. C. Ho, R. E. Rutledge, and W. L. W. Sargent. POX 52: A Dwarf Seyfert 1 Galaxy with an Intermediate-Mass Black Hole. ApJ, 607:90–102, May 2004. doi: 10.1086/383302.

A. J. Barth, J. E. Greene, and L. C. Ho. Low-Mass Seyfert 2 Galaxies in the Sloan Digital Sky Survey. AJ, 136:1179–1200, September 2008. doi: 10.1088/0004-6256/136/3/1179.

F. Becerra, T. H. Greif, V. Springel, and L. E. Hernquist. Formation of massive protostars in atomic cooling haloes. MNRAS, 446:2380–2393, January 2015. doi: 10.1093/mnras/stu2284.

G. D. Becker, W. L. W. Sargent, M. Rauch, and R. A. Simcoe. Discovery of Excess O I Absorption toward the z=6.42 QSO SDSS J1148+5251. ApJ, 640:69–80, March 2006. doi: 10.1086/500079.

A. Beelen, P. Cox, D. J. Benford, C. D. Dowell, A. Kovács, F. Bertoldi, A. Omont, and C. L. Carilli. 350 μm Dust Emission from High-Redshift Quasars. ApJ, 642:694–701, May 2006. doi: 10.1086/500636.

M. C. Begelman. Radiatively inefficient accretion: breezes, winds and hyperaccretion. MNRAS, 420:2912–2923, March 2012. doi: 10.1111/j.1365-2966.2011.20071.x.

M. C. Begelman and M. Volonteri. Hyperaccreting black holes in galactic nuclei. MNRAS, 464:1102–1107, January 2017. doi: 10.1093/mnras/stw2446.

M. C. Begelman, M. Volonteri, and M. J. Rees. Formation of supermassive black holes by direct collapse in pre-galactic haloes. MNRAS, 370:289–298, July 2006. doi: 10.1111/j.1365-2966.2006.10467.x.

Mitchell C Begelman, Elena M Rossi, and Philip J Armitage. Quasi-stars: accreting black holes inside massive envelopes. *MNRAS*, 387:1649, July 2008.

J. Bellovary, M. Volonteri, F. Governato, S. Shen, T. Quinn, and J. Wadsley. The First Massive Black Hole Seeds and Their Hosts. ApJ, 742:13, November 2011. doi: 10.1088/0004-637X/742/1/13.

R. Bender, J. Kormendy, G. Bower, R. Green, J. Thomas, A. C. Danks, T. Gull, J. B. Hutchings, C. L. Joseph, M. E. Kaiser, T. R. Lauer, C. H. Nelson, D. Richstone, D. Weistrop, and B. Woodgate. HST STIS Spectroscopy of the Triple Nucleus of M31: Two Nested Disks in Keplerian Rotation around a Supermassive Black Hole. ApJ, 631:280–300, September 2005. doi: 10.1086/432434.

M. C. Bentz and S. Katz. The AGN Black Hole Mass Database. PASP, 127:67, January 2015. doi: 10.1086/679601.

F. Bertoldi, C. L. Carilli, P. Cox, X. Fan, M. A. Strauss, A. Beelen, A. Omont, and R. Zylka. Dust emission from the most distant quasars. A&A, 406:L55–L58, July 2003. doi: 10.1051/0004-6361:20030710.

R. Bieri, Y. Dubois, J. Silk, and G. A. Mamon. Playing with Positive Feedback: External Pressure-triggering of a Star-forming Disk Galaxy. ApJ, 812:L36, October 2015. doi: 10.1088/2041-8205/812/2/L36.

R. Bieri, Y. Dubois, J. Rosdahl, A. Wagner, J. Silk, and G. A. Mamon. Outflows driven by quasars in high-redshift galaxies with radiation hydrodynamics. MNRAS, 464:1854–1873, January 2017. doi: 10.1093/mnras/stw2380.

G. S. Bisnovatyi-Kogan and S. I. Blinnikov. Disk accretion onto a black hole at subcritical luminosity. A&A, 59:111–125, July 1977.

L. Blecha, D. Sijacki, L. Z. Kelley, P. Torrey, M. Vogelsberger, D. Nelson, V. Springel, G. Snyder, and L. Hernquist. Recoiling black holes: prospects for detection and implications of spin alignment. MNRAS, 456:961–989, February 2016. doi: 10.1093/mnras/stv2646.

A. Boehle, A. M. Ghez, R. Schödel, L. Meyer, S. Yelda, S. Albers, G. D. Martinez, E. E. Becklin, T. Do, J. R. Lu, K. Matthews, M. R. Morris, B. Sitarski, and G. Witzel. An Improved Distance and Mass Estimate for Sgr A* from a Multistar Orbit Analysis. ApJ, 830:17, October 2016. doi: 10.3847/0004-637X/830/1/17.

H. Bondi. On spherically symmetrical accretion. MNRAS, 112:195, 1952. doi: 10.1093/mnras/112.2.195.

S. Bonoli, L. Mayer, S. Kazantzidis, P. Madau, J. Bellovary, and F. Governato. Black hole starvation and bulge evolution in a Milky Way-like galaxy. MNRAS, 459:2603–2617, July 2016. doi: 10.1093/mnras/stw694.

F. Bournaud, F. Combes, C. J. Jog, and I. Puerari. Lopsided spiral galaxies: evidence for gas accretion. A&A, 438:507–520, August 2005. doi: 10.1051/0004-6361:20052631.

R. J. Bouwens, G. D. Illingworth, M. Franx, and H. Ford. z $\sim$ 7-10 Galaxies in the HUDF and GOODS Fields: UV Luminosity Functions. ApJ, 686:230-250, October 2008. doi: 10.1086/590103.

J. Bovy and H.-W. Rix. A Direct Dynamical Measurement of the Milky Way's Disk Surface Density Profile, Disk Scale Length, and Dark Matter Profile at 4 kpc $\lesssim$ R $\lesssim$ 9 kpc. ApJ, 779:115, December 2013. doi: 10.1088/0004-637X/779/2/115.

R. G. Bower, A. J. Benson, C. G. Lacey, C. M. Baugh, S. Cole, and C. S. Frenk. The impact of galaxy formation on the X-ray evolution of clusters. MNRAS, 325:497–508, August 2001. doi: 10.1046/j.1365-8711.2001.04382.x.

R. G. Bower, A. J. Benson, R. Malbon, J. C. Helly, C. S. Frenk, C. M. Baugh, S. Cole, and C. G. Lacey. Breaking the hierarchy of galaxy formation. MNRAS, 370:645–655, August 2006. doi: 10.1111/j.1365-2966.2006.10519.x.

R A A Bowler, R J McLure, J S Dunlop, D J McLeod, E R Stanway, J J Eldridge, and M J Jarvis. No evidence for Population III stars or a Direct Collapse Black Hole in the z = 6.6 Lyman-α emitter 'CR7'. *arXiv.org*, page arXiv:1609.00727, September 2016.

M. Boylan-Kolchin, C.-P. Ma, and E. Quataert. Dynamical friction and galaxy merging time-scales. MNRAS, 383:93–101, January 2008. doi: 10.1111/j.1365-2966.2007.12530.x.

M. Boylan-Kolchin, J. S. Bullock, and M. Kaplinghat. Too big to fail? The puzzling darkness of massive Milky Way subhaloes. MNRAS, 415:L40–L44, July 2011. doi: 10.1111/j.1745-3933.2011.01074.x.

M. Brightman and Y. Ueda. The evolution of the Compton thick fraction and the nature of obscuration for active galactic nuclei in the Chandra Deep Field South. MNRAS, 423: 702–717, June 2012. doi: 10.1111/j.1365-2966.2012.20908.x.

M. Brightman, J. D. Silverman, V. Mainieri, Y. Ueda, M. Schramm, K. Matsuoka, T. Nagao, C. Steinhardt, J. Kartaltepe, D. B. Sanders, E. Treister, O. Shemmer, W. N. Brandt, M. Brusa, A. Comastri, L. C. Ho, G. Lanzuisi, E. Lusso, K. Nandra, M. Salvato, G. Zamorani, M. Akiyama, D. M. Alexander, A. Bongiorno, P. Capak, F. Civano, A. Del Moro, A. Doi, M. Elvis, G. Hasinger, E. S. Laird, D. Masters, M. Mignoli, K. Ohta, K. Schawinski, and Y. Taniguchi. A statistical relation between the X-ray spectral index and Eddington ratio of active galactic nuclei in deep surveys. MNRAS, 433:2485–2496, August 2013. doi: 10.1093/mnras/stt920.

V. Bromm. Formation of the first stars. *Reports on Progress in Physics*, 76(11):112901, November 2013. doi: 10.1088/0034-4885/76/11/112901.

V. Bromm and A. Loeb. Formation of the First Supermassive Black Holes. ApJ, 596: 34–46, October 2003a. doi: 10.1086/377529.

V. Bromm and A. Loeb. Formation of the First Supermassive Black Holes. ApJ, 596: 34–46, October 2003b. doi: 10.1086/377529.

V. Bromm and A. Loeb. Accretion onto a primordial protostar. New A, 9:353–364, June 2004. doi: 10.1016/j.newast.2003.12.006.

V. Bromm, P. S. Coppi, and R. B. Larson. The Formation of the First Stars. I. The Primordial Star-forming Cloud. ApJ, 564:23–51, January 2002. doi: 10.1086/323947.

Greg L. Bryan and Michael L. Norman. Statistical properties of x-ray clusters: Analytic and numerical comparisons. *The Astrophysical Journal*, 495(1):80, 1998. URL `http://stacks.iop.org/0004-637X/495/i=1/a=80`.

J. Buchner, A. Georgakakis, K. Nandra, M. Brightman, M.-L. Menzel, Z. Liu, L.-T. Hsu, M. Salvato, C. Rangel, J. Aird, A. Merloni, and N. Ross. Obscuration-dependent Evolution of Active Galactic Nuclei. ApJ, 802:89, April 2015. doi: 10.1088/0004-637X/802/2/89.

F. Calura, R. Gilli, C. Vignali, F. Pozzi, A. Pipino, and F. Matteucci. The dust content of QSO hosts at high redshift. MNRAS, 438:2765–2783, March 2014. doi: 10.1093/mnras/stt2329.

M. Campanelli, C. Lousto, Y. Zlochower, and D. Merritt. Large Merger Recoils and Spin Flips from Generic Black Hole Binaries. ApJ, 659:L5–L8, April 2007. doi: 10.1086/516712.

M. Cano-Díaz, R. Maiolino, A. Marconi, H. Netzer, O. Shemmer, and G. Cresci. Observational evidence of quasar feedback quenching star formation at high redshift. A&A, 537:L8, January 2012. doi: 10.1051/0004-6361/201118358.

P. R. Capelo, M. Volonteri, M. Dotti, J. M. Bellovary, L. Mayer, and F. Governato. Growth and activity of black holes in galaxy mergers with varying mass ratios. MNRAS, 447:2123–2143, March 2015. doi: 10.1093/mnras/stu2500.

N. Cappelluti, P. Ranalli, M. Roncarelli, P. Arevalo, G. Zamorani, A. Comastri, R. Gilli, E. Rovilos, C. Vignali, V. Allevato, A. Finoguenov, T. Miyaji, F. Nicastro, I. Georgantopoulos, and A. Kashlinsky. The nature of the unresolved extragalactic cosmic soft x-ray background. MNRAS, 427:651, 2012.

N. Cappelluti, A. Kashlinsky, R. G. Arendt, A. Comastri, G. G. Fazio, A. Finoguenov, G. Hasinger, J. C. Mather, T. Miyaji, and S. H. Moseley. Cross-correlating cosmic infrared and x-ray background fluctuations: Evidence of significant black hole populations among the cib sources. ApJ, 769:68, 2013.

N. Cappelluti, A. Comastri, A. Fontana, G. Zamorani, R. Amorin, M. Castellano, E. Merlin, P. Santini, D. Elbaz, C. Schreiber, X. Shu, T. Wang, J. S. Dunlop, N. Bourne, V. A. Bruce, F. Buitrago, M. J. Michałowski, S. Derriere, H. C. Ferguson, S. M. Faber, and F. Vito. Chandra Counterparts of CANDELS GOODS-S Sources. ApJ, 823:95, June 2016. doi: 10.3847/0004-637X/823/2/95.

S. Carniani, A. Marconi, R. Maiolino, B. Balmaverde, M. Brusa, M. Cano-Díaz, C. Cicone, A. Comastri, G. Cresci, F. Fiore, C. Feruglio, F. La Franca, V. Mainieri, F. Mannucci, T. Nagao, H. Netzer, E. Piconcelli, G. Risaliti, R. Schneider, and O. Shemmer. Ionised outflows in z ~ 2.4 quasar host galaxies. A&A, 580:A102, August 2015. doi: 10.1051/0004-6361/201526557.

S. Carniani, A. Marconi, R. Maiolino, B. Balmaverde, M. Brusa, M. Cano-Díaz, C. Cicone, A. Comastri, G. Cresci, F. Fiore, C. Feruglio, F. La Franca, V. Mainieri, F. Mannucci, T. Nagao, H. Netzer, E. Piconcelli, G. Risaliti, R. Schneider, and O. Shemmer. Fast outflows and star formation quenching in quasar host galaxies. A&A, 591:A28, June 2016. doi: 10.1051/0004-6361/201528037.

S. M. Carroll, W. H. Press, and E. L. Turner. The cosmological constant. ARA&A, 30: 499–542, 1992. doi: 10.1146/annurev.aa.30.090192.002435.

B. Carter. Axisymmetric black hole has only two degrees of freedom. *Phys. Rev. Lett.*, 26:331–333, Feb 1971. doi: 10.1103/PhysRevLett.26.331. URL `https://link.aps.org/doi/10.1103/PhysRevLett.26.331`.

A. Cavaliere, A. Lapi, and N. Menci. Quasar Feedback on the Intracluster Medium. ApJ, 581:L1–L4, December 2002. doi: 10.1086/345890.

R. Cen and M. A. Riquelme. Lower Metal Enrichment of Virialized Gas in Minihalos. ApJ, 674:644-652, February 2008. doi: 10.1086/524724.

S. Chandrasekhar. The Stability of Non-Dissipative Couette Flow in Hydromagnetics. *Proceedings of the National Academy of Science*, 46:253–257, February 1960. doi: 10.1073/pnas.46.2.253.

K.-J. Chen, D. J. Whalen, K. M. J. Wollenberg, S. C. O. Glover, and R. S. Klessen. How the First Stars Regulated Star Formation: Enrichment by Nearby Supernovae. *ArXiv e-prints*, October 2016.

S. Chon, S. Hirano, T. Hosokawa, and N. Yoshida. Cosmological Simulations of Early Black Hole Formation: Halo Mergers, Tidal Disruption, and the Conditions for Direct Collapse. ApJ, 832:134, December 2016. doi: 10.3847/0004-637X/832/2/134.

C. Cicone, R. Maiolino, S. Gallerani, R. Neri, A. Ferrara, E. Sturm, F. Fiore, E. Piconcelli, and C. Feruglio. Very extended cold gas, star formation and outflows in the halo of a bright quasar at z > 6. A&A, 574:A14, February 2015. doi: 10.1051/0004-6361/201424980.

L. Ciotti, J. P. Ostriker, and D. Proga. Feedback from Central Black Holes in Elliptical Galaxies. I. Models with Either Radiative or Mechanical Feedback but not Both. ApJ, 699:89–104, July 2009. doi: 10.1088/0004-637X/699/1/89.

L. Ciotti, J. P. Ostriker, and D. Proga. Feedback from Central Black Holes in Elliptical Galaxies. III. Models with Both Radiative and Mechanical Feedback. ApJ, 717:708–723, July 2010. doi: 10.1088/0004-637X/717/2/708.

F. Civano, S. Marchesi, A. Comastri, M. C. Urry, M. Elvis, N. Cappelluti, S. Puccetti, M. Brusa, G. Zamorani, G. Hasinger, T. Aldcroft, D. M. Alexander, V. Allevato, H. Brunner, P. Capak, A. Finoguenov, F. Fiore, A. Fruscione, R. Gilli, K. Glotfelty, R. E. Griffiths, H. Hao, F. A. Harrison, K. Jahnke, J. Kartaltepe, A. Karim, S. M. LaMassa, G. Lanzuisi, T. Miyaji, P. Ranalli, M. Salvato, M. Sargent, N. J. Scoville, K. Schawinski, E. Schinnerer, J. Silverman, V. Smolcic, D. Stern, S. Toft, B. Trakhtenbrot, E. Treister, and C. Vignali. The Chandra Cosmos Legacy Survey: Overview and Point Source Catalog. ApJ, 819:62, March 2016. doi: 10.3847/0004-637X/819/1/62.

P. C. Clark, S. C. O. Glover, and R. S. Klessen. The First Stellar Cluster. ApJ, 672:757-764, January 2008. doi: 10.1086/524187.

P. C. Clark, S. C. O. Glover, R. J. Smith, T. H. Greif, R. S. Klessen, and V. Bromm. The Formation and Fragmentation of Disks Around Primordial Protostars. *Science*, 331: 1040, February 2011. doi: 10.1126/science.1198027.

M. Colless, G. Dalton, S. Maddox, W. Sutherland, P. Norberg, S. Cole, J. Bland-Hawthorn, T. Bridges, R. Cannon, C. Collins, W. Couch, N. Cross, K. Deeley, R. De Propris, S. P. Driver, G. Efstathiou, R. S. Ellis, C. S. Frenk, K. Glazebrook, C. Jackson, O. Lahav, I. Lewis, S. Lumsden, D. Madgwick, J. A. Peacock, B. A. Peterson, I. Price, M. Seaborne, and K. Taylor. The 2dF Galaxy Redshift Survey: spectra and redshifts. MNRAS, 328:1039–1063, December 2001. doi: 10.1046/j.1365-8711.2001.04902.x.

T. Costa, D. Sijacki, and M. G. Haehnelt. Feedback from active galactic nuclei: energy-versus momentum-driving. MNRAS, 444:2355–2376, November 2014. doi: 10.1093/mnras/stu1632.

T. Costa, D. Sijacki, and M. G. Haehnelt. Fast cold gas in hot AGN outflows. MNRAS, 448:L30–L34, March 2015. doi: 10.1093/mnrasl/slu193.

T. J. Cox, P. Jonsson, R. S. Somerville, J. R. Primack, and A. Dekel. The effect of galaxy mass ratio on merger-driven starbursts. MNRAS, 384:386–409, February 2008. doi: 10.1111/j.1365-2966.2007.12730.x.

G. Cresci, A. Marconi, S. Zibetti, G. Risaliti, S. Carniani, F. Mannucci, A. Gallazzi, R. Maiolino, B. Balmaverde, M. Brusa, A. Capetti, C. Cicone, C. Feruglio, J. Bland-Hawthorn, T. Nagao, E. Oliva, M. Salvato, E. Sani, P. Tozzi, T. Urrutia, and G. Venturi. The MAGNUM survey: positive feedback in the nuclear region of NGC 5643 suggested by MUSE. A&A, 582:A63, October 2015. doi: 10.1051/0004-6361/201526581.

D. J. Croton, V. Springel, S. D. M. White, G. De Lucia, C. S. Frenk, L. Gao, A. Jenkins, G. Kauffmann, J. F. Navarro, and N. Yoshida. The many lives of active galactic nuclei: cooling flows, black holes and the luminosities and colours of galaxies. MNRAS, 365: 11–28, January 2006. doi: 10.1111/j.1365-2966.2005.09675.x.

A. D'Aloisio, P. R. Upton Sanderbeck, M. McQuinn, H. Trac, and P. R. Shapiro. On the Contribution of Active Galactic Nuclei to the High-Redshift Metagalactic Ionizing Background. *ArXiv e-prints*, July 2016.

M. B. Davies, M. C. Miller, and J. M. Bellovary. Supermassive Black Hole Formation Via Gas Accretion in Nuclear Stellar Clusters. ApJ, 740:L42, 2011.

M. de Bennassuti, R. Schneider, R. Valiante, and S. Salvadori. Decoding the stellar fossils of the dusty Milky Way progenitors. MNRAS, 445:3039–3054, December 2014. doi: 10.1093/mnras/stu1962.

M. de Bennassuti, S. Salvadori, R. Schneider, R. Valiante, and K. Omukai. Limits on Population III star formation with the most iron-poor stars. MNRAS, 465:926–940, February 2017. doi: 10.1093/mnras/stw2687.

G. De Lucia, M. Boylan-Kolchin, A. J. Benson, F. Fontanot, and P. Monaco. A semi-analytic model comparison - gas cooling and galaxy mergers. MNRAS, 406:1533–1552, August 2010. doi: 10.1111/j.1365-2966.2010.16806.x.

G. De Rosa, R. Decarli, F. Walter, X. Fan, L. Jiang, J. Kurk, A. Pasquali, and H. W. Rix. Evidence for Non-evolving Fe II/Mg II Ratios in Rapidly Accreting z ˜ 6 QSOs. ApJ, 739:56, October 2011. doi: 10.1088/0004-637X/739/2/56.

G. De Rosa, B. P. Venemans, R. Decarli, M. Gennaro, R. A. Simcoe, M. Dietrich, B. M. Peterson, F. Walter, S. Frank, R. G. McMahon, P. C. Hewett, D. J. Mortlock, and C. Simpson. Black Hole Mass Estimates and Emission-line Properties of a Sample of Redshift z > 6.5 Quasars. ApJ, 790:145, August 2014. doi: 10.1088/0004-637X/790/2/145.

M. den Brok, A. C. Seth, A. J. Barth, D. J. Carson, N. Neumayer, M. Cappellari, V. P. Debattista, L. C. Ho, C. E. Hood, and R. M. McDermid. Measuring the Mass of the Central Black Hole in the Bulgeless Galaxy NGC 4395 from Gas Dynamical Modeling. ApJ, 809:101, August 2015. doi: 10.1088/0004-637X/809/1/101.

B. Devecchi and M. Volonteri. Formation of the First Nuclear Clusters and Massive Black Holes at High Redshift. ApJ, 694:302–313, March 2009. doi: 10.1088/0004-637X/694/1/302.

B. Devecchi, M. Volonteri, M. Colpi, and F. Haardt. High-redshift formation and evolution of central massive objects - I. Model description. MNRAS, 409:1057–1067, December 2010. doi: 10.1111/j.1365-2966.2010.17363.x.

B. Devecchi, M. Volonteri, E. M. Rossi, M. Colpi, and S. Portegies Zwart. High-redshift formation and evolution of central massive objects - II. The census of BH seeds. MNRAS, 421:1465–1475, April 2012. doi: 10.1111/j.1365-2966.2012.20406.x.

T. Di Matteo, V. Springel, and L. Hernquist. Energy input from quasars regulates the growth and activity of black holes and their host galaxies. Nature, 433:604–607, February 2005. doi: 10.1038/nature03335.

T. Di Matteo, N. Khandai, C. DeGraf, Y. Feng, R. A. C. Croft, J. Lopez, and V. Springel.

Cold Flows and the First Quasars. ApJ, 745:L29, February 2012. doi: 10.1088/2041-8205/745/2/L29.

T. Di Matteo, R. A. C. Croft, Y. Feng, D. Waters, and S. Wilkins. The origin of most massive black holes at high-z: BLUETIDES and the next quasar frontier. *ArXiv e-prints*, June 2016.

R. Diehl, H. Halloin, K. Kretschmer, G. G. Lichti, V. Schönfelder, A. W. Strong, A. von Kienlin, W. Wang, P. Jean, J. Knödlseder, J.-P. Roques, G. Weidenspointner, S. Schanne, D. H. Hartmann, C. Winkler, and C. Wunderer. Radioactive ^{26}Al from massive stars in the Galaxy. Nature, 439:45–47, January 2006. doi: 10.1038/nature04364.

M. Dijkstra, Z. Haiman, A. Mesinger, and J. S. B. Wyithe. Fluctuations in the high-redshift Lyman-Werner background: close halo pairs as the origin of supermassive black holes. MNRAS, 391:1961–1972, December 2008. doi: 10.1111/j.1365-2966.2008.14031.x.

M. Dijkstra, A. Ferrara, and A. Mesinger. Feedback-regulated supermassive black hole seed formation. MNRAS, 442:2036–2047, August 2014. doi: 10.1093/mnras/stu1007.

M. Dijkstra, M. Gronke, and D. Sobral. Lyα Signatures from Direct Collapse Black Holes. ApJ, 823:74, June 2016. doi: 10.3847/0004-637X/823/2/74.

D. Downes and P. M. Solomon. Rotating Nuclear Rings and Extreme Starbursts in Ultraluminous Galaxies. ApJ, 507:615–654, November 1998. doi: 10.1086/306339.

Y. Dubois, C. Pichon, C. Welker, D. Le Borgne, J. Devriendt, C. Laigle, S. Codis, D. Pogosyan, S. Arnouts, K. Benabed, E. Bertin, J. Blaizot, F. Bouchet, J.-F. Cardoso, S. Colombi, V. de Lapparent, V. Desjacques, R. Gavazzi, S. Kassin, T. Kimm, H. McCracken, B. Milliard, S. Peirani, S. Prunet, S. Rouberol, J. Silk, A. Slyz, T. Sousbie, R. Teyssier, L. Tresse, M. Treyer, D. Vibert, and M. Volonteri. Dancing in the dark: galactic properties trace spin swings along the cosmic web. MNRAS, 444:1453–1468, October 2014a. doi: 10.1093/mnras/stu1227.

Y. Dubois, M. Volonteri, and J. Silk. Black hole evolution - III. Statistical properties of mass growth and spin evolution using large-scale hydrodynamical cosmological simulations. MNRAS, 440:1590–1606, May 2014b. doi: 10.1093/mnras/stu373.

E. Dwek and I. Cherchneff. The Origin of Dust in the Early Universe: Probing the Star Formation History of Galaxies by Their Dust Content. ApJ, 727:63, February 2011. doi: 10.1088/0004-637X/727/2/63.

E. Dwek, F. Galliano, and A. P. Jones. The Evolution of Dust in the Early Universe with Applications to the Galaxy SDSS J1148+5251. ApJ, 662:927–939, June 2007. doi: 10.1086/518430.

D. J. Eisenstein and A. Loeb. Origin of quasar progenitors from the collapse of low-spin cosmological perturbations. ApJ, 443:11–17, April 1995. doi: 10.1086/175498.

X. Fan, V. K. Narayanan, R. H. Lupton, M. A. Strauss, G. R. Knapp, R. H. Becker, R. L. White, L. Pentericci, S. K. Leggett, Z. Haiman, J. E. Gunn, Ž. Ivezić, D. P. Schneider, S. F. Anderson, J. Brinkmann, N. A. Bahcall, A. J. Connolly, I. Csabai, M. Doi, M. Fukugita, T. Geballe, E. K. Grebel, D. Harbeck, G. Hennessy, D. Q. Lamb, G. Miknaitis, J. A. Munn, R. Nichol, S. Okamura, J. R. Pier, F. Prada, G. T. Richards, A. Szalay, and D. G. York. A Survey of z>5.8 Quasars in the Sloan Digital Sky Survey. I. Discovery of Three New Quasars and the Spatial Density of Luminous Quasars at z~6. AJ, 122: 2833–2849, December 2001. doi: 10.1086/324111.

X. Fan, M. A. Strauss, D. P. Schneider, R. H. Becker, R. L. White, Z. Haiman, M. Gregg, L. Pentericci, E. K. Grebel, V. K. Narayanan, Y.-S. Loh, G. T. Richards, J. E. Gunn, R. H. Lupton, G. R. Knapp, Ž. Ivezić, W. N. Brandt, M. Collinge, L. Hao, D. Harbeck, F. Prada, J. Schaye, I. Strateva, N. Zakamska, S. Anderson, J. Brinkmann, N. A. Bahcall, D. Q. Lamb, S. Okamura, A. Szalay, and D. G. York. A Survey of z>5.7 Quasars in the Sloan Digital Sky Survey. II. Discovery of Three Additional Quasars at z>6. AJ, 125: 1649–1659, April 2003. doi: 10.1086/368246.

X. Fan, J. F. Hennawi, G. T. Richards, M. A. Strauss, D. P. Schneider, J. L. Donley, J. E. Young, J. Annis, H. Lin, H. Lampeitl, R. H. Lupton, J. E. Gunn, G. R. Knapp, W. N. Brandt, S. Anderson, N. A. Bahcall, J. Brinkmann, R. J. Brunner, M. Fukugita, A. S. Szalay, G. P. Szokoly, and D. G. York. A Survey of z>5.7 Quasars in the Sloan Digital Sky Survey. III. Discovery of Five Additional Quasars. AJ, 128:515–522, August 2004. doi: 10.1086/422434.

X. Fan, M. A. Strauss, G. T. Richards, J. F. Hennawi, R. H. Becker, R. L. White, A. M. Diamond-Stanic, J. L. Donley, L. Jiang, J. S. Kim, M. Vestergaard, J. E. Young, J. E. Gunn, R. H. Lupton, G. R. Knapp, D. P. Schneider, W. N. Brandt, N. A. Bahcall, J. C. Barentine, J. Brinkmann, H. J. Brewington, M. Fukugita, M. Harvanek, S. J. Kleinman, J. Krzesinski, D. Long, E. H. Neilsen, Jr., A. Nitta, S. A. Snedden, and W. Voges. A Survey of z>5.7 Quasars in the Sloan Digital Sky Survey. IV. Discovery of Seven Additional Quasars. AJ, 131:1203–1209, March 2006. doi: 10.1086/500296.

D. Farrah, T. Urrutia, M. Lacy, A. Efstathiou, J. Afonso, K. Coppin, P. B. Hall, C. Lonsdale, T. Jarrett, C. Bridge, C. Borys, and S. Petty. Direct Evidence for Termination of Obscured Star Formation by Radiatively Driven Outflows in Reddened QSOs. ApJ, 745: 178, February 2012. doi: 10.1088/0004-637X/745/2/178.

A. Fattahi, J. F. Navarro, T. Sawala, C. S. Frenk, L. V. Sales, K. Oman, M. Schaller, and J. Wang. The cold dark matter content of Galactic dwarf spheroidals: no cores, no failures, no problem. *ArXiv e-prints*, July 2016.

Y. Feng, T. Di Matteo, R. Croft, and N. Khandai. High-redshift supermassive black holes: accretion through cold flows. MNRAS, 440:1865–1879, May 2014. doi: 10.1093/mnras/stu432.

Y. Feng, T. Di Matteo, R. Croft, A. Tenneti, S. Bird, N. Battaglia, and S. Wilkins. The Formation of Milky Way-mass Disk Galaxies in the First 500 Million Years of a Cold Dark Matter Universe. ApJ, 808:L17, July 2015. doi: 10.1088/2041-8205/808/1/L17.

Y. Feng, T. Di-Matteo, R. A. Croft, S. Bird, N. Battaglia, and S. Wilkins. The BlueTides simulation: first galaxies and reionization. MNRAS, 455:2778–2791, January 2016. doi: 10.1093/mnras/stv2484.

A. Ferrara, S. Salvadori, B. Yue, and D. Schleicher. Initial mass function of intermediate-mass black hole seeds. MNRAS, 443:2410–2425, September 2014. doi: 10.1093/mnras/stu1280.

A. Ferrara, S. Viti, and C. Ceccarelli. The problematic growth of dust in high-redshift galaxies. MNRAS, 463:L112–L116, November 2016. doi: 10.1093/mnrasl/slw165.

C. Feruglio, R. Maiolino, E. Piconcelli, N. Menci, H. Aussel, A. Lamastra, and F. Fiore. Quasar feedback revealed by giant molecular outflows. A&A, 518:L155, July 2010. doi: 10.1051/0004-6361/201015164.

C. Feruglio, F. Fiore, S. Carniani, E. Piconcelli, L. Zappacosta, A. Bongiorno, C. Cicone, R. Maiolino, A. Marconi, N. Menci, S. Puccetti, and S. Veilleux. The multi-phase winds of Markarian 231: from the hot, nuclear, ultra-fast wind to the galaxy-scale, molecular outflow. A&A, 583:A99, November 2015. doi: 10.1051/0004-6361/201526020.

M. Fiocchi, A. Bazzano, P. Ubertini, and A. A. Zdziarski. The First Detection of Compton Reflection in the Low-Mass X-Ray Binary 4U 1705-44 with INTEGRAL and BeppoSax. ApJ, 657:448–452, March 2007. doi: 10.1086/510573.

F. Fiore, S. Puccetti, A. Grazian, N. Menci, F. Shankar, P. Santini, E. Piconcelli, A. M. Koekemoer, A. Fontana, K. Boutsia, M. Castellano, A. Lamastra, C. Malacaria, C. Feruglio, S. Mathur, N. Miller, and M. Pannella. Faint high-redshift AGN in the Chandra deep field south: the evolution of the AGN luminosity function and black hole demography. A&A, 537:A16, January 2012. doi: 10.1051/0004-6361/201117581.

M. Fumagalli, J. M. O'Meara, and J. X. Prochaska. Detection of Pristine Gas Two Billion Years After the Big Bang. *Science*, 334:1245, December 2011. doi: 10.1126/science.1213581.

V. Gaibler, S. Khochfar, M. Krause, and J. Silk. Jet-induced star formation in gas-rich galaxies. MNRAS, 425:438–449, September 2012. doi: 10.1111/j.1365-2966.2012.21479.x.

C. Gall, A. C. Andersen, and J. Hjorth. Genesis and evolution of dust in galaxies in the early Universe. II. Rapid dust evolution in quasars at z $\gtrsim$ 6. A&A, 528:A14, April 2011a. doi: 10.1051/0004-6361/201015605.

C. Gall, J. Hjorth, and A. C. Andersen. Production of dust by massive stars at high redshift. A&A Rev., 19:43, September 2011b. doi: 10.1007/s00159-011-0043-7.

S. Gallerani, R. Maiolino, Y. Juarez, T. Nagao, A. Marconi, S. Bianchi, R. Schneider, F. Mannucci, T. Oliva, C. J. Willott, L. Jiang, and X. Fan. The extinction law at high redshift and its implications. A&A, 523:A85, November 2010. doi: 10.1051/0004-6361/201014721.

S. Gallerani, A. Ferrara, R. Neri, and R. Maiolino. First CO(17-16) emission line detected in a $z > 6$ quasar. MNRAS, 445:2848–2853, December 2014. doi: 10.1093/mnras/stu2031.

S. Gallerani, X. Fan, R. Maiolino, and F. Pacucci. Physical Properties of the First Quasars. PASA, 34:e022, May 2017. doi: 10.1017/pasa.2017.14.

E. Gallo, T. Treu, J. Jacob, J.-H. Woo, P. J. Marshall, and R. Antonucci. AMUSE-Virgo. I. Supermassive Black Holes in Low-Mass Spheroids. ApJ, 680:154-168, June 2008. doi: 10.1086/588012.

E. Gallo, T. Treu, P. J. Marshall, J.-H. Woo, C. Leipski, and R. Antonucci. AMUSE-Virgo. II. Down-sizing in Black Hole Accretion. ApJ, 714:25–36, May 2010. doi: 10.1088/0004-637X/714/1/25.

P. Gandhi, O. Garcet, L. Disseau, F. Pacaud, M. Pierre, A. Gueguen, D. Alloin, L. Chiappetti, E. Gosset, D. Maccagni, J. Surdej, and I. Valtchanov. The XMM large scale structure survey: properties and two-point angular correlations of point-like sources. A&A, 457:393–404, October 2006. doi: 10.1051/0004-6361:20065284.

K. Gebhardt, T. R. Lauer, J. Kormendy, J. Pinkney, G. A. Bower, R. Green, T. Gull, J. B. Hutchings, M. E. Kaiser, C. H. Nelson, D. Richstone, and D. Weistrop. M33: A Galaxy with No Supermassive Black Hole. AJ, 122:2469–2476, November 2001. doi: 10.1086/323481.

A. Georgakakis, J. Aird, J. Buchner, M. Salvato, M.-L. Menzel, W. N. Brandt, I. D. McGreer, T. Dwelly, G. Mountrichas, C. Koki, I. Georgantopoulos, L.-T. Hsu, A. Merloni, Z. Liu, K. Nandra, and N. P. Ross. The X-ray luminosity function of active galactic nuclei in the redshift interval z=3-5. MNRAS, 453:1946–1964, October 2015. doi: 10.1093/mnras/stv1703.

G. Ghisellini, F. Haardt, and G. Matt. The Contribution of the Obscuring Torus to the X-

Ray Spectrum of Seyfert Galaxies - a Test for the Unification Model. MNRAS, 267:743, April 1994. doi: 10.1093/mnras/267.3.743.

E. Giallongo, N. Menci, A. Grazian, R. Fassbender, A. Fontana, D. Paris, and L. Pentericci. The Detection of Ultra-faint Low Surface Brightness Dwarf Galaxies in the Virgo Cluster: A Probe of Dark Matter and Baryonic Physics. ApJ, 813:68, November 2015. doi: 10.1088/0004-637X/813/1/68.

R. Gilli, A. Comastri, and G. Hasinger. The synthesis of the cosmic X-ray background in the Chandra and XMM-Newton era. A&A, 463:79–96, February 2007. doi: 10.1051/0004-6361:20066334.

S. Glover. The First Stars. In T. Wiklind, B. Mobasher, and V. Bromm, editors, *Astrophysics and Space Science Library*, volume 396 of *Astrophysics and Space Science Library*, page 103, 2013. doi: 10.1007/978-3-642-32362-1_3.

S. C. O. Glover. Simulating the formation of massive seed black holes in the early Universe - I. An improved chemical model. MNRAS, 451:2082–2096, August 2015a. doi: 10.1093/mnras/stv1059.

S. C. O. Glover. Simulating the formation of massive seed black holes in the early Universe - II. Impact of rate coefficient uncertainties. MNRAS, 453:2901–2918, November 2015b. doi: 10.1093/mnras/stv1781.

N. Y. Gnedin. Effect of Reionization on Structure Formation in the Universe. ApJ, 542:535–541, October 2000. doi: 10.1086/317042.

G. L. Granato, G. De Zotti, L. Silva, A. Bressan, and L. Danese. A Physical Model for the Coevolution of QSOs and Their Spheroidal Hosts. ApJ, 600:580–594, January 2004. doi: 10.1086/379875.

L. Graziani, A. Maselli, and B. Ciardi. CRASH3: cosmological radiative transfer through metals. *MNRAS*, 431:722–740, May 2013. doi: 10.1093/mnras/stt206.

L. Graziani, S. Salvadori, R. Schneider, D. Kawata, M. de Bennassuti, and A. Maselli. Galaxy formation with radiative and chemical feedback. MNRAS, 449:3137–3148, May 2015. doi: 10.1093/mnras/stv494.

L. Graziani, M. de Bennassuti, R. Schneider, D. Kawata, and S. Salvadori. The history of the dark and luminous side of Milky Way-like progenitors. MNRAS, 469:1101–1116, July 2017. doi: 10.1093/mnras/stx900.

J. E. Greene. Low-mass black holes as the remnants of primordial black hole formation. *Nature Communications*, 3:1304, December 2012. doi: 10.1038/ncomms2314.

J. E. Greene and L. C. Ho. Active Galactic Nuclei with Candidate Intermediate-Mass Black Holes. ApJ, 610:722–736, August 2004. doi: 10.1086/421719.

J. E. Greene and L. C. Ho. Estimating Black Hole Masses in Active Galaxies Using the Hα Emission Line. ApJ, 630:122–129, September 2005. doi: 10.1086/431897.

J. E. Greene and L. C. Ho. A New Sample of Low-Mass Black Holes in Active Galaxies. ApJ, 670:92–104, November 2007. doi: 10.1086/522082.

J. E. Greene, C. Y. Peng, M. Kim, C.-Y. Kuo, J. A. Braatz, C. M. V. Impellizzeri, J. J. Condon, K. Y. Lo, C. Henkel, and M. J. Reid. Precise Black Hole Masses from Megamaser Disks: Black Hole-Bulge Relations at Low Mass. ApJ, 721:26–45, September 2010. doi: 10.1088/0004-637X/721/1/26.

T. H. Greif and V. Bromm. Two populations of metal-free stars in the early Universe. MNRAS, 373:128–138, November 2006. doi: 10.1111/j.1365-2966.2006.11017.x.

T. H. Greif, J. L. Johnson, V. Bromm, and R. S. Klessen. The First Supernova Explosions: Energetics, Feedback, and Chemical Enrichment. ApJ, 670:1–14, November 2007. doi: 10.1086/522028.

T. H. Greif, V. Springel, S. D. M. White, S. C. O. Glover, P. C. Clark, R. J. Smith, R. S. Klessen, and V. Bromm. Simulations on a Moving Mesh: The Clustered Formation of Population III Protostars. ApJ, 737:75, August 2011. doi: 10.1088/0004-637X/737/2/75.

T. H. Greif, V. Bromm, P. C. Clark, S. C. O. Glover, R. J. Smith, R. S. Klessen, N. Yoshida, and V. Springel. Formation and evolution of primordial protostellar systems. MNRAS, 424:399–415, July 2012. doi: 10.1111/j.1365-2966.2012.21212.x.

D. Grupe. A Complete Sample of Soft X-Ray-selected AGNs. II. Statistical Analysis. AJ, 127:1799–1810, April 2004. doi: 10.1086/382516.

K. Gültekin, D. O. Richstone, K. Gebhardt, T. R. Lauer, S. Tremaine, M. C. Aller, R. Bender, A. Dressler, S. M. Faber, A. V. Filippenko, R. Green, L. C. Ho, J. Kormendy, J. Magorrian, J. Pinkney, and C. Siopis. The M-σ and M-L Relations in Galactic Bulges, and Determinations of Their Intrinsic Scatter. ApJ, 698:198–221, June 2009. doi: 10.1088/0004-637X/698/1/198.

Y. Guo, H. C. Ferguson, M. Giavalisco, G. Barro, S. P. Willner, M. L. N. Ashby, T. Dahlen, J. L. Donley, S. M. Faber, A. Fontana, A. Galametz, A. Grazian, K.-H. Huang, D. D. Kocevski, A. M. Koekemoer, D. C. Koo, E. J. McGrath, M. Peth, M. Salvato, S. Wuyts, M. Castellano, A. R. Cooray, M. E. Dickinson, J. S. Dunlop, G. G. Fazio, J. P. Gardner, E. Gawiser, N. A. Grogin, N. P. Hathi, L.-T. Hsu, K.-S. Lee, R. A. Lucas, B. Mobasher, K. Nandra, J. A. Newman, and A. van der Wel. CANDELS Multi-wavelength Catalogs: Source Detection and Photometry in the GOODS-South Field. ApJS, 207:24, August 2013. doi: 10.1088/0067-0049/207/2/24.

M. Habouzit, M. Volonteri, and Y. Dubois. Blossoms from black hole seeds: properties and early growth regulated by supernova feedback. *ArXiv e-prints*, May 2016a.

M. Habouzit, M. Volonteri, M. Latif, Y. Dubois, and S. Peirani. On the number density of 'direct collapse' black hole seeds. MNRAS, 463:529–540, November 2016b. doi: 10.1093/mnras/stw1924.

M. Habouzit, M. Volonteri, M. Latif, T. Nishimichi, S. Peirani, Y. Dubois, G. A. Mamon, J. Silk, and J. Chevallard. Black hole formation and growth with non-Gaussian primordial density perturbations. MNRAS, 456:1901–1912, February 2016c. doi: 10.1093/mnras/stv2740.

L. Haemmerlé, T. E. Woods, R. S. Klessen, A. Heger, and D. J. Whalen. The Evolution of Supermassive Population III Stars. *ArXiv e-prints*, May 2017.

D. Haggard, P. J. Green, S. F. Anderson, A. Constantin, T. L. Aldcroft, D.-W. Kim, and W. A. Barkhouse. The Field X-ray AGN Fraction to z = 0.7 from the Chandra Multiwavelength Project and the Sloan Digital Sky Survey. ApJ, 723:1447–1468, November 2010. doi: 10.1088/0004-637X/723/2/1447.

O. Hahn and T. Abel. Multi-scale initial conditions for cosmological simulations. MNRAS, 415:2101–2121, August 2011. doi: 10.1111/j.1365-2966.2011.18820.x.

Z. Haiman. Constraints from Gravitational Recoil on the Growth of Supermassive Black Holes at High Redshift. ApJ, 613:36–40, September 2004. doi: 10.1086/422910.

Z. Haiman. The Formation of the First Massive Black Holes. In T. Wiklind, B. Mobasher, and V. Bromm, editors, *The First Galaxies*, volume 396 of *Astrophysics and Space Science Library*, page 293, 2013. doi: 10.1007/978-3-642-32362-1_6.

Z. Haiman and A. Loeb. Signatures of Stellar Reionization of the Universe. ApJ, 483: 21–37, July 1997. doi: 10.1086/304238.

Z. Haiman and A. Loeb. What Is the Highest Plausible Redshift of Luminous Quasars? ApJ, 552:459–463, May 2001. doi: 10.1086/320586.

Z. Haiman, M. J. Rees, and A. Loeb. H 2 Cooling of Primordial Gas Triggered by UV Irradiation. ApJ, 467:522, August 1996. doi: 10.1086/177628.

T. Hartwig, S. C. O. Glover, R. S. Klessen, M. A. Latif, and M. Volonteri. How an improved implementation of H_2 self-shielding influences the formation of massive stars and black holes. MNRAS, 452:1233–1244, September 2015. doi: 10.1093/mnras/stv1368.

T. Hartwig, M. A. Latif, M. Magg, V. Bromm, R. S. Klessen, S. C. O. Glover, D. J. Whalen, E. W. Pellegrini, and M. Volonteri. Exploring the nature of the Lyman-α emitter CR7. MNRAS, 462:2184–2202, October 2016. doi: 10.1093/mnras/stw1775.

A. Heger and S. E. Woosley. The Nucleosynthetic Signature of Population III. ApJ, 567: 532–543, March 2002. doi: 10.1086/338487.

A. Heger and S. E. Woosley. Nucleosynthesis and Evolution of Massive Metal-free Stars. ApJ, 724:341–373, November 2010. doi: 10.1088/0004-637X/724/1/341.

A. Heger, C. L. Fryer, S. E. Woosley, N. Langer, and D. H. Hartmann. How Massive Single Stars End Their Life. ApJ, 591:288–300, July 2003. doi: 10.1086/375341.

L. Hernquist. An analytical model for spherical galaxies and bulges. ApJ, 356:359–364, June 1990. doi: 10.1086/168845.

S. Hirano, T. Hosokawa, N. Yoshida, H. Umeda, K. Omukai, G. Chiaki, and H. W. Yorke. One Hundred First Stars: Protostellar Evolution and the Final Masses. ApJ, 781:60, February 2014. doi: 10.1088/0004-637X/781/2/60.

S. Hirano, T. Hosokawa, N. Yoshida, K. Omukai, and H. W. Yorke. Primordial star formation under the influence of far ultraviolet radiation: 1540 cosmological haloes and the stellar mass distribution. MNRAS, 448:568–587, March 2015. doi: 10.1093/mnras/stv044.

H. Hirashita and A. Ferrara. Effects of dust grains on early galaxy evolution. MNRAS, 337:921–937, December 2002. doi: 10.1046/j.1365-8711.2002.05968.x.

A. M. Hopkins. On the Evolution of Star-forming Galaxies. ApJ, 615:209–221, November 2004. doi: 10.1086/424032.

P. F. Hopkins and M. Elvis. Quasar feedback: more bang for your buck. MNRAS, 401: 7–14, January 2010. doi: 10.1111/j.1365-2966.2009.15643.x.

T. Hosokawa, K. Omukai, N. Yoshida, and H. W. Yorke. Protostellar Feedback Halts the Growth of the First Stars in the Universe. *Science*, 334:1250–, December 2011. doi: 10.1126/science.1207433.

T. Hosokawa, S. Hirano, R. Kuiper, H. W. Yorke, K. Omukai, and N. Yoshida. Formation of Massive Primordial Stars: Intermittent UV Feedback with Episodic Mass Accretion. ApJ, 824:119, June 2016. doi: 10.3847/0004-637X/824/2/119.

E. Hubble. A Relation between Distance and Radial Velocity among Extra-Galactic Nebulae. *Proceedings of the National Academy of Science*, 15:168–173, March 1929. doi: 10.1073/pnas.15.3.168.

L. Hunt, L. Magrini, D. Galli, R. Schneider, S. Bianchi, R. Maiolino, D. Romano, M. Tosi, and R. Valiante. Scaling relations of metallicity, stellar mass and star formation rate in metal-poor starbursts - I. A Fundamental Plane. MNRAS, 427:906–918, December 2012. doi: 10.1111/j.1365-2966.2012.21761.x.

L. Hunt, P. Dayal, L. Magrini, and A. Ferrara. Coevolution of metallicity and star formation in galaxies to z $\simeq$ 3.7 - II. A theoretical model. MNRAS, 463:2020–2031, December 2016. doi: 10.1093/mnras/stw2091.

K. Husband, M. N. Bremer, E. R. Stanway, L. J. M. Davies, M. D. Lehnert, and L. S. Douglas. Are z $\sim$ 5 quasars found in the most massive high-redshift overdensities? MNRAS, 432:2869–2877, July 2013. doi: 10.1093/mnras/stt642.

V. Icke. Gas flow above an alpha disk. AJ, 85:329–347, March 1980. doi: 10.1086/112678.

I. T. Iliev, G. Mellema, P. R. Shapiro, and U.-L. Pen. Self-regulated reionization. MNRAS, 376:534–548, April 2007. doi: 10.1111/j.1365-2966.2007.11482.x.

K. Inayoshi and K. Omukai. Effect of cosmic ray/x-ray ionization on supermassive black hole formation. MNRAS, 416:2748, 2011.

K. Inayoshi and K. Omukai. Supermassive black hole formation by cold accretion shocks in the first galaxies. MNRAS, 422:2539–2546, May 2012. doi: 10.1111/j.1365-2966.2012.20812.x.

K. Inayoshi and T. L. Tanaka. The suppression of direct collapse black hole formation by soft X-ray irradiation. MNRAS, 450:4350–4363, July 2015. doi: 10.1093/mnras/stv871.

K. Inayoshi, K. Omukai, and E. Tasker. Formation of an embryonic supermassive star in the first galaxy. MNRAS, 445:L109–L113, November 2014. doi: 10.1093/mnrasl/slu151.

K. Inayoshi, Z. Haiman, and J. P. Ostriker. Hyper-Eddington accretion flows onto massive black holes. *ArXiv e-prints*, November 2015.

W. Israel. Event Horizons in Static Vacuum Space-Times. *Physical Review*, 164:1776–1779, December 1967. doi: 10.1103/PhysRev.164.1776.

J. R. Jardel and K. Gebhardt. The Dark Matter Density Profile of the Fornax Dwarf. ApJ, 746:89, February 2012. doi: 10.1088/0004-637X/746/1/89.

M. Jeon, G. Besla, and V. Bromm. Connecting the First Galaxies with Ultrafaint Dwarfs in the Local Group: Chemical Signatures of Population III Stars. ApJ, 848:85, October 2017. doi: 10.3847/1538-4357/aa8c80.

L. Jiang, X. Fan, M. Vestergaard, J. D. Kurk, F. Walter, B. C. Kelly, and M. A. Strauss. Gemini Near-Infrared Spectroscopy of Luminous z ~ 6 Quasars: Chemical Abundances, Black Hole Masses, and Mg II Absorption. AJ, 134:1150, September 2007. doi: 10.1086/520811.

Y.-F. Jiang, J. M. Stone, and S. W. Davis. A Global Three-dimensional Radiation Magnetohydrodynamic Simulation of Super-Eddington Accretion Disks. ApJ, 796:106, December 2014. doi: 10.1088/0004-637X/796/2/106.

C. C. Joggerst, A. Almgren, J. Bell, A. Heger, D. Whalen, and S. E. Woosley. The Nucleosynthetic Imprint of 15-40 M $_{sun}$ Primordial Supernovae on Metal-Poor Stars. ApJ, 709:11–26, January 2010. doi: 10.1088/0004-637X/709/1/11.

J. L. Johnson and V. Bromm. The aftermath of the first stars: massive black holes. MNRAS, 374:1557–1568, February 2007. doi: 10.1111/j.1365-2966.2006.11275.x.

J. L. Johnson and F. Haardt. The Early Growth of the First Black Holes. PASA, 33:e007, March 2016. doi: 10.1017/pasa.2016.4.

J. L. Johnson, D. J. Whalen, C. L. Fryer, and H. Li. The Growth of the Stellar Seeds of Supermassive Black Holes. ApJ, 750:66, May 2012. doi: 10.1088/0004-637X/750/1/66.

J. L. Johnson, D. J. Whalen, H. Li, and D. E. Holz. Supermassive Seeds for Supermassive Black Holes. ApJ, 771:116, July 2013. doi: 10.1088/0004-637X/771/2/116.

J. L. Johnson, D. J. Whalen, B. Agarwal, J.-P. Paardekooper, and S. Khochfar. The impact of reionization on the formation of supermassive black hole seeds. MNRAS, 445:686–693, November 2014. doi: 10.1093/mnras/stu1676.

Y. Juarez, R. Maiolino, R. Mujica, M. Pedani, S. Marinoni, T. Nagao, A. Marconi, and E. Oliva. The metallicity of the most distant quasars. A&A, 494:L25–L28, February 2009. doi: 10.1051/0004-6361:200811415.

D. W. Just, W. N. Brandt, O. Shemmer, A. T. Steffen, D. P. Schneider, G. Chartas, and G. P. Garmire. The X-Ray Properties of the Most Luminous Quasars from the Sloan Digital Sky Survey. ApJ, 665:1004–1022, August 2007. doi: 10.1086/519990.

A. Kashlinsky, R. G. Arendt, M. L. N. Ashby, G. G. Fazio, J. Mather, and S. H. Moseley. New measurements of the cosmic infrared background fluctuations in deep spitzer/irac survey data and their cosmological implications. ApJ, 753:63, 2012.

H. Katz, D. Sijacki, and M. G. Haehnelt. Seeding high-redshift QSOs by collisional runaway in primordial star clusters. MNRAS, 451:2352–2369, August 2015. doi: 10.1093/mnras/stv1048.

G. Kauffmann, B. Guiderdoni, and S. D. M. White. Faint Galaxy Counts in a Hierarchical Universe. MNRAS, 267:981, April 1994. doi: 10.1093/mnras/267.4.981.

D. Kawata and B. K. Gibson. GCD+: a new chemodynamical approach to modelling supernovae and chemical enrichment in elliptical galaxies. MNRAS, 340:908–922, April 2003. doi: 10.1046/j.1365-8711.2003.06356.x.

B. C. Kelly and Y. Shen. The Demographics of Broad-line Quasars in the Mass-Luminosity Plane. II. Black Hole Mass and Eddington Ratio Functions. ApJ, 764:45, February 2013. doi: 10.1088/0004-637X/764/1/45.

R. C. Kennicutt, Jr. The Global Schmidt Law in Star-forming Galaxies. ApJ, 498:541–552, May 1998. doi: 10.1086/305588.

N. Khandai, Y. Feng, C. DeGraf, T. Di Matteo, and R. A. C. Croft. The formation of galaxies hosting z $\sim$ 6 quasars. MNRAS, 423:2397–2406, July 2012. doi: 10.1111/j.1365-2966.2012.21047.x.

S. Kim, M. Stiavelli, M. Trenti, C. M. Pavlovsky, S. G. Djorgovski, C. Scarlata, D. Stern, A. Mahabal, D. Thompson, M. Dickinson, N. Panagia, and G. Meylan. The Environments of High-Redshift Quasi-Stellar Objects. ApJ, 695:809–817, April 2009. doi: 10.1088/0004-637X/695/2/809.

A. King. Black Holes, Galaxy Formation, and the M_{BH}-σ Relation. ApJ, 596:L27–L29, October 2003. doi: 10.1086/379143.

A. King. The AGN-Starburst Connection, Galactic Superwinds, and M_{BH}-σ. ApJ, 635:L121–L123, December 2005. doi: 10.1086/499430.

A. R. King. Black hole outflows. MNRAS, 402:1516–1522, March 2010. doi: 10.1111/j.1365-2966.2009.16013.x.

T. Kitayama, N. Yoshida, H. Susa, and M. Umemura. The Structure and Evolution of Early Cosmological H II Regions. ApJ, 613:631–645, October 2004. doi: 10.1086/423313.

A. Klypin, A. V. Kravtsov, O. Valenzuela, and F. Prada. Where Are the Missing Galactic Satellites? ApJ, 522:82–92, September 1999. doi: 10.1086/307643.

J. Kormendy and L. C. Ho. Coevolution (Or Not) of Supermassive Black Holes and Host Galaxies. ARA&A, 51:511–653, August 2013. doi: 10.1146/annurev-astro-082708-101811.

M. Kubryk, N. Prantzos, and E. Athanassoula. Evolution of the Milky Way with radial motions of stars and gas. I. The solar neighbourhood and the thin and thick disks. A&A, 580:A126, August 2015. doi: 10.1051/0004-6361/201424171.

F. La Franca, F. Fiore, A. Comastri, G. C. Perola, N. Sacchi, M. Brusa, F. Cocchia, C. Feruglio, G. Matt, C. Vignali, N. Carangelo, P. Ciliegi, A. Lamastra, R. Maiolino, M. Mignoli, S. Molendi, and S. Puccetti. The hellas2xmm survey. vii. the hard x-ray luminosity function of agns up to z = 4: More absorbed agns at low luminosities and high redshifts. ApJ, 635:864, 2005.

C. Lacey and S. Cole. Merger rates in hierarchical models of galaxy formation. MNRAS, 262:627–649, June 1993. doi: 10.1093/mnras/262.3.627.

E. S. Laird, K. Nandra, A. Georgakakis, J. A. Aird, P. Barmby, C. J. Conselice, A. L. Coil, M. Davis, S. M. Faber, G. G. Fazio, P. Guhathakurta, D. C. Koo, V. Sarajedini, and C. N. A. Willmer. AEGIS-X: the Chandra Deep Survey of the Extended Groth Strip. ApJS, 180:102–116, January 2009. doi: 10.1088/0067-0049/180/1/102.

A. Lamastra, N. Menci, R. Maiolino, F. Fiore, and A. Merloni. The building up of the black hole-stellar mass relation. MNRAS, 405:29–40, June 2010. doi: 10.1111/j.1365-2966.2010.16439.x.

A. Lapi, A. Cavaliere, and N. Menci. Intracluster and Intragroup Entropy from Quasar Activity. ApJ, 619:60–72, January 2005. doi: 10.1086/426376.

N. Laporte, R. Pelló, M. Hayes, D. Schaerer, F. Boone, J. Richard, J. F. Le Borgne, J. P. Kneib, and F. Combes. The bright end of the luminosity function at z ∼ 9. A&A, 542: L31, June 2012. doi: 10.1051/0004-6361/201219486.

R. B. Larson. Early star formation and the evolution of the stellar initial mass function in galaxies. MNRAS, 301:569–581, December 1998. doi: 10.1046/j.1365-8711.1998.02045.x.

M. A. Latif and A. Ferrara. Formation of supermassive black hole seeds. *ArXiv e-prints*, May 2016.

M. A. Latif and M. Volonteri. Assessing inflow rates in atomic cooling haloes: implications for direct collapse black holes. MNRAS, 452:1026–1044, September 2015. doi: 10.1093/mnras/stv1337.

M. A. Latif, D. R. G. Schleicher, W. Schmidt, and J. Niemeyer. Black hole formation in the early Universe. MNRAS, 433:1607–1618, August 2013a. doi: 10.1093/mnras/stt834.

M. A. Latif, D. R. G. Schleicher, W. Schmidt, and J. C. Niemeyer. The characteristic black hole mass resulting from direct collapse in the early Universe. MNRAS, 436:2989–2996, December 2013b. doi: 10.1093/mnras/stt1786.

M. A. Latif, S. Bovino, C. Van Borm, T. Grassi, D. R. G. Schleicher, and M. Spaans. A UV flux constraint on the formation of direct collapse black holes. MNRAS, 443:1979–1987, September 2014. doi: 10.1093/mnras/stu1230.

M. A. Latif, K. Omukai, M. Habouzit, D. R. G. Schleicher, and M. Volonteri. Impact of Dust Cooling on Direct-collapse Black Hole Formation. ApJ, 823:40, May 2016. doi: 10.3847/0004-637X/823/1/40.

T. R. Lauer, S. Tremaine, D. Richstone, and S. M. Faber. Selection Bias in Observing the Cosmological Evolution of the M-σ and M-L Relationships. ApJ, 670:249–260, November 2007. doi: 10.1086/522083.

B. D. Lehmer, Y. Q. Xue, W. N. Brandt, D. M. Alexander, F. E. Bauer, M. Brusa, A. Comastri, R. Gilli, A. E. Hornschemeier, B. Luo, M. Paolillo, A. Ptak, O. Shemmer, D. P. Schneider, P. Tozzi, and C. Vignali. The 4 ms chandra deep field-south number counts apportioned by source class: Pervasive active galactic nuclei and the ascent of normal galaxies. ApJ, 752:46, 2012.

Y. Li, L. Hernquist, B. Robertson, T. J. Cox, P. F. Hopkins, V. Springel, L. Gao, T. Di Matteo, A. R. Zentner, A. Jenkins, and N. Yoshida. Formation of z~6 Quasars from Hierarchical Galaxy Mergers. ApJ, 665:187–208, August 2007. doi: 10.1086/519297.

Y. Li, P. F. Hopkins, L. Hernquist, D. P. Finkbeiner, T. J. Cox, V. Springel, L. Jiang, X. Fan, and N. Yoshida. Modeling the Dust Properties of z $\sim$ 6 Quasars with ART^2-All-Wavelength Radiative Transfer with Adaptive Refinement Tree. ApJ, 678:41-63, May 2008. doi: 10.1086/529364.

A. D. Linde. A new inflationary universe scenario: A possible solution of the horizon, flatness, homogeneity, isotropy and primordial monopole problems. *Physics Letters B*, 108:389–393, February 1982. doi: 10.1016/0370-2693(82)91219-9.

G. Lodato and P. Natarajan. Supermassive black hole formation during the assembly of pre-galactic discs. MNRAS, 371:1813–1823, October 2006. doi: 10.1111/j.1365-2966.2006.10801.x.

G. Lodato and P. Natarajan. The mass function of high-redshift seed black holes. MNRAS, 377:L64–L68, May 2007. doi: 10.1111/j.1745-3933.2007.00304.x.

A. Loeb and F. A. Rasio. Collapse of primordial gas clouds and the formation of quasar black holes. ApJ, 432:52–61, September 1994. doi: 10.1086/174548.

V. Lora, F. J. Sánchez-Salcedo, A. C. Raga, and A. Esquivel. An Upper Limit on the Mass of the Black Hole in Ursa Minor Dwarf Galaxy. ApJ, 699:L113–L117, July 2009. doi: 10.1088/0004-637X/699/2/L113.

A. Lupi, M. Colpi, B. Devecchi, G. Galanti, and M. Volonteri. Constraining the high-redshift formation of black hole seeds in nuclear star clusters with gas inflows. MNRAS, 442:3616, 2014.

A. Lupi, F. Haardt, M. Dotti, D. Fiacconi, L. Mayer, and P. Madau. Growing massive black holes through supercritical accretion of stellar-mass seeds. MNRAS, 456:2993–3003, March 2016. doi: 10.1093/mnras/stv2877.

E. Lusso and G. Risaliti. The Tight Relation between X-Ray and Ultraviolet Luminosity of Quasars. ApJ, 819:154, March 2016. doi: 10.3847/0004-637X/819/2/154.

E. Lusso, A. Comastri, C. Vignali, G. Zamorani, M. Brusa, R. Gilli, K. Iwasawa, M. Salvato, F. Civano, M. Elvis, A. Merloni, A. Bongiorno, J. R. Trump, A. M. Koekemoer, E. Schinnerer, E. Le Floc'h, N. Cappelluti, K. Jahnke, M. Sargent, J. Silverman, V. Mainieri, F. Fiore, M. Bolzonella, O. Le Fèvre, B. Garilli, A. Iovino, J. P. Kneib, F. Lamareille, S. Lilly, M. Mignoli, M. Scodeggio, and D. Vergani. The X-ray to optical-UV luminosity ratio of X-ray selected type 1 AGN in XMM-COSMOS. A&A, 512:A34, March 2010. doi: 10.1051/0004-6361/200913298.

J. Lyu, G. H. Rieke, and S. Alberts. The Contribution of Host Galaxies to the Infrared Energy Output of z $\gtrsim$ 5.0 Quasars. ApJ, 816:85, January 2016. doi: 10.3847/0004-637X/816/2/85.

M. E. Machacek, G. L. Bryan, and T. Abel. Simulations of Pregalactic Structure Formation with Radiative Feedback. ApJ, 548:509–521, February 2001. doi: 10.1086/319014.

J. Mackey, V. Bromm, and L. Hernquist. Three Epochs of Star Formation in the High-Redshift Universe. ApJ, 586:1–11, March 2003. doi: 10.1086/367613.

P. Madau and F. Haardt. Cosmic Reionization after Planck: Could Quasars Do It All? ApJ, 813:L8, November 2015. doi: 10.1088/2041-8205/813/1/L8.

P. Madau and M. J. Rees. Massive Black Holes as Population III Remnants. ApJ, 551: L27–L30, April 2001. doi: 10.1086/319848.

P. Madau, M. J. Rees, M. Volonteri, F. Haardt, and S. P. Oh. Early Reionization by Miniquasars. ApJ, 604:484–494, April 2004. doi: 10.1086/381935.

P. Madau, F. Haardt, and M. Dotti. Super-critical Growth of Massive Black Holes from Stellar-mass Seeds. ApJ, 784:L38, April 2014. doi: 10.1088/2041-8205/784/2/L38.

P. Magdziarz and A. A. Zdziarski. Angle-dependent Compton reflection of X-rays and gamma-rays. MNRAS, 273:837–848, April 1995. doi: 10.1093/mnras/273.3.837.

B. Magnelli, D. Lutz, P. Santini, A. Saintonge, S. Berta, M. Albrecht, B. Altieri, P. Andreani, H. Aussel, F. Bertoldi, M. Béthermin, A. Bongiovanni, P. Capak, S. Chapman, J. Cepa, A. Cimatti, A. Cooray, E. Daddi, A. L. R. Danielson, H. Dannerbauer, J. S. Dunlop, D. Elbaz, D. Farrah, N. M. Förster Schreiber, R. Genzel, H. S. Hwang, E. Ibar, R. J. Ivison, E. Le Floc'h, G. Magdis, R. Maiolino, R. Nordon, S. J. Oliver, A. Pérez García, A. Poglitsch, P. Popesso, F. Pozzi, L. Riguccini, G. Rodighiero, D. Rosario, I. Roseboom, M. Salvato, M. Sanchez-Portal, D. Scott, I. Smail, E. Sturm, A. M. Swinbank, L. J. Tacconi, I. Valtchanov, L. Wang, and S. Wuyts. A Herschel view of the far-infrared properties of submillimetre galaxies. A&A, 539:A155, March 2012. doi: 10.1051/0004-6361/201118312.

J. Magorrian, S. Tremaine, D. Richstone, R. Bender, G. Bower, A. Dressler, S. M. Faber, K. Gebhardt, R. Green, C. Grillmair, J. Kormendy, and T. Lauer. The Demography of Massive Dark Objects in Galaxy Centers. AJ, 115:2285–2305, June 1998. doi: 10.1086/300353.

R. Maiolino, R. Schneider, E. Oliva, S. Bianchi, A. Ferrara, F. Mannucci, M. Pedani, and M. Roca Sogorb. A supernova origin for dust in a high-redshift quasar. Nature, 431: 533–535, September 2004. doi: 10.1038/nature02930.

R. Maiolino, P. Cox, P. Caselli, A. Beelen, F. Bertoldi, C. L. Carilli, M. J. Kaufman, K. M. Menten, T. Nagao, A. Omont, A. Weiß, C. M. Walmsley, and F. Walter. First detection of [CII]158 μm at high redshift: vigorous star formation in the early universe. A&A, 440:L51–L54, September 2005. doi: 10.1051/0004-6361:200500165.

R. Maiolino, R. Neri, A. Beelen, F. Bertoldi, C. L. Carilli, P. Caselli, P. Cox, K. M. Menten, T. Nagao, A. Omont, C. M. Walmsley, F. Walter, and A. Weiß. Molecular gas in QSO host galaxies at z > 5. A&A, 472:L33–L37, September 2007. doi: 10.1051/0004-6361:20078136.

R. Maiolino, S. Gallerani, R. Neri, C. Cicone, A. Ferrara, R. Genzel, D. Lutz, E. Sturm, L. J. Tacconi, F. Walter, C. Feruglio, F. Fiore, and E. Piconcelli. Evidence of strong quasar feedback in the early Universe. MNRAS, 425:L66–L70, September 2012. doi: 10.1111/j.1745-3933.2012.01303.x.

R. Makiya, M. Enoki, T. Ishiyama, M. A. R. Kobayashi, M. Nagashima, T. Okamoto, K. Okoshi, T. Oogi, and H. Shirakata. The New Numerical Galaxy Catalog (ν^2GC): An updated semi-analytic model of galaxy and active galactic nucleus formation with large cosmological N-body simulations. PASJ, 68:25, April 2016. doi: 10.1093/pasj/psw005.

F. Mannucci, H. Buttery, R. Maiolino, A. Marconi, and L. Pozzetti. Evidence for strong evolution of the cosmic star formation density at high redshifts. A&A, 461:423–431, January 2007. doi: 10.1051/0004-6361:20065993.

F. Mannucci, G. Cresci, R. Maiolino, A. Marconi, and A. Gnerucci. A fundamental relation between mass, star formation rate and metallicity in local and high-redshift galaxies. MNRAS, 408:2115–2127, November 2010. doi: 10.1111/j.1365-2966.2010.17291.x.

S. Marassi, R. Schneider, M. Limongi, A. Chieffi, M. Bocchio, and S. Bianchi. The metal and dust yields of the first massive stars. MNRAS, October 2015.

A. Marconi and L. K. Hunt. The Relation between Black Hole Mass, Bulge Mass, and Near-Infrared Luminosity. ApJ, 589:L21–L24, May 2003. doi: 10.1086/375804.

A. Marconi, G. Risaliti, R. Gilli, L. K. Hunt, R. Maiolino, and M. Salvati. Local supermassive black holes, relics of active galactic nuclei and the X-ray background. MNRAS, 351:169–185, June 2004. doi: 10.1111/j.1365-2966.2004.07765.x.

F. Marinacci, R. Pakmor, and V. Springel. The formation of disc galaxies in high-resolution moving-mesh cosmological simulations. MNRAS, 437:1750–1775, January 2014. doi: 10.1093/mnras/stt2003.

R. O. Marzke and L. N. da Costa. The Galaxy Luminosity Function at zlt0.05: Dependence on Color. AJ, 113:185, January 1997. doi: 10.1086/118243.

K. Matsuoka, T. Nagao, R. Maiolino, A. Marconi, and Y. Taniguchi. Chemical evolution of high-redshift radio galaxies. A&A, 503:721–730, September 2009. doi: 10.1051/0004-6361/200811478.

J. Matthee, D. Sobral, S. Santos, H. Röttgering, B. Darvish, and B. Mobasher. Identification of the brightest Lyα emitters at z = 6.6: implications for the evolution of the luminosity function in the reionization era. MNRAS, 451:400–417, July 2015. doi: 10.1093/mnras/stv947.

L. Mattsson. Dust in the early Universe: evidence for non-stellar dust production or observational errors? MNRAS, 414:781–791, June 2011. doi: 10.1111/j.1365-2966.2011.18447.x.

L. Mayer, S. Kazantzidis, P. Madau, M. Colpi, T. Quinn, and J. Wadsley. Rapid Formation of Supermassive Black Hole Binaries in Galaxy Mergers with Gas. *Science*, 316:1874, June 2007. doi: 10.1126/science.1141858.

L. Mayer, S. Kazantzidis, A. Escala, and S. Callegari. Direct formation of supermassive black holes via multi-scale gas inflows in galaxy mergers. Nature, 466:1082–1084, August 2010. doi: 10.1038/nature09294.

C. Mazzucchelli, E. Bañados, R. Decarli, E. P. Farina, B. P. Venemans, F. Walter, and R. Overzier. No Overdensity of Lyman-Alpha Emitting Galaxies around a Quasar at z ∼ 5.7. ApJ, 834:83, January 2017. doi: 10.3847/1538-4357/834/1/83.

J. E. McClintock, R. Shafee, R. Narayan, R. A. Remillard, S. W. Davis, and L.-X. Li. The Spin of the Near-Extreme Kerr Black Hole GRS 1915+105. ApJ, 652:518–539, November 2006. doi: 10.1086/508457.

N. J. McConnell, C.-P. Ma, J. D. Murphy, K. Gebhardt, T. R. Lauer, J. R. Graham, S. A. Wright, and D. O. Richstone. Dynamical Measurements of Black Hole Masses in Four Brightest Cluster Galaxies at 100 Mpc. ApJ, 756:179, September 2012. doi: 10.1088/0004-637X/756/2/179.

I. D. McGreer, S. Eftekharzadeh, A. D. Myers, and X. Fan. A Constraint on Quasar Clustering at z = 5 from a Binary Quasar. AJ, 151:61, March 2016. doi: 10.3847/0004-6256/151/3/61.

J. C. McKinney, A. Tchekhovskoy, A. Sadowski, and R. Narayan. Three-dimensional general relativistic radiation magnetohydrodynamical simulation of super-Eddington accretion, using a new code HARMRAD with M1 closure. MNRAS, 441:3177–3208, July 2014. doi: 10.1093/mnras/stu762.

N. Menci, A. Cavaliere, A. Fontana, E. Giallongo, F. Poli, and V. Vittorini. Early Hierarchical Formation of Massive Galaxies Triggered by Interactions. ApJ, 604:12–17, March 2004. doi: 10.1086/381522.

N. Menci, A. Fontana, E. Giallongo, and S. Salimbeni. Bimodal Color Distribution in Hierarchical Galaxy Formation. ApJ, 632:49–57, October 2005. doi: 10.1086/432788.

N. Menci, F. Fiore, S. Puccetti, and A. Cavaliere. The Blast Wave Model for AGN Feedback: Effects on AGN Obscuration. ApJ, 686:219-229, October 2008. doi: 10.1086/591438.

K. Menou, Z. Haiman, and V. K. Narayanan. The Merger History of Supermassive Black Holes in Galaxiesd. ApJ, 558:535–542, September 2001. doi: 10.1086/322310.

D. Merritt, L. Ferrarese, and C. L. Joseph. No Supermassive Black Hole in M33? *Science*, 293:1116–1119, August 2001. doi: 10.1126/science.1063896.

M. J. Michałowski, E. J. Murphy, J. Hjorth, D. Watson, C. Gall, and J. S. Dunlop. Dust grain growth in the interstellar medium of $5 < z < 6.5$ quasars. A&A, 522:A15, November 2010. doi: 10.1051/0004-6361/201014902.

M. J. Middleton, J. C. A. Miller-Jones, S. Markoff, R. Fender, M. Henze, N. Hurley-Walker, A. M. M. Scaife, T. P. Roberts, D. Walton, J. Carpenter, J.-P. Macquart, G. C. Bower, M. Gurwell, W. Pietsch, F. Haberl, J. Harris, M. Daniel, J. Miah, C. Done, J. S. Morgan, H. Dickinson, P. Charles, V. Burwitz, M. Della Valle, M. Freyberg, J. Greiner, M. Hernanz, D. H. Hartmann, D. Hatzidimitriou, A. Riffeser, G. Sala, S. Seitz, P. Reig, A. Rau, M. Orio, D. Titterington, and K. Grainge. Bright radio emission from an ultraluminous stellar-mass microquasar in M 31. Nature, 493:187–190, January 2013. doi: 10.1038/nature11697.

J. C. Mihos and L. Hernquist. Ultraluminous starbursts in major mergers. ApJ, 431:L9–L12, August 1994. doi: 10.1086/187460.

B. Miller, E. Gallo, T. Treu, and J.-H. Woo. AMUSE-Field I: Nuclear X-Ray Properties of Local Field and Group Spheroids across the Stellar Mass Scale. ApJ, 747:57, March 2012. doi: 10.1088/0004-637X/747/1/57.

B. P. Miller, E. Gallo, J. E. Greene, B. C. Kelly, T. Treu, J.-H. Woo, and V. Baldassare. X-Ray Constraints on the Local Supermassive Black Hole Occupation Fraction. ApJ, 799:98, January 2015. doi: 10.1088/0004-637X/799/1/98.

M. Milosavljević, V. Bromm, S. M. Couch, and S. P. Oh. Accretion onto "Seed" Black Holes in the First Galaxies. ApJ, 698:766–780, June 2009a. doi: 10.1088/0004-637X/698/1/766.

M. Milosavljević, S. M. Couch, and V. Bromm. Accretion Onto Intermediate-Mass Black Holes in Dense Protogalactic Clouds. ApJ, 696:L146–L149, May 2009b. doi: 10.1088/0004-637X/696/2/L146.

S. Mineshige, T. Kawaguchi, M. Takeuchi, and K. Hayashida. Slim-Disk Model for Soft X-Ray Excess and Variability of Narrow-Line Seyfert 1 Galaxies. PASJ, 52:499–508, June 2000. doi: 10.1093/pasj/52.3.499.

H. J. Mo, S. Mao, and S. D. M. White. The formation of galactic discs. MNRAS, 295:319–336, April 1998. doi: 10.1046/j.1365-8711.1998.01227.x.

E. C. Moran, K. Shahinyan, H. R. Sugarman, D. O. Vélez, and M. Eracleous. Black Holes At the Centers of Nearby Dwarf Galaxies. AJ, 148:136, December 2014. doi: 10.1088/0004-6256/148/6/136.

H. L. Morgan and M. G. Edmunds. Dust formation in early galaxies. MNRAS, 343:427–442, August 2003. doi: 10.1046/j.1365-8711.2003.06681.x.

R. Morrison and D. McCammon. Interstellar photoelectric absorption cross sections, 0.03-10 keV. ApJ, 270:119–122, July 1983. doi: 10.1086/161102.

L. Morselli, M. Mignoli, R. Gilli, C. Vignali, A. Comastri, E. Sani, N. Cappelluti, G. Zamorani, M. Brusa, S. Gallozzi, and E. Vanzella. Primordial environment of super massive black holes: large-scale galaxy overdensities around z $\sim$ 6 quasars with LBT. A&A, 568:A1, August 2014. doi: 10.1051/0004-6361/201423853.

D. J. Mortlock, S. J. Warren, B. P. Venemans, M. Patel, P. C. Hewett, R. G. McMahon, C. Simpson, T. Theuns, E. A. Gonzáles-Solares, A. Adamson, S. Dye, N. C. Hambly,

P. Hirst, M. J. Irwin, E. Kuiper, A. Lawrence, and H. J. A. Röttgering. A luminous quasar at a redshift of z = 7.085. Nature, 474:616–619, June 2011. doi: 10.1038/nature10159.

J. C. Muñoz-Cuartas, A. V. Macciò, S. Gottlöber, and A. A. Dutton. The redshift evolution of Λ cold dark matter halo parameters: concentration, spin and shape. MNRAS, 411: 584–594, February 2011. doi: 10.1111/j.1365-2966.2010.17704.x.

Alexander L Muratov, Dusan Keres, Claude-Andre Faucher-Giguere, Philip F Hopkins, Eliot Quataert, and Norman Murray. Gusty, gaseous flows of FIRE: galactic winds in cosmological simulations with explicit stellar feedback. *MNRAS*, 454(3):2691–2713, December 2015.

T. Naab and A. Burkert. Statistical Properties of Collisionless Equal- and Unequal-Mass Merger Remnants of Disk Galaxies. ApJ, 597:893–906, November 2003. doi: 10.1086/378581.

T. Nagao, A. Marconi, and R. Maiolino. The evolution of the broad-line region among SDSS quasars. A&A, 447:157–172, February 2006. doi: 10.1051/0004-6361:20054024.

P. Natarajan. The mass assembly history of black holes in the Universe. *ArXiv e-prints*, May 2011.

P. Natarajan, F. Pacucci, A. Ferrara, B. Agarwal, A. Ricarte, E. Zackrisson, and N. Cappelluti. Unveiling the first black holes with jwst: multi-wavelength spectral predictions. *ArXiv e-print 1610.05312*, oct 2016.

N. P. H. Nesvadba, F. Boulanger, P. Salomé, P. Guillard, M. D. Lehnert, P. Ogle, P. Appleton, E. Falgarone, and G. Pineau Des Forets. Energetics of the molecular gas in the H_2 luminous radio galaxy 3C 326: Evidence for negative AGN feedback. A&A, 521:A65, October 2010. doi: 10.1051/0004-6361/200913333.

N. P. H. Nesvadba, M. Polletta, M. D. Lehnert, J. Bergeron, C. De Breuck, G. Lagache, and A. Omont. The dynamics of the ionized and molecular interstellar medium in powerful obscured quasars at $z \geq 3.5$. MNRAS, 415:2359–2372, August 2011. doi: 10.1111/j.1365-2966.2011.18862.x.

H. Netzer, R. Mor, B. Trakhtenbrot, O. Shemmer, and P. Lira. Star Formation and Black Hole Growth at z ˜= 4.8. ApJ, 791:34, August 2014. doi: 10.1088/0004-637X/791/1/34.

T. Nozawa, T. Kozasa, A. Habe, E. Dwek, H. Umeda, N. Tominaga, K. Maeda, and K. Nomoto. Evolution of Dust in Primordial Supernova Remnants: Can Dust Grains Formed in the Ejecta Survive and Be Injected into the Early Interstellar Medium? ApJ, 666:955–966, September 2007. doi: 10.1086/520621.

P. A. Oesch, G. Brammer, P. G. van Dokkum, G. D. Illingworth, R. J. Bouwens, I. Labbé, M. Franx, I. Momcheva, M. L. N. Ashby, G. G. Fazio, V. Gonzalez, B. Holden, D. Magee, R. E. Skelton, R. Smit, L. R. Spitler, M. Trenti, and S. P. Willner. A Remarkably Luminous Galaxy at z=11.1 Measured with Hubble Space Telescope Grism Spectroscopy. ApJ, 819:129, March 2016. doi: 10.3847/0004-637X/819/2/129.

K. Ohsuga and S. Mineshige. Why Is Supercritical Disk Accretion Feasible? ApJ, 670: 1283–1290, December 2007. doi: 10.1086/522324.

K. Ohsuga, S. Mineshige, M. Mori, and M. Umemura. Does the Slim-Disk Model Correctly Consider Photon-trapping Effects? ApJ, 574:315–324, July 2002. doi: 10.1086/340798.

K. Ohsuga, S. Mineshige, and K.-y. Watarai. Spectral Energy Distribution in Supercritical Disk Accretion Flows through Photon-trapping Effects. ApJ, 596:429–436, October 2003. doi: 10.1086/377686.

K. Ohsuga, M. Mori, T. Nakamoto, and S. Mineshige. Supercritical Accretion Flows around Black Holes: Two-dimensional, Radiation Pressure-dominated Disks with Photon Trapping. ApJ, 628:368–381, July 2005. doi: 10.1086/430728.

K. Omukai. Protostellar Collapse with Various Metallicities. ApJ, 534:809–824, May 2000. doi: 10.1086/308776.

K. Omukai. Primordial Star Formation under Far-Ultraviolet Radiation. ApJ, 546:635–651, January 2001. doi: 10.1086/318296.

K. Omukai, T. Tsuribe, R. Schneider, and A. Ferrara. Thermal and Fragmentation Properties of Star-forming Clouds in Low-Metallicity Environments. ApJ, 626:627–643, June 2005. doi: 10.1086/429955.

K. Omukai, R. Schneider, and Z. Haiman. Can Supermassive Black Holes Form in Metal-enriched High-Redshift Protogalaxies? ApJ, 686:801-814, October 2008. doi: 10.1086/591636.

B. W. O'Shea and M. L. Norman. Population III Star Formation in a ΛCDM Universe. I. The Effect of Formation Redshift and Environment on Protostellar Accretion Rate. ApJ, 654:66–92, January 2007. doi: 10.1086/509250.

B. W. O'Shea and M. L. Norman. Population III Star Formation in a ΛCDM Universe. II. Effects of a Photodissociating Background. ApJ, 673:14-33, January 2008. doi: 10.1086/524006.

R. A. Overzier, Q. Guo, G. Kauffmann, G. De Lucia, R. Bouwens, and G. Lemson. ΛCDM predictions for galaxy protoclusters - I. The relation between galaxies, protoclusters and quasars at z ~ 6. MNRAS, 394:577–594, April 2009. doi: 10.1111/j.1365-2966.2008.14264.x.

F. Pacucci, A. Ferrara, M. Volonteri, and G. Dubus. Shining in the dark: the spectral evolution of the first black holes. MNRAS, 454:3771–3777, December 2015. doi: 10.1093/mnras/stv2196.

F. Pacucci, A. Ferrara, A. Grazian, F. Fiore, E. Giallongo, and S. Puccetti. First identification of direct collapse black hole candidates in the early Universe in CANDELS/GOODS-S. MNRAS, 459:1432–1439, June 2016. doi: 10.1093/mnras/stw725.

M. J. Page. The fraction of galaxies that contain active nuclei and their accretion rates. MNRAS, 328:925–930, December 2001. doi: 10.1046/j.1365-8711.2001.04919.x.

M. J. Page, C. Simpson, D. J. Mortlock, S. J. Warren, P. C. Hewett, B. P. Venemans, and R. G. McMahon. X-rays from the redshift 7.1 quasar ULAS J1120+0641. MNRAS, 440:L91–L95, May 2014. doi: 10.1093/mnrasl/slu022.

A. Pallottini, A. Ferrara, S. Gallerani, S. Salvadori, and V. D'Odorico. Simulating cosmic metal enrichment by the first galaxies. MNRAS, 440:2498–2518, May 2014. doi: 10.1093/mnras/stu451.

A. Pallottini, A. Ferrara, F. Pacucci, S. Gallerani, S. Salvadori, R. Schneider, D. Schaerer, D. Sobral, and J. Matthee. The brightest Ly α emitter: Pop III or black hole? MNRAS, 453:2465–2470, November 2015. doi: 10.1093/mnras/stv1795.

K. Park and M. Ricotti. Accretion onto Intermediate-mass Black Holes Regulated by Radiative Feedback. I. Parametric Study for Spherically Symmetric Accretion. ApJ, 739:2, September 2011. doi: 10.1088/0004-637X/739/1/2.

K. Park and M. Ricotti. Accretion onto Black Holes from Large Scales Regulated by Radiative Feedback. II. Growth Rate and Duty Cycle. ApJ, 747:9, March 2012. doi: 10.1088/0004-637X/747/1/9.

K. Park and M. Ricotti. Accretion onto Black Holes from Large Scales Regulated by Radiative Feedback. III. Enhanced Luminosity of Intermediate-mass Black Holes Moving at Supersonic Speeds. ApJ, 767:163, April 2013. doi: 10.1088/0004-637X/767/2/163.

H. Parkinson, S. Cole, and J. Helly. Generating dark matter halo merger trees. MNRAS, 383:557–564, January 2008. doi: 10.1111/j.1365-2966.2007.12517.x.

A. H. Pawlik, V. Bromm, and M. Milosavljević. Assembly of the first disk galaxies under radiative feedback from the first stars. Mem. Soc. Astron. Italiana, 85:565, 2014.

P. J. E. Peebles. Origin of the Angular Momentum of Galaxies. ApJ, 155:393, February 1969. doi: 10.1086/149876.

M. S. Peeples, J. K. Werk, J. Tumlinson, B. D. Oppenheimer, J. X. Prochaska, N. Katz, and D. H. Weinberg. A Budget and Accounting of Metals at z $\sim$ 0: Results from the COS-Halos Survey. ApJ, 786:54, May 2014. doi: 10.1088/0004-637X/786/1/54.

S. Peirani, Y. Dubois, M. Volonteri, J. Devriendt, K. Bundy, J. Silk, C. Pichon, S. Kaviraj, R. Gavazzi, and M. Habouzit. Density profile of dark matter haloes and galaxies in the Horizon-AGN simulation: the impact of AGN feedback. *ArXiv e-prints*, November 2016.

F. I. Pelupessy, T. Di Matteo, and B. Ciardi. How Rapidly Do Supermassive Black Hole "Seeds" Grow at Early Times? ApJ, 665:107–119, August 2007. doi: 10.1086/519235.

Y. Peng, R. Maiolino, and R. Cochrane. Strangulation as the primary mechanism for shutting down star formation in galaxies. Nature, 521:192–195, May 2015. doi: 10.1038/nature14439.

R. Penrose. Gravitational Collapse: the Role of General Relativity. *Nuovo Cimento Rivista Serie*, 1, 1969.

L. Pentericci, X. Fan, H.-W. Rix, M. A. Strauss, V. K. Narayanan, G. T. Richards, D. P. Schneider, J. Krolik, T. Heckman, J. Brinkmann, D. Q. Lamb, and G. P. Szokoly. VLT Optical and Near-Infrared Observations of the z = 6.28 Quasar SDSS J1030+0524. AJ, 123:2151–2158, May 2002. doi: 10.1086/340077.

D. A. Perley, J. S. Bloom, C. R. Klein, S. Covino, T. Minezaki, P. Woźniak, W. T. Vestrand, G. G. Williams, P. Milne, N. R. Butler, A. C. Updike, T. Krühler, P. Afonso, A. Antonelli, L. Cowie, P. Ferrero, J. Greiner, D. H. Hartmann, Y. Kakazu, A. Küpcü Yoldaş, A. N. Morgan, P. A. Price, J. X. Prochaska, and Y. Yoshii. Evidence for supernova-synthesized dust from the rising afterglow of GRB071025 at z ˜ 5. MNRAS, 406:2473–2487, August 2010. doi: 10.1111/j.1365-2966.2010.16772.x.

A. Petri, A. Ferrara, and R. Salvaterra. Supermassive black hole ancestors. MNRAS, 422: 1690–1699, May 2012. doi: 10.1111/j.1365-2966.2012.20743.x.

E. Pezzulli, R. Valiante, and R. Schneider. Super-Eddington growth of the first black holes. MNRAS, 458:3047–3059, May 2016. doi: 10.1093/mnras/stw505.

E. Pezzulli, R. Valiante, M. C. Orofino, R. Schneider, S. Gallerani, and T. Sbarrato. Faint progenitors of luminous z $\sim$ 6 quasars: Why do not we see them? MNRAS, 466:2131–2142, April 2017. doi: 10.1093/mnras/stw3243.

E. Piconcelli, E. Jimenez-Bailón, M. Guainazzi, N. Schartel, P. M. Rodríguez-Pascual, and M. Santos-Lleó. The XMM-Newton view of PG quasars. I. X-ray continuum and absorption. A&A, 432:15–30, March 2005. doi: 10.1051/0004-6361:20041621.

M. Pierre, F. Pacaud, C. Adami, S. Alis, B. Altieri, N. Baran, C. Benoist, M. Birkinshaw, A. Bongiorno, M. N. Bremer, M. Brusa, A. Butler, P. Ciliegi, L. Chiappetti, N. Clerc,

P. S. Corasaniti, J. Coupon, C. De Breuck, J. Democles, S. Desai, J. Delhaize, J. Devriendt, Y. Dubois, D. Eckert, A. Elyiv, S. Ettori, A. Evrard, L. Faccioli, A. Farahi, C. Ferrari, F. Finet, S. Fotopoulou, N. Fourmanoit, P. Gandhi, F. Gastaldello, R. Gastaud, I. Georgantopoulos, P. Giles, L. Guennou, V. Guglielmo, C. Horellou, K. Husband, M. Huynh, A. Iovino, M. Kilbinger, E. Koulouridis, S. Lavoie, A. M. C. Le Brun, J. P. Le Fevre, C. Lidman, M. Lieu, C. A. Lin, A. Mantz, B. J. Maughan, S. Maurogordato, I. G. McCarthy, S. McGee, J. B. Melin, O. Melnyk, F. Menanteau, M. Novak, S. Paltani, M. Plionis, B. M. Poggianti, D. Pomarede, E. Pompei, T. J. Ponman, M. E. Ramos-Ceja, P. Ranalli, D. Rapetti, S. Raychaudury, T. H. Reiprich, H. Rottgering, E. Rozo, E. Rykoff, T. Sadibekova, J. Santos, J. L. Sauvageot, C. Schimd, M. Sereno, G. P. Smith, V. Smolčić, S. Snowden, D. Spergel, S. Stanford, J. Surdej, P. Valageas, A. Valotti, I. Valtchanov, C. Vignali, J. Willis, and F. Ziparo. The XXL Survey. I. Scientific motivations - XMM-Newton observing plan - Follow-up observations and simulation programme. A&A, 592: A1, June 2016. doi: 10.1051/0004-6361/201526766.

A. Pipino, X. L. Fan, F. Matteucci, F. Calura, L. Silva, G. Granato, and R. Maiolino. The chemical evolution of elliptical galaxies with stellar and QSO dust production. A&A, 525:A61, January 2011. doi: 10.1051/0004-6361/201014843.

Planck Collaboration, P. A. R. Ade, N. Aghanim, M. I. R. Alves, C. Armitage-Caplan, M. Arnaud, M. Ashdown, F. Atrio-Barandela, J. Aumont, H. Aussel, and et al. Planck 2013 results. I. Overview of products and scientific results. A&A, 571:A1, November 2014. doi: 10.1051/0004-6361/201321529.

Planck Collaboration, P. A. R. Ade, N. Aghanim, M. Arnaud, M. Ashdown, J. Aumont, C. Baccigalupi, A. J. Banday, R. B. Barreiro, J. G. Bartlett, and et al. Planck 2015 results. XIII. Cosmological parameters. A&A, 594:A13, September 2016. doi: 10.1051/0004-6361/201525830.

J. Poutanen, G. Lipunova, S. Fabrika, A. G. Butkevich, and P. Abolmasov. Supercritically accreting stellar mass black holes as ultraluminous X-ray sources. MNRAS, 377:1187–1194, May 2007. doi: 10.1111/j.1365-2966.2007.11668.x.

W. H. Press and P. Schechter. Formation of Galaxies and Clusters of Galaxies by Self-

Similar Gravitational Condensation. ApJ, 187:425–438, February 1974. doi: 10.1086/152650.

R. S. Priddey, K. G. Isaak, R. G. McMahon, E. I. Robson, and C. P. Pearson. Quasars as probes of the submillimetre cosmos at z > 5 - I. Preliminary SCUBA photometry. MNRAS, 344:L74–L78, October 2003. doi: 10.1046/j.1365-8711.2003.07076.x.

M. J. Rees and J. P. Ostriker. Cooling, dynamics and fragmentation of massive gas clouds - Clues to the masses and radii of galaxies and clusters. MNRAS, 179:541–559, June 1977. doi: 10.1093/mnras/179.4.541.

J. A. Regan and M. G. Haehnelt. The formation of compact massive self-gravitating discs in metal-free haloes with virial temperatures of ˜13000-30000K. MNRAS, 393:858–871, March 2009a. doi: 10.1111/j.1365-2966.2008.14088.x.

J. A. Regan and M. G. Haehnelt. Pathways to massive black holes and compact star clusters in pre-galactic dark matter haloes with virial temperatures >˜10000K. MNRAS, 396:343–353, June 2009b. doi: 10.1111/j.1365-2966.2009.14579.x.

J. A. Regan, P. H. Johansson, and J. H. Wise. The Direct Collapse of a Massive Black Hole Seed under the Influence of an Anisotropic Lyman-Werner Source. ApJ, 795:137, November 2014. doi: 10.1088/0004-637X/795/2/137.

J. A. Regan, P. H. Johansson, and J. H. Wise. Forming supermassive black hole seeds under the influence of a nearby anisotropic multifrequency source. MNRAS, 459:3377–3394, July 2016. doi: 10.1093/mnras/stw899.

J. A. Regan, E. Visbal, J. H. Wise, Z. Haiman, P. H. Johansson, and G. L. Bryan. Rapid formation of massive black holes in close proximity to embryonic protogalaxies. *Nature Astronomy*, 1:0075, March 2017. doi: 10.1038/s41550-017-0075.

A. E. Reines and A. Comastri. Observational Signatures of High-Redshift Quasars and Local Relics of Black Hole Seeds. PASA, 33:e054, October 2016. doi: 10.1017/pasa.2016.46.

A. E. Reines and M. Volonteri. Relations between Central Black Hole Mass and Total

Galaxy Stellar Mass in the Local Universe. ApJ, 813:82, November 2015. doi: 10.1088/0004-637X/813/2/82.

A. E. Reines, J. E. Greene, and M. Geha. Dwarf Galaxies with Optical Signatures of Active Massive Black Holes. ApJ, 775:116, October 2013. doi: 10.1088/0004-637X/775/2/116.

A. E. Reines, R. M. Plotkin, T. D. Russell, M. Mezcua, J. J. Condon, G. R. Sivakoff, and K. E. Johnson. A Candidate Massive Black Hole in the Low-metallicity Dwarf Galaxy Pair Mrk 709. ApJ, 787:L30, June 2014. doi: 10.1088/2041-8205/787/2/L30.

G. T. Richards, M. Lacy, L. J. Storrie-Lombardi, P. B. Hall, S. C. Gallagher, D. C. Hines, X. Fan, C. Papovich, D. E. Vanden Berk, G. B. Trammell, D. P. Schneider, M. Vestergaard, D. G. York, S. Jester, S. F. Anderson, T. Budavári, and A. S. Szalay. Spectral Energy Distributions and Multiwavelength Selection of Type 1 Quasars. ApJS, 166:470–497, October 2006. doi: 10.1086/506525.

D. Richstone, E. A. Ajhar, R. Bender, G. Bower, A. Dressler, S. M. Faber, A. V. Filippenko, K. Gebhardt, R. Green, L. C. Ho, J. Kormendy, T. R. Lauer, J. Magorrian, and S. Tremaine. Supermassive black holes and the evolution of galaxies. Nature, 395:A14, October 1998.

A. G. Riess, A. V. Filippenko, P. Challis, A. Clocchiatti, A. Diercks, P. M. Garnavich, R. L. Gilliland, C. J. Hogan, S. Jha, R. P. Kirshner, B. Leibundgut, M. M. Phillips, D. Reiss, B. P. Schmidt, R. A. Schommer, R. C. Smith, J. Spyromilio, C. Stubbs, N. B. Suntzeff, and J. Tonry. Observational Evidence from Supernovae for an Accelerating Universe and a Cosmological Constant. AJ, 116:1009–1038, September 1998. doi: 10.1086/300499.

J. S. Ritter, C. Safranek-Shrader, O. Gnat, M. Milosavljević, and V. Bromm. Confined Population III Enrichment and the Prospects for Prompt Second-generation Star Formation. ApJ, 761:56, December 2012. doi: 10.1088/0004-637X/761/1/56.

D. C. Robinson. Uniqueness of the Kerr black hole. *Physical Review Letters*, 34:905, April 1975. doi: 10.1103/PhysRevLett.34.905.

I. Robson, R. S. Priddey, K. G. Isaak, and R. G. McMahon. Submillimetre observations of z > 6 quasars. MNRAS, 351:L29–L33, June 2004. doi: 10.1111/j.1365-2966.2004.07923.x.

K. Rowlands, H. L. Gomez, L. Dunne, A. Aragón-Salamanca, S. Dye, S. Maddox, E. da Cunha, and P. van der Werf. The dust budget crisis in high-redshift submillimetre galaxies. MNRAS, 441:1040–1058, June 2014. doi: 10.1093/mnras/stu605.

T. Ryu, T. L. Tanaka, R. Perna, and Z. Haiman. Intermediate-mass black holes from Population III remnants in the first galactic nuclei. MNRAS, 460:4122–4134, August 2016. doi: 10.1093/mnras/stw1241.

Y. Sakurai, K. Inayoshi, and Z. Haiman. Hyper-Eddington mass accretion on to a black hole with super-Eddington luminosity. MNRAS, 461:4496–4504, October 2016. doi: 10.1093/mnras/stw1652.

S. Salvadori and A. Ferrara. Ultra faint dwarfs: probing early cosmic star formation. MNRAS, 395:L6–L10, May 2009. doi: 10.1111/j.1745-3933.2009.00627.x.

S. Salvadori and A. Ferrara. First stars in damped Lyα systems. MNRAS, 421:L29–L33, March 2012. doi: 10.1111/j.1745-3933.2011.01200.x.

E. Sani, A. Marconi, L. K. Hunt, and G. Risaliti. The Spitzer/IRAC view of black hole-bulge scaling relations. MNRAS, 413:1479–1494, May 2011. doi: 10.1111/j.1365-2966.2011.18229.x.

P. Santini, R. Maiolino, B. Magnelli, L. Silva, A. Grazian, B. Altieri, P. Andreani, H. Aussel, S. Berta, A. Bongiovanni, D. Brisbin, F. Calura, A. Cava, J. Cepa, A. Cimatti, E. Daddi, H. Dannerbauer, H. Dominguez-Sanchez, D. Elbaz, A. Fontana, N. Förster Schreiber, R. Genzel, G. L. Granato, C. Gruppioni, D. Lutz, G. Magdis, M. Magliocchetti, F. Matteucci, R. Nordon, I. Pérez Garcia, A. Poglitsch, P. Popesso, F. Pozzi, L. Riguccini, G. Rodighiero, A. Saintonge, M. Sanchez-Portal, L. Shao, E. Sturm, L. Tacconi, and I. Valtchanov. The dust content of high-z submillimeter galaxies revealed by Herschel. A&A, 518:L154, July 2010. doi: 10.1051/0004-6361/201014748.

S. Y. Sazonov, J. P. Ostriker, and R. A. Sunyaev. Quasars: the characteristic spectrum and the induced radiative heating. MNRAS, 347:144–156, January 2004. doi: 10.1111/j.1365-2966.2004.07184.x.

A. Sądowski. Slim Disks Around Kerr Black Holes Revisited. ApJS, 183:171–178, August 2009. doi: 10.1088/0067-0049/183/2/171.

A. Sądowski. Slim accretion disks around black holes. *ArXiv e-prints*, August 2011.

A. Sądowski and R. Narayan. Three-dimensional simulations of supercritical black hole accretion discs - luminosities, photon trapping and variability. MNRAS, 456:3929, 2016.

A. Sądowski, M. Abramowicz, M. Bursa, W. Kluźniak, J.-P. Lasota, and A. Różańska. Relativistic slim disks with vertical structure. A&A, 527:A17, March 2011. doi: 10.1051/0004-6361/201015256.

A. Sądowski, R. Narayan, R. Penna, and Y. Zhu. Energy, momentum and mass outflows and feedback from thick accretion discs around rotating black holes. MNRAS, 436:3856–3874, December 2013. doi: 10.1093/mnras/stt1881.

A. Sądowski, R. Narayan, J. C. McKinney, and A. Tchekhovskoy. Numerical simulations of super-critical black hole accretion flows in general relativity. MNRAS, 439:503–520, March 2014. doi: 10.1093/mnras/stt2479.

D. Schaerer. On the properties of massive Population III stars and metal-free stellar populations. A&A, 382:28–42, January 2002. doi: 10.1051/0004-6361:20011619.

A. T. P. Schauer, D. J. Whalen, S. C. O. Glover, and R. S. Klessen. Lyman-Werner UV escape fractions from primordial haloes. MNRAS, 454:2441–2450, December 2015. doi: 10.1093/mnras/stv2117.

A. T. P. Schauer, B. Agarwal, S. C. O. Glover, R. S. Klessen, M. A. Latif, L. Mas-Ribas, C.-E. Rydberg, D. J. Whalen, and E. Zackrisson. Lyman-Werner escape fractions from the first galaxies. MNRAS, 467:2288–2300, May 2017a. doi: 10.1093/mnras/stx264.

A. T. P. Schauer, J. Regan, S. C. O. Glover, and R. S. Klessen. The formation of direct collapse black holes under the influence of streaming velocities. *ArXiv e-prints*, May 2017b.

D. R. G. Schleicher, M. Spaans, and R. S. Klessen. Probing high-redshift quasars with ALMA. I. Expected observables and potential number of sources. A&A, 513:A7, April 2010. doi: 10.1051/0004-6361/200913467.

R. Schneider, A. Ferrara, P. Natarajan, and K. Omukai. First Stars, Very Massive Black Holes, and Metals. ApJ, 571:30–39, May 2002. doi: 10.1086/339917.

R. Schneider, A. Ferrara, R. Salvaterra, K. Omukai, and V. Bromm. Low-mass relics of early star formation. Nature, 422:869–871, April 2003.

R. Schneider, K. Omukai, A. K. Inoue, and A. Ferrara. Fragmentation of star-forming clouds enriched with the first dust. MNRAS, 369:1437–1444, July 2006a. doi: 10.1111/j.1365-2966.2006.10391.x.

R. Schneider, R. Salvaterra, A. Ferrara, and B. Ciardi. Constraints on the initial mass function of the first stars. MNRAS, 369:825–834, June 2006b. doi: 10.1111/j.1365-2966.2006.10331.x.

R. Schneider, K. Omukai, S. Bianchi, and R. Valiante. The first low-mass stars: critical metallicity or dust-to-gas ratio? MNRAS, 419:1566–1575, January 2012a. doi: 10.1111/j.1365-2966.2011.19818.x.

R. Schneider, K. Omukai, M. Limongi, A. Ferrara, R. Salvaterra, A. Chieffi, and S. Bianchi. The formation of the extremely primitive star SDSS J102915+172927 relies on dust. MNRAS, 423:L60–L64, June 2012b. doi: 10.1111/j.1745-3933.2012.01257.x.

R. Schneider, S. Bianchi, R. Valiante, G. Risaliti, and S. Salvadori. The origin of the far-infrared continuum of z $\sim$ 6 quasars. A radiative transfer model for SDSS J1148+5251. A&A, 579:A60, July 2015. doi: 10.1051/0004-6361/201526105.

J. D. Schnittman, A. Buonanno, J. R. van Meter, J. G. Baker, W. D. Boggs, J. Centrella, B. J. Kelly, and S. T. McWilliams. Anatomy of the binary black hole recoil: A multipolar analysis. Phys. Rev. D, 77(4):044031, February 2008. doi: 10.1103/PhysRevD.77.044031.

C. Schreiber, M. Pannella, D. Elbaz, M. Béthermin, H. Inami, M. Dickinson, B. Magnelli, T. Wang, H. Aussel, E. Daddi, S. Juneau, X. Shu, M. T. Sargent, V. Buat, S. M.

Faber, H. C. Ferguson, M. Giavalisco, A. M. Koekemoer, G. Magdis, G. E. Morrison, C. Papovich, P. Santini, and D. Scott. The Herschel view of the dominant mode of galaxy growth from z = 4 to the present day. A&A, 575:A74, March 2015. doi: 10.1051/0004-6361/201425017.

K. Schwarzschild. On the Gravitational Field of a Mass Point According to Einstein's Theory. *Abh. Konigl. Preuss. Akad. Wissenschaften Jahre 1906,92, Berlin,1907*, 1916, 1916.

A. C. Seth, M. Cappellari, N. Neumayer, N. Caldwell, N. Bastian, K. Olsen, R. D. Blum, V. P. Debattista, R. McDermid, T. Puzia, and A. Stephens. The NGC 404 Nucleus: Star Cluster and Possible Intermediate-mass Black Hole. ApJ, 714:713–731, May 2010. doi: 10.1088/0004-637X/714/1/713.

N. I. Shakura and R. A. Sunyaev. Black holes in binary systems. Observational appearance. A&A, 24:337–355, 1973.

C. Shang, G. L. Bryan, and Z. Haiman. Supermassive black hole formation by direct collapse: keeping protogalactic gas H_2 free in dark matter haloes with virial temperatures $T_{vir} \gtrsim 10^4$ K. MNRAS, 402:1249–1262, February 2010. doi: 10.1111/j.1365-2966.2009.15960.x.

S. L. Shapiro. Spin, Accretion, and the Cosmological Growth of Supermassive Black Holes. ApJ, 620:59–68, February 2005. doi: 10.1086/427065.

O. Shemmer, W. N. Brandt, H. Netzer, R. Maiolino, and S. Kaspi. The Hard X-Ray Spectrum as a Probe for Black Hole Growth in Radio-Quiet Active Galactic Nuclei. ApJ, 682:81-93, July 2008. doi: 10.1086/588776.

S. Shen, H. J. Mo, S. D. M. White, M. R. Blanton, G. Kauffmann, W. Voges, J. Brinkmann, and I. Csabai. The size distribution of galaxies in the Sloan Digital Sky Survey. MNRAS, 343:978–994, August 2003. doi: 10.1046/j.1365-8711.2003.06740.x.

D. C. Shih, K. Iwasawa, and A. C. Fabian. Evidence for an intermediate-mass black hole and a multi-zone warm absorber in NGC 4395. MNRAS, 341:973–980, May 2003. doi: 10.1046/j.1365-8711.2003.06482.x.

T. Shimura and T. Manmoto. Radiation spectrum from relativistic slim accretion discs: an effect of photon trapping. MNRAS, 338:1013–1024, February 2003. doi: 10.1046/j.1365-8711.2003.06158.x.

H. Shirakata, T. Kawaguchi, T. Okamoto, R. Makiya, T. Ishiyama, Y. Matsuoka, M. Nagashima, M. Enoki, T. Oogi, and M. A. R. Kobayashi. Theoretical re-evaluations of the black hole mass-bulge mass relation - I. Effect of seed black hole mass. MNRAS, 461:4389–4394, October 2016. doi: 10.1093/mnras/stw1798.

F. H. Shu. *The physics of astrophysics. Volume 1: Radiation.* University Science Books, 1991.

D. Sijacki, V. Springel, and M. G. Haehnelt. Growing the first bright quasars in cosmological simulations of structure formation. MNRAS, 400:100–122, November 2009. doi: 10.1111/j.1365-2966.2009.15452.x.

J. Silk. Unleashing Positive Feedback: Linking the Rates of Star Formation, Supermassive Black Hole Accretion, and Outflows in Distant Galaxies. ApJ, 772:112, August 2013. doi: 10.1088/0004-637X/772/2/112.

J. Silk and M. J. Rees. Quasars and galaxy formation. A&A, 331:L1–L4, March 1998.

J. D. Silverman, K. Kovač, C. Knobel, S. Lilly, M. Bolzonella, F. Lamareille, V. Mainieri, M. Brusa, N. Cappelluti, Y. Peng, G. Hasinger, G. Zamorani, M. Scodeggio, T. Contini, C. M. Carollo, K. Jahnke, J.-P. Kneib, O. Le Fevre, S. Bardelli, A. Bongiorno, H. Brunner, K. Caputi, F. Civano, A. Comastri, G. Coppa, O. Cucciati, S. de la Torre, L. de Ravel, M. Elvis, A. Finoguenov, F. Fiore, P. Franzetti, B. Garilli, R. Gilli, R. Griffiths, A. Iovino, P. Kampczyk, A. Koekemoer, J.-F. Le Borgne, V. Le Brun, C. Maier, M. Mignoli, R. Pello, E. Perez Montero, E. Ricciardelli, M. Tanaka, L. Tasca, L. Tresse, D. Vergani, C. Vignali, E. Zucca, D. Bottini, A. Cappi, P. Cassata, C. Marinoni, H. J. McCracken, P. Memeo, B. Meneux, P. Oesch, C. Porciani, and M. Salvato. The Environments of Active Galactic Nuclei within the zCOSMOS Density Field. ApJ, 695:171–182, April 2009. doi: 10.1088/0004-637X/695/1/171.

C. Simpson, D. Mortlock, S. Warren, S. Cantalupo, P. Hewett, R. McLure, R. McMahon, and B. Venemans. No excess of bright galaxies around the redshift 7.1 quasar ULAS J1120+0641. MNRAS, 442:3454–3461, August 2014. doi: 10.1093/mnras/stu1116.

J. Smidt, B. K. Wiggins, and J. L. Johnson. Ab Initio Cosmological Simulations of CR7 as an Active Black Hole. ApJ, 829:L6, September 2016. doi: 10.3847/2041-8205/829/1/L6.

J. Smidt, D. J. Whalen, J. L. Johnson, and H. Li. The Formation of the First Quasars in the Universe. *ArXiv e-prints*, March 2017.

A. Smith, V. Bromm, and A. Loeb. Evidence for a direct collapse black hole in the Lyman α source CR7. MNRAS, 460:3143–3151, August 2016. doi: 10.1093/mnras/stw1129.

B. D. Smith, J. H. Wise, B. W. O'Shea, M. L. Norman, and S. Khochfar. The first Population II stars formed in externally enriched mini-haloes. MNRAS, 452:2822–2836, September 2015. doi: 10.1093/mnras/stv1509.

L. F. Smith, P. Biermann, and P. G. Mezger. Star formation rates in the Galaxy. A&A, 66: 65–76, May 1978.

D. Sobral, J. Matthee, B. Darvish, D. Schaerer, B. Mobasher, H. J. A. Röttgering, S. Santos, and S. Hemmati. Evidence for PopIII-like Stellar Populations in the Most Luminous Lyman-α Emitters at the Epoch of Reionization: Spectroscopic Confirmation. ApJ, 808: 139, August 2015. doi: 10.1088/0004-637X/808/2/139.

P. M. Solomon, D. Downes, S. J. E. Radford, and J. W. Barrett. The Molecular Interstellar Medium in Ultraluminous Infrared Galaxies. ApJ, 478:144–161, March 1997.

R. S. Somerville and T. S. Kolatt. How to plant a merger tree. MNRAS, 305:1–14, May 1999. doi: 10.1046/j.1365-8711.1999.02154.x.

M. Spaans and R. Meijerink. On the Detection of High-Redshift Black Holes with ALMA through CO and H_2 Emission. ApJ, 678:L5, May 2008. doi: 10.1086/588253.

M. Spaans and J. Silk. Pregalactic Black Hole Formation with an Atomic Hydrogen Equation of State. ApJ, 652:902–906, December 2006. doi: 10.1086/508444.

V. Springel. Modelling star formation and feedback in simulations of interacting galaxies. MNRAS, 312:859–879, March 2000. doi: 10.1046/j.1365-8711.2000.03187.x.

V. Springel, T. Di Matteo, and L. Hernquist. Modelling feedback from stars and black holes in galaxy mergers. MNRAS, 361:776–794, August 2005. doi: 10.1111/j.1365-2966.2005.09238.x.

A. Stacy, T. H. Greif, and V. Bromm. The first stars: formation of binaries and small multiple systems. MNRAS, 403:45–60, March 2010. doi: 10.1111/j.1365-2966.2009.16113.x.

A. Stacy, T. H. Greif, and V. Bromm. The first stars: mass growth under protostellar feedback. MNRAS, 422:290–309, May 2012. doi: 10.1111/j.1365-2966.2012.20605.x.

A. Stacy, V. Bromm, and A. T. Lee. Building up the Population III initial mass function from cosmological initial conditions. MNRAS, 462:1307–1328, October 2016. doi: 10.1093/mnras/stw1728.

A. T. Steffen, I. Strateva, W. N. Brandt, D. M. Alexander, A. M. Koekemoer, B. D. Lehmer, D. P. Schneider, and C. Vignali. The X-Ray-to-Optical Properties of Optically Selected Active Galaxies over Wide Luminosity and Redshift Ranges. AJ, 131:2826–2842, June 2006. doi: 10.1086/503627.

M. Stiavelli, S. G. Djorgovski, C. Pavlovsky, C. Scarlata, D. Stern, A. Mahabal, D. Thompson, M. Dickinson, N. Panagia, and G. Meylan. Evidence of Primordial Clustering around the QSO SDSS J1030+0524 at z=6.28. ApJ, 622:L1–L4, March 2005. doi: 10.1086/429406.

G. Stratta, R. Maiolino, F. Fiore, and V. D'Elia. Dust Properties at z = 6.3 in the Host Galaxy of GRB 050904. ApJ, 661:L9–L12, May 2007. doi: 10.1086/518502.

K. Sugimura, K. Omukai, and A. K. Inoue. The critical radiation intensity for direct collapse black hole formation: dependence on the radiation spectral shape. MNRAS, 445: 544–553, November 2014. doi: 10.1093/mnras/stu1778.

H. Susa, K. Hasegawa, and N. Tominaga. The Mass Spectrum of the First Stars. ApJ, 792: 32, September 2014. doi: 10.1088/0004-637X/792/1/32.

R. S. Sutherland and M. A. Dopita. Cooling functions for low-density astrophysical plasmas. ApJS, 88:253–327, September 1993. doi: 10.1086/191823.

K. Takahashi, T. Yoshida, H. Umeda, K. Sumiyoshi, and S. Yamada. Exact and approximate expressions of energy generation rates and their impact on the explosion properties of pair instability supernovae. MNRAS, 456:1320–1331, February 2016. doi: 10.1093/mnras/stv2649.

S. Takeuchi, S. Mineshige, and K. Ohsuga. Modified Slim-Disk Model Based on Radiation-Hydrodynamic Simulation Data: The Conflict between Outflow and Photon Trapping. PASJ, 61:783–790, August 2009. doi: 10.1093/pasj/61.4.783.

T. Tanaka and Z. Haiman. The Assembly of Supermassive Black Holes at High Redshifts. ApJ, 696:1798–1822, May 2009. doi: 10.1088/0004-637X/696/2/1798.

The LIGO Scientific Collaboration, the Virgo Collaboration, B. P. Abbott, R. Abbott, T. D. Abbott, F. Acernese, K. Ackley, C. Adams, T. Adams, P. Addesso, and et al. GW170814: A Three-Detector Observation of Gravitational Waves from a Binary Black Hole Coalescence. *ArXiv e-prints*, September 2017.

C. E. Thornton, A. J. Barth, L. C. Ho, R. E. Rutledge, and J. E. Greene. The Host Galaxy and Central Engine of the Dwarf Active Galactic Nucleus POX 52. ApJ, 686:892-910, October 2008. doi: 10.1086/591519.

L. Tornatore, S. Borgani, K. Dolag, and F. Matteucci. Chemical enrichment of galaxy clusters from hydrodynamical simulations. MNRAS, 382:1050–1072, December 2007. doi: 10.1111/j.1365-2966.2007.12070.x.

B. Trakhtenbrot, P. Lira, H. Netzer, C. Cicone, R. Maiolino, and O. Shemmer. ALMA Observations Show Major Mergers Among the Host Galaxies of Fast-growing, High-redshift#8203 Supermassive#8203 Black Holes. ApJ, 836:8, February 2017a. doi: 10.3847/1538-4357/836/1/8.

B. Trakhtenbrot, M. Volonteri, and P. Natarajan. On the Accretion Rates and Radiative Efficiencies of the Highest-redshift Quasars. ApJ, 836:L1, February 2017b. doi: 10.3847/2041-8213/836/1/L1.

E. Treister, C. M. Urry, and S. Virani. The Space Density of Compton-Thick Active Galactic Nucleus and the X-Ray Background. ApJ, 696:110–120, May 2009. doi: 10.1088/0004-637X/696/1/110.

E. Treister, K. Schawinski, M. Volonteri, and P. Natarajan. New Observational Constraints on the Growth of the First Supermassive Black Holes. ApJ, 778:130, December 2013. doi: 10.1088/0004-637X/778/2/130.

M. Trichas, P. J. Green, J. D. Silverman, T. Aldcroft, W. Barkhouse, R. A. Cameron, A. Constantin, S. L. Ellison, C. Foltz, D. Haggard, B. T. Jannuzi, D.-W. Kim, H. L. Marshall, A. Mossman, L. M. Pérez, E. Romero-Colmenero, A. Ruiz, M. G. Smith, P. S. Smith, G. Torres, D. R. Wik, B. J. Wilkes, and A. Wolfgang. The Chandra Multi-wavelength Project: Optical Spectroscopy and the Broadband Spectral Energy Distributions of X-Ray-selected AGNs. ApJS, 200:17, June 2012. doi: 10.1088/0067-0049/200/2/17.

M. J. Turk, T. Abel, and B. O'Shea. The Formation of Population III Binaries from Cosmological Initial Conditions. *Science*, 325:601, July 2009. doi: 10.1126/science.1173540.

Y. Ueda, M. Akiyama, K. Ohta, and T. Miyaji. Cosmological evolution of the hard x-ray active galactic nucleus luminosity function and the origin of the hard x-ray background. ApJ, 598:886, 2003.

Y. Utsumi, T. Goto, N. Kashikawa, S. Miyazaki, Y. Komiyama, H. Furusawa, and R. Overzier. A Large Number of z > 6 Galaxies Around a QSO at z = 6.43: Evidence for a Protocluster? ApJ, 721:1680–1688, October 2010. doi: 10.1088/0004-637X/721/2/1680.

R. Valiante, R. Schneider, S. Bianchi, and A. C. Andersen. Stellar sources of dust in the high-redshift Universe. MNRAS, 397:1661–1671, August 2009. doi: 10.1111/j.1365-2966.2009.15076.x.

R. Valiante, R. Schneider, S. Salvadori, and S. Bianchi. The origin of the dust in high-redshift quasars: the case of SDSS J1148+5251. MNRAS, 416:1916–1935, September 2011. doi: 10.1111/j.1365-2966.2011.19168.x.

R. Valiante, R. Schneider, R. Maiolino, S. Salvadori, and S. Bianchi. Quasar feedback in the early Universe: the case of SDSS J1148+5251. MNRAS, 427:L60–L64, November 2012. doi: 10.1111/j.1745-3933.2012.01345.x.

R. Valiante, R. Schneider, S. Salvadori, and S. Gallerani. High-redshift quasars host galaxies: is there a stellar mass crisis? MNRAS, 444:2442–2455, November 2014. doi: 10.1093/mnras/stu1613.

R. Valiante, R. Schneider, M. Volonteri, and K. Omukai. From the first stars to the first black holes. MNRAS, 457:3356–3371, April 2016. doi: 10.1093/mnras/stw225.

R. Valiante, B. Agarwal, M. Habouzit, and E. Pezzulli. On the formation of the first quasars. *ArXiv e-prints*, March 2017.

M. Valluri, L. Ferrarese, D. Merritt, and C. L. Joseph. The Low End of the Supermassive Black Hole Mass Function: Constraining the Mass of a Nuclear Black Hole in NGC 205 via Stellar Kinematics. ApJ, 628:137–152, July 2005. doi: 10.1086/430752.

S. van Wassenhove, M. Volonteri, M. G. Walker, and J. R. Gair. Massive black holes lurking in Milky Way satellites. MNRAS, 408:1139–1146, October 2010. doi: 10.1111/j.1365-2966.2010.17189.x.

B. P. Venemans, J. R. Findlay, W. J. Sutherland, G. De Rosa, R. G. McMahon, R. Simcoe, E. A. Gonzalez-Solares, K. Kuijken, and J. R. Lewis. Discovery of three z>6.5 quasars in the VISTA Kilo-degree Infrared Galaxy (VIKING) survey. *ArXiv e-prints:1311.3666*, November 2013.

B. P. Venemans, G. A. Verdoes Kleijn, J. Mwebaze, E. A. Valentijn, E. Bañados, R. Decarli, J. T. A. de Jong, J. R. Findlay, K. H. Kuijken, F. L. Barbera, J. P. McFarland, R. G. McMahon, N. Napolitano, G. Sikkema, and W. J. Sutherland. First discoveries of z ∼ 6 quasars with the Kilo-Degree Survey and VISTA Kilo-Degree Infrared Galaxy survey. MNRAS, 453:2259–2266, November 2015. doi: 10.1093/mnras/stv1774.

B. P. Venemans, F. Walter, L. Zschaechner, R. Decarli, G. De Rosa, J. R. Findlay, R. G. McMahon, and W. J. Sutherland. Bright [C ii] and Dust Emission in Three z > 6.6

Quasar Host Galaxies Observed by ALMA. ApJ, 816:37, January 2016. doi: 10.3847/0004-637X/816/1/37.

B. P. Venemans, F. Walter, R. Decarli, E. Bañados, J. Hodge, P. Hewett, R. G. McMahon, D. J. Mortlock, and C. Simpson. The Compact, ∼1 kpc Host Galaxy of a Quasar at a Redshift of 7.1. ApJ, 837:146, March 2017. doi: 10.3847/1538-4357/aa62ac.

E. Visbal, Z. Haiman, and G. L. Bryan. Direct collapse black hole formation from synchronized pairs of atomic cooling haloes. MNRAS, 445:1056–1063, November 2014. doi: 10.1093/mnras/stu1794.

E. Visbal, Z. Haiman, and G. L. Bryan. Formation of massive Population III galaxies through photoionization feedback: a possible explanation for CR 7. MNRAS, 460:L59–L63, July 2016. doi: 10.1093/mnrasl/slw071.

F. Vito, C. Vignali, R. Gilli, A. Comastri, K. Iwasawa, W. N. Brandt, D. M. Alexander, M. Brusa, B. Lehmer, F. E. Bauer, D. P. Schneider, Y. Q. Xue, and B. Luo. The high-redshift ($z > 3$) active galactic nucleus population in the 4-ms chandra deep field-south. MNRAS, 428:354, 2013.

F. Vito, R. Gilli, C. Vignali, W. N. Brandt, A. Comastri, G. Yang, B. D. Lehmer, B. Luo, A. Basu-Zych, F. E. Bauer, N. Cappelluti, A. Koekemoer, V. Mainieri, M. Paolillo, P. Ranalli, O. Shemmer, J. Trump, J. X. Wang, and Y. Q. Xue. The deepest X-ray view of high-redshift galaxies: constraints on low-rate black hole accretion. MNRAS, 463:348–374, November 2016. doi: 10.1093/mnras/stw1998.

M. Volonteri. Formation of supermassive black holes. A&A Rev., 18:279–315, July 2010. doi: 10.1007/s00159-010-0029-x.

M. Volonteri and J. Bellovary. Black holes in the early Universe. *Reports on Progress in Physics*, 75(12):124901, December 2012. doi: 10.1088/0034-4885/75/12/124901.

M. Volonteri and P. Natarajan. Journey to the M_{BH}-σ relation: the fate of low-mass black holes in the Universe. MNRAS, 400:1911–1918, December 2009. doi: 10.1111/j.1365-2966.2009.15577.x.

M. Volonteri and M. J. Rees. Rapid Growth of High-Redshift Black Holes. ApJ, 633: 624–629, November 2005. doi: 10.1086/466521.

M. Volonteri and M. J. Rees. Quasars at z=6: The Survival of the Fittest. ApJ, 650: 669–678, October 2006. doi: 10.1086/507444.

M. Volonteri and D. P. Stark. Assessing the redshift evolution of massive black holes and their hosts. MNRAS, 417:2085–2093, November 2011. doi: 10.1111/j.1365-2966.2011.19391.x.

M. Volonteri, F. Haardt, and P. Madau. The Assembly and Merging History of Supermassive Black Holes in Hierarchical Models of Galaxy Formation. ApJ, 582:559–573, January 2003. doi: 10.1086/344675.

M. Volonteri, G. Lodato, and P. Natarajan. The evolution of massive black hole seeds. MNRAS, 383:1079–1088, January 2008. doi: 10.1111/j.1365-2966.2007.12589.x.

M. Volonteri, J. Silk, and G. Dubus. The Case for Supercritical Accretion onto Massive Black Holes at High Redshift. ApJ, 804:148, May 2015. doi: 10.1088/0004-637X/804/2/148.

M. Volonteri, T. Bogdanović, M. Dotti, and M. Colpi. Massive Black Holes in Merging Galaxies. *IAU Focus Meeting*, 29:285–291, 2016a. doi: 10.1017/S1743921316005366.

M. Volonteri, Y. Dubois, C. Pichon, and J. Devriendt. The cosmic evolution of massive black holes in the Horizon-AGN simulation. MNRAS, 460:2979–2996, August 2016b. doi: 10.1093/mnras/stw1123.

A. Y. Wagner, M. Umemura, and G. V. Bicknell. Ultrafast Outflows: Galaxy-scale Active Galactic Nucleus Feedback. ApJ, 763:L18, January 2013. doi: 10.1088/2041-8205/763/1/L18.

F. Walter, C. Carilli, F. Bertoldi, K. Menten, P. Cox, K. Y. Lo, X. Fan, and M. A. Strauss. Resolved Molecular Gas in a Quasar Host Galaxy at Redshift z=6.42. ApJ, 615:L17–L20, November 2004. doi: 10.1086/426017.

J.-M. Wang, E. Szuszkiewicz, F.-J. Lu, and Y.-Y. Zhou. Emergent Spectra from Slim Accretion Disks in Active Galactic Nuclei. ApJ, 522:839–845, September 1999. doi: 10.1086/307686.

J. X. Wang, S. Malhotra, and J. E. Rhoads. An Overdensity of Lyα Emitters at Redshift z$\sim$ 5.7 near the Hubble Ultra Deep Field. ApJ, 622:L77–L80, April 2005. doi: 10.1086/429617.

R. Wang, C. L. Carilli, J. Wagg, F. Bertoldi, F. Walter, K. M. Menten, A. Omont, P. Cox, M. A. Strauss, X. Fan, L. Jiang, and D. P. Schneider. Thermal Emission from Warm Dust in the Most Distant Quasars. ApJ, 687:848-858, November 2008. doi: 10.1086/591076.

R. Wang, C. L. Carilli, R. Neri, D. A. Riechers, J. Wagg, F. Walter, F. Bertoldi, K. M. Menten, A. Omont, P. Cox, and X. Fan. Molecular Gas in z $\sim$ 6 Quasar Host Galaxies. ApJ, 714:699–712, May 2010. doi: 10.1088/0004-637X/714/1/699.

R. Wang, J. Wagg, C. L. Carilli, F. Walter, L. Lentati, X. Fan, D. A. Riechers, F. Bertoldi, D. Narayanan, M. A. Strauss, P. Cox, A. Omont, K. M. Menten, K. K. Knudsen, R. Neri, and L. Jiang. Star Formation and Gas Kinematics of Quasar Host Galaxies at z $\sim$ 6: New Insights from ALMA. ApJ, 773:44, August 2013. doi: 10.1088/0004-637X/773/1/44.

K.-y. Watarai, J. Fukue, M. Takeuchi, and S. Mineshige. Galactic Black-Hole Candidates Shining at the Eddington Luminosity. PASJ, 52:133, February 2000. doi: 10.1093/pasj/52.1.133.

A. K. Weigel, K. Schawinski, E. Treister, C. M. Urry, M. Koss, and B. Trakhtenbrot. The systematic search for z $\gtrsim$ 5 active galactic nuclei in the Chandra Deep Field South. MNRAS, 448:3167–3195, April 2015. doi: 10.1093/mnras/stv184.

D. R. Weisz and M. Boylan-Kolchin. Local Group ultra-faint dwarf galaxies in the reionization era. MNRAS, 469:L83–L88, July 2017. doi: 10.1093/mnrasl/slx043.

D. Whalen, T. Abel, and M. L. Norman. Radiation Hydrodynamic Evolution of Primordial H II Regions. ApJ, 610:14–22, July 2004. doi: 10.1086/421548.

D. Whalen, B. van Veelen, B. W. O'Shea, and M. L. Norman. The Destruction of Cosmological Minihalos by Primordial Supernovae. ApJ, 682:49-67, July 2008. doi: 10.1086/589643.

D. J. Whalen and C. L. Fryer. The Formation of Supermassive Black Holes from Low-mass Pop III Seeds. ApJ, 756:L19, September 2012. doi: 10.1088/2041-8205/756/1/L19.

C. J. Willott, R. J. McLure, and M. J. Jarvis. A 3×10^9 M_{solar} Black Hole in the Quasar SDSS J1148+5251 at z=6.41. ApJ, 587:L15–L18, April 2003. doi: 10.1086/375126.

C. J. Willott, D. Crampton, J. B. Hutchings, M. Sawicki, L. Simard, M. J. Jarvis, R. J. McLure, and W. J. Percival. A Search for the First Massive Galaxy Clusters. In A. Merloni, S. Nayakshin, and R. A. Sunyaev, editors, *Growing Black Holes: Accretion in a Cosmological Context*, pages 102–107, 2005. doi: 10.1007/11403913_12.

C. J. Willott, L. Albert, D. Arzoumanian, J. Bergeron, D. Crampton, P. Delorme, J. B. Hutchings, A. Omont, C. Reylé, and D. Schade. Eddington-limited Accretion and the Black Hole Mass Function at Redshift 6. AJ, 140:546–560, August 2010. doi: 10.1088/0004-6256/140/2/546.

C. J. Willott, J. Bergeron, and A. Omont. Star Formation Rate and Dynamical Mass of 10^8 Solar Mass Black Hole Host Galaxies At Redshift 6. ApJ, 801:123, March 2015. doi: 10.1088/0004-637X/801/2/123.

J. H. Wise and T. Abel. Suppression of H_2 Cooling in the Ultraviolet Background. ApJ, 671:1559–1567, December 2007. doi: 10.1086/522876.

J. H. Wise and T. Abel. Resolving the Formation of Protogalaxies. III. Feedback from the First Stars. ApJ, 685:40-56, September 2008. doi: 10.1086/590417.

J. Wolcott-Green, Z. Haiman, and G. L. Bryan. Photodissociation of H_2 in protogalaxies: modelling self-shielding in three-dimensional simulations. MNRAS, 418:838–852, December 2011. doi: 10.1111/j.1365-2966.2011.19538.x.

J Wolcott-Green, Z Haiman, and G L Bryan. Beyond Jcrit: a critical curve for suppression of H2-cooling in protogalaxies. *MNRAS*, page stx167, January 2017.

J. M. Wrobel and L. C. Ho. Radio Emission on Subparsec Scales from the Intermediate-Mass Black Hole in NGC 4395. ApJ, 646:L95–L98, August 2006. doi: 10.1086/507102.

X.-B. Wu, F. Wang, X. Fan, W. Yi, W. Zuo, F. Bian, L. Jiang, I. D. McGreer, R. Wang, J. Yang, Q. Yang, D. Thompson, and Y. Beletsky. An ultraluminous quasar with a twelve-billion-solar-mass black hole at redshift 6.30. Nature, 518:512–515, February 2015. doi: 10.1038/nature14241.

J. S. B. Wyithe and A. Loeb. Photon trapping enables super-Eddington growth of black hole seeds in galaxies at high redshift. MNRAS, 425:2892–2902, October 2012. doi: 10.1111/j.1365-2966.2012.21127.x.

Y. Q. Xue, B. Luo, W. N. Brandt, F. E. Bauer, B. D. Lehmer, P. S. Broos, D. P. Schneider, D. M. Alexander, M. Brusa, A. Comastri, A. C. Fabian, R. Gilli, G. Hasinger, A. E. Hornschemeier, A. Koekemoer, T. Liu, V. Mainieri, M. Paolillo, D. A. Rafferty, P. Rosati, O. Shemmer, J. D. Silverman, I. Smail, P. Tozzi, and C. Vignali. The Chandra Deep Field-South Survey: 4 Ms Source Catalogs. ApJS, 195:10, July 2011. doi: 10.1088/0067-0049/195/1/10.

H. Yajima and S. Khochfar. The role of stellar relaxation in the formation and evolution of the first massive black holes. MNRAS, 457:2423–2432, April 2016. doi: 10.1093/mnras/stw058.

T. Yaqoob. X-Ray Transmission in Cold Matter: Nonrelativistic Corrections for Compton Scattering. ApJ, 479:184–189, April 1997.

J. Yoo and J. Miralda-Escudé. Formation of the Black Holes in the Highest Redshift Quasars. ApJ, 614:L25–L28, October 2004. doi: 10.1086/425416.

N. Yoshida, K. Omukai, L. Hernquist, and T. Abel. Formation of Primordial Stars in a ΛCDM Universe. ApJ, 652:6–25, November 2006. doi: 10.1086/507978.

N. Yoshida, K. Omukai, and L. Hernquist. Protostar Formation in the Early Universe. *Science*, 321:669–, August 2008. doi: 10.1126/science.1160259.

M. Young, M. Elvis, and G. Risaliti. The Fifth Data Release Sloan Digital Sky

Survey/XMM-Newton Quasar Survey. ApJS, 183:17–32, July 2009. doi: 10.1088/0067-0049/183/1/17.

B. Yue, A. Ferrara, R. Salvaterra, Y. Xu, and X. Chen. Infrared background signatures of the first black holes. MNRAS, 433:1556–1566, August 2013. doi: 10.1093/mnras/stt826.

B. Yue, A. Ferrara, R. Salvaterra, Y. Xu, and X. Chen. The brief era of direct collapse black hole formation. MNRAS, 440:1263–1273, May 2014. doi: 10.1093/mnras/stu351.

B. Yue, A. Ferrara, and K. Helgason. Detecting high-z galaxies in the near-infrared background. MNRAS, 458:4008, 2016.

W. Zhang, S. E. Woosley, and A. Heger. Fallback and Black Hole Production in Massive Stars. ApJ, 679:639-654, May 2008. doi: 10.1086/526404.

W. Zheng, R. A. Overzier, R. J. Bouwens, R. L. White, H. C. Ford, N. Benítez, J. P. Blakeslee, L. D. Bradley, M. J. Jee, A. R. Martel, S. Mei, A. W. Zirm, G. D. Illingworth, M. Clampin, G. F. Hartig, D. R. Ardila, F. Bartko, T. J. Broadhurst, R. A. Brown, C. J. Burrows, E. S. Cheng, N. J. G. Cross, R. Demarco, P. D. Feldman, M. Franx, D. A. Golimowski, T. Goto, C. Gronwall, B. Holden, N. Homeier, L. Infante, R. A. Kimble, J. E. Krist, M. P. Lesser, F. Menanteau, G. R. Meurer, G. K. Miley, V. Motta, M. Postman, P. Rosati, M. Sirianni, W. B. Sparks, H. D. Tran, and Z. I. Tsvetanov. An Overdensity of Galaxies near the Most Distant Radio-loud Quasar. ApJ, 640:574–578, April 2006. doi: 10.1086/500167.

X.-L. Zhou and Y.-H. Zhao. Hard X-ray Photon Index as an Indicator of Bolometric Correction in Active Galactic Nuclei. ApJ, 720:L206–L210, September 2010. doi: 10.1088/2041-8205/720/2/L206.

P.-C. Zinn, E. Middelberg, R. P. Norris, and R.-J. Dettmar. Active Galactic Nucleus Feedback Works Both Ways. ApJ, 774:66, September 2013. doi: 10.1088/0004-637X/774/1/66.

K. Zubovas and A. King. Clearing Out a Galaxy. ApJ, 745:L34, February 2012. doi: 10.1088/2041-8205/745/2/L34.

K. Zubovas and A. R. King. Galaxy-wide outflows: cold gas and star formation at high speeds. MNRAS, 439:400–406, March 2014. doi: 10.1093/mnras/stt2472.